

# Habitability Of Terrestrial Planets Around Active M-Stars

The Effect Of Stellar Radiation And Cosmic Rays  
Upon Climate And Photochemistry

vorgelegt von  
Ing. MSc.  
Markus Scheucher  
ORCID: [0000-0003-4331-2277](https://orcid.org/0000-0003-4331-2277)

an der Fakultät II - Mathematik und Naturwissenschaften  
der Technischen Universität Berlin  
zur Erlangung des akademischen Grades  
Doktor der Naturwissenschaften  
-Dr.rer.nat.-  
genehmigte Dissertation

Promotionsausschuss:

Vorsitzender: Prof. Dr. Michael Lehmann

Gutachterin: Prof. Dr. Heike Rauer

Gutachter: Prof. Dr. Dieter Breitschwerdt

Gutachter: Prof. Dr. Thomas Trautmann

Tag der wissenschaftlichen Aussprache: 8. Dezember 2020

Berlin 2021



## Abstract

Although the search for life on other planets is an age old endeavor, rapid advancements in recent years are bringing this tantalising goal ever closer. There are two main steps, firstly identifying suitable targets and secondly correctly attributing the measured signals. The majority of stars in the solar neighborhood consist of cool, small M-dwarfs which can be orders of magnitude more active than the Sun.

Key issues concern the potential habitability of their planets and the range of possible atmospheric signals. These issues can be addressed in a combined effort between on the one hand observers obtaining high precision atmospheric data, and on the other hand theorists defining how life can form and persist and developing next-generation atmospheric models capable of handling a wide variety of stellar, planetary and atmospheric conditions, as well as biological phenomena. This cumulative thesis addresses the latter theoretical point of atmospheric conditions conducive to life and consists of three, first-author publications studying the effect of stellar radiation and cosmic rays upon the climates and atmospheric chemistry on potentially terrestrial exoplanets. This work has developed and applied a radiative-convective-photochemical model and provides a complimentary and theoretical background on the science behind a major radiative transfer upgrade as well as the scientific field of exoplanetary space weather which were required to address the main science questions of this thesis.

Scheucher et al. (2020b) (paper 1) describe an extensive radiative transfer upgrade of a cloud-free radiative-convective-photochemical model (1D-TERRA) resulting in a flexibility in the treatment of the host star's energy spectrum as well as in the variety of possible planetary atmospheric conditions and compositions which to our knowledge is new in the literature in this form. The new model is capable of qualitatively reproducing global atmospheric

---

temperatures for modern Earth, aerosol-free Mars, and cloud-free Venus, as shown in paper 1. With the new model, a variety of plausible atmospheres are modeled and compared to the very exciting, first ever observed water features in the atmosphere of the potentially temperate super-Earth / sub-Neptune, K2-18b. Paper 1 simulated Earth-like, Venus-like, and primordial atmospheres with varying solar metallicities, as well as mixtures thereof. A major result of paper 1 is that atmospheres heavier than a hydrogen-helium composition can likely be excluded for K2-18b. Unlike other studies with simpler climate, this study suggested that the possibility of a water ocean directly exposed to the atmosphere is unlikely.

Scheucher et al. (2018) (paper 2) perform an extensive study of uncertainties in the flare-related stellar energetic particle ranges assumed for active M-dwarfs, and the subsequent chemical production efficiency ranges in Earth-like atmospheres, which determine the atmospheric response to cosmic ray bombardment. Paper 2 investigated a hypothetical Earth-like world placed in the habitable zone around the highly active M-dwarf star AD Leonis. Cosmic ray induced photochemical responses impacting biosignature abundances and UV surface dosage are discussed in detail. A major result of paper 2 is the discovery of an enhanced spectroscopic signature for nitric acid which could be interpreted as a potential “marker” for Earth-like atmospheres which are heavily bombarded with cosmic rays.

Scheucher et al. (2020a) (paper 3) presents a habitability study of our nearest known exoplanetary neighbor, Proxima Centauri b. Its host star, Proxima Centauri, is a known flaring star. Therefore, an extensive cosmic ray model suite, developed during the course of this work as part of a collaboration of three German universities, is applied to consistently model the impact of Proxima’s activity onto global planetary temperatures and atmospheric spectral appearance. Starting with an Earth-like atmosphere, paper 3 showed that additional greenhouse gases, such as carbon dioxide, are required to achieve habitability. Methane abundances (assuming Earth’s surface methane emission) strongly increase (since the incoming stellar radiation favors weak methane loss rates) compared with Earth such that methane efficiently blocks incoming radiation and cools (the anti-greenhouse effect). Paper 3 suggests that cosmic rays effectively destroy methane, subsequently further warming the planet. Large amounts of cosmic ray induced nitrogen dioxide are formed in this study, with many absorption bands in the visible spectrum which



---

pose a potential problem for Rayleigh slope extraction from observed spectra which could complicate bulk composition estimates. Spectral band overlap due to increased carbon dioxide complicates the interpretation of another cosmic ray marker known on Earth, nitric oxide.

The above three papers present valuable contributions to the interpretation of individual spectral atmospheric features in terms of potential habitability of exoplanets around M-dwarf stars, including highly active stars. The updated methodologies used in these works set a benchmark and will serve as a foundation for future studies assessing habitability and biosignatures on such worlds.



## Zusammenfassung

Die Suche nach Leben auf anderen Planeten ist ein uraltes Unterfangen. Die rapiden Fortschritte der letzten Jahre bringen uns immer näher an das verlockende Ziel, die Entdeckung solchen Lebens. Hierzu gibt es zwei Forschungsschwerpunkte: Erstens die Identifizierung von Planeten, auf denen Leben möglich ist (habitable Planeten), und zweitens die korrekte Interpretation gemessener Signale. Die Mehrheit der Sterne in der Sonnenumgebung besteht aus kühlen, kleinen M-Zwergen, die um Größenordnungen aktiver sein können als die Sonne. Themen von besonderem Interesse sind die potenzielle Bewohnbarkeit ihrer Planeten und die zu erwartende Vielfalt an atmosphärischen Signalen. Einen Einblick hierzu liefern kombinierte Anstrengungen zwischen Beobachtern, die hochpräzise atmosphärische Daten erhalten, und Theoretikern, die zum einen definieren unter welchen Umständen Leben entstehen und fortbestehen kann, und zum anderen atmosphärische Modelle der nächsten Generation entwickeln, welche in der Lage sind, eine Vielzahl von stellaren, planetaren, atmosphärischen und biologischen Bedingungen zu bewältigen. Diese kumulative Dissertation befasst sich mit dem letztgenannten theoretischen Punkt, den atmosphärischen Bedingungen förderlich für das Entstehen und Weiterbestehen von Leben, und besteht aus drei Veröffentlichungen als Erstautor, in denen die Auswirkungen von Sternstrahlung und kosmischer Strahlung auf das Klima und die chemische Zusammensetzung der Atmosphäre möglicher terrestrischer Exoplaneten untersucht werden. Im Zuge dieser Arbeit wurde ein strahlungs-konvektiv-photochemisches Modell entwickelt und auf fiktive, sowohl als reale Planetenatmosphären angewandt. Darüber hinaus werden die zugrunde liegende Theorien des Strahlungstransfers skizziert und ein Einblick in das wissenschaftliche Feld des *exoplanetaren Weltraumwetters* gegeben.

---

Scheucher u. a. (2020b) (Publikation I) beschreibt ein umfassendes Upgrade des Strahlungstransfers eines wolkenfreien strahlungs-konvektiv-photochemischen Modells (1D-TERRA). Dieses Modell kann eine große Vielzahl an möglichen Sternspektren und möglichen planetaren atmosphärischen Bedingungen und Zusammensetzungen berücksichtigen. Diese Flexibilität ist unseres Wissens nach in dieser Form neu. Wie in Publikation I gezeigt, ist das neue Modell in der Lage, die globalen atmosphärischen Temperaturen für die moderne Erde, einen aerosolfreien Mars, und eine wolkenfreie Venus qualitativ zu reproduzieren. Des weiteren wurden mit dem neuen Modell verschiedene plausible Atmosphären für die potenziell temperierte Supererde / Sub-Neptun, K2-18b modelliert, für die erstmals Wasserabsorption in der Atmosphäre gemessen wurde. Publikation I simulierte Erdähnliche, Venusähnliche und Wasserstoffatmosphären mit unterschiedlichen solaren Metallizitäten sowie Mischungen derjenigen. Ein Hauptergebnis von Publikation I ist, dass Atmosphären, die schwerer sind als eine Wasserstoff-Helium-Zusammensetzung, für K2-18b ausgeschlossen werden können. Im Gegensatz zu anderen Studien, mit weniger komplexen Klimamodellen, folgt aus dieser Studie, dass ein der Atmosphäre ausgesetzter Wasserozean unwahrscheinlich ist.

Scheucher u. a. (2018) (Publikation II) untersuchen die atmosphärische Reaktion auf den Beschuss mit kosmischer Strahlung in erdähnlichen Atmosphären um M-Zwerg. Hierzu werden Flüsse energetischer Teilchen (hauptsächlich Protonen) angenommen, die den von stellaren Flares für aktive M-Zwerg abgedeckten Bereich beschreiben sollen, und chemische Produktionseffizienzen für erdähnliche ( $\text{O}_2\text{-N}_2$ ) Atmosphären. In Publikation II wurde eine hypothetische erdähnliche Welt in der habitablen Zone um den hochaktiven M-Zwergstern AD Leonis untersucht. Durch kosmische Strahlung induzierte photochemische Reaktionen, die sich auf Biosignaturen und die UV-Strahlung an der Oberfläche auswirken, werden ausführlich diskutiert. Ein Hauptergebnis von Publikation II ist die Entdeckung einer erhöhten spektroskopischen Signatur für Salpetersäure, die als potenzieller „Marker“ für erdähnliche Atmosphären interpretiert werden könnte, die stark mit kosmischer Strahlung bombardiert sind.

Scheucher u. a. (2020a) (Publikation III) präsentiert eine Habilitätsstudie unseres nächsten exoplanetaren Nachbarn, Proxima Centauri b. Sein Zentralstern, Proxima Centauri, ist bekannt für seine besonders hohe Aktivität. Im Rahmen dieser Arbeit wurden Verschiedene etablierten Modelle kombiniert,

---

die in Zusammenarbeit von drei Gruppen an verschiedenen deutschen Forschungseinrichtungen entwickelt wurden, um den Einfluss von kosmischer Strahlung von der Astrosphäre bis zur Planetenoberfläche zu modellieren. Damit wurden die Auswirkungen der Aktivität von Proxima Centauri auf die globalen Planetentemperaturen und die spektrale Signatur des Planeten - man denke an einen *spektralen Fingerabdruck* - konsistent untersucht. Ausgehend von einer erdähnlichen Atmosphäre zeigte Publikation III, dass zusätzliche Treibhausgase wie Kohlendioxid in höheren Konzentrationen als auf der Erde erforderlich sind, um Habitabilität zu erreichen. Der atmosphärische Methangehalt, unter Annahme von Methanemissionen wie auf der Erdoberfläche, nimmt im Vergleich zur Erde stark zu, da Proximas einfallende Sternstrahlung schwache Methanverlusten begünstigt. Dieser erhöhte Methangehalt blockiert die einfallende Strahlung effizient, was den Planeten abkühlt, bekannt als Anti-Treibhauseffekt. Publikation III legt nahe, dass kosmische Strahlung Methan effektiv zerstört was in dieser Studie wiederum zur Erwärmung des Planeten führt. In dieser Studie wird weiterhin gezeigt, dass durch die kosmische Strahlung große Mengen an Stickstoffdioxid gebildet werden. Dessen Absorptionsbanden im sichtbaren Bereich des stellaren Spektrums stellen ein potenzielles Problem für die Extraktion der Rayleigh-Steigung aus beobachteten Spektren dar. Dies könnte die Abschätzung der atmosphärischen Zusammensetzung aus Beobachtungen erschweren. Die spektrale Bandüberlappung aufgrund von erhöhtem Kohlendioxid erschwert darüber hinaus die Interpretation eines anderen auf der Erde bekannten Markers für kosmische Strahlung, Stickstoffmonoxid.

Die obigen drei Arbeiten liefern wertvolle neue Beiträge zur Interpretation einzelner spektraler atmosphärischer Merkmale im Hinblick auf die potenzielle Habitabilität von Exoplaneten um M-Zwergsterne, einschließlich hochaktiver Sterne. Mit den in dieser Arbeit entwickelten Methoden wird es in Zukunft möglich sein, vorhandene und zukünftige Messungen von atmosphärischen spektralen Signaturen zur Bewertung der Habitabilität und dem Vorhandensein von Biosignaturen zu interpretieren.



Dedicated to my beautiful wife **Christina** for all her support and patience  
with me on this enduring journey together, and our lovely daughters  
**Scarlett & Zoey** for lifting the spirit and filling our home  
with joy every day.





## Acknowledgements

I would like to especially thank my supervisor and true scientist, Prof. Heike Rauer for all her wisdom, advice and guidance on my path to research, and for always reminding me of the big pictures when my focus and interests were derailing me into potentially decades worth of remotely thesis related questions about physical processes to explore.

My sincere gratitude also goes to my mentor Lee Grenfell for his extraordinary patience with me and my endless, sometimes ridiculous questions. I have yet to meet anyone else who can seemingly recall any chemical reaction and pathway ever written down on a piece of paper and deemed remotely important for atmospheric science.

I also want to thank my collaborators Konstantin Herbst, Miriam Sinnhuber and Franz Schreier for all our fruitful discussions either in person, at conferences, via telecons, or over good-old phone calls. Further, I would like to extend my appreciation to my colleagues Mareike Godolt and Fabian Wunderlich for all our theoretical and modeling related debates and for always ensuring a friendly atmosphere in the office and all the countless meetings.

Finally I want to express my deepest gratitude to my family for their continuous support, even over long distances.



# Table of Contents

<b>1</b>	<b>Introduction</b>	<b>1</b>
1.1	Aims & Outline . . . . .	7
1.2	Radiation and Opacities in Planetary Atmospheres . . . . .	11
1.2.1	Radiative Transfer and the Two-Stream Approximation	11
1.2.2	The Importance of Optical Depth . . . . .	14
1.2.3	The Voigt Profile and Broadening Parameters . . . . .	15
1.2.4	Modeling Absorption in a Gas Mixture . . . . .	19
1.2.5	Relevance for Atmospheric Climate modeling . . . . .	24
1.3	The Effect of Energetic Particle Bombardment . . . . .	29
1.3.1	Sources and Types of Cosmic Rays . . . . .	29
1.3.2	Flares and CMEs on other stars . . . . .	33
1.3.3	Propagation and Secondary Particles . . . . .	35
1.3.4	Impact on Habitability and Biosignatures . . . . .	41
1.4	Relevant Publications . . . . .	47
<b>2</b>	<b>Publication I: Consistently Simulating a Wide Range of Atmospheric Scenarios for K2-18b with a Flexible Radiative Transfer Module</b>	<b>51</b>
<b>3</b>	<b>Publication II: New Insights into Cosmic-Ray-induced Biosignature Chemistry in Earth-like Atmospheres</b>	<b>71</b>
<b>4</b>	<b>Publication III: Proxima Centauri b: A Strong Case for Including Cosmic-Ray-induced Chemistry in Atmospheric Biosignature Studies</b>	<b>83</b>
<b>5</b>	<b>Summary &amp; Outlook</b>	<b>91</b>
5.1	Summary . . . . .	91

## TABLE OF CONTENTS

---

5.2 Outlook . . . . .	94
References	97
A Appendix	117

# List of Figures

1.1	Graphical representation of the classical habitable zone around stars with different stellar temperatures, normalized by solar values to give the effective stellar flux. Included are a few famous examples of possibly terrestrial exoplanets, as well as some of our terrestrial Solar system planets. Note that the existence of Gliese-581d is strongly debated (e.g. Robertson et al., 2014). Credit: Ramirez (2018) . . . . .	4
1.2	SED for various stars of different stellar type taken from Wunderlich et al. (2019). Observed SEDs are reconstructed and completed with theoretical predictions where necessary. .	15
1.3	Schematic representation of electromagnetic transition levels (left), and vibration and rotation modes for a symmetric linear triatomic molecule such as $\text{H}_2\text{O}$ or $\text{CO}_2$ (right). Figure adapted from Pierrehumbert (2010) . . . . .	16
1.4	Gauss (Doppler), Lorentz, and convolved Voigt profiles for different definitions of half-width, adapted from Schreier (2009)	18
1.5	Sample opacity ( $\kappa [m^{-1}]$ ) function in a spectral interval shown for an arbitrary wavelength domain $x$ (left), versus the associated $k$ -distribution in the $g$ -function domain (right) (adapted from Heng, 2017) . . . . .	21
1.6	Illustration of convective adjustment performed in 1D-TERRA.	25
1.7	Spectral Energy Distribution of GCRs at earth measured by different experiments (Blasi, 2013). Electron, positron, and antiproton spectra as measured by PAMELA (Payload for Antimatter Matter Exploration and Light-nuclei Astrophysics) (Adriani et al., 2011). . . . .	30

## LIST OF FIGURES

---

1.8	Oxygen fluence of solar energetic particles as measured by instruments on-board the ACE (Advanced Composition Explorer) spacecraft (adapted from Desai and Giacalone, 2016).	32
1.9	Occurance rate ( $\nu$ ) of flares on 373 superflaring F, K, and M-dwarf stars (having produced at least one flare of $> 5 \times 10^{34}$ erg in the <i>Kepler</i> data set) over total observed flare energy ( $E$ ) (adapted from Candelaresi et al., 2014).	33
1.10	Flare occurence rate ( $\nu$ ) over stellar effective temperature ( $T_{\text{eff}}$ ) for 115.984 G, K, and M-dwarf stars from the <i>Kepler</i> data set (adapted form Candelaresi et al., 2014).	34
1.11	Schematic of secondary particle cascades produced in a collision of a primary CR with an atom (Schlickeiser, 2002). Three types of cascade are illustrated: hadronic (center), muon ( $\pi \rightarrow \mu$ ) cascade, and the soft cascade (outer) involving X-ray photons $\gamma$ .	38
1.12	Ionization from various primary (grey and blue) and secondary (pink and green) CR sources and from photoionization (orange) in Earth's atmosphere (Mironova et al., 2015).	39
1.13	Schematic illustration of the atmospheric chemical response to CRs in an Earth-like $\text{N}_2\text{-O}_2$ atmosphere. Highlighted (colored boxes) are responses for some species which have been proposed in the literature to be biosignatures or bioindicators (adapted from Scheucher et al., 2018).	45
A.1	Comprehensive example of absorption features with 20 atmospheric constituents at $p=1$ bar and $T=300$ K calculated from the line-list HITRAN 2016, used in the new radiative transfer module REDFOX developed in this thesis.	119

# List of Tables

1.1	Summary of <a href="#">two-stream</a> approximation coefficients for absorption ( $\gamma_A$ ), scattering ( $\gamma_S$ ), isotropic thermal source ( $\gamma_B$ ), and stellar source ( $\gamma_*$ ). . . . .	<a href="#">13</a>
-----	--	--------------------





# Abbreviations

$\kappa$ Opacity <a href="#">14</a> , <a href="#">15</a> , <a href="#">20</a> , <a href="#">22</a>	<b>HWHM</b> Half-Width at Half-Maximum <a href="#">17</a> , <a href="#">18</a> , <a href="#">20</a>
$\nu$ Wavenumber [ $\text{cm}^{-1}$ ] <a href="#">20</a>	<b>HZ</b> Habitable Zone <a href="#">5</a> , <a href="#">6</a> , <a href="#">26</a> , <a href="#">92</a> , <a href="#">94</a>
$\sigma$ Absorption Cross Section <a href="#">14</a> , <a href="#">15</a> , <a href="#">20</a> , <a href="#">23</a> , <a href="#">26</a>	<b>IR</b> Infra-Red <a href="#">2</a> , <a href="#">3</a> , <a href="#">16</a> , <a href="#">19</a> , <a href="#">44</a> , <a href="#">92</a>
$\tau$ Optical Depth <a href="#">14</a> , <a href="#">15</a>	<b>IRAC</b> Infrared Array Camera <a href="#">2</a>
<b>ACR</b> Anomalous Cosmic Rays <a href="#">32</a>	<b>ISM</b> Interstellar Medium <a href="#">35</a> , <a href="#">36</a>
<b>BoA</b> Bottom of Atmosphere <a href="#">11</a> , <a href="#">20</a>	<b>JWST</b> James Webb Space Telescope <a href="#">2</a> , <a href="#">49</a> , <a href="#">94</a>
<b>CIA</b> Collision-Induced Absorption <a href="#">19</a>	<b>Keck</b> W. M. Keck Observatory <a href="#">2</a>
<b>CIR</b> Corotating Interaction Region <a href="#">31</a>	<b>Kepler</b> Kepler Space Telescope <a href="#">2</a> , <a href="#">33</a>
<b>CME</b> Coronal Mass Ejection <a href="#">3</a> , <a href="#">14</a> , <a href="#">31</a> , <a href="#">33</a> , <a href="#">35</a> , <a href="#">36</a> , <a href="#">94</a>	<b>LBL</b> Line-by-Line <a href="#">18–22</a> , <a href="#">27</a> , <a href="#">51</a>
<b>CPE</b> Chemical Production Efficiency <a href="#">8</a> , <a href="#">40</a> , <a href="#">43</a> , <a href="#">44</a> , <a href="#">83</a> , <a href="#">92</a> , <a href="#">93</a>	<b>LBT</b> Large Binocular Telescope <a href="#">2</a>
<b>CR</b> Cosmic Rays <a href="#">xvi</a> , <a href="#">8</a> , <a href="#">9</a> , <a href="#">29–32</a> , <a href="#">35–45</a> , <a href="#">47</a> , <a href="#">71</a> , <a href="#">92–95</a>	<b>LUVOIR</b> Large Ultraviolet Optical Infrared Surveyor <a href="#">94</a>
<b>ELT</b> Extremely Large Telescope <a href="#">94</a>	<b>OLR</b> Outgoing Long-Wave Radiation <a href="#">5</a> , <a href="#">26</a>
<b>EUV</b> Extreme Ultra-Violet <a href="#">14</a> , <a href="#">31</a> , <a href="#">33</a>	<b>RO</b> Random Overlap <a href="#">9</a> , <a href="#">23</a>
<b>FUV</b> Far Ultra-Violet <a href="#">14</a>	<b>RST</b> Nancy Grace Roman Space Telescope, formerly <i>Wide Field Infrared Survey Telescope (WFIRST)</i> <a href="#">94</a>
<b>GCR</b> Galactic Cosmic Rays <a href="#">xv</a> , <a href="#">7</a> , <a href="#">8</a> , <a href="#">29</a> , <a href="#">30</a> , <a href="#">32</a> , <a href="#">36</a> , <a href="#">37</a> , <a href="#">39</a> , <a href="#">45</a>	<b>RV</b> Radial Velocity Method <a href="#">1</a> , <a href="#">2</a>
<b>GLE</b> Ground Level Enhancement <a href="#">39</a> , <a href="#">93</a>	<b>SED</b> Spectral Energy Distribution <a href="#">xv</a> , <a href="#">29</a> , <a href="#">30</a> , <a href="#">93</a>
<b>GMT</b> Giant Magellan Telescope <a href="#">94</a>	<b>SEP</b> Stellar Energetic Particles <a href="#">7</a> , <a href="#">8</a> , <a href="#">29</a> , <a href="#">31</a> , <a href="#">32</a> , <a href="#">35</a> , <a href="#">37</a> , <a href="#">40</a> , <a href="#">41</a> , <a href="#">44</a> , <a href="#">45</a> , <a href="#">92–95</a>
<b>HabEx</b> The Habitable Exoplanet Observatory <a href="#">94</a>	<b>SNR</b> Supernova Remnant <a href="#">30</a>
<b>HST</b> Hubble Space Telescope <a href="#">2</a> , <a href="#">33</a> , <a href="#">92</a>	<b>SOHO</b> Solar and Heliospheric Observatory <a href="#">35</a>
	<b>SPE</b> Stellar Proton Event <a href="#">39</a> , <a href="#">92</a>
	<b>SST</b> Spitzer Space Telescope <a href="#">2</a> , <a href="#">92</a>
	<b>Stereo</b> Solar Terrestrial Relations Observatory <a href="#">35</a>
	<b>STIS</b> Space Telescope Imaging Spectrograph <a href="#">2</a>

**TMT** Thirty Meter Telescope [94](#)

**ToA** Top of Atmosphere [11](#), [20](#)

**UV** Ultra-Violet [3](#), [4](#), [14–16](#), [19](#), [26](#), [33](#),  
[43](#), [92](#)

**VIS** Visible [16](#), [19](#), [26](#), [43](#), [44](#), [93](#)

**VLT** Very Large Telescope [2](#)

**WFC3** Wide Field Camera 3 [2](#)

# Nomenclature

**1D-TERRA** Coupled climate chemistry model including [REDFOX](#) and [BLACKWOLF](#), described in Scheucher et al. (2020b) and Wunderlich et al. (2020) xv, xxi, xxii, 25, 27, 41, 43, 51, 92, 94, 95

**Astrosphere** Local bubble of magnetized plasma wind from a star surrounded by interstellar medium xxi, 35–37

**Biosignature** In this context, spectral features of molecules, or combinations thereof, commonly associated with biotic activity on a planet 6, 41, 43, 44, 92

**BLACKWOLF** The chemical network model used in [1D-TERRA](#), described in Wunderlich et al. (2020) xxi, 43

**CH<sub>3</sub>Cl** Chloromethane 44

**CH<sub>4</sub>** Methane 44, 92, 93

**CO<sub>2</sub>** Carbon Dioxide xv, 5, 8, 16, 19, 42, 93

**Coronal Mass Ejection** Event of significant release of plasma and magnetic fields originating from active stellar regions 3

**Flare** Rapid release of magnetic energy in stellar active regions xvi, 3, 31, 33–35, 41, 44

**H<sub>2</sub>** Hydrogen molecule 2, 42, 44, 92

**H<sub>2</sub>O** Water xv, 3, 5, 6, 8, 16, 18, 19, 42–44, 91, 92, 94

**Habitable Zone** Classically the range of star-planet separation for which liquid surface water is possible 5

**He** Helium 2, 37, 42, 92

**Heliosphere** The Sun’s astrosphere 29, 30, 35, 37

**HNO<sub>2</sub>** Nitrous Acid 42

**HNO<sub>3</sub>** Nitric Acid 42, 93

**M<sub>⊕</sub>** Mass of the Earth ( $5.972 \cdot 10^{24}$  kg) 3

**Metallicity** Elemental abundance of substances heavier than helium 6

**MHD** Magnetohydrodynamics. Describing the motions of ionized and magnetized fluids, or plasma 33, 35–37

**N<sub>2</sub>** Nitrogen molecule xvi, 40, 42, 45

**N<sub>2</sub>O** Nitrous Oxide 6, 44

**NH<sub>3</sub>** Ammonia 44

**NO** Nitric oxide 42, 93

**NO<sub>2</sub>** Nitrogen Dioxide 93

**O<sub>2</sub>** Oxygen xvi, 6, 40, 42, 44, 45

**O<sub>3</sub>** Ozone 6, 44, 92, 93

**OH** Hydroxyl radical 42, 93

**Outgoing Long-Wave Radiation**

Planetary blackbody radiation emitted to space 5

**Radial Velocity Method** Measures the motion of a planet’s host star orbiting around the star-planet common center of mass 1

**Radiative Transfer** Refers to the propagation of electromagnetic radiation through a medium including energy transfer via absorption, emission, and scattering processes 8, 11, 14, 15, 19, 20, 22, 27

## Nomenclature

---

**Random Overlap Approximation** A concept applied when dealing with absorption of radiation by multiple species which assumes no correlation of spectral features across species [9](#)

**REDFOX** The  $k$ -distribution radiative transfer model developed as part of this thesis, used in [1D-TERRA](#), described in Scheucher et al. ([2020b](#)) [xvi](#), [xxi](#), [8](#), [23](#), [27](#), [51](#), [91](#), [92](#)

**Transit Method** Measures the planet's dimming of its host star's luminosity during a transit in the line of sight between star and observer [2](#)

**Two-Stream** Plane parallel approximation to solve the *radiative transfer equation* [xvii](#), [12](#), [13](#), [20](#)

# 1

## Introduction

Are we alone? How many other worlds are out there for us to explore? What kind of worlds are they? What types of atmosphere do they come with? Could we actually live on another planet? How could the type of host star affect a planet's potential habitability? And how can we address these issues with only remote observations? All big questions. All seem in some way very challenging. And yet, the last few decades have provided more and more pieces to the big puzzle concerning the potential habitability of planets. Certainly, this work will not be able to answer all of the above questions. This work focuses on furthering our understanding of how the host star and its activity affect a planetary atmosphere through both radiation as well as energetic particle bombardment.

In the early 1990s, the first exoplanets were finally found (Wolszczan and Frail, 1992; Mayor and Queloz, 1995) using the [Radial Velocity method \(RV\)](#). After decades of serious efforts and centuries of wondering, this marks a new era - that of exoplanetary science. In the decades that followed, many more exoplanets were found, new techniques have found even more diverse planets, constantly surprising us and challenging our understanding of planetary formation, diversity and sometimes even their very existence. Many of these newly found planets are advancing new theories which in turn shed light on the inner workings of our own planet and its neighbors.

## 1. Introduction

---

Now in 2020, while thousands of planets have been confirmed around various types of host-stars using different methods, the ultimate question: *Are we alone?* still stands. On the road to an answer to this question we need to pin down which kinds of planets should be the focus of our investigation and characterization. Planets found with [RV](#) so far by nature of the method tend to be mostly hot gas giants, massive and close enough to induce strong Doppler motion around their common center of mass with the star. [RV](#) constrains the masses of planets. In contrast, the transit method measures the star-planet contrast, i.e. the size ratio of planet to host-star, which favors planets orbiting very close-in to smaller, late-type stars, such as M-dwarfs. This method favors both massive and inflated planets alike and short orbital periods allow for a multitude of cumulative transit observations with large space telescopes such as the [Hubble Space Telescope \(HST\)](#) or the retired [Kepler Space Telescope \(Kepler\)](#), bringing detections of terrestrial - sized planets already in the realm of possibility. Transit measurements in different band passes such as the likes of the [Infrared Array Camera \(IRAC\)](#) onboard the [Spitzer Space Telescope \(SST\)](#) or in combination with spectrographs, such as the [Space Telescope Imaging Spectrograph \(STIS\)](#) or the [Wide Field Camera 3 \(WFC3\)](#) onboard the [HST](#) give additional, invaluable information about the existence and properties of exoplanetary atmospheres. The [James Webb Space Telescope \(JWST\)](#), operating in the [Infra-Red \(IR\)](#) is expected to provide an unprecedented possibility to characterize the atmospheres of terrestrial - sized planets.

Although ground-based telescopes have made rapid progress, exoplanetary atmospheric characterization is nevertheless somewhat limited by the strong absorption of [IR](#) radiation through Earth's atmosphere. A good fraction of planets found so far, discovered by the methods explained above, are hot-Jupiters. These are giant planets orbiting in very close orbits around their host-star, hence the middle atmospheres of most of these planets can be heated up well beyond 1000 K or even the melting point of silicate rocks ( $\sim 1200$  K) (see e.g. Sing et al., [2016](#)). Many of their atmospheres, mostly [H<sub>2</sub>-He](#) dominated, have been characterized in recent years in a combined effort from ground-based and space telescopes, with the former being able to detect very small signatures through high-resolution spectrographs attached to ground-based telescopes such as the [Very Large Telescope \(VLT\)](#), [Large Binocular Telescope \(LBT\)](#), or [W. M. Keck Observatory \(Keck\)](#), with their

---

apertures substantially larger than modern space telescopes. For smaller, temperate planets we are not in such a fortunate position. Generally speaking, the cooler a planet, the further its emitted radiation is shifted from shorter wavelengths into the [IR](#). In order to characterize their possible atmospheres, one has to observe over a wide spectral range, ideally extending from the [Ultra-Violet \(UV\)](#) well into the [IR](#), which can only be achieved so far from space. To date, there are relatively few spectral observations of atmospheric constituents of terrestrial - sized planets, or even temperate sub - Neptunes. One highlight observation in recent years was the first confirmed measurement of  $\text{H}_2\text{O}$  in the atmosphere of K2-18b, an  $\sim 8 M_{\oplus}$  planet around an early - type M-dwarf star (Benneke et al., [2019b](#); Tsiaras et al., [2019](#)).

Recent years have witnessed an astonishing diversification and maturation in exoplanetary science. A major developing theme is star-planet interaction and exoplanetary space weather. This is the science of how the planet is influenced by its host star via e.g. gravity (tidal effects), stellar radiation, magnetic and chromospheric activity, stellar winds, [flares](#) and [Coronal Mass Ejections \(CME\)](#). One of its goals is to address which of the many planets out there could provide stable conditions conducive to life as we know it for an extended period of time, or even be inhabited. A number of authors in recent years have argued that we need to understand if planets around active stars could in-fact be habitable on the surface, whether they e.g. lose their atmosphere due to the strong stellar wind (e.g. Dong et al., [2018](#)), or whether high energetic radiation would prevent any upcoming life forms from evolving on the planetary surface (e.g. Cockell et al., [2016](#)). This is especially important for our search for habitable conditions on planetary surfaces, since most of the possibly temperate, terrestrial - sized planets found so far, orbit M-dwarfs at distances substantially closer than Mercury's distance to the Sun. Such worlds are observationally favored because (see e.g. Shields et al., [2016](#)):

- (A) Most stars ( $\sim 70\%$ ) in the solar neighborhood are, in fact, M-dwarfs.
- (B) The planet / star luminosity contrast is higher around these small, cool stars.
- (C) The less massive the star, the smaller the orbit of a temperate planet, the more observations of the same planet are possible within the same observational campaign, the better the resulting signal to noise ratio.

## 1. Introduction

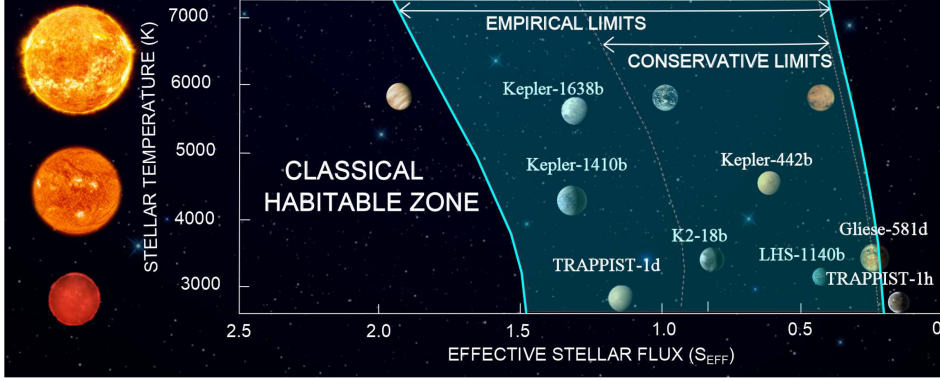


**Figure 1.1:** Graphical representation of the classical habitable zone around stars with different stellar temperatures, normalized by solar values to give the effective stellar flux. Included are a few famous examples of possibly terrestrial exoplanets, as well as some of our terrestrial Solar system planets. Note that the existence of Gliese-581d is strongly debated (e.g. Robertson et al., 2014). Credit: Ramirez (2018)

(D) Close-in planets have viewing geometries with a higher transit probability.

Not only do M-dwarfs have a long pre-main sequence phase, in which enhanced stellar UV fluxes are expected, many of them are also very active stars later on. The latter however might again be observationally biased, as active stars tend to be brighter and are therefore easier to observe.

Another key factor driving planetary habitability is the planet’s intrinsic energy budget, driven mostly by the host star’s luminosity, the star-planet separation, internal heating of the planet from long-lived radionuclides or tidal heating, and the atmospheric greenhouse effect which hinders energy escaping to space. The simplest consideration of planetary energy balance with the stellar radiation follows from simple geometry and can be written as:

$$4\pi R_p^2 F_p = (1 - A_B)\pi R_p^2 F_* \left(\frac{R_*}{d}\right)^2 \quad (1.1)$$

The left hand side represents the planet’s outgoing radiative flux ( $F_p$ ) over the whole surface of radius  $R_p$ . This is to a good approximation in equilibrium with the stellar radiative flux ( $F_*$ ) hitting the planetary cross-section at the planetary orbit ( $d$ ), minus the back-scattered part of stellar radiation, described by the planetary bond albedo  $A_B$ . Assuming star and planet behave as black-body emitters to a first approximation, radiative fluxes can



---

be rewritten using the Stefan Boltzmann law,  $F = \sigma_{\text{R}} T_{\text{eff}}^4$ , with the Stefan Boltzmann constant ( $\sigma_{\text{R}}$ ) and effective temperature ( $T_{\text{eff}}$ ), the temperature of a black-body emitting the same total radiative energy. With this, Eq. (1.1) rewritten in terms of planetary temperature, gives the planetary equilibrium temperature:

$$T_{\text{eq,p}} = T_{\text{eff,*}} \sqrt{\frac{R_*}{d}} \left( \frac{1 - A_{\text{B}}}{4} \right)^{1/4} \quad (1.2)$$

This represents the temperature of a planet in full equilibrium with the radiation from its host star. The so-called classical [Habitable Zone \(HZ\)](#) is defined as the range of star-planet separations for which liquid  $\text{H}_2\text{O}$  can exist on a planetary surface (e.g. Kasting et al., 1993). Figure 1.1 shows the [HZ](#) for different stellar types in terms of normalized effective stellar flux,  $S_{\text{eff}} = d^{-2} L / L_{\odot}$ , with  $d$  being the orbital distance and  $L$  the stellar luminosity compared to the Sun’s luminosity  $L_{\odot}$ . Around M-dwarfs, close orbital distance can compensate for the significantly lower intrinsic stellar luminosity compared to our Sun, for a planet to receive similar input stellar energy integrated over wavelength. There exist multiple definitions for the inner separation limits of the [HZ](#). One lies where the planet’s atmosphere becomes wet enough that spectral atmospheric windows for [Outgoing Long-Wave Radiation \(OLR\)](#) close up, leading to *moist greenhouse*. Another limit is the *runaway greenhouse* (even closer to the star), where oceans would evaporate entirely. Once the stratosphere is saturated, atomic hydrogen from e.g. water photolysis can escape to space, leaving behind a dry but hot planet. The outer [HZ](#) limit can be defined as the point beyond which surface temperatures above 273 K can not be sustained, dependent on the abundance of atmospheric greenhouse gases such as  $\text{CO}_2$ , known as the *maximum greenhouse limit*. This is based on the assumption that e.g.  $\text{CO}_2$  abundances would be strongly enhanced for cooler planets because of the negative feedback from the *carbonate-silicate cycle* (for further details see e.g. Walker et al., 1981). Another definition of the outer [HZ](#) limit includes the additional warming effect an  $\text{H}_2\text{O}$  ocean would have upon the resulting  $\text{CO}_2\text{-H}_2\text{O}$  atmosphere. All the above mentioned limits disregard radiative effects from cloud formation and other greenhouse gases, possibly significantly shifting these limits (see e.g. Kasting et al., 1993; Kopparapu et al., 2013, for an overview). The [HZ](#) further depends on planetary parameters such as mass and rotation rate, amongst others (see e.g. Godolt et al., 2016; Kopparapu

## 1. Introduction

---

et al., 2017). Over time, the HZ as a whole moves outward as the host star ages and becomes brighter through its evolution along the main sequence.

Why is the HZ mainly based on  $\text{H}_2\text{O}$ ? While we are only starting to understand more about how life formed on Earth in the first place, biologists agree that  $\text{H}_2\text{O}$  is required by carbon-based life forms e.g. for essential metabolic chemistry (e.g. Owen, 1980). The  $\text{H}_2\text{O}$  molecule, due to its bent shape and its differing atomic constituents, is highly polar, which makes it an excellent solvent for a wide range of substances (for further details see e.g. Lynden-Bell et al., 2010). Although there exist some extremophiles on Earth that can endure without  $\text{H}_2\text{O}$  for extended periods of time, none are known to metabolize or reproduce without liquid  $\text{H}_2\text{O}$ . In addition,  $\text{H}_2\text{O}$  is thought to be one of the most abundant molecules in the universe and the constituents of water are available in most stars, as it is built from two parts hydrogen, the most abundant element by far, and oxygen, the third most abundant. Hence, most planets around a wide variety of stars may be expected to also contain  $\text{H}_2\text{O}$  if they form within the ice-line or if they migrate and water is delivered during the late accretion (e.g. Morbidelli et al., 2000). One could argue that this picture might be different for planets around late-type stars with high metallicity, where heavier elements become abundant enough to form significant amounts of other polar compounds. See e.g. Catling and Kasting (2017), Perryman (2018), Schwieterman et al. (2018), and references therein for a review. In an effort to overcome this Earth-centric bias, there have also been other definitions of life supporting zones for life forms that may not use  $\text{H}_2\text{O}$  as their major solvent. However, it is unclear as to what such life forms - and signatures thereof - would look like. A more general idea is to look for extreme thermodynamic or chemical disequilibrium in planetary atmospheres (see e.g. Catling and Kasting, 2017), but again these may be difficult to interpret without understanding the chemical signatures of alien life. Therefore it seems logical that our search for habitable worlds has started, and continues for now, to focus on the search for liquid  $\text{H}_2\text{O}$ .

This thesis also assesses atmospheric biosignature signals including photochemical and spectral responses. Recent reviews of the relevant processes for commonly considered atmospheric biosignatures such as  $\text{O}_2$ ,  $\text{O}_3$  and  $\text{N}_2\text{O}$  can be found in e.g. Grenfell (2017) and Schwieterman et al. (2018).

## 1.1 Aims & Outline

Planetary habitability depends strongly on the interaction between the planetary atmosphere and the energy from its host star. Due to both the anticipated diversity of exoplanetary atmospheres as well as the large range of stellar classes and activities, modeling possible planetary climate states and atmospheric conditions is a challenging endeavour. A central aim of this work is to extend the understanding of the effects of stellar radiation upon atmospheric temperatures, and the multitude of cascading effects which [Stellar Energetic Particles \(SEPs\)](#) together with [Galactic Cosmic Rays \(GCRs\)](#) may have upon atmospheric composition. Both these effects are likely to be key factors affecting potential surface habitability. This thesis therefore addresses the following scientific questions for some well-chosen scenarios:

- What kind of atmospheres may provide habitable conditions?
- Which atmospheres can explain observed spectral features?
- How does the host star's spectral type affect planetary habitability?
- How do energetic particle showers impact atmospheric composition and habitability?

This cumulative thesis gives a summary of the works published in Scheucher et al. (2018) and Scheucher et al. (2020a) focusing on the effect of energetic particle bombardment onto exoplanetary atmospheres and habitability, and Scheucher et al. (2020b) focusing on the effect of opacities in radiative transfer through a large variety of atmospheric conditions upon planetary climate and atmospheric spectral characteristics.

To address the questions stated above, a comprehensive one-dimensional coupled climate chemistry model from the group of Prof. Rauer (formerly at the Zentrum für Astronomie und Astrophysik of Technische Universität Berlin, now at the Institut für Geologische Wissenschaften of Freie Universität Berlin, and also director of the Institut für Planetenforschung at Deutsches Zentrum für Luft- und Raumfahrt in Berlin) was developed and applied during the course of this thesis. Earlier versions of this model had originally been developed by Kasting and Ackerman (1986), Pavlov et al. (2000), and

## 1. Introduction

---

Segura et al. (2003), for habitability studies of Earth and Earth-like planets, and has since then been extensively updated in Prof. Rauer’s group. General descriptions of these model updates and various applications can be found in e.g. Rauer et al. (2011), Grenfell et al. (2013), Paris et al. (2013), Godolt et al. (2016), Gebauer et al. (2017), Gebauer et al. (2018), Keles et al. (2018), and Godolt et al. (2019). In order to address the scientific questions raised above it was necessary to update (1) the [radiative transfer](#) and (2) the treatment of [Cosmic Rays \(CRs\)](#) in the original code.

(1) There had already been efforts to adapt the [radiative transfer](#) originally developed for Earth, to  $\text{CO}_2$ -dominated atmospheres (see Paris et al., 2008; Paris et al., 2010; Paris et al., 2015). With those updates however, stellar radiation could only be treated up to 4.5  $\mu\text{m}$ , fine for our own Sun, yet the far cooler M-dwarf stars radiate a significant portion of their energy above this limit, potentially significantly impacting any habitability calculations. Further, absorption at atmospheric pressures above 1.5 bars could only be modeled for  $\text{H}_2\text{O}$  and  $\text{CO}_2$ , a critical restriction when investigating habitable conditions for a broad range of atmospheres. To overcome such issues, Scheucher et al. (2020b) (publication I) describe the necessary steps that led to a more inclusive and flexible radiative transfer model, called [REDFOX](#), including a thorough validation for Earth, Mars, Venus-like, and  $\text{H}_2\text{O}$ -steam atmospheres. Additionally, publication I presents the first comprehensive study investigating spectral appearance of exoplanetary atmospheres over a wide range of theoretical atmospheric conditions, which compare to the first ever observed  $\text{H}_2\text{O}$  features of an exoplanet orbiting close to the HZ around its host star.

(2) The other concern was the treatment of [CRs](#) in the model. In previous updates in Prof. Rauer’s group, Grenfell et al. (2007), Grenfell et al. (2012) and later Tabataba-Vakili et al. (2016) had already implemented the effect of either [galactic cosmic rays](#) or [stellar energetic particles](#) onto Earth’s atmosphere. This involved a number of parameterizations specific to the nature of Earth’s atmospheric composition and physical conditions. Scheucher et al. (2018) (publication II) generalized the effect [GCRs](#) and [SEPs](#) together could have upon Earth-like atmospheres and investigated the effect of varying [CPEs](#) of neutral species due to the action of energetic particles. Scheucher et al. (2020a) (publication III) coupled the atmospheric model to a particle propagation (in the astrosphere), a particle precipitation (in magnetosphere,

ionosphere and atmosphere) and an ion chemistry model to consistently study the CR-induced effects upon all the combined processes in this model suite. This includes e.g. the sensitivity of ionization to the neutral (non-ionized) atmosphere, the efficiency of changing the neutral atmosphere through CR-induced ions, and the CR-induced changes upon neutral atmospheric composition, climate, habitability, and spectral appearance.

This thesis is structured in an intuitive way starting with the effects of electromagnetic radiation and followed by the influence of energetic particles upon (exo)planetary atmospheres - and is not compiled chronologically via paper publication date. A brief introduction is given in Sec. 1.2 into some key concepts in radiative transfer modeling of planetary atmospheres. Special importance is given to necessary steps leading to the calculation of atmospheric opacity using the [Random Overlap \(RO\)](#) approximation, allowing for the treatment of a wide variety of atmospheric composition and conditions. Section 1.3 introduces and highlights some of the key steps needed to consistently model the interaction of energetic particles with the surrounding medium from the source through the astrosphere, a potential magnetosphere and finally through the atmosphere down to the planetary surface. Chapters 2, 3, and 4 present the published works that form the basis of this cumulative thesis, and concluding remarks together with a future outlook are given in chapter 5.



## 1.2 Radiation and Opacities in Planetary Atmospheres

Radiation, i.e. an electromagnetic wave, interacts with and influences the medium through which it travels. A wide variety of interactions with a gas, such as absorption, emission, and scattering processes, with atoms, molecules, and particles, define the global atmospheric radiative-energy budget. The stellar incoming energy hits the [Top of Atmosphere \(ToA\)](#) and is absorbed and scattered on its way through the atmosphere. Similarly, internal planetary radiative sources travel from the surface, or [Bottom of Atmosphere \(BoA\)](#) in the case of an undefined boundary between atmosphere and interior as in the case for gas planets, through the atmosphere (where absorption and scattering occur) into space. Additionally, the atmosphere's black-body radiation is emitted uniformly in every direction from anywhere within the atmosphere and scattered, absorbed, and re-emitted along the way to the surface and interplanetary space.

### 1.2.1 Radiative Transfer and the Two-Stream Approximation

The formalism describing the above mentioned interactions of radiation on its way through a medium is called [radiative transfer](#). In its general, plane-parallel form, the equation of radiative transfer with non-isotropic but coherent scattering (i.e. no inelastic or Raman scattering) can be written as:

$$\mu \frac{\partial I}{\partial \tau} = I - \omega_0 \int_0^{4\pi} \mathcal{P} I d\Omega - (1 - \omega_0) B - \frac{\omega_0}{4} F_* \mathcal{P} \exp\left(\frac{-\tau}{\mu}\right) \quad (1.3)$$

Here,  $\mu = \cos \Theta$ , with  $\Theta$  the polar angle,  $I$  the intensity,  $\mathcal{P}$  the scattering phase function (in the isotropic case  $1/4\pi$ ),  $\tau$  the optical depth,  $\omega_0$  the single-scattering albedo. The term including the Planck function ( $B$ ) describes the internal atmospheric isotropic source function, and the last term including the stellar incoming flux ( $F_*$ ) describes the external stellar source function. Obtaining atmospheric optical depths ( $\tau$ ) will be discussed in the sections to follow. A detailed derivation of Eq. (1.3) can be found in e.g. Chandrasekhar (1960), Goody and Yung (1996), or Zdunkowski et al. (2007). The classical concept of solving Eq. (1.3) is similar to solving the central equation in fluid dynamics, the Boltzmann equation, where solving it for moments of mass

## 1. Introduction

---

with respect to velocity leads to the famous Navier-Stokes equations (see, e.g. Scheuchner, 2015, and references therein). Solving Eq. (1.3) for moments of the radiation field (with respect to  $\mu$ ) gives total intensity ( $J$ ), radiative fluxes ( $F$ ), and radiation pressure ( $K$ -integrals).

In an atmospheric model, one is interested in the fraction of radiation transmitted between adjacent atmospheric layers. This is done by calculating the radiative upward and downward fluxes for each atmospheric layer. Depending on the scientific problem at hand and the complexity of scattering needed to be resolved, it may be sufficient to divide calculations purely into upward and downward, commonly referred to as [two-stream](#) approximations, or one may need to resolve scattering of radiation by bigger particles such as clouds in multiple polar angles ( $\Theta$ ) before combining them into upward and downward fluxes. An example of the latter would be the *discrete ordinate method* (e.g. Stamnes et al., 1988). It should be noted that such multi-stream methods take considerably more calculation time in a climate model and are therefore only invoked when necessary. As the effect and treatment of clouds is not part of this thesis, utilizing the [two-stream](#) approximation is sufficient for this work.

Over the last decades, numerous works (e.g. Meador and Weaver, 1980; Toon et al., 1989; Heng et al., 2018) have been dedicated to finding solutions for different source functions, and types of scattering in the atmosphere (isotropic, non-isotropic). To date there exist multiple methods valid under certain conditions, tested against physical limits such as *pure absorption* or *pure scattering*. The following text provides a brief overview of some selected methods and solutions, as well as the limitations and validity ranges of the approximations used. Detailed derivations, proofs of energy conservation, and validations can be found, for example, in Shettle and Weinman (1970), Liou (1974), Meador and Weaver (1980), Toon et al. (1989), or Heng (2017). In the [two-stream](#) approximation, upward ( $F_{\uparrow}$ ) and downward ( $F_{\downarrow}$ ) radiative fluxes can be written in the form:

$$\begin{aligned}\frac{\partial F_{\uparrow}}{\partial \tau} &= \gamma_A F_{\uparrow} - \gamma_S F_{\downarrow} - \gamma_B B - \gamma_* \pi F_* \omega_0 \exp\left(\frac{-\tau}{\mu}\right), \\ \frac{\partial F_{\downarrow}}{\partial \tau} &= \gamma_S F_{\uparrow} - \gamma_A F_{\downarrow} + \gamma_B B + (1 - \gamma_*) \pi F_* \omega_0 \exp\left(\frac{-\tau}{\mu}\right).\end{aligned}\tag{1.4}$$

Here, coefficients  $\gamma$  represent method dependent *closures* of the [two-stream](#) approximation, shown in Tbl. 1.1 for commonly used closures. In the case of



## 1.2 Radiation and Opacities in Planetary Atmospheres

Method	$\gamma_A$	$\gamma_S$
Eddington	$\frac{1}{4}[7 - \omega_0(4 + 3g_0)]$	$-\frac{1}{4}[1 - \omega_0(4 - 3g_0)]$
Quadrature	$\frac{\sqrt{3}}{2}[2 - \omega_0(1 + g_0)]$	$\frac{\sqrt{3}\omega_0}{2}(1 - g_0)$
Hemispheric mean	$2 - \omega_0(1 + g_0)$	$\omega_0(1 - g_0)$

Method	$\gamma_B$	$\gamma_*$
Eddington	$2\pi(1 - \omega_0)$	$\frac{1}{4}(2 - 3g_o\mu_0)$
Quadrature	$\sqrt{3}\pi(1 - \omega_0)$	$\frac{1}{2}(1 - \sqrt{3}g_o\mu_0)$
Hemispheric mean	$2\pi(1 - \omega_0)$	—

**Table 1.1:** Summary of [two-stream](#) approximation coefficients for absorption ( $\gamma_A$ ), scattering ( $\gamma_S$ ), isotropic thermal source ( $\gamma_B$ ), and stellar source ( $\gamma_*$ ).

no scattering ( $\omega_0 = 0$ ), the two equations decouple into a pair of first-order ordinary differential equations that can be solved separately. Note that in the no scattering limit, the Eddington closure should be avoided, as it does not fully decouple Eqs. (1.4) ( $\gamma_S \neq 0$ ), which would lead to unphysical behavior. In the case of isotropic scattering, the asymmetry factor ( $g_0$ ) becomes zero, simplifying numerous coefficients of the methods presented in Tbl. 1.1. The *Eddington* and *quadrature* closures have shown to be reasonably accurate for the treatment of stellar incoming radiation together with scattering, especially in combination with so-called  $\delta$ -scalings replacing  $\omega_0$  and  $g_0$  (see Joseph et al., 1976). Toon et al. (1989) has argued that the Eddington closure may introduce errors to downward fluxes for isotropic sources in combination with back-scattering, and Heng (2017) has argued that the Eddington closure is to be avoided in the pure-absorption limit (see also above). When an isotropic source such as thermal radiation (Planck function) is introduced, both of these closures are inferior to the commonly used *hemispheric mean* closure, which is also the only one of the three that is reasonably accurate in the no-scattering limit ( $\omega_0 = 0$ ). On the contrary, the hemispheric mean closure produces unphysical results when a stellar source is added, therefore  $\gamma_*$  was intentionally left blank in Tbl. 1.1. Following this, the quadrature closure may be used for solving radiative transfer for a stellar source, while the

## 1. Introduction

---

hemispheric mean closure is appropriate when solving for isotropic Planck radiation.

### 1.2.2 The Importance of Optical Depth

A fundamental quantity in radiative transfer is the optical depth ( $\tau$ ), defined as:

$$\tau = \int n\sigma dz, \quad (1.5)$$

the atmospheric number density ( $n$ ) multiplied by the absorption cross section ( $\sigma$ ), along the path ( $dz$ ) through the atmosphere. For reference, absorption cross section per unit mass is called opacity ( $\kappa$ ). From Eq. (1.5) we can see that  $\tau$  increases with the extent of an atmosphere and its density, which becomes crucial when observing planets and stars because when  $\tau$  becomes sufficiently large ( $\tau \sim 1$ ), a medium such as a planetary or stellar atmosphere becomes opaque, which precludes observations from the underlying atmosphere.

In our own solar system, the atmospheres of Earth and Mars are thin enough to provide spectral windows which probe the lower atmosphere and surface over a wide spectral range from afar. On the contrary, observing Venus in the visible from afar is a different story. Venusian atmospheric pressures and composition do not reveal its surface in the visible range, which makes Venus appear slightly bigger to an observer than the solid body. This effect becomes more so evident when looking at gas planets where we only see down to a certain depth into the atmosphere, and e.g. the characteristics of the solid planetary cores of the solar system gas and ice giants (see e.g. review by Helled et al., 2020) are still debated in the scientific community.

Another prominent example for the fundamental importance of  $\tau$  in the solar system is our own host star, the Sun. Observing the Sun in the visible spectral range gives the impression of a surface-like edge, or solid body, where in fact this optical illusion called the *photosphere* simply represents the distance, where radiative absorption integrated from the observer up to a certain depth into the solar plasma atmosphere leads to  $\tau \sim 1$ . Probing the Sun over different wavelength ranges, mostly in the UV, EUV, or FUV, enables the study of different parts of the Sun's chromosphere and corona, including various features that become optically thick at specific wavelength ranges, such as e.g. magnetic loops, faculae, coronal holes, filament eruptions, or CMEs.

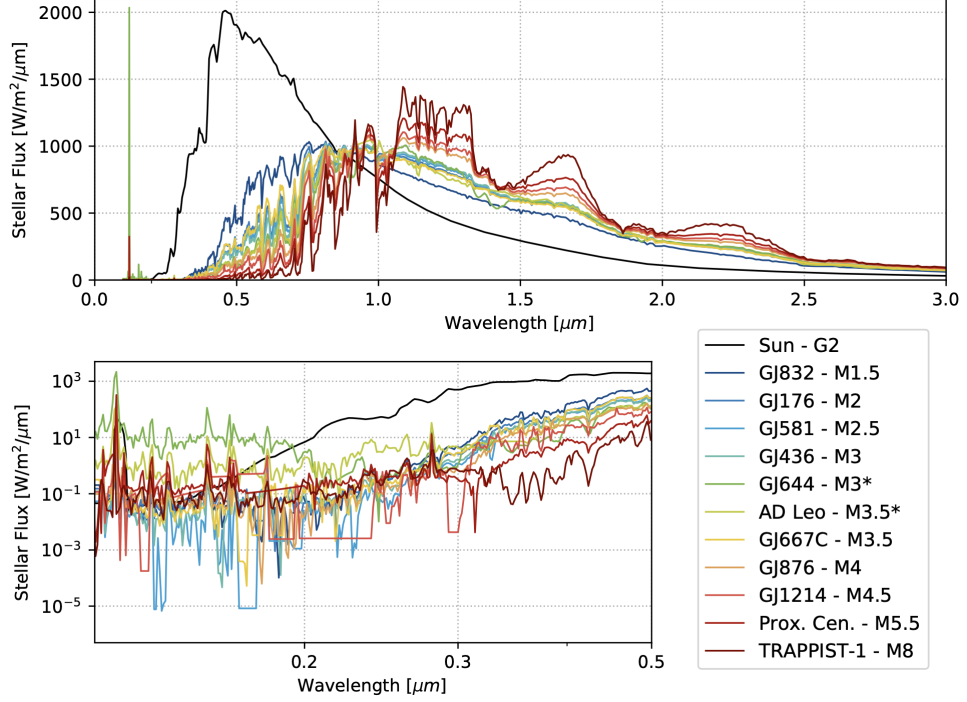


**Figure 1.2:** SED for various stars of different stellar type taken from Wunderlich et al. (2019). Observed SEDs are reconstructed and completed with theoretical predictions where necessary.

The fact that  $\tau$  is absorption integrated along the path from observer to source is crucial to bear in mind when observing other stars and their planets. There are a number of spectral regions in the UV where the interstellar medium between observer and star absorbs most and in some cases virtually all the the stellar photons, indicated by flat lines in Fig. 1.2. There are in fact even more such regions which have been reconstructed by various theoretical methods in Fig. 1.2. This is an important source of uncertainty when determining the habitability of a specific planet.

### 1.2.3 The Voigt Profile and Broadening Parameters

The central parameters in radiative transfer,  $\sigma$ ,  $\kappa$ , and therefore  $\tau$ , all depend on the underlying physics of how electromagnetic radiation interacts with an atom or molecule, and its electrons. From quantum mechanics we know that atoms and molecules may be described as harmonic oscillators visualized as having discrete energy states ( $E_i$ ) regularly spaced in frequency or wavenumber ( $\nu$  [cm<sup>-1</sup>]), calculated using the Hamiltonian operator,  $\mathcal{H}\psi_i =$

## 1. Introduction

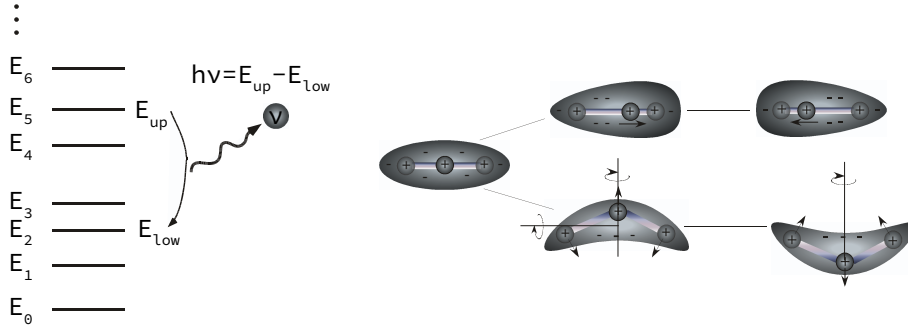


**Figure 1.3:** Schematic representation of electromagnetic transition levels (left), and vibration and rotation modes for a symmetric linear triatomic molecule such as  $\text{H}_2\text{O}$  or  $\text{CO}_2$  (right). Figure adapted from Pierrehumbert (2010)

$E_i\psi_i$ , upon the atom's or molecule's eigenfunctions ( $\psi_i$ ). Electrons in a higher energy state may spontaneously decay in a so-called *electronic transition* into a lower energetic state, emitting a photon of that energy difference. Photons with the appropriate energy may be absorbed by an atom or molecule through *electronic transitions*, promoting an electron into a higher energy state. These transitions typically involve energies of a few eV ( $\sim 10^4 \text{ cm}^{-1}$ ), corresponding to the **visible (VIS)** and **UV** range. Molecules provide even more degrees of freedom that can store and release energy. Displacement of nuclei away from equilibrium will lead to restoring electromagnetic forces, causing the molecule to vibrate. Molecules are not perfect springs, and may also store energy in the form of rotation. These vibrational, rotational and rovibrational transitions do not require as much energy and occur mainly in the **IR** spectral regime. Fig. 1.3 sketches these transitions. A central challenge when calculating atmospheric opacities is the sheer number of transitions that need to be included for each atmospheric constituent at any given combination of atmospheric pressure and temperature, together with the numerous effects that arise when dealing with mixtures of such gases. These will be elaborated on in Section 1.2.4, for now let us focus on modeling a single transition.

All the transitions mentioned above, result in distinct spectral absorption and emission features, called *spectral lines* or *spectral bands*. The shapes of spectral lines can be described by e.g. the *Voigt profile*, a convolution of a thermal Doppler (Gauss) profile at the line center, and Lorentzian line wings.

## 1.2 Radiation and Opacities in Planetary Atmospheres

At finite temperature, molecules in a gas have thermal speed given by:

$$v_{\text{th}} = \sqrt{\frac{2k_{\text{B}}T}{m}}, \quad (1.6)$$

with the Boltzmann constant  $k_{\text{B}}$ , temperature  $T$ , and mean molecular mass  $m$ . The Maxwell-Boltzmann distribution gives us the standard deviation of thermal velocities:

$$\alpha_{\text{D}} = \frac{\nu_0}{c} v_{\text{th}}. \quad (1.7)$$

Here  $\nu_0$  is the wavenumber at line-center, and  $c$  is the speed of light. With the [Half-Width at Half-Maximum \(HWHM\)](#),  $\gamma_{\text{D}} = \sqrt{\ln 2} \alpha_{\text{D}}$ , the Doppler profile can be written as:

$$\Phi_{\text{D}} = \frac{1}{\gamma_{\text{D}}\sqrt{\pi}} \exp\left(-\left[\frac{\nu - \nu_0}{\alpha_{\text{D}}}\right]^2\right). \quad (1.8)$$

Unlike Doppler broadening, the theory behind pressure broadening is not exact. The *Lorentz profile* can be written as:

$$\Phi_{\text{L}} = \frac{\gamma_{\text{L}}}{\pi} \frac{1}{(\nu - \nu_0)^2 + \gamma_{\text{L}}^2}. \quad (1.9)$$

Here,  $\gamma_{\text{L}}$  is the Lorentzian [HWHM](#) (and  $\gamma_{\text{L}} = \alpha_{\text{L}}$ ), related to the time between collisions of atoms and molecules, and can be written as:

$$\gamma_{\text{L}} = \frac{A_{21}}{4\pi c} + \left( \gamma_{\text{L}}^{\text{self}} \frac{p_{\text{self}}}{p_{\text{ref}}} + \gamma_{\text{L}}^{\text{air}} \frac{p - p_{\text{self}}}{p_{\text{ref}}} \right) \left( \frac{T_{\text{ref}}}{T} \right)^n. \quad (1.10)$$

Here  $A_{21}$  is Einstein's A-coefficient, describing spontaneous decay from a higher to a lower energy state, hence the first term, *natural broadening* arises due to Heisenberg's uncertainty principle. The second term describes pressure broadening through empirical fitting parameters, the self-broadened [HWHM](#) ( $\gamma_{\text{L}}^{\text{self}}$ ), the [HWHM](#) due to broadening by the background atmosphere ( $\gamma_{\text{L}}^{\text{air}}$ ), and the temperature exponent ( $n$ ), all three given by so-called *line-lists* such as the HITRAN database<sup>1</sup>(Gordon et al., 2017), HITEMP<sup>2</sup>(Rothman et al., 2010) or the Exomol database<sup>3</sup>(Tennyson et al., 2016). Reference pressure

<sup>1</sup>[www.hitran.org](http://www.hitran.org)

<sup>2</sup>[www.hitran.org/hitemp](http://www.hitran.org/hitemp)

<sup>3</sup>[www.exomol.com](http://www.exomol.com)

## 1. Introduction

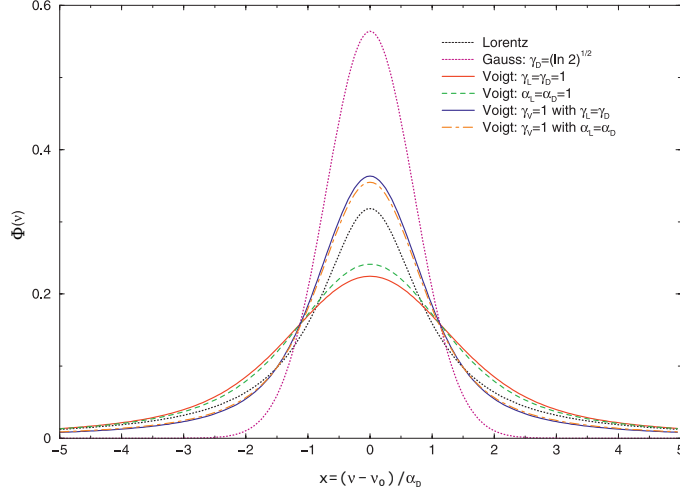


**Figure 1.4:** Gauss (Doppler), Lorentz, and convolved Voigt profiles for different definitions of half-width, adapted from Schreier (2009)

( $p_{\text{ref}}$ ) and reference temperature ( $T_{\text{ref}}$ ) are specific to the methods of obtaining the above mentioned parameters for a line-list.

With all of the above, the *Voigt profile* is then a mixture or convolution of Doppler and Lorentz profiles, which can be written as:

$$\Phi_\nu = \Phi_L \otimes \Phi_D = \frac{\alpha_L}{\alpha_D^2 \pi^{3/2}} \int_{-\infty}^{+\infty} \frac{e^{-x'^2}}{(x - x')^2 + \left(\frac{\alpha_L}{\alpha_D}\right)^2} dx'. \quad (1.11)$$

Figure 1.4 shows the Doppler, Lorentz and the corresponding convolved Voigt profile. There has been a debate regarding how to *correctly* plot all three in one plot, since the **FWHM** is different for all three profiles (see, e.g., Huang and Yung, 2004; Schreier, 2009, for a discussion). Therefore Fig. 1.4 shows Voigt functions plotted for four different assumptions and combinations of Doppler and Lorentz **FWHM**.

Modeling absorption through the Voigt profiles of every single known electronic and rovibrational transition through so-called **Line-by-Line (LBL)** cross section calculations, has suggested differences to absorption by real gases. One reason for this is that the Lorentz profile was derived for single molecules in isolation, which makes it only accurate in the line center. Comparisons to spectroscopic observations of **H<sub>2</sub>O** absorption features have shown that the far Lorentz wings may underestimate absorption compared to reality. Exactly what *far* means in this case is not clear, but there have been

efforts (e.g. Clough et al., 1992) to correct the Lorentzian wing shape for  $\text{H}_2\text{O}$  leading to *super-Lorentzian* line wings. Observations of Venus have shown that absorption by  $\text{CO}_2$  in the Venusian high pressure atmosphere is overestimated by Voigt profiles, leading to the use of *sub-Lorentzian* line wings (see e.g. Takagi et al., 2010).

In addition to absorption by spectral lines, a real atmosphere also displays relatively flat spectral regions, commonly called *continuum absorption*. There have been efforts to characterize continuum absorption as the accumulation of all far line wings but as seen above, this is difficult to model especially when the line profiles themselves may need correction (see Scheucher et al., 2020b, and references therein). Small errors made in these assumptions can accumulate over millions and billions of spectral lines. Also, there are additional processes that occur in a real gas. Energy may also be transferred across molecules through inelastic collisions. This is generally known as *Collision-Induced Absorption* (CIA) and is dependent upon particle densities, hence pressure. Collisions can e.g. induce dipoles leading to new absorption features, mainly in the IR. Further, molecules can form clusters including dimers, trimers and polymers, offering a wide range of new rovibrational transitions. See e.g. Edwards (1988), Shine et al. (2012), or Shine et al. (2016) for a review of this topic. In addition, in the VIS and UV photoionization and photodissociation may contribute to strong continuum absorption. Implementing all these absorption features commonly requires cutting the line wings at a specific cut-off (typically in half-widths or fixed wavenumbers distance from line centers) in LBL calculations and adding CIAs and continua where needed. Scheucher et al. (2020b) [see Chapter 2] discuss and elaborate further on the need for cutting the line wings when performing LBL calculations of individual cross sections or atmospheric opacities, and adding CIA and other continuum absorption where appropriate.

### 1.2.4 Modeling Absorption in a Gas Mixture

Radiative transfer models are typically categorized by the method in which the frequency spectrum of interest is discretized, and further upon how opacities within these discrete intervals are obtained. One could imagine that solving the radiative transfer equation (1.3) should be the core concept, around which a comprehensive radiative transfer model were to be built. In practice however, multiple approximations used to solve Eq. (1.3) such as e.g.

## 1. Introduction

---

the [two-stream](#) approximation described in Section 1.2.1 may be attached as self-contained packages using a solver appropriate for the application of interest chosen at model execution. Such a procedure, while somewhat more elaborate, may also be applied when calculating opacities for every layer and each spectral interval, yet historically most [radiative transfer](#) models have evolved around the method of choice for obtaining the opacities.

The most exact yet slowest method was already mentioned in Section 1.2.3, the [LBL](#) calculation of cross sections. This takes parameters stored in line-lists as described in Sec. 1.2.3, builds the Voigt profiles for a unique pressure-temperature and gas-mixture set, and calculates  $\sigma$  or  $\kappa$  on a discretized grid in  $\nu$ . Usually, discretization or spectral intervals ( $\Delta\nu$ ) are chosen to be a fraction of a representative [HWHM](#), either a minimum, median, or mean value, over the whole spectral range of interest. This is to ensure that every significant absorption feature is sampled sufficiently. With the number of lines for a single molecule reaching into millions for higher temperatures and the Lorentz broadening (i.e. [HWHM](#)) becoming very small for low pressures, one can see how this will lead to a huge computational effort (and potentially a matter of memory and storage). There is no way around [LBL](#) if one is interested in comparing synthetic spectra to high-resolution spectroscopic observations, and many other approaches developed in an effort to reduce calculation times in atmospheric climate models, where dozens or hundreds of  $p$ - $T$  combinations have to be calculated multiple times and in some way, shape, or form, rely on [LBL](#) calculations to begin with.

One straightforward approach is to simply reduce the sampling from a few points per line by orders of magnitude. This is called *opacity sampling* and needs to be thoroughly validated against [LBL](#) calculations to ensure sufficiently high accuracy for the intended application. While some information on single absorption features is lost, spectral information is preserved, ensuring that radiation from [ToA](#) to [BoA](#) and back interacts with, and only with, features associated with this energy. There are two more methods loosely associated with this approach, driving the reduction of sampling points to the maximum, namely the *semi-grey* and *grey* approximations. Semi-grey simply means that all radiative transfer is reduced to only two spectral bins, one short-wave bin for the incoming stellar radiation, and one long-wave bin for the planetary Planck radiation. For both bins a representative opacity has to be calculated, but in contrast to the



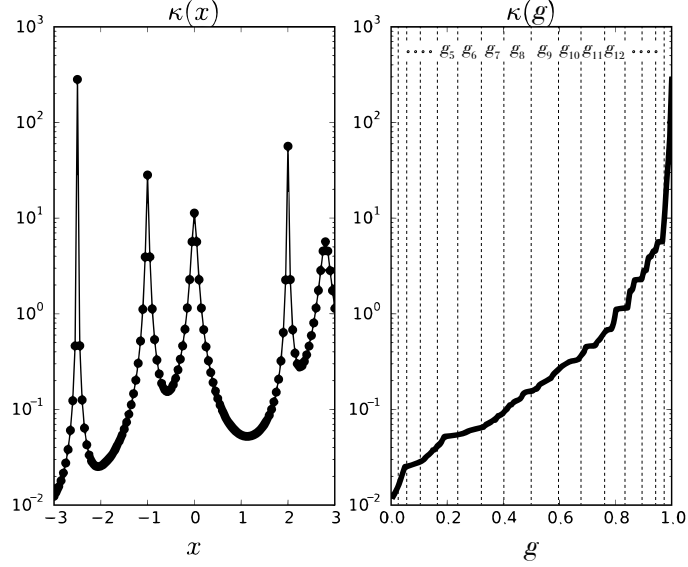


**Figure 1.5:** Sample opacity ( $\kappa [m^{-1}]$ ) function in a spectral interval shown for an arbitrary wavelength domain  $x$  (left), versus the associated  $k$ -distribution in the  $g$ -function domain (right) (adapted from Heng, 2017)

aforementioned opacity sampling approach, where opacities are calculated on a coarser grid, it is quite intuitive to understand that finding two representative frequencies with which to calculate the opacity, may not be an accurate assumption. Instead, a mean opacity has to be calculated for each of the two bins. This is not an easy task that comes with a number of assumptions and approximations, but given the extraordinary gain in calculation speeds, hence capabilities in covering wide parameter spaces for e.g. habitability studies, much effort is still put into calculating these representative opacities. One example would be the *Rosseland mean opacity*, representing the harmonic mean opacity over e.g. the whole Planck function of an atmospheric layer. The same holds for the grey atmosphere approximation, with only one spectral bin and opacity per p-T layer (see e.g. Heng, 2017, for an overview).

A very different approach is the *k-distribution method* which is in some ways a hybrid of all the above, and yet very unique. Instead of using opacities ( $\kappa(\nu)$ ) for every LBL sampling point directly, their cumulative counterpart within a spectral interval or bin is calculated. Figure 1.5 illustrates the method, where  $x$  denotes an arbitrary spectral interval  $\nu_1, \nu_2$ . The plot on the left shows the LBL sampling points of spectral features. The plot on the right shows the associated  $k$ -distribution ( $\kappa(g)$ ) which refers to the

## 1. Introduction

---

cumulative function of the sampled opacities ( $\kappa(x)$ ) in the left plot. Clearly, the opacity function  $\kappa(x)$  varies by orders of magnitude for every spectral feature, whereas the resulting  $k$ -distribution function ( $\kappa(g)$ ) is a smooth, monotonously increasing function. The total range of  $\kappa$  values stays the same, since the  $\kappa(g)$  is merely a remapping of every LBL sampling point onto the cumulative function. As an example,  $\kappa(g = 0.4) \sim 10^{-1}$ . This means that 40% ( $g=0.4$ ) of all sampled  $\kappa(x)$  have a value of or below  $10^{-1}$ . The innovative part is that  $\kappa(g)$  because of its smooth and monotonous nature can now be down-sampled by orders of magnitude to typically 8-24 sub-intervals, for which a representative mean opacity is generated. In the right plot of Fig. 1.5, 16 so-called  $g_i$ -sub-intervals are illustrated. In contrast to opacity sampling, the  $k$ -distribution method retains all spectral features of full LBL calculations, but one drawback of this method is that spectral information within an interval is lost. The required number of these bins, and  $g$ -sub-intervals, has to be validated against LBL and commonly the number of spectral bins lies in the order of dozens to hundreds. Radiative transfer is then calculated for each of the  $g$ -sub-intervals of every spectral bin. A considerable benefit in calculation speeds comes from the fact that  $k$ -distribution functions can be pre-computed on a  $p$ - $T$  and chemical composition grid which can serve as a look-up table when running an atmospheric model. With increasing number of chemical species, and the resulting need for numerous sampling points in all possible mixing ratio combinations, there may be however a limit to how many chemical species are feasible to consider in such an approach.

The  $k$ -distribution method is strictly speaking only valid for a homogeneous atmosphere, meaning isothermal, isobar, and constant chemical composition throughout the atmosphere (Heng, 2017). In an atmospheric model where atmospheric composition,  $p$ , and  $T$ , change with height, the *correlated- $k$*  approximation is invoked. This approximation states that the  $\kappa(g_i)$  in one layer may contain spectral features arising from different wavenumbers compared with the same  $\kappa(g_i)$  in another layer. In this case, LBL calculations are first performed for pure gases of single molecules, later the cumulative opacity functions are added, or correlated. If one assumes that spectral features of all individual species are *perfectly correlated* with each other, i.e. always populate the same wavenumber region, the opacity of

the whole gas mixture can be calculated as:

$$\kappa(l, b, g_i) = \sum_m \chi_m(l) \kappa_m(l, b, g_i). \quad (1.12)$$

Here  $l$  denotes the atmospheric layer,  $g_i$  the sub-interval in band  $b$ , and  $m$  is the individual molecule or atmospheric species with volume-mixing-ratio  $\chi$ . This assumption is reasonable for atmospheres of only few absorbing species such as primary atmospheres but may be difficult to justify for cool, secondary atmospheres with many more climate relevant trace gases. If spectral lines of different species completely avoid each other, then they are called *disjoint*. If one assumes that spectral lines are not correlated with lines from other molecules, this is called *randomly overlapping* (RO), or *perfectly uncorrelated* (see e.g. Pierrehumbert, 2010, for a review on these assumptions). This assumption becomes more and more compelling, the more molecules of different sizes, shapes, and electronic properties, are present in an atmosphere. With this assumption, the calculation of a gas mixture opacity is more elaborate and computationally slightly more expensive (factor of a few) than the assumption of perfect correlation, because contributions of different species have to be convoluted across sub-intervals. This however is generally a small price to pay, compared to the large gains in flexibility in computing atmospheric conditions and the number of absorbing species one can model at the same time with the randomly overlapping assumption. For the convolution of two species  $m$ , and  $n$ , this can be written as:

$$\kappa_{m,n}(l, b, g_{ij}) = \frac{\chi_m(l) \kappa_m(l, b, g_i) + \chi_n(l) \kappa_n(l, b, g_j)}{\chi_m(l) + \chi_n(l)}. \quad (1.13)$$

Here,  $g_{ij}$  is the resulting sub-interval with contributions from molecule  $m$  in interval  $g_i$  and molecule  $n$  in interval  $g_j$ . These new  $g$ -sub-intervals then have to be re-sorted into a monotonous function and re-binned before another molecule can be added. More background and details on the implementation of this assumption in REDFOX can be found in Scheucher et al. (2020b) [see Chapter 2]. A comprehensive example of  $\sigma$  for 20 species calculated for REDFOX from the HITRAN 2016 line list for 1 bar and 300 K, can be found in the fold-out plot (Fig. A.1) in the Appendix.

## 1. Introduction

---

### 1.2.5 Relevance for Atmospheric Climate modeling

Having calculated atmospheric opacities and radiative fluxes for an atmospheric temperature pressure profile, these can then be used in a climate model to calculate amongst other things:

- Atmospheric temperatures in radiative equilibrium
- Atmospheric convection based on adiabatic lapse rates
- Photolysis of atmospheric constituents, i.e. changes in atmospheric composition
- Characteristic atmospheric transmission, emission, and reflectance spectra

**Atmospheric Temperatures in radiative equilibrium** Radiative equilibrium, i.e. local energy conservation, in the absence of atmospheric dynamics can be solved directly from the first law of thermodynamics:

$$\rho c_p \frac{\partial T}{\partial t} = \frac{DP}{Dt} + \rho Q \quad (1.14)$$

Here,  $\rho$  is the mass density,  $c_p$  the heat capacity,  $DP/Dt$  the work done onto the system, and  $Q$  the heating in the system. Assuming no work done onto the system, heating only to be radiative,  $\rho Q = -\partial F/\partial z$  ( $F$  being the net radiative flux), and substituting for pressure coordinates using hydrostatic equilibrium,  $dp/dz = -g\rho$  ( $g$  as in gravitational acceleration), results in the equation solving for temperature assuming radiative equilibrium in our climate model:

$$\frac{\partial T}{\partial t} = \frac{g}{c_p} \frac{\partial F}{\partial p} \quad (1.15)$$

Given a certain set of starting values (e.g. for modern Earth), fluxes and temperatures are iterated in our climate model until a steady state is reached for a given set of exoplanetary boundary conditions. Note that Eq. (1.15) can be found in various works with a minus sign coming from model specific definitions of flux directions.

**Atmospheric convection based on adiabatic lapse rates** Intrinsically, convection is a multi-dimensional hydrodynamic problem. Solving for

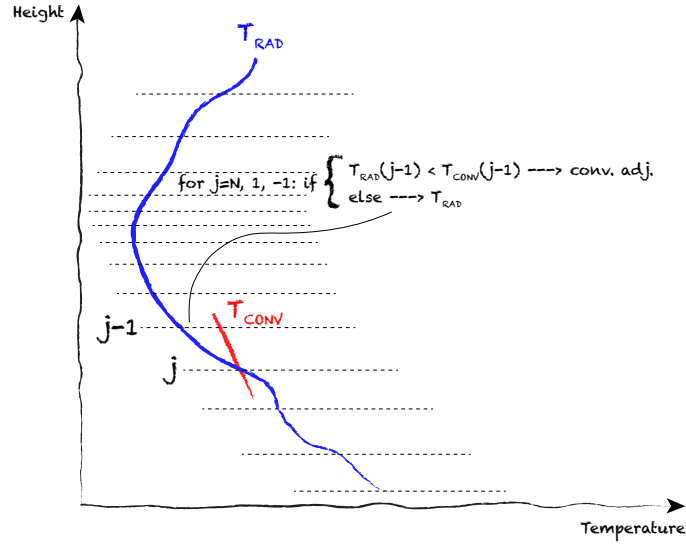


**Figure 1.6:** Illustration of convective adjustment performed in [1D-TERRA](#).

convection in a one-dimensional model such as [1D-TERRA](#) will depend on a parameterisation from thermodynamics and / or hydrodynamics in some way, shape, or form. The simplest and fastest approach is to impose *adiabatic lapse rates* ( $\Gamma = -dT/dp$ ) for atmospheres assumed to be in convective equilibrium. A common implementation of such an approach into a climate model is illustrated in Fig. 1.6. First, temperatures in radiative equilibrium are calculated, then *convective adjustment* is performed for atmospheric layers where  $\Gamma_{\text{RAD}} > \Gamma_{\text{CONV}}$ , which is known as the *Schwarzschild criterion*. This approach is implemented in [1D-TERRA](#), and is a good first approximation if one is interested in atmospheres in global thermodynamic equilibrium, or steady state, called *radiative-convective equilibrium*, involving the most general processes important to estimate overall planetary habitability. A different approach called *mixing-length theory* (e.g. Prandtl, 1925) may be utilized, especially if one is interested in short-term processes affecting atmospheric temperatures, such as day-night cycles or atmospheric responses to single event phenomena, amongst others. This approach heavily relies on parameters derived from hydrodynamics such as from highly sophisticated 3D general circulation models (GCM). A general drawback of this method is that GCMs rely on numerous modeling parameters specific to a certain planet of interest, and its environment such as e.g. rotation speed, land mass distribution, vegetation, ocean currents, and many more. This restriction is

## 1. Introduction

---

therefore passed on to the parameters used in mixing-length theory in a 1D model, which is restrictive compared with some of the major benefits of a 1D model over a GCM, namely flexibility and broad applicability.

**Photolysis of atmospheric constituents** Absorption through electromagnetic transitions not only affects atmospheric temperatures but may also lead to photolytic dissociation which can be written as:



Here  $AB$  represents a molecule dissociated by radiation, or photon, of energy  $h\nu$  into the products  $A$  and  $B$ . To photodissociate a molecule hence change atmospheric composition, the photon has to have an energy of at least the dissociation energy needed to overcome the respective molecular bond. This occurs commonly in the [UV](#) and [VIS](#) spectral ranges and most photolysis reactions require energies of more than  $\sim 1.4$  eV ( $\lambda \sim 880$  nm). The photolytic rate coefficient ( $J$ ) of one specific photolysis reaction ( $r$ ) at height  $z$  in an atmosphere can be written as:

$$J_r(z) = \int F_{\text{tot}}(z) \sigma_{AB}(\nu, z) \eta_r(\nu) d\nu. \quad (1.17)$$

Here,  $F_{\text{tot}} = F_{\downarrow}(z + \delta z) + F_{\uparrow}(z - \delta z)$  is the sum of radiative fluxes that may hit a specific molecule  $AB$  at height  $z$ , comprised of the remainder of incoming stellar radiation at that height ( $F_{\downarrow}$ ), plus the portion of back-scattered radiation from lower atmospheric layers ( $F_{\uparrow}$ ). Atmospheric thermal radiation is anticipated to play only a minor photolytic role for temperate planets in, or close to, the [HZ](#).  $\sigma$  is the photolytic (i.e. absorption) cross section of the molecule at the respective wavenumber, as described in [Sec. 1.2.3](#) and [1.2.4](#). The equation so far resembles the calculation of molecular absorption of radiation, except for the reaction specific quantum efficiency ( $\eta$ ), which describes the probability function over frequency of photolysis actually occurring when a photon of specific energy hits the molecule in question.

**Characteristic atmospheric spectra** There are several ways in which planetary atmospheres can be observed. The [Outgoing Long-Wave Radiation \(OLR\)](#) i.e. the upward fluxes as described in [Sec. 1.2.1](#) over wavelength at the emitting layer make up the planet's emission spectrum. Theoretically, if

the main focus lies with very low resolution bin-wise emission, this could be achieved directly with the fluxes calculated by our  $k$ -distribution [radiative transfer REDFOX](#) as part of our climate model [1D-TERRA](#). More often than not, one is interested in comparing modeled spectra to observations performed by spectrographs mounted on telescopes. For these spectra, p-T profiles calculated from radiative-convective equilibrium as described in [Sec. 1.2.5](#) together with atmospheric chemical composition profiles, serve as input for [LBL radiative transfer](#) models calculating emission, transmission, or reflectance spectrum at a user-determined spectral resolution. A transmission spectrum typically refers to the spectral appearance of radiation from the host star which has travelled through the planetary atmosphere during a planetary transit, capturing the atmospheric absorption of the stellar light. A reflectance spectrum is typically calculated for a planet in orbital phases where radiation from the host star, reflected by the planet’s atmosphere or surface, reaches the observer. All three together are crucial to gain deep insights into an exoplanet, its atmosphere, and ultimately, potential habitability. Many groups around the world have developed world class theoretical spectral models including e.g. *SMART* (Meadows and Crisp, [1996](#)), *NEMESIS* (Irwin et al., [2008](#)), or *GARLIC* (Schreier et al., [2014](#); Schreier et al., [2018b](#); Schreier et al., [2018a](#)) – used in publications Scheucher et al. ([2018](#)), Scheucher et al. ([2020a](#)), and Scheucher et al. ([2020b](#)), to name but a few.





## 1.3 The Effect of Energetic Particle Bombardment

Planets are embedded in a moving (collisionless) plasma derived from different sources, with some of the components (charged particles) being very highly energetic, depending on the source and acceleration processes. This is commonly called *space weather*. Characterization of exoplanetary space weather and its impact on planetary habitability as well as detectability of potential exo-life, relies on numerous interlinked processes from various scientific disciplines. *Theoretical astrophysics* and *heliophysics* provide information on the generation of (high) energetic particles in the Sun and other stellar objects. The *space weather community* provides detailed heliospheric information which is useful to understand other astrospheres and together with *Plasma physics* deals with particle propagation through an astrosphere, magnetosphere, and ionosphere. Last but not least *Earth* and *planetary sciences* describe the impact of all the above upon a planet and its atmosphere.

### 1.3.1 Sources and Types of Cosmic Rays

**Cosmic Rays (CRs)** are high-energetic particles, protons,  $\alpha$ -particles and heavier ions, with energies in the MeV to EeV ( $10^{18}$  eV) range (e.g. Thoudam et al., 2016) traveling through interstellar and interplanetary space, first discovered during balloon flights by Viktor Hess (Hess, 1912). CRs are distinguished by their origin into **Galactic Cosmic Rays (GCRs)** and **Stellar Energetic Particles (SEPs)**.

**Galactic Cosmic Rays** As the name suggests, these are thought to be of galactic (or extragalactic) origin. Earth is bombarded by GCRs isotropically from all directions, their **Spectral Energy Distribution (SED)** at Earth is shown in Fig. 1.7. Particles of energies below  $\sim 30$  GeV are modulated, and partially deflected by the Solar magnetic field and magnetized wind of plasma, i.e. the **heliosphere**. Particle fluxes distinctly slope off above  $\sim 3 \times 10^6$  GeV, from  $dN/dE \propto E^{-2.7}$  to  $\sim E^{-3.1}$  known as *the knee* in the **GCR SED** (see e.g. Cronin et al., 1997; Hillas, 2005; Blasi, 2013). Around energies of  $10^9$  GeV exists another change of slope, known as *the ankle*, recently argued to possibly indicate a gradual transition from galactic to extragalactic particles due to a potential change in elemental composition (see e.g. Aartsen et al., 2013; Apel et al., 2013) and add-hoc arguments about gyroradii in the interstellar

## 1. Introduction

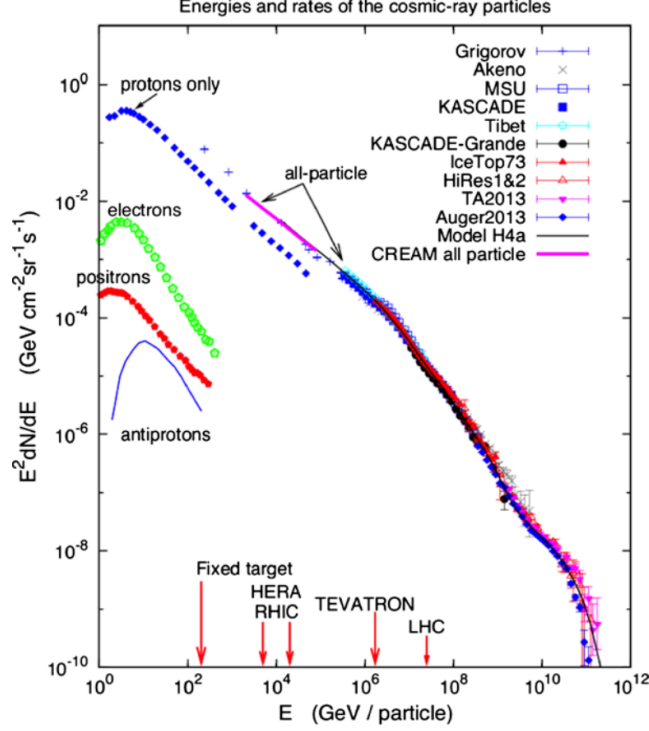


**Figure 1.7:** Spectral Energy Distribution of GCRs at earth measured by different experiments (Blasi, 2013). Electron, positron, and antiproton spectra as measured by PAMELA (Payload for Antimatter Matter Exploration and Light-nuclei Astrophysics) (Adriani et al., 2011).

magnetic fields exceeding the scale height of the galactic disk (e.g. Simpson, 1983).

Pinning down the actual sources of individual particles, or even groups thereof, is a problem still under debate. What we measure on Earth, namely direction and SED of GCRs, is a convolution of numerous acceleration processes from the source regions and propagation in the interstellar medium, to the alteration and modulation by our heliosphere. The most plausible candidates for GCR sources to date are Supernova Remnants (SNRs), which may energize CRs at the supernova shock front through various possible processes up to  $\sim 10^8$  GeV. The acceleration processes involved in pushing particles of galactic origin to even higher energies are not well known (see e.g. Schlickeiser, 2002; Blasi, 2013, for a discussion).

### 1.3 The Effect of Energetic Particle Bombardment

---

**Stellar Energetic Particles** refer to the directional, lower energetic component of **CRs**, associated with a planet's host star. Stars continuously lose mass by supersonic particle flow escaping into interplanetary space through open magnetic fields, known as *stellar wind*. The Sun's stellar wind, called *solar wind*, can be distinguished by speed and origin into slow and fast components. The fast solar wind escapes the Sun in the polar regions through so-called *coronal holes* and reaches velocities up to  $\sim 800 \text{ km s}^{-1}$  and densities of  $\sim 1\text{-}5 \text{ cm}^{-3}$  at 1 AU, whereas the slow component, associated with low-latitude *coronal streamers*, reaches around half the speeds, at 3-10 times the particle density (McComas et al., 2007). Driven by stellar rotation, the two wind components form what is known as the *Parker spiral* in interplanetary space. While particle energies of the solar wind itself are generally too low to significantly impact a planet's lower atmosphere, it forms the ionosphere, deforms the Earth's magnetic field in the wind and the Parker spiral may form propagation channels for *stellar eruptions* and **Coronal Mass Ejections (CMEs)**.

The complex structure of the *toroidal* component of the solar magnetic field, associated with *sunspots*, regularly causes explosive bursts of X-ray and **EUUV** radiation in *solar flares*, together with accelerated electron and proton outflows. Twisting of magnetic field lines may cause *magnetic reconnection* in the lower solar corona, shooting parts of the plasma back onto the Sun's photosphere during reconfiguration of the underlying magnetic fields, triggering a **flare**. Simultaneously, plasma gets accelerated outward, sometimes triggering short-lived, or *impulsive SEP* events with particle energies up to  $\sim 10 \text{ MeV}$  (Kallenrode, 2003). The explosive nature of **flares** in addition to numerous heating processes in the solar corona also cause massive plasma outflow in the solar corona, known as **CMEs**. At the shock front of such **CMEs**, and further out in interplanetary space via interaction with **Corotating Interaction Regions (CIRs)**, pockets of density and magnetic field enhancements caused by the solar wind can lead to protons becoming accelerated very efficiently (up to a few GeV) through e.g. *diffusive shock acceleration* (see e.g. Zank et al., 2000; Schlickeiser, 2002; Li et al., 2012), which may be the primary source of **SEPs** subsequently reaching Earth's atmosphere within a few days of the associated **flare** (Airapetian et al., 2020). There exist, however, also **flares**, even X-class **flares**, where only electromagnetic radiation seems to escape the Sun (Gopalswamy et al., 2008;

## 1. Introduction

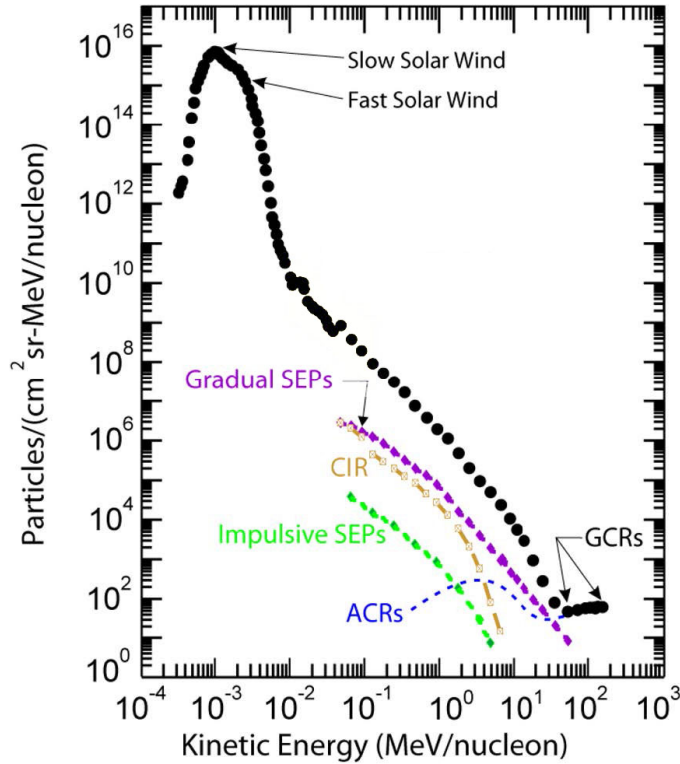


**Figure 1.8:** Oxygen fluence of solar energetic particles as measured by instruments on-board the ACE (Advanced Composition Explorer) spacecraft (adapted from Desai and Giacalone, 2016).

Gopalswamy et al., 2015). Figure 1.8 shows oxygen fluences measured with different particle sensors onboard the *ACE* spacecraft in the late 1990s. The oxygen fluence is generally 2-3 orders of magnitude lower than proton or helium fluences, but following very similar trends (see e.g. Mewaldt et al., 2001; Mewaldt et al., 2005). The black dots in Fig. 1.8 represent a superposition of numerous SEP events plotted against kinetic energy. Note that SEP fluxes and fluences, while by far not as highly energetic, are generally orders of magnitude higher than for GCRs. Also indicated in Fig. 1.8 is another class of CRs, somewhat intermediate in energy between GCRs and SEPs, called Anomalous Cosmic Rays (ACRs) (e.g. Cummings et al., 2002; Drake et al., 2010). These most likely represent neutral particles of galactic source that become ionized and modulated in the heliosphere.

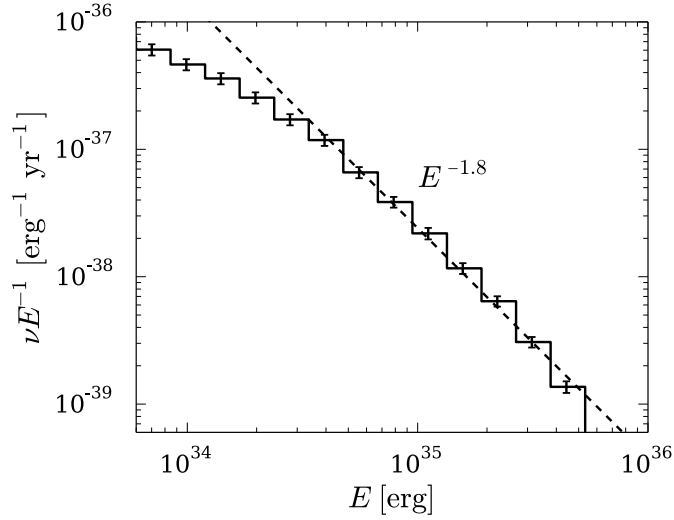


**Figure 1.9:** Occurance rate ( $\nu$ ) of flares on 373 superflaring F, K, and M-dwarf stars (having produced at least one flare of  $> 5 \times 10^{34}$  erg in the *Kepler* data set) over total observed flare energy ( $E$ ) (adapted from Candelaresi et al., 2014).

### 1.3.2 Flares and CMEs on other stars

Numerous authors have studied the Sun and its current activity in the context of its evolution and compared it to other stars and stellar types. An *activity-rotation-age* relation was proposed by multiple authors following UV and X-ray observations, and magnetohydrodynamic (MHD) modeling, with the understanding that stars lose momentum and spin down over time through stellar wind and CME-driven mass loss (see e.g. Kraft, 1967; Weber and Davis, 1967; Pallavicini et al., 1981; Walter and Bowyer, 1981; Walter, 1981; Walter, 1982; Zahnle and Walker, 1982). In recent years special focus has been laid upon the occurrence rate and intensity of flares and superflares on other stars (e.g. Shibata et al., 2013; Shibayama et al., 2013; Maehara et al., 2012; Maehara et al., 2015; Notsu et al., 2013; Notsu et al., 2019; Candelaresi et al., 2014; Davenport, 2016). Recent X-ray and UV observations with XMM-NEWTON, CHANDRA, HST, and Kepler, have given invaluable insights on stellar flaring properties, although observations in the EUV are especially difficult because of absorption by the interstellar medium. Figure 1.9 shows the energy distribution of a sample of superflaring F, K, and M-dwarf stars in quarters 0-6 of the Kepler survey (Koch et al., 2010), where superflaring here indicates that the stars considered in Fig. 1.9 showed at least one flare of event-integrated energy above  $5 \times 10^{34}$  erg during

## 1. Introduction

---

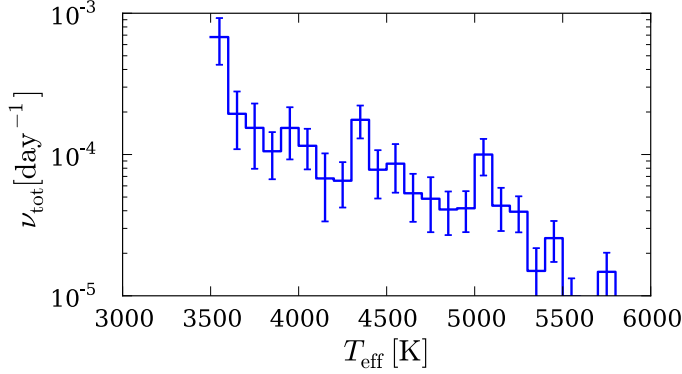


**Figure 1.10:** Flare occurrence rate ( $\nu$ ) over stellar effective temperature ( $T_{\text{eff}}$ ) for 115,984 G, K, and M-dwarf stars from the *Kepler* data set (adapted from Candelaresi et al., 2014).

this particular survey. The slope in flare occurrence over energy has been well established over the last few years, the *drop-off* on both ends on the energy scale, however, may be an observational artefact. The rate of highest energetic flares is limited by our observational baseline, i.e. we may require an extended observational timeline to capture sufficient flares with event-integrated energies above  $10^{36}$  erg for a statistically significant conclusion. At the lower energetic end flare rates seem to saturate. This phenomenon is well known and is likely caused by observational sensitivity limits (e.g. Maehara et al., 2012; Shibayama et al., 2013; Muheki et al., 2020). It can be challenging even for state-of-the-art instruments to distinguish such small brightness enhancements from instrument and photon noise. Note that even these so-called *small flares* with energies of  $10^{33}$  -  $10^{34}$  erg are still very strong compared to the energy of the largest Solar event in modern history, the *Carrington event* estimated to have been  $\sim 10^{33}$  erg (Carrington, 1859).

Fig. 1.10 shows the total rate of flares per day over effective stellar temperature for a much larger sample of over  $10^5$  active stars of various stellar types. While the  $dN/dE$  slope illustrated in Fig. 1.9 remains approximately constant across stellar types, it is evident from Fig. 1.10 that cooler stars ( $T_{\text{eff}} < 3700$  K), namely M-dwarf stars, show on average orders of magnitude higher flaring activity than e.g. G stars ( $T_{\text{eff}} > 5200$  K). Events like the aforementioned Carrington event on Earth, may happen multiple times a day on active M-dwarf stars. This fact is especially important for the investigation of potentially habitable worlds around other stars, since most of the stars in the solar neighborhood are in fact M-dwarf stars, and because of observational

---

### 1.3 The Effect of Energetic Particle Bombardment

---

benefits, many potentially-terrestrial exoplanets have been found around these cool stars. Further, because of the comparably low bolometric luminosity of M-dwarf stars, such planets need to orbit such stars very close-in for the chance to be habitable (e.g. Scalo et al., 2007; Shields et al., 2016), making them highly vulnerable to strong bombardment from associated SEPs, as particle fluxes to a first approximation drop-off  $\propto d^{-2}$  with distance ( $d$ ) from the star.

Although it is well-established that stars other than the Sun generate flares, CMEs and SEPs are much more challenging to observe (see e.g. Odert et al., 2017). Additionally, CME signatures have to be carefully disentangled from flare signatures which are highly correlated in time and space. Visualization of solar CMEs propagating in the heliosphere already takes *difference-imaging* from images taken by e.g. Solar and Heliospheric Observatory (SOHO) or Solar Terrestrial Relations Observatory (Stereo). The most promising observational efforts involve e.g. Doppler-shifts of chromospheric lines such as Ca II, signatures of the previously mentioned type-II radio bursts, or enhanced continuous X-ray absorption (e.g. Franciosini et al., 2001; Favata and Schmitt, 1999). Houdebine et al. (1990) reported blue-shifted chromospheric hydrogen and Ca II lines during a superflare on the active M star *AD Leo* which could possibly be attributed to a  $5800 \text{ km s}^{-1}$  CME. For now, simple scaling of known solar SEP producing events is applied to other stars to estimate values at the location of exoplanets, or sophisticated MHD modeling is applied to estimate the impact of SEPs upon the habitability of exoplanets. Interestingly, 3D MHD simulations with the *magnetic breakout model* (Lynch et al., 2016) have suggested that CMEs with  $E < \sim 10^{34} \text{ erg}$  may be confined by the strong magnetic fields suggested for M-dwarfs and young G type stars, which is remarkably similar to the drop in flare rates in the same energy range (Fig. 1.9). While the potential non-existence of such smaller flares on M-dwarf stars may not change much the overall habitability of worlds which orbit them, this potential flare-CME relationship may hint towards complex, not yet fully understood magnetically rooted processes worth investigating.

#### 1.3.3 Propagation and Secondary Particles

Energetic, ionized particles, such as CRs, interact with any magnetized, or ionized medium, including the Interstellar Medium (ISM), astrospheres, planetary magnetospheres, and atmospheres, all acting as energy or/and

## 1. Introduction

---

charge-dependent *particle filters*, allowing only high energetic particles to pass through, while diverting or deflecting particles of lower energies. [Astrospheres](#) may be defined by three distinctive boundaries, the *termination shock* where stellar wind becomes subsonic, the *astropause* where the thermal pressure from the hot ionized stellar wind equals the thermal particle pressure from the surrounding [ISM](#), and, depending on the star’s relative movement within the local [ISM](#), a possible interstellar bow shock, where the [ISM](#) becomes subsonic. Between the termination shock and the astropause, stellar wind particles are diverted downstream forming an *astrotail* (e.g. Schlickeiser, 2002; Muller et al., 2006; Scherer et al., 2015). Our local astropause, the *heliopause*, lies at around 120 AU upstream, around four times the orbital distance of Neptune. As explained above, only highly energetic [GCRs](#) make it past these boundaries into an [astrosphere](#), in which [CR](#) fluxes are further modulated, generally described by the *transport equation* (e.g. Parker, 1965; Caballero-Lopez and Moraal, 2004; Gieseler et al., 2017; Herbst et al., 2020), which can be written in 1D and spherical coordinates ( $r$ ) as:

$$\frac{\partial f}{\partial t} = -v_{\text{SW}} \frac{\partial f}{\partial r} + \frac{1}{r^2} \frac{\partial}{\partial r} \left( r^2 \kappa \frac{\partial f}{\partial r} \right) + \frac{1}{3r^2} \frac{\partial}{\partial r} (r^2 v_{\text{SW}}) \frac{\partial f}{\partial \ln(p)} \quad (1.18)$$

In steady state, the time derivative  $\partial f / \partial t$  of the [CR](#) distribution function ( $f$ ) would vanish. The first term on the right-hand side describes outward convection due to the stellar wind with speed  $v_{\text{SW}}$ , the second term describes diffusion (with coefficient  $\kappa$ ) in the astrospheric magnetic field, and the last term denotes energy changes of [CRs](#) with momentum  $p$  due to adiabatic expansion of the stellar wind. Note that, instead of  $p$ , particle rigidity  $R$ , describing momentum per charge, is often used in the literature, since particles of similar  $R$  interact similarly with magnetic fields. A well observed phenomenon, also evident from Eq. (1.18), is the anti-correlation of solar activity and [GCR](#) fluxes at Earth. The stronger the solar or stellar wind and the more [CMEs](#) are produced, the more [GCRs](#) are deflected within an [astrosphere](#). Because Eq. (1.18) needs to be solved through computationally expensive [MHD](#) simulations, numerous quasi-analytical approximations have emerged over the decades. For certain applications, a solution of the transport equation (Eq. (1.18)) may be approximated e.g. by the *Convection-Diffusion Solution* or by the *Force-Field Solution* (see e.g. Moraal, 2013, for a review). In the latter case, fluxes ( $J$ ) at a specific planetary position ( $r$ ) in an astrosphere



### 1.3 The Effect of Energetic Particle Bombardment

can be approximated by:

$$J(E, r) = J_{\text{LIS}}(E + \Phi) \frac{E^2 - E_0^2}{(E + \Phi)^2 - E_0^2}. \quad (1.19)$$

Here  $J_{\text{LIS}}$  is the unmodulated CR flux outside the astrosphere,  $E_0$  a particle's rest mass energy,  $E$  a particle's total energy (kinetic plus rest energy), and  $\Phi = Ze\phi$  is a modulation function with charge  $Z$ , unit charge  $e$ , and the astrospheric modulation potential  $\phi$  (see e.g. Caballero-Lopez and Moraal, 2004; Gieseler et al., 2017). While the above mentioned approximation delivers satisfactory results for GCR fluxes measured at Earth, recent studies (e.g. Caballero-Lopez and Moraal, 2004; Herbst et al., 2020) have shown the limits to the above approximations and suggested the need for 3D MHD simulations for planetary positions in the heliosphere other than Earth, and for planets within astrospheres around M-dwarf stars.

Essentially, SEPs and GCRs, in a planetary magnetosphere and ionosphere, undergo similar modulation. A magnetosphere can shield a planet from particles of rigidity lower than a so-called *cut-off rigidity*  $R_c$ , thereby preventing them from reaching further down into the atmosphere (e.g. Smart et al., 2006; Mironova et al., 2015).  $R_c$  varies significantly with latitude and longitude for a planet with a dipolar field, such as Earth, leaving the poles by far less protected (e.g. Smart et al., 2000). With the increase in densities lower down in a planetary atmosphere, particle collisions become increasingly important. Not only do they further alter particle fluxes and energy distribution, energy is deposited in the atmosphere, with subsequent showers of secondary particles, atmospheric ionization, and potential atmospheric escape in the upper atmosphere. Figure 1.11 illustrates the creation of numerous secondary energetic particles, including nucleons, pions, muons, X-rays and gamma radiation, positrons and electrons, arising from a single collision of an initial energetic particle with an atmospheric atom or molecule in a *nuclear-electromagnetic-muon cascade*. Near Earth, CRs consist of mostly protons,  $\sim 10\%$   $\alpha$ -particles (He), and  $< 1\%$  heavier nucleons (Mironova et al., 2015). In addition, lower energetic particles not triggering nuclear reactions ( $< 500$  MeV) can produce high energetic secondary electrons through inelastic collisions with atmospheric atoms in a second kind of air shower, in which the atmospheric molecules may either excite, ionize, or be dissociated (Simmhuber and Funke, 2020). These high energetic electrons can

## 1. Introduction

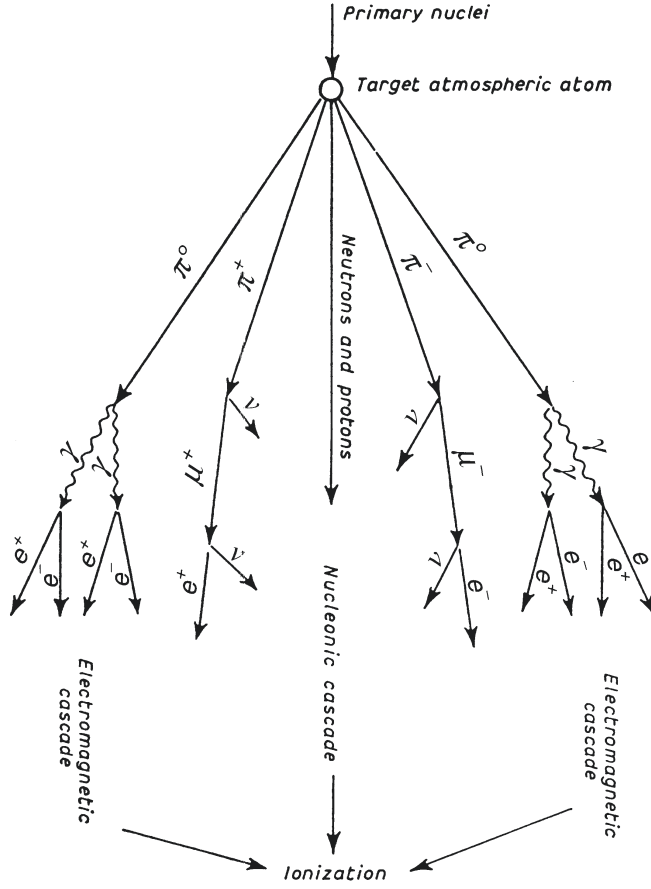


**Figure 1.11:** Schematic of secondary particle cascades produced in a collision of a primary CR with an atom (Schlickeiser, 2002). Three types of cascade are illustrated: hadronic (center), muon ( $\pi \rightarrow \mu$ ) cascade, and the soft cascade (outer) involving X-ray photons  $\gamma$ .

themselves also act as the initial particle for another collision-induced cascade of further particles or generate further gamma rays via *bremsstrahlung*. The higher the kinetic energy of the primary CR particle, the deeper down into a planetary atmosphere such showers of resulting ionized secondary particles precipitate.

Depending on the atmospheric composition, at a certain atmospheric depth this CR-induced ion flux, or *ionization rate*, reaches a maximum, known as *Pfotzer maximum* (Pfotzer, 1936), below which energies of remaining secondary particles become too low to trigger further particle showers. Such a maximum lies at an altitude of  $\sim 17$ -27 km on Earth, while on Mars it is only

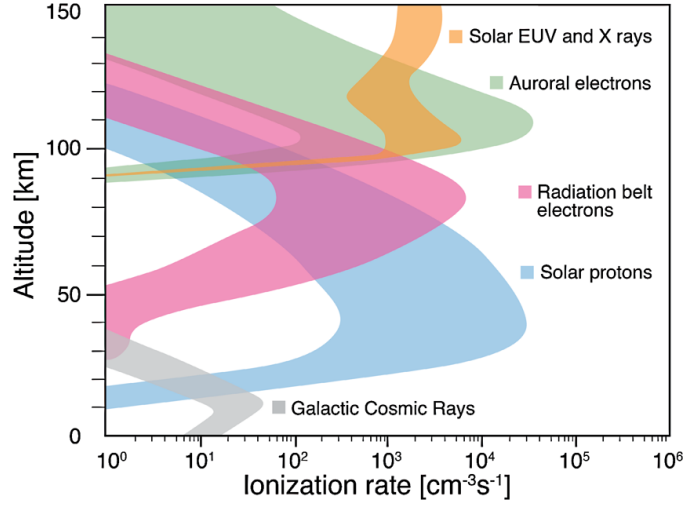


**Figure 1.12:** Ionization from various primary (grey and blue) and secondary (pink and green) CR sources and from photoionization (orange) in Earth's atmosphere (Mironova et al., 2015).

reached sub-surface. The highest energetic CRs can cause life-threatening Ground Level Enhancements (GLEs) which occur when high fluxes of either primary or secondary energetic particles reach a planet's surface. Figure 1.12 shows typical ranges of ionization rate profiles in modern Earth's atmosphere for different primary sources. Very characteristic is the ionization from GCRs deep in the atmosphere around the tropopause (grey) due to their high initial energies, compared to the much larger ionization rates coming from high fluxes of the lower energetic SPEs (blue) in the stratosphere and mesosphere. However, these are highly sporadic, while GCRs are nearly continuous. Note that due to Earth's magnetic field and related  $R_c$ , there is an additional latitudinal and longitudinal variation in both the altitude and magnitude of this ionization rate maximum (Mironova et al., 2015).

**Modeling ionization rates** CR induced atmospheric ionization has long been studied because of its potentially significant impact on atmospheric chemistry and climate (e.g. Neher, 1967; Neher, 1971; Anderson, 1973; Ferrari and Szuszkiewicz, 2009; Gaisser et al., 2016). In numerical models usually an *ionization yield function* ( $Y$ ), corresponding to the number of ion pairs produced from a primary CR, is introduced to calculate the CR-induced

## 1. Introduction

---

ionization rate ( $Q$ ) via:

$$Q(h) = \sum_i \int_{E_c}^{\infty} J_i(E) \cdot Y_i(E, h) dE. \quad (1.20)$$

Here  $J$  is the primary particle energy distribution of species  $i$ . Analytical approaches have been developed to calculate  $Y_i$  from lower energetic particles ionizing the upper atmosphere without collisions (e.g. Velinov and Mateev, 1990; Vitt and Jackman, 1996). Above particle energies of a few hundred MeV however, the collisions of primary and subsequent secondary particles with atmospheric nuclei shown in Fig. 1.11 become increasingly significant. Such complex processes cannot be modeled anymore in a straightforward analytical approach. Gaisser and Hillas (1977), instead of solving Eq. (1.20), introduced a fit function to CR measurements in the lower Earth atmosphere to estimate secondary electrons produced in particle showers. This uses the common assumption that ion-electron pairs are produced through collisions and alpha particles and heavier particles are neglected, therefore ionization can be calculated from the production rate of secondary electrons from protons via:

$$Q(h) = \sum_j \int_{E_1}^{E_2} \left( n_j(h) \cdot \sigma_j^{\text{ion}}(E_{\text{el}}) \cdot S_{\text{el}} \int_{\Omega} \int_E N_{\text{el}}(h, E) \cdot J_p(E) dE d\Omega \right) dE_{\text{el}}. \quad (1.21)$$

Here, the summation is over atmospheric species  $j$  (for Earth:  $\text{N}_2, \text{O}_2$ ) of number densities  $n$  with respective ionisation cross sections via electron impact  $\sigma^{\text{ion}}$ . Electron energies ( $E_{\text{el}}$ ) are discretized into bins ( $E_1, E_2$ ) with electron energy distribution  $S_{\text{el}}$ , and  $N_{\text{el}}$  represents the flux of secondary electrons at height  $h$  from protons of energy  $E$  over solid angle  $\Omega$ .  $N_{\text{el}}$  is obtained using the fit:

$$N_{\text{el}}(h, E) = N_{\text{max}}(E) e^{\frac{h_{\text{max}}(E) - h}{\lambda(E)}} \left( \frac{h - h_0(E)}{h_{\text{max}}(E) - h_0(E)} \right) e^{\frac{h_{\text{max}}(E) - h_0(E)}{\lambda(E)}}. \quad (1.22)$$

Here  $\lambda$  is the electron attenuation length and  $N_{\text{max}}$ ,  $h_{\text{max}}$ , and  $h_0$ , represent the fitting parameters used by Gaisser and Hillas (1977), which have been adapted by e.g. Grenfell et al. (2007) or Tabataba-Vakili et al. (2016) to model SEP event specific ionization rates for Earth-like exoplanets. Scheucher et al. (2018) [see Chapter 3] used this approach to conduct a parameter study, together with Chemical Production Efficiency (CPE) parameters explained

### 1.3 The Effect of Energetic Particle Bombardment

in Sec. 1.3.4, to investigate the sensitivity of climate, habitability, and biosignature abundances, to uncertainties in SEP strengths and abundance associated with M-dwarf flares, as well as uncertainties in the atmospheric ion-chemical responses.

A more complex approach to model atmospheric cascades and ionization rates in the deeper atmosphere, is through *Monte-Carlo modeling* (see e.g. Usoskin and Kovaltsov, 2006; Bazilevskaya et al., 2008). Numerous works using different numerical approaches have been developed over the years to obtain the ionization yield function ( $Y$ ) in Eq. (1.20), given by:

$$Y_i(E, h) = \frac{1}{E_{\text{ion}}} \frac{\partial E_i}{\partial h}. \quad (1.23)$$

Here  $E_{\text{ion}}$  is the energy necessary for atmospheric ionization (e.g.  $\sim 35$  eV in air), and  $\partial E$  is the energy loss in layer  $\partial h$  at atmospheric depth,  $h$ . Some of the commonly used Monte-Carlo models calculating  $Y$  in planetary atmospheres include the *Cosmic Ray Atmospheric Cascade (CRAC)* model based on the *CORSIKA+FLUKA* Monte-Carlo packages, as well as *ATMOCOSMICS/PLANETOCOSMICS* (and derivatives) and the *Atmospheric Ionization Model of Osnabrück (AIMOS)* based on the *GEANT4* package (see e.g. Mironova et al., 2015, for an overview). Scheucher et al. (2020a) [see Chapter 4] utilized ionization rates modeled through a combination of PLANETOCOSMICS (Desorgher et al., 2005; Herbst et al., 2013) for transport through a planetary magnetosphere and the *Atmospheric Radiation Interaction Simulator (AtRIS)* (Banjac et al., 2019c; Banjac et al., 2019b; Banjac et al., 2019a) for atmospheric ionization, iteratively with the climate chemistry model *ID-TERRA* to consistently model CR-induced ionization and its impact on habitability, spectral appearance, surface dosage of ionizing radiation, and potential biosignatures for the exoplanet Proxima Centauri b.

#### 1.3.4 Impact on Habitability and Biosignatures

Broadly speaking there are many ways in which CRs could influence atmospheric habitability and composition. Firstly, they could drive atmospheric escape as studied for numerous close-in exoplanets e.g. Dong et al. (2018) for the TRAPPIST system. Secondly, CRs could influence cloud formation although this mechanism is strongly debated (see e.g. Rusov et al., 2010).

## 1. Introduction

---

Thirdly, CRs could influence atmospheric composition via e.g. secondary electrons destroying atmospheric constituents. In this thesis we concentrate on the third effect.

Following initial collisions of CRs with atmospheric molecules, an avalanche of subsequent chemical processes, potentially impacting habitability and spectral appearance, is initiated. Significant effects arise for collisions with dominant species such as  $\text{H}_2$  and  $\text{He}$  in upper planetary atmospheres, and in the deeper atmospheres e.g. with  $\text{N}_2$ ,  $\text{O}_2$  on Earth, or with  $\text{CO}_2$  on Mars and Venus. However, subsequent *ion chemistry* distributes initial charges to other species and significantly changes atmospheric ion and neutral composition through charge and ion charge reactions, electron attachment, electron-ion and ion-ion recombination, as well as dissociative recombination and quenching reactions of the most abundant species with primary excited products (see e.g. Mironova et al., 2015; Sinnhuber and Funke, 2020). Since ions and electronically excited species are generally very reactive in the gas-phase, the resulting reaction chains tend to be fast and can be complex. In the second half of the last century numerous authors extensively studied the dissociative ionisation of  $\text{N}_2$  and  $\text{O}_2$  in Earth’s atmosphere through theory, laboratory experiments, and observations (e.g. Rapp and Englander-Golden, 1965; Porter et al., 1976), including the production and subsequent reaction chains of odd nitrogen (e.g. Crutzen et al., 1975; Jackman et al., 1980; Rusch et al., 1981) and odd hydrogen (e.g. Solomon et al., 1981). Rusch et al. (1981) calculated the fractions of  $\text{N}^+$ ,  $\text{N}_2^+$ ,  $\text{O}^+$ , and  $\text{O}_2^+$  directly from dissociation of  $\text{N}_2$  and  $\text{O}_2$ , and subsequent production of odd nitrogen ( $\text{N}(^4\text{S})$ ,  $\text{N}(^2\text{D})$ ,  $\text{NO}$ ), the sum of which is commonly called  $\text{NO}_x$ . Solomon et al. (1981) calculated the formation of odd hydrogen ( $\text{H}$ ,  $\text{OH}$ ,  $\text{HO}_2$ ), the sum of which is commonly called  $\text{HO}_x$ , in the presence of  $\text{H}_2\text{O}$  vapor in Earth’s atmosphere based on the above mentioned ion fractions. In the last decades, full 3D ion chemistry modeling efforts were able to qualitatively reproduce observations of Earth’s atmospheric responses, providing invaluable insights into the driving chemical processes (e.g. Jackman et al., 2001; Jackman et al., 2005; Winkler et al., 2009; Funke et al., 2011; Verronen et al., 2016). In the stratosphere and mesosphere, negative ion chemistry and the production of cluster ions (e.g.  $\text{H}^+(\text{H}_2\text{O})_n$  and  $\text{NO}_3^-(\text{HNO}_3)_n$ ) becomes increasingly important, leading to production of e.g.  $\text{HNO}_2$  and  $\text{HNO}_3$  in Earth’s low to mid atmosphere. All of these production (and destruction e.g. of  $\text{H}_2\text{O}$ ) rates undergo daily and seasonal

### 1.3 The Effect of Energetic Particle Bombardment

changes as well as vary with latitude and height in the atmosphere. Taking into account uncertainties and variations, the [CPE](#) i.e. the net production of NO<sub>x</sub> from atmospheric ionization in Earth’s atmosphere is estimated to be 1-2 NO<sub>x</sub> per ion pair, whereas HO<sub>x</sub>, depending on [H<sub>2</sub>O](#) vapor in the atmosphere is around 0-2 HO<sub>x</sub> per initial ion pair (see e.g. Sinnhuber et al., 2012; Sinnhuber and Funke, 2020, for a review).

The production and destruction rates of neutral species from [CR](#)-induced ions can have wide ranging effects on other atmospheric constituents as calculated in photochemical models (see e.g. Segura et al., 2010; Grenfell et al., 2012; Rugheimer et al., 2013; Rugheimer et al., 2015; Tabataba-Vakili et al., 2016) through bimolecular and three body reactions. Photochemistry solves the set of coupled *stiff ordinary differential equations (ODEs)* describing changes in species abundances ( $n$ ) through production and loss processes via:

$$\frac{\partial n}{\partial t} = \frac{\partial}{\partial z} \left( K \cdot \frac{\partial n}{\partial z} \right) + P - nL. \quad (1.24)$$

Here  $P$  describes the production ( $\text{cm}^{-3} \text{s}^{-1}$ ) of chemical species  $n$  ( $\text{cm}^{-3}$ ),  $L$  is the loss rate ( $\text{s}^{-1}$ ), and  $K$  is the so-called *eddy diffusion coefficient* ( $\text{cm}^2 \text{s}^{-1}$ ) describing atmospheric dynamics. The full network of [BLACKWOLF](#), the photochemistry module in [1D-TERRA](#), consists of 1127 reactions for 115 species (i.e. 115 coupled ODEs) including bimolecular and three-body reactions as well as photolysis for 81 absorbers in the [UV](#) and [VIS](#) spectral range (see Wunderlich et al., 2020, in print.). The term *stiff* refers to the fact that the involved processes, here mostly chemical reactions, occur over a wide range of time scales (many orders of magnitude). Solving such a system of equations in a straightforward explicit time stepping manner would require an extraordinary amount of very small time steps to accurately calculate the system’s responses to external driving forces, such as the [CR](#)-induced [CPEs](#). Instead, implicit solvers such as e.g. the *backward-euler scheme* using a *Newtonian* solver, as implemented in [BLACKWOLF](#), are used (e.g. Press et al., 2007; Hairer and Wanner, 1996).

Figure 1.13 illustrates some important effects of [CR](#)-induced changes in Earth’s neutral atmosphere. Highlighted (colored) are some species considered [biosignatures](#) or *biomarkers* in Earth’s atmosphere. That is, species with abundances in Earth’s atmosphere which cannot be explained without life i.e. with sources either directly, or indirectly, related to life (see e.g. Grenfell,

## 1. Introduction

---

2017; Schwieterman et al., 2018, for a review). In the context of exoplanet science, an ideal biosignature would typically have spectral features that are easily detectable remotely, their signals would be distinctly extractable from the data, and abiotic sources (false positives) would be excludable (see e.g. Airapetian et al., 2020, and references therein). No single known biosignature however features all of these properties perfectly and therefore a range of different biosignatures would be sought out in practice. On Earth, proposed biosignatures include  $O_2$  (almost exclusively from photosynthesis) and its photochemical product  $O_3$ ,  $N_2O$  (from micro-organisms), and  $CH_3Cl$  (fungi, algae, and other plants).  $CH_4$  (from methanogenic bacteria but also abiotic submarine and volcanic outgassing) is referred to as bioindicator i.e. it gives a possible indication of life but more information is required. Water, although not a biosignature, is essential for life as we know it (see e.g. Sagan et al., 1993; Segura et al., 2005; Grenfell et al., 2007; Kaltenegger et al., 2007). Relatively large  $O_2$  abundances are needed for associated spectral features to become apparent (e.g. in the VIS and near-IR), only a few ppb of its photolytic product  $O_3$  are needed to form strong spectral features e.g. around  $9.6\mu m$  and in the VIS (e.g. B  tr  mieux and Kaltenegger, 2013) in Earth’s atmospheric spectrum.  $N_2O$  has absorption bands at e.g. 7.8 and  $8.5\mu m$ ;  $CH_4$  has a band close by at  $7.7\mu m$  as well as numerous bands in the near-IR (e.g. at  $0.76$  and  $1.2\mu m$ ). The search for habitable conditions centers around the search for  $H_2O$ , which has numerous strong absorption bands throughout the VIS and IR spectral range hence it may be challenging to distinguish these from biosignatures in spectral observations. For planets with  $H_2$  dominated atmospheres, Seager et al. (2013) proposed  $NH_3$  as a possible biosignature. Due to its short chemical lifetime against photolysis in clear atmospheres, large sources are required for detection. It is likely that a combination of the above mentioned species will ultimately be required to claim a robust detection of life on an exoplanet (e.g. Airapetian et al., 2020).

Scheucher et al. (2018) [see Chapter 3] investigated the influence of uncertainties in SEP strength from M-dwarf flares and the wide range of the above-mentioned NOx and HOx CPEs onto atmospheric temperatures and changes in biosignature abundances for an Earth-like atmosphere in an extensive parameter study. Special focus was placed upon understanding biosignature responses to the CR-induced photochemical changes as shown in Fig. 1.13, as well as consequential significant changes in atmospheric







## 1.4 Relevant Publications

As part of this work, four relevant publications as first author (one of these as equal contribution first author), plus a number of contributions as co-author in other works have been published in scientific journals. Three of these are appended as part of this cumulative thesis in the chapters to follow. This section provides a brief overview of all the relevant publications with my personal contributions in historical order, starting with the first author publications, followed by articles I co-authored.

M. Scheucher, J.L. Grenfell, F. Wunderlich, M. Godolt, F. Schreier, H. Rauer. *New Insights into Cosmic-Ray-induced Biosignature Chemistry in Earth-like Atmospheres*, ApJ, 863:6, 2018 [see Chapter 3]

Contribution: First Author, see chapter 3 for more details

Relevance: By investigating various CR-related parameters within their plausible ranges for an Earth around an active M-dwarf, this work addresses the science questions *How does the host star's spectral type affect planetary habitability?* and *How do energetic particle showers impact atmospheric composition and habitability?*

Method: 1D coupled climate chemistry modeling and spectral analysis

Status: published in peer reviewed journal

M. Scheucher, K. Herbst, V. Schmidt, J.L. Grenfell, F. Schreier, S. Banjac, B. Heber, H. Rauer, M. Sinnhuber. *Proxima Centauri b: A Strong Case for Including Cosmic-Ray-induced Chemistry in Atmospheric Biosignature Studies*, ApJ, 893:12, 2020 [see Chapter 4]

Contribution: First Author, see chapter 4 for more details

Relevance: This work builds on the publication above by consistently treating the incoming flux of energetic particles and its propagation through a magnetosphere, ionosphere, and atmosphere as well as chemical

## 1. Introduction

---

responses. By applying it to an existing exoplanet it addresses *What kind of atmospheres can provide habitable conditions? How does the host star’s spectral type affect planetary habitability?* and *How do energetic particle showers impact atmospheric composition and habitability?*

Method: A suite of models including 3D magnetospheric shielding, 3D atmospheric ionization and radiation dosages, 1D ion chemistry, and 1D coupled climate chemistry, spectral analysis

Status: published in peer reviewed journal

**M. Scheucher, F. Wunderlich, J.L. Grenfell, M. Godolt, F. Schreier, D. Kappel, R. Haus, K. Herbst, H. Rauer. *Consistently Simulating a Wide Range of Atmospheric Scenarios for K2-18b with a Flexible Radiative Transfer Module*, ApJ, 898:44, 2020 [see Chapter 2]**

Contribution: First Author, see chapter 2 for more details

Relevance: This work describes a central aspect of this thesis, a major update of our 1D coupled climate chemistry model’s capabilities regarding radiative transfer and atmospheric variety, to address the questions *What kind of atmospheres can provide habitable conditions?*, *Which atmospheres can explain observed spectral features?* and *How does the host star’s spectral type affect planetary habitability?*

Method: 1D coupled climate chemistry modeling, spectral analysis

Status: published in peer reviewed journal

**F. Wunderlich\*, M. Scheucher\*, M. Godolt, J.L. Grenfell, F. Schreier, P.C. Schneider, D.J. Wilson, A. Sánchez-López, M. López-Puertas, H. Rauer. *Distinguishing between wet and dry atmospheres of TRAPPIST-1 e and f*, ApJ, 2020, in print**

Contribution: Equal contribution first Author (i.e. the first two authors share equal first co-authorship); climate relevant modeling.

Relevance: Part of this work investigates surface conditions on the terrestrial sized exoplanets in the TRAPPIST-1 system for a variety of plausible atmospheres. It also investigates spectral appearances and detectability which could be achieved from upcoming [JWST](#) observations.

Method: 1D coupled climate chemistry modeling, spectral analysis, signal to noise analysis

Status: accepted for publication in peer reviewed journal

**K. Herbst, J.L. Grenfell, M. Sinnhuber, H. Rauer, B. Heber, S. Banjac, [M. Scheucher](#), V. Schmidt, S. Gebauer, R. Lehmann, F. Schreier. *A new model suite to determine the influence of cosmic rays on (exo)planetary atmospheric biosignatures - Validation based on modern Earth*, *A&A*, 631, A101, 2019**

Contribution: coupled climate photo-chemistry modeling including the consistent treatment of cosmic rays iterated with other models within the model suite; spectral analysis

Relevance: This work validates the newly developed model suite, which was later applied for exoplanets in [Scheucher et al. \(2020a\)](#) (Chapter 4), against Earth observations.

Method: A suite of models including 3D magnetospheric shielding, 3D atmospheric ionization and radiation dosages, 1D ion chemistry, and 1D coupled climate chemistry, spectral analysis

Status: published in peer reviewed journal

**V.S. Airapetian, R. Barnes, O. Cohen, G.A. Collinson, W.C. Danchi, C.F. Dong, A.D. Del Genio, K. France, K. Garcia-Sage, A. Gloer, N. Gopalswamy, J.L. Grenfell, G. Gronoff, M. Güdel, K. Herbst, W.G. Henning, C.H. Jackman, M. Jin, C.P. Johnstone, L. Kaltenegger, C.D. Kay, K. Kobayashi, W. Kuang, G. Li, B.J. Lynch, T. Lüftinger, J.G. Luhmann, H. Maehara, M.G. Mlynczak, Y. Notsu, R.A. Osten, R.M. Ramirez, S. Rugheimer, [M. Scheucher](#), J.E. Schlieder, K. Shibata, C. Sousa-Silva, V. Stamenković, R.J. Strangeway,**

## 1. Introduction

---

A.V. Usmanov, P.Vergados, O.P. Verkhoglyadova, A.A. Vidotto, M. Voytek, M.J. Way, G.P. Zank, Y. Yamashiki. *Impact of space weather on climate and habitability of terrestrial-type exoplanets*, International Journal of Astrobiology, 19(2), 136-194, 2020.

Contribution: contributions in various chapters of this review paper.

Relevance: This is a review paper outlining *How does stellar activity and space weather affect planetary atmospheres and habitability?* and *which stars are good / bad host stars for life as we know it?*

Method: sharing accumulated expertise through a topical review

Status: published in peer reviewed journal

# 2

## **Publication I: Consistently Simulating a Wide Range of Atmospheric Scenarios for K2-18b with a Flexible Radiative Transfer Module**

**Personal and co-authors contributions:** I developed the new radiative transfer module ([REDFOX](#)), including the research of existing methods and theories, testing, implementation, calculation of cross sections, validations against known atmospheres, amongst others. I also conducted the study of K2-18b including initial setups, [1D-TERRA](#) runs, as well as producing synthetic spectra. The manuscript was written by myself.

F. Wunderlich updated the photochemistry module in [1D-TERRA](#); F. Schreier supported the model validation against his [LBL](#) model; D. Kappel and R. Haus provided Venus model validation data; All co-authors provided comments on the manuscript and in the journal's peer-review phase.



# Consistently Simulating a Wide Range of Atmospheric Scenarios for K2-18b with a Flexible Radiative Transfer Module

Markus Scheucher<sup>1,2,8</sup>, F. Wunderlich<sup>1,2,8</sup>, J. L. Grenfell<sup>2</sup>, M. Godolt<sup>1</sup>, F. Schreier<sup>3</sup>, D. Kappel<sup>2,4</sup>, R. Haus<sup>5</sup>, K. Herbst<sup>6</sup>, and H. Rauer<sup>1,2,7</sup>

<sup>1</sup> Zentrum für Astronomie und Astrophysik, Technische Universität Berlin, D-10623 Berlin, Germany; [scheucher@tu-berlin.de](mailto:scheucher@tu-berlin.de), [markus.scheucher@dlr.de](mailto:markus.scheucher@dlr.de)

<sup>2</sup> Institut für Planetenforschung, Deutsches Zentrum für Luft- und Raumfahrt, D-12489 Berlin, Germany

<sup>3</sup> Institut für Methodik der Fernerkundung, Deutsches Zentrum für Luft- und Raumfahrt, D-82234 Oberpfaffenhofen, Germany

<sup>4</sup> Institut für Physik und Astronomie, Universität Potsdam, D-14476 Potsdam, Germany

<sup>5</sup> Institut für Geowissenschaften, Universität Potsdam, D-14476 Potsdam, Germany

<sup>6</sup> Institut für Experimentelle und Angewandte Physik, Christian-Albrechts-Universität zu Kiel, D-24118 Kiel, Germany

<sup>7</sup> Institut für Geologische Wissenschaften, Freie Universität Berlin, D-12249 Berlin, Germany

Received 2019 December 20; revised 2020 April 28; accepted 2020 May 4; published 2020 July 21

## Abstract

The atmospheres of small, potentially rocky exoplanets are expected to cover a diverse range in composition and mass. Studying such objects therefore requires flexible and wide-ranging modeling capabilities. We present in this work the essential development steps that lead to our flexible radiative transfer module, REDFOX, and validate REDFOX for the solar system planets Earth, Venus, and Mars, as well as for steam atmospheres. REDFOX is a  $k$ -distribution model using the correlated- $k$  approach with the random overlap method for the calculation of opacities used in the  $\delta$ -two-stream approximation for radiative transfer. Opacity contributions from Rayleigh scattering, UV/visible cross sections, and continua can be added selectively. With the improved capabilities of our new model, we calculate various atmospheric scenarios for K2-18b, a super-Earth/sub-Neptune with  $\sim 8 M_{\oplus}$  orbiting in the temperate zone around an M star, with recently observed H<sub>2</sub>O spectral features in the infrared. We model Earth-like, Venus-like, and H<sub>2</sub>–He primary atmospheres of different solar metallicity and show resulting climates and spectral characteristics compared to observed data. Our results suggest that K2-18b has an H<sub>2</sub>–He atmosphere with limited amounts of H<sub>2</sub>O and CH<sub>4</sub>. Results do not support the possibility of K2-18b having a water reservoir directly exposed to the atmosphere, which would reduce atmospheric scale heights, and with it the amplitudes of spectral features, making the latter inconsistent with the observations. We also performed tests for H<sub>2</sub>–He atmospheres up to 50 times solar metallicity, all compatible with the observations.

*Unified Astronomy Thesaurus concepts:* Radiative transfer simulations (1367); Radiative transfer (1335); Computational methods (1965); Exoplanets (498); Extrasolar rocky planets (511); Exoplanet atmospheres (487); Planetary atmospheres (1244); Mini Neptunes (1063); Super Earths (1655)

## 1. Introduction

Exciting recent discoveries in exoplanetary science include the TRAPPIST-1 system (Gillon et al. 2017), Proxima Centauri b (Anglada-Escudé et al. 2016), and potential super-Earths/warm sub-Neptunes like LHS 1140b and c (Ment et al. 2019), K2-18b (Montet et al. 2015), and GJ 1214b (Charbonneau et al. 2009). Exoplanet science is transitioning from detection into first atmospheric characterizations from spectral observations, giving us insights into their composition and possible formation and evolution. Numerous spectral observations of Jupiter-sized to warm Neptune-sized planets have been reported and discussed in recent years (see, e.g., Sing et al. 2016; Crossfield & Kreidberg 2017), but the first detection of water features in the atmosphere of the temperate ( $T_{\text{eq}} \sim 272$  K) super-Earth/sub-Neptune K2-18b (Benneke et al. 2019b; Tsiaras et al. 2019) orbiting an early-type M star is especially exciting, as it offers an unprecedented possibility of gaining insights into the atmosphere and climate of objects in the regime between rocky and gas planets that do not exist in the solar system. Detailed understanding of atmospheric processes, such as radiative transfer, convection, and disequilibrium chemistry, is key for the interpretation of such spectral detections.

The atmospheres of terrestrial planets lying in the habitable zone of their respective host stars could be from H<sub>2</sub>–He-dominated, to H<sub>2</sub>O-, CO<sub>2</sub>-, and N<sub>2</sub>-dominated, or even O<sub>2</sub>- or CO-dominated for warmer and cooler planets, respectively (see, e.g., Forget & Leconte 2014; Madhusudhan et al. 2016).

A main motivation for our model development is as follows. The radiative transfer schemes, based on the  $k$ -distribution method, implemented in previous versions of our model, as well as other similar models developed for the study of terrestrial planets (e.g., Segura et al. 2010; Kopparapu et al. 2013), rely on premeditated  $k$ -tables for atmospheric conditions, such as pressure, temperature, and composition. Especially the latter can be a considerable restriction for simulating atmospheres that are more and more different from that of Earth. Adding radiation-absorbing constituents often requires a recalculation of all  $k$ -tables. The same applies for including updates of line lists, for example, for one constituent. There are, however, multiple ways of treating the overlap of spectral absorption lines of gaseous components in  $k$ -distribution radiative transfer calculations for more flexibility, assuming perfect correlation, random overlap, or disjoint lines (see, e.g., Pierrehumbert 2010). Lacis & Oinas (1991) described how the overlap of absorption by gaseous components can be treated quickly and accurately using the random overlap assumption in

<sup>8</sup> Equal Contribution Authors.



the  $k$ -distribution method, which has been implemented and tested for hot Jupiter studies by Amundsen et al. (2017). Malik et al. (2017) recently developed a GPU-based open-source radiative transfer model using the faster assumption of perfect correlation between spectral lines of different molecules in the correlated- $k$  approximation for studying hot Jupiters and other planets with primary atmospheres. This assumption, however, becomes less accurate the more absorbers are present. While  $k$ -distribution models operate in cross-section space, Kitzmann (2017) used opacity sampling in his CO<sub>2</sub> cloud studies, which can be seen as a degraded line-by-line (LBL) radiative transfer model. Then, the addition of absorbing gases is fully additive, but opacity sampling is generally computationally more expensive than the  $k$ -distribution method and becomes less accurate for lower pressures, where many thin absorption lines can be missed by wavelength discretization. Lincowski et al. (2018) adopted a different approach by introducing an LBL radiative transfer module into a climate-chemistry model using the linearized flux evolution approach (Robinson & Crisp 2018) in order to reduce the number of time-consuming radiative transfer calculations for the study of terrestrial climates. This approach is fast as long as changes in important parameters influencing radiative fluxes, such as temperature and composition of major absorbers, are small. In that case, fluxes are approximated by linear flux gradients stored in a Jacobian for the last calculated state, rather than invoking full radiative transfer calculations.

Our new radiative transfer model, REDFOX, using the random overlap assumption, aims to combine the flexibility with regard to stellar spectra and atmospheric conditions similar to an LBL model but with calculation times approaching those of other  $k$ -distribution models using the correlated- $k$  approach. A central aim of this work is to show our new extensive capabilities for studying terrestrial exoplanets with REDFOX as part of our 1D coupled climate-chemistry model, 1D-TERRA.

In Section 2, we provide information on general climate and chemistry model updates that lead to our new 1D climate-chemistry model 1D-TERRA. Section 2.1 focuses in detail on the essentials of REDFOX, including the  $k$ -distribution method using the random overlap approximation. Section 3 validates REDFOX against known properties of atmospheres in the solar system. Section 4.2 presents our results for the super-Earth/sub-Neptune K2-18b before our final remarks in Section 5.

## 2. Methodology

Our 1D coupled climate-chemistry model has a long heritage dating back to, e.g., Kasting & Ackerman (1986), Pavlov et al. (2000), and Segura et al. (2003) for the study of Earth-like planets. Since then, it has been extensively updated in our group by, for example, Rauer et al. (2011), Grenfell et al. (2012), and Scheucher et al. (2020). Von Paris et al. (2008, 2010, 2015) implemented MRAC, a modified version of the rapid radiative transfer model (RRTM; Mlawer et al. 1997) for CO<sub>2</sub>-dominated atmospheres in the climate module to study, e.g., early Mars or planets at the outer edge of the habitable zone. Our new radiative transfer module, REDFOX, is designed to operate over a wide range of stellar energy spectra, as well as diverse neutral composition (without ion chemistry) and pressure-temperature conditions in terrestrial atmospheres.

Grenfell et al. (2007), Tabataba-Vakili et al. (2016), and Scheucher et al. (2018) implemented parameterizations of cosmic rays and stellar energetic particles into our chemical solver. The latter can be part of an extensive model suite, calculating the precipitation of energetic particles through a magnetosphere and atmosphere, induced atmospheric ionization, and the impact on climate and neutral atmospheric composition, as described in Herbst et al. (2019). In conjunction with the companion paper (Wunderlich et al. 2020), we briefly describe in Section 2.3 key aspects of our extensively updated chemical reaction scheme that can simulate diverse terrestrial atmospheres.

The new model with updated climate and chemistry will be referred to as 1D-TERRA. Figure 1 provides a schematic overview of the 1D-TERRA model.

For postprocessing, we use the Generic Atmospheric Radiation Line-by-line Infrared Code (GARLIC; e.g., Schreier et al. 2014, 2018a, 2018b) to calculate planetary transit and emission spectra as described in, e.g., Scheucher et al. (2018) and Wunderlich et al. (2020).

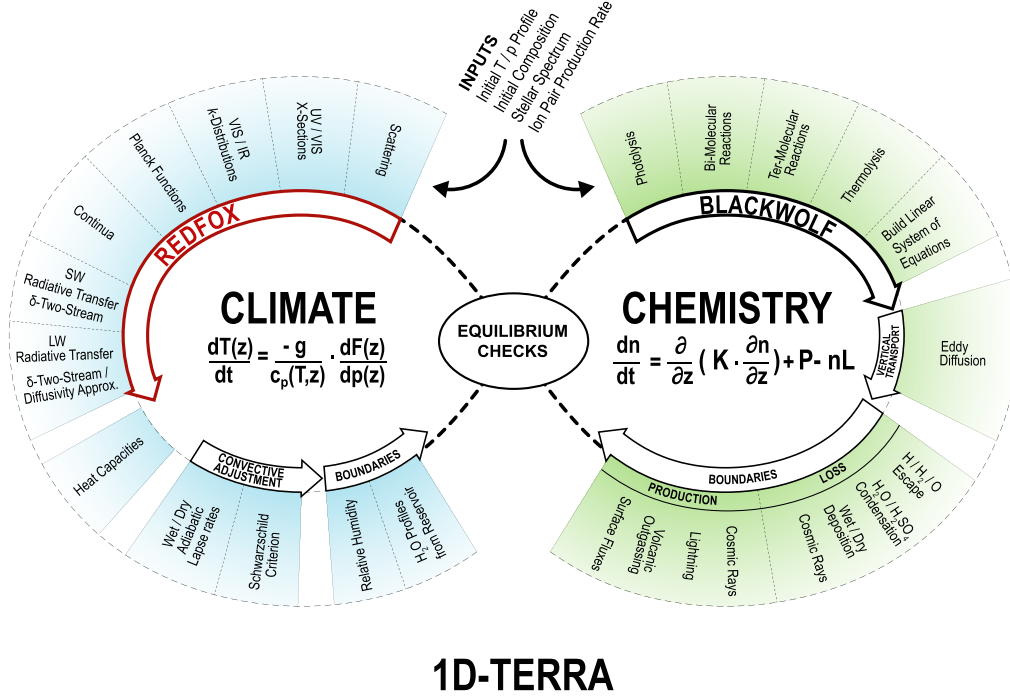
### 2.1. Radiative Transfer Module REDFOX

REDFOX calculates radiative transfer for discrete intervals, or bands, in the spectral range from  $\nu = 0$  to  $10^5 \text{ cm}^{-1}$ , where any of the spectral intervals can be used for the short-wave (SW) and long-wave (LW) treatment of radiative transfer to allow for, e.g., more complete coverage of the irradiation of late-M dwarfs. Also, in the LW, the choice of the spectral interval is now flexible to include colder, temperate, and warmer planets alike. In addition, we extended the pressure and temperature range for the correlated- $k$  calculations so that absorption by, for example, O<sub>3</sub>, H<sub>2</sub>O, CO<sub>2</sub>, and CH<sub>4</sub> can also be treated for planets close to the inner edge of the habitable zone, where evaporation of water can lead to surface pressures higher than 1.5 bars, which was our previous pressure limit for Earth-like atmospheres. Note that von Paris et al. (2010) implemented absorption by CO<sub>2</sub> and H<sub>2</sub>O for pressures up to 1000 bars for a high-CO<sub>2</sub> atmospheric study without trace gases in an earlier model version. In contrast, our extended range now includes absorption by all molecules presented in Table 1, which, e.g., also allows for modeling steam atmospheres, habitable zones, and the upper atmospheres of sub-Neptunes or other H<sub>2</sub>-dominated atmospheres.

#### 2.1.1. Calculation of VIS/IR Cross Sections

In the random overlap method, cross sections calculated for each gas constituent separately are then cross-correlated in the radiative transfer calculations of atmospheric transmission functions. For the calculation of spectroscopic cross sections, we use the HITRAN 2016 line list (Gordon et al. 2017) and the open-source KSPECTRUM code originally developed by Eymet et al. (2016). We downloaded KSPECTRUM1.2.0<sup>9</sup> in 2017, included the treatment of HITRAN 2016 in KSPECTRUM, and also implemented the Total Internal Partition Sums (TIPS) from Gamache et al. (2017), used to calculate temperature conversion factors applied to line intensities, into what we now refer to as KSPECTRUM\_Htr16. In 2018, KSPECTRUM1.3 was released with updates on CO<sub>2</sub> treatment. These updates, e.g., removed the possibility of line truncation

<sup>9</sup> Downloaded from <https://www.meso-star.com/projects/art/kspectrum.html>.



## 1D-TERRA

**Figure 1.** Schematic overview of our 1D coupled climate disequilibrium-chemistry model 1D-TERRA, including the new radiative transfer module, REDFOX, and the updated chemistry scheme, BLACKWOLF.

when sub-Lorentzian wings are used. Since we decided to cut line wings and add missing contributions from far wings with collision-induced absorption (CIA), these modifications are not included in our calculations. A short discussion of our approach follows below. Our KSPECTRUM\_Htr16 source code is available on our group’s software page.<sup>10</sup>

For the spectral discretization of the Voigt profiles, we define line center regions up to 10 half-widths (HWs) from the nominal line center wavenumbers, which are calculated at 8 points per HW and 16 points in the far wings and use a cutoff at  $25 \text{ cm}^{-1}$  from the line center for every molecule (see below). After extensive testing on numerous computing platforms (not shown), the abovementioned parameter set for spectral discretization represented a reasonable trade-off between accuracy and computing time (<several months for low pressures). KSPECTRUM also has one integrated discretization algorithm that aims to keep the error from discretizing the Voigt profiles below a user-defined value. Unfortunately, this algorithm becomes computationally inefficient for low pressures where lines are very narrow, leading to a sharp increase in points needed for the wavenumber grid discretization. Our choice of discretization showed less than  $10^{-5}$  relative deviation in resulting cross sections from results using that error-limited algorithm for tests at 1 Pa (and even less deviation at higher pressures), except for  $\text{H}_2\text{O}$ , which showed higher deviations of up to 1%. It is noteworthy that calculation times for cross sections should go down significantly with the use of GPU-based algorithms, such as, e.g., Helios-*k* (Grimm & Heng 2015). The trade-off between wavenumber discretization and accuracy is a common challenge in molecular absorption

modeling, and different LBL codes use different approaches for the grid discretization and interpolation to speed up calculations; see, e.g., Schreier (2006) for a discussion.

Further, one has to be careful with regard to which line cutoff value to choose (Figure 2). Appropriate line-wing cutoff parameterizations, together with the right pressure-broadened wing profiles, are still debated in the literature (see, e.g., Sharp & Burrows 2007; Takagi et al. 2010; Grimm & Heng 2015; Hedges & Madhusudhan 2016). It is beyond the scope of this paper to outline all proposed theories, discussions, and possible assumptions surrounding this topic; instead, we would like to quickly motivate our choices. Assuming we could produce all true line-wing shapes, their deviation from Lorentzian profiles and their changes with temperature, pressure, and composition, adding up the contribution of all absorption lines to infinity may, theoretically, reproduce most known spectral features, including absorption bands, window regions, and possibly some continua. Unfortunately, many line wings differ substantially from the classical Lorentzian approximation. Clough et al. (1992) already argued that the super-Lorentzian nature of  $\text{H}_2\text{O}$  absorption is too complex to parameterize with wing shapes and rather developed continuum parameterizations to be used in addition to LBL calculations with a  $25 \text{ cm}^{-1}$  cutoff. The sub-Lorentzian nature of  $\text{CO}_2$  line wings has proven to be even more difficult, since numerous major absorption bands need their own parameterization (see, e.g., Perrin & Hartmann 1989; Pollack et al. 1993; Tonkov et al. 1996). Therefore, a multitude of continuum and CIA parameterizations have emerged (see, e.g., Gruszka & Borysow 1997; Baranov et al. 2004). Sharp & Burrows (2007) recommended a general pressure-dependent cutoff,  $d = \min(25p, 100) \text{ cm}^{-1}$ , with  $p$  being the atmospheric pressure in atm, leading to cutoff values

<sup>10</sup> KSPECTRUM\_Htr16: <http://www.dlr.de/kspectrum>.

**Table 1**  
List of Molecules Included in REDFOX and the Corresponding VIS/IR Line List and UV/VIS Cross-section Sources

Data Source	Molecules
HITRAN 2016 Line List <sup>a</sup>	CH <sub>3</sub> Cl, CH <sub>4</sub> , CO, CO <sub>2</sub> , H <sub>2</sub> , H <sub>2</sub> O, HCl, HCN, HNO <sub>3</sub> , HO <sub>2</sub> , HOCl, N <sub>2</sub> , N <sub>2</sub> O, NH <sub>3</sub> , NO, NO <sub>2</sub> , O <sub>2</sub> , O <sub>3</sub> , OH, SO <sub>2</sub>
MPI Mainz Spectral Atlas <sup>b</sup>	C <sub>2</sub> H <sub>2</sub> , C <sub>2</sub> H <sub>2</sub> O, C <sub>2</sub> H <sub>3</sub> , C <sub>2</sub> H <sub>4</sub> , C <sub>2</sub> H <sub>4</sub> NH, C <sub>2</sub> H <sub>5</sub> , C <sub>2</sub> H <sub>5</sub> CHO, C <sub>2</sub> H <sub>6</sub> , C <sub>3</sub> H <sub>3</sub> , C <sub>3</sub> H <sub>6</sub> , C <sub>3</sub> H <sub>8</sub> , C <sub>4</sub> H <sub>2</sub> , CH <sub>2</sub> CCH <sub>2</sub> , CH <sub>2</sub> CO, CH <sub>3</sub> , CH <sub>3</sub> C <sub>2</sub> H, CH <sub>3</sub> CHO, CH <sub>3</sub> Cl, CH <sub>3</sub> NH <sub>2</sub> , CH <sub>3</sub> OH, CH <sub>3</sub> ONO, CH <sub>3</sub> ONO <sub>2</sub> , CH <sub>3</sub> OOH, CH <sub>4</sub> , Cl <sub>2</sub> , Cl <sub>2</sub> O, Cl <sub>2</sub> O <sub>2</sub> , ClCO <sub>3</sub> , ClO, ClONO, ClONO <sub>2</sub> , ClOO, ClS <sub>2</sub> , CO, CO <sub>2</sub> , COCl <sub>2</sub> , CS <sub>2</sub> , H <sub>2</sub> , H <sub>2</sub> CO, H <sub>2</sub> O, H <sub>2</sub> O <sub>2</sub> , H <sub>2</sub> S, H <sub>2</sub> SO <sub>4</sub> , HCl, HCN, HCO, HCOOH, HNO, HNO <sub>2</sub> , HNO <sub>3</sub> , HO <sub>2</sub> , HO <sub>2</sub> NO <sub>2</sub> , HOCl, HSO, N <sub>2</sub> , N <sub>2</sub> H <sub>2</sub> , N <sub>2</sub> H <sub>4</sub> , N <sub>2</sub> O, N <sub>2</sub> O <sub>5</sub> , NH <sub>3</sub> , NO, NO <sub>2</sub> , NO <sub>3</sub> , NOCl, O <sub>2</sub> , O <sub>3</sub> , OClO, OCS, OH, S <sub>2</sub> , S <sub>2</sub> O, S <sub>2</sub> O <sub>2</sub> , S <sub>3</sub> , S <sub>4</sub> , SCI, SCl <sub>2</sub> , SNO, SO, SO <sub>2</sub> , SO <sub>2</sub> Cl <sub>2</sub> , SO <sub>3</sub>

**Notes.**<sup>a</sup> <https://hitran.org/lbl/> (Gordon et al. 2017).<sup>b</sup> [http://satellite.mpic.de/spectral\\_atlas/cross\\_sections/](http://satellite.mpic.de/spectral_atlas/cross_sections/) (Keller-Rudek et al. 2013).

$>25 \text{ cm}^{-1}$  for pressures  $>1 \text{ atm}$  and therefore being important for high-pressure atmospheric studies, such as gas planet atmospheres. Wordsworth et al. (2010a) conducted a thorough comparison of a  $25 \text{ cm}^{-1}$  cutoff versus untruncated line wings for CO<sub>2</sub>, together with various CIA parameterizations. Following these and similar studies, some authors studying terrestrial atmospheres started adopting larger cutoff values of  $500 \text{ cm}^{-1}$  (e.g., Kopparapu et al. 2013) or even untruncated line shapes for selected molecules (e.g., Wordsworth et al. 2010b; Wordsworth & Pierrehumbert 2013).

Figure 2 suggests that taking into account the far wings of all absorption lines of a specific molecule over the whole wavenumber range may reproduce certain parts of continuum absorption in specific wavelength ranges but at the same time may overestimate absorption in other spectral regions where the addition of many Lorentzian line wings from the whole absorption spectrum would create additional artificial continua not observed in experiments. For pressures above a few bars, this effect can effectively mask any CO<sub>2</sub> or H<sub>2</sub>O absorption features in the visible and near-infrared range. While we tested for a wide range of  $p$ - $T$  conditions (for CO<sub>2</sub> and H<sub>2</sub>O) and various sub-Lorentzian profiles (Perrin & Hartmann 1989; Pollack et al. 1993; Tonkov et al. 1996), in Figure 2, we show this effect for CO<sub>2</sub> with sub-Lorentzian wings after Perrin & Hartmann (1989) at 100 bars (98.7 atm) and 300 K for different line-wing cutoff values (colors) compared to results without any cutoff (black). We also show (dotted) absorption spectra based on our  $25 \text{ cm}^{-1}$  cutoffs including CO<sub>2</sub> CIAs, namely the induced dipoles after Gruszka & Borysow (1997) and the CO<sub>2</sub>-CO<sub>2</sub> dimers from Baranov et al. (2004). Our results suggest that too-large line cutoff values in the LBL calculations can lead to absorption coefficients far exceeding CIA continua contributions in certain spectral window regions, e.g., 8–14 or 20–50  $\mu\text{m}$ . Probably the main difference from the work by Wordsworth et al. (2010a) is the extensive update for CO<sub>2</sub> in HITRAN 2016, especially in the mid-infrared. When no cutoff is used at all (black solid), any CO<sub>2</sub> features in the visible and near-infrared are masked by the far wing contributions. This is mainly due to the previously discussed poorly understood behavior of the far line wings. See, e.g., Takagi et al. (2010) for a detailed discussion of the influence of pressure-broadened CO<sub>2</sub> line shapes upon radiative-convective equilibrium temperatures.

After testing for a range of molecules, pressures, and temperatures, we chose a line-wing cutoff of  $25 \text{ cm}^{-1}$  for all of our calculations of  $k$ -distributions for all molecules. For CO<sub>2</sub>, we calculated sub-Lorentzian wings from Perrin & Hartmann (1989) within its validity range and with the same  $25 \text{ cm}^{-1}$

cutoff. As described in Section 2.1.3, CIAs are added and interpolated directly in REDFOX when performing radiative transfer calculations together with other continua. We would like to emphasize that we do not claim that this approach is superior to others in accuracy, but it allows for flexible treatment of continua and easy substitution when updated parameterizations or measurements become available.

Since we calculate absorption cross sections for pure gases of a given molecule (Table 1) separately, we can only account for self-broadening and not foreign broadening of absorption lines. Since pressure broadening of any given molecule by the total atmospheric gas pressure is therefore approximated by self broadening for that pressure environment, this could become relevant for trace species in high-pressure environments for which self-broadening coefficients could differ significantly from their foreign-broadening coefficients. That said, one should note that the foreign broadening listed in HITRAN refers to (Earth) air broadening only, which should be used with caution for non-Earth-like atmospheres as discussed, e.g., by Wordsworth & Pierrehumbert (2013). For selected molecules, however, there exist more general pressure-broadening descriptions in the Exomol database (Tennyson et al. 2016). To tackle this problem consistently for any species of interest would require a tabulated parameter for broadening by any possible major constituent in an atmosphere of interest. Then the line wings would have to be calculated in LBL calculations using, e.g., the broadened HW  $\gamma = \text{vmr}_{\text{self}} \cdot \gamma_{\text{self}} + \sum_i (\text{vmr}_i \cdot \gamma_i)$ , with  $\text{vmr}$  being the volume mixing ratio and  $i$  any atmospheric constituent other than the considered species itself. This then needs to be tabulated in premixed  $k$ -tables in  $n$  dimensions for  $n$  major constituents of interest calculated on a discrete volume mixing ratio grid, which would somewhat contradict our main aim here, namely a flexible radiative transfer model that is also straightforward to update with additional molecules of interest.

High-resolution cross-section lists have been calculated in this work for each of the 20 HITRAN 2016 molecules shown in Table 1 on a pressure-temperature grid for a total of 121 points. We thereby considered 11 pressures equally spaced in  $\log(p)$  ranging from  $10^{-7}$  to  $10^3$  bars, or  $0.01$ – $10^8$  Pa, and the following 11 temperatures:  $T(\text{K}) = [100, 150, 200, 250, 300, 350, 400, 500, 600, 800, 1000]$ . Studies calculating the outgoing LW radiation (OLR) of hot atmospheres ( $\gtrsim 800 \text{ K}$ ), e.g., Kopparapu et al. (2013) and Katyal et al. (2019), have shown that these cases may require the calculation of cross sections from databases that focus on high temperatures, such as HITEMP (Rothman et al. 2010) or Exomol (Tennyson et al.

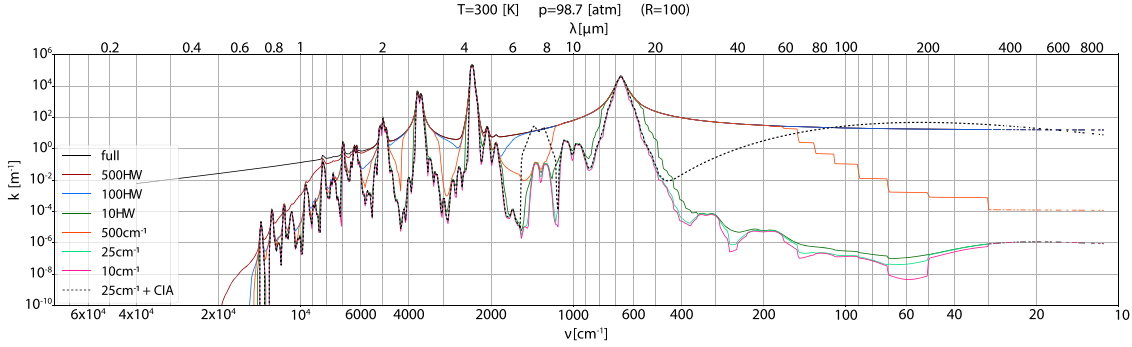


**Figure 2.** Comparison of  $\text{CO}_2$  absorption coefficients calculated with KSPECTRUM from HITRAN 2016 with sub-Lorentzian wings after Perrin & Hartmann (1989) at  $T = 300$  K and  $p = 100$  bars for different line-wing cutoff values (solid lines). We compare cutoff values in HW (=line HWs,  $\gamma_b$ ) and fixed wavenumber values ( $\text{cm}^{-1}$ ). Overplotted (black dashed lines) are results for a line-wing cutoff at  $25 \text{ cm}^{-1}$  including CIA parameterizations from Gruszka & Borysow (1997) and Baranov et al. (2004).

2016), although our Venus validation (Section 3) suggests that this effect may not be central for the atmospheres studied here.

### 2.1.2. $k$ -distributions and Spectral Bands

The  $k$ -distributions are cross-section ( $\sigma$ ) probability distributions within a frequency band, represented by a small number of  $k$ -coefficients and respective weighting quadratures. For a detailed description of the  $k$ -distribution method and the implementation of the Random Overlap approximation with the “Ranking and Reblocking” or “Resorting and Rebinning” RORR method, we refer to, for example, Lacis & Oinas (1991) or Amundsen et al. (2017). The assumption behind random overlap is that absorption lines of individual molecules are uncorrelated. Although computationally more expensive than the simple addition of all molecular cross sections with their respective concentrations, this assumption is certainly a good approximation when including multiple molecules of different shapes and sizes as we do here, leading to very different roto-vibrational and translational absorption features. In random overlap,  $k$ -distributions—or  $\sigma$ -distributions, to be more precise—need to be calculated separately for every pressure  $p$ , temperature  $T$ , and molecule. To calculate individual  $k$ -distributions from cross sections, we make use of the KDISTRIBUTION package, developed by V. Eymet, for easy handling of high-resolution cross-section files previously generated by KSPECTRUM. While we require REDFOX to be as flexible as possible in handling different gas mixtures and atmospheric conditions, note that we will lose any frequency dependence within spectral bands when converting cross sections into  $k$ -distributions. The  $k$ -coefficients of different gas mixtures within one band will not generally map to the same frequencies as in a different gas mixture. This means that we cannot directly map a given source function such as a stellar spectrum or atmospheric Planck function, or other opacity sources like Rayleigh scattering coefficients, continua, or aerosols, into individual  $k$ -coefficients. These have to be added as band-integrated averages. For this reason, individual bands should be as small in frequency range as possible to minimize inaccuracies introduced by using the abovementioned band mean values, while at the same time being fast enough for climate evolution studies. We tested different bandwidths for an Earth-like atmosphere ranging from the original bands (38 for SW, 25 for LW) up to 480 bands over the whole spectral range (not shown). We chose 128 bands in total between

$\nu = 0 \text{ cm}^{-1} (\lambda = \infty)$  and  $\nu = 10^5 \text{ cm}^{-1} (\lambda = 100 \text{ nm})$ , as further increases in band numbers resulted in OLR changes of  $<1\%$ . Bands are evenly spaced in  $\log(\nu)$  above  $\nu = 100 \text{ cm}^{-1}$ , plus 10 bands with  $\Delta\nu = 10 \text{ cm}^{-1}$  in the range  $\nu = 0\text{--}100 \text{ cm}^{-1}$ . The design is such that we can subsequently change the spectral bands for a specific study if accuracy or computational efficiency become an issue. Such a change requires only recalculation of  $k$ -distributions from the high-resolution (8 points per HW) cross-section files, which takes approximately a total of 24 hr on 100 CPUs on our university server for all 20 molecules and 121  $p$ - $T$  points currently included. Details on band-averaged sources and opacities follow later in this section.

Additionally, one must choose a suitable number of quadrature weights or  $k$ -coefficients within a band and the quadrature rule. The quadrature rule used in previous versions of our code dates back to the RRTM (Mlawer et al. 1997) and is a modification of the half Gauss–Legendre weighting, placing more emphasis on the absorption line centers ( $g \sim 1$ ), as described in their paper. We use those quadratures for comparison, since their weighting was specifically designed to well resolve the line center absorption for cooling rates in Earth’s atmosphere. For exoplanet applications, however, we cannot generally assume that the main contribution to cooling rates arises mainly from the line centers alone; there can be additional cooling, e.g., from extensive broadening at higher pressures or temperatures. To test this, we also calculate  $k$ -distributions by applying the standard Gauss–Legendre quadrature rule using the 16th-order Legendre polynomial  $P_{16}(\phi)$  shifted to the  $[0,1]$  interval. For transmission  $\mathcal{T}$  through a homogeneous layer, this is

$$\mathcal{T} = \int_0^1 f(g) dg = \frac{1}{2} \sum_{i=1}^{16} w_i f\left(\frac{1+g_i}{2}\right), \quad (1)$$

with  $g_i$  being the  $i$ th root of  $P_{16}$  and  $f = \exp(-\Delta\tau/\mu)$ , where  $\mu = \cos \Theta$  and  $\Theta$  is the mean zenith angle used in the two-stream approximation. As given by Abramowitz & Stegun (1972), the associated quadrature weights  $w_i$  are a function of the derivatives of  $P_{16}$ , specifically,

$$w_i = \frac{2}{(1-g_i)P'_{16}(g_i)^2}, \quad \sum_i w_i \stackrel{!}{=} 1. \quad (2)$$



**Table 2**Comparison of Quadrature Weights and Respective  $g$  Subintervals in Brackets from RRTM ( $w_{\text{RRTM}}$ ) and Gauss–Legendre Polynomials ( $w_{\text{GL}}$ )

$i$	$w_{\text{RRTM}}$ [g-bin]	$w_{\text{GL}}$ [g-bin]
1	0.15275 [0.00000–0.15275]	0.01358 [0.00000–0.01358]
2	0.14917 [0.15275–0.30192]	0.03113 [0.01358–0.04471]
3	0.14210 [0.30192–0.44402]	0.04758 [0.04471–0.09229]
4	0.13169 [0.44402–0.57571]	0.06231 [0.09229–0.15460]
5	0.11819 [0.57571–0.69390]	0.07480 [0.15460–0.22940]
6	0.10193 [0.69390–0.79583]	0.08458 [0.22940–0.31398]
7	0.08328 [0.79583–0.87911]	0.09130 [0.31398–0.40528]
8	0.06267 [0.87911–0.94178]	0.09472 [0.40528–0.50000]
9	0.04249 [0.94178–0.98427]	0.09472 [0.50000–0.59472]
10	0.00463 [0.98427–0.98890]	0.09130 [0.59472–0.68602]
11	0.00383 [0.98890–0.99273]	0.08458 [0.68602–0.77060]
12	0.00303 [0.99273–0.99576]	0.07480 [0.77060–0.84540]
13	0.00222 [0.99576–0.99798]	0.06231 [0.84540–0.90771]
14	0.00141 [0.99798–0.99939]	0.04758 [0.90771–0.95529]
15	0.00054 [0.99939–0.99993]	0.03113 [0.95529–0.98642]
16	0.00007 [0.99993–1.00000]	0.01358 [0.98642–1.00000]

We tested 8th-, 16th-, 20th-, and 24th-order Legendre polynomials and corresponding weights in an Earth atmosphere setting with the 128-band model but did not find any significant differences ( $<10^{-3} \text{ W m}^{-2}$ ) in total up/down radiative fluxes above 16th order (not shown). In comparison, Malik et al. (2017) used 20th-order Gauss–Legendre polynomials after comparing to Simpson’s rule integration for their radiative transfer code. Table 2 shows a comparison of the quadrature weights used in the RRTM and the Gauss–Legendre weights (Equation (2)). One can see the emphasis placed in the RRTM upon probability function values close to unity, indicated by very small values for weights  $i > 10$ , together only representing the largest  $\sim 1\%$  of absorption cross sections within a band. On the contrary, Gauss–Legendre weighting is symmetric around medium values of cross sections within the band, and the largest and smallest 1.3% of values are represented collectively in weights 16 and 1, respectively. The representative cross-section value  $\sigma_i$ , or  $k$ -coefficient, corresponding to a quadrature of weight  $w_i$  is then simply the arithmetic mean of the cumulative cross-section function within the respective quadrature.

### 2.1.3. Continuum Absorption

The CIA is taken from the HITRAN CIA database (Karman et al. 2019). A complete list of the currently implemented CIAs in REDFOX is shown in Table 3. Since the HITRAN CIA formatting is identical, any missing CIA from the list can be flexibly added in REDFOX for a specific study. Additionally, REDFOX utilizes MT\_CKD (Mlawer et al. 2012) version 3.2.<sup>11</sup> Although originally developed for the  $\text{H}_2\text{O}$  continuum, this now also includes continua for other molecules. In REDFOX, one can choose which CIA and MT\_CKD continua from Table 3 are used. These continua are first calculated on a finer grid with 10 points per band using the same interpolation method as for MT\_CKD in LBLRTM (Clough et al.

**Table 3**List of Continua from the HITRAN CIA List<sup>a</sup> Included in REDFOX and the Corresponding Sources

Molecule	Continuum
$\text{H}_2\text{--H}_2$	Abel et al. (2011)
$\text{H}_2\text{--He}$	Abel et al. (2012)
$\text{CO}_2\text{--H}_2$	Wordsworth et al. (2017)
$\text{CO}_2\text{--CH}_4$	Wordsworth et al. (2017)
$\text{CO}_2\text{--CO}_2$	Gruszka & Borysow (1997) & Baranov et al. (2003)
$\text{H}_2\text{O}_{\text{self}}$	MT_CKD_3.2 <sup>b</sup>
$\text{H}_2\text{O}_{\text{foreign}}$	MT_CKD_3.2 <sup>b</sup>
$\text{CO}_2_{\text{foreign}}$	MT_CKD_3.2 <sup>b</sup>
$\text{N}_2_{\text{mixed}}$	MT_CKD_3.2 <sup>b</sup>
$\text{O}_2_{\text{self}}$	MT_CKD_3.2 <sup>b</sup>
$\text{O}_2_{\text{foreign}}$	MT_CKD_3.2 <sup>b</sup>
$\text{O}_3_{\text{foreign}}$	MT_CKD_3.2 <sup>b</sup>

### Notes.

<sup>a</sup> [www.hitran.org/cia/](http://www.hitran.org/cia/) (Karman et al. 2019).<sup>b</sup> [http://rtweb.aer.com/continuum\\_frame.html](http://rtweb.aer.com/continuum_frame.html) (Mlawer et al. 2012).

1992, 2005), which gives the cross sections

$$\begin{aligned} \sigma_i = & -\sigma_{j-1} \left[ \frac{f_\nu}{2} (1 - f_\nu)^2 \right] \\ & + \sigma_j \left[ 1 - (3 - 2f_\nu)f_\nu^2 + \frac{f_\nu^2}{2} (1 - f_\nu) \right] \\ & + \sigma_{j+1} \left[ (3 - 2f_\nu)f_\nu^2 + \frac{f_\nu}{2} (1 - f_\nu)^2 \right] \\ & + \sigma_{j+2} \left[ \frac{f_\nu}{2} (1 - f_\nu) \right], \end{aligned} \quad (3)$$

with

$$f_\nu = \frac{\nu_i - \nu_j}{\nu_{j+1} - \nu_j}, \quad (4)$$

where  $i$  are the 10 grid points in a band interval and  $j$  are linearly interpolated from tabulated cross sections at neighboring temperatures from either MT\_CKD or HITRAN CIA, where applicable. Values at the band boundaries are linearly interpolated from tabulated values at neighboring frequencies. We tested different numbers of points per band for the interpolation, but convergence was found for 10 or more points per band. From these interpolated cross sections, band-integrated averages are calculated via  $1/(\Delta\nu_{\text{band}}) \sum_{i=1}^n (\sigma_i \Delta\nu_i)$  and added to other opacity sources with their corresponding volume mixing ratio.

### 2.1.4. UV/VIS Cross Sections

In the current version of 1D-TERRA, we include 81 absorbers from the MPI Mainz Spectral Atlas (Keller-Rudek et al. 2013) in the visible, UV, and far-UV (FUV) range. These were initially chosen for the photochemistry module as described in Section 2.3 but are also available for radiative transfer in REDFOX. Where available, we follow the recommendation of the JPL Evaluation 18 (Burkholder et al. 2015). Otherwise, we took the latest reference in the JPL report, unless the data coverage was poor. The full list of cross-

<sup>11</sup> [http://rtweb.aer.com/continuum\\_frame.html](http://rtweb.aer.com/continuum_frame.html)

**Table 4**  
List of Parameters for the Rayleigh Cross-section Calculations

Molecule	A	B	D
CO	32.7	8.1	$9.49 \times 10^{-3}$
CO <sub>2</sub>	43.9	6.4	$8.05 \times 10^{-2}$
H <sub>2</sub> O	...	...	$3.00 \times 10^{-4a}$
N <sub>2</sub>	29.06	7.7	$3.05 \times 10^{-2}$
O <sub>2</sub>	26.63	5.07	$5.40 \times 10^{-2}$

**Notes.** Here A and B from Allen (1973) and Vardavas & Carver (1984) are used for the refractivity approximation; D (Sneep & Ubachs 2005) is for depolarization in the King factor  $K_{\lambda}$ .

<sup>a</sup> Murphy (1977).

section data used in the climate and chemistry model is given in the companion paper (Wunderlich et al. 2020). These cross sections are arithmetically averaged into the corresponding REDFOX bands and added to the other opacities discussed above. For the remaining HITRAN absorbers in the band, the UV/VIS cross sections are directly added to the  $k$ -distributions for cross-correlation using the random overlap approach, as described earlier. In this case, UV/VIS cross sections are interpolated and band-averaged from the MPI Mainz Spectral Atlas data with the same method as described in Section 2.1.3 for the continua. They are used in the spectral range from the highest available energies or wavenumbers ( $10^5 \text{ cm}^{-1}$  in the current version) up to the band with the first HITRAN data point of the given species. This approach was chosen to avoid accounting for absorption of a given species twice (i.e., in both the HITRAN and MPI Mainz databases). In overlapping data regions, we preferentially chose line list data rather than measured cross sections because the latter could also include experimental noise between absorption features, which would add artificial UV “continua” to our heating rates. For molecules where line list data were not included in a certain band, the cross sections are simply added as mean opacities per band in the same way as the continua are added in Section 2.1.3.

#### 2.1.5. Rayleigh Scattering

Rayleigh scattering is included in our model (see also von Paris et al. 2015) for CH<sub>4</sub>, CO, CO<sub>2</sub>, H<sub>2</sub>, H<sub>2</sub>O, He, N<sub>2</sub>, and O<sub>2</sub>. The Rayleigh scattering cross sections ( $\text{cm}^2$ ) for CO, CO<sub>2</sub>, H<sub>2</sub>O, N<sub>2</sub>, and O<sub>2</sub> are calculated using (Allen 1973)

$$\sigma_{\text{Ray},i}(\lambda) = \frac{32\pi^3}{3n^2} \frac{r_i^2 K_{\lambda,i}}{\lambda^4}, \quad (5)$$

and with number density  $n = 2.688 \times 10^{19} \text{ cm}^{-3}$  for standard temperature and pressure (STP),

$$\sigma_{\text{Ray},i}(\lambda) = 4.577 \times 10^{-21} \frac{r_i^2 K_{\lambda,i}}{\lambda^4}, \quad (6)$$

where  $\lambda$  is in  $\mu\text{m}$ ,  $r_i$  represents the refractive index ( $n - 1$ ) of species  $i$ , and the “King factor”  $K_{\lambda,i}$  is a correction for polarization, given by

$$K_{\lambda,i} = \frac{6 + 3D_i}{6 - 7D_i}, \quad (7)$$

with  $D_i$  being the depolarization factor calculated from Sneep & Ubachs (2005) shown in Table 4. Further, for CO, CO<sub>2</sub>, N<sub>2</sub>, and O<sub>2</sub>, the refractive index  $r$  is approximated using

**Table 5**  
List of Measured Reference Rayleigh Cross Sections  $\sigma_{0,i}$  at Wavelength  $\lambda_{0,i}$  from Shardanand & Rao (1977)

Molecule	$\sigma_{0,i} (\text{cm}^2)$	$\lambda_{0,i} (\mu\text{m})$
H <sub>2</sub>	$1.17 \times 10^{-27}$	0.5145
He	$8.6 \times 10^{-29}$	0.5145
CH <sub>4</sub>	$1.244 \times 10^{-26}$	0.5145

(Allen 1973)

$$r_i = 10^{-5} A_i \left( 1 + \frac{10^{-3} B_i}{\lambda^2} \right), \quad (8)$$

with the two additional parameters  $A_i$  and  $B_i$ , also shown in Table 4, and  $\lambda$  again in  $\mu\text{m}$ . For H<sub>2</sub>O, the refractive index is calculated as  $r_{\text{H}_2\text{O}} = 0.85 r_{\text{dry air}}$  (Edlén 1966), with the approximation for the refractive index of dry air (Bucholtz 1995):

$$r_{\text{dry air}} = 10^{-8} \left( \frac{5.7918 \times 10^6}{2.38 \times 10^2 - \lambda^{-2}} + \frac{1.679 \times 10^5}{57.362 - \lambda^{-2}} \right). \quad (9)$$

Rayleigh scattering cross sections for H<sub>2</sub>, He, and CH<sub>4</sub> are included using reference measurements of  $\sigma_{0,i}$  at wavelengths  $\lambda_{0,i}$  from Shardanand & Rao (1977) shown in Table 5. These cross sections are then approximated for other wavelengths using the simple  $\lambda^{-4}$  relationship,

$$\sigma_{\text{Ray},i}(\lambda) = \sigma_{0,i} \left( \frac{\lambda_{0,i}}{\lambda} \right)^4, \quad (10)$$

where  $\sigma_{\text{Ray},i}$  of species  $i$  are given in  $\text{cm}^2 \text{ molecule}^{-1}$ ,  $\lambda$  is the wavelength of interest in  $\mu\text{m}$ , and  $\lambda_{0,i}$  is a reference wavelength where  $\sigma_{0,i}$  was measured. In REDFOX, we updated the calculation of band-integrated scattering cross sections, which is now performed for all spectral bands, rather than only the SW bands. The band mean values are now calculated from one specific wavelength per band, representative of the band-integrated average. We emphasize that this does not correspond to the band-mid wavelength. Instead, we use the equivalence of the integrals,

$$\begin{aligned} \int_{\lambda_1}^{\lambda_2} \lambda^{-4} d\lambda &\stackrel{!}{=} \int_{\lambda_1}^{\lambda_2} \lambda_{\text{ray}}^{-4} d\lambda = \lambda_{\text{ray}}^{-4} \int_{\lambda_1}^{\lambda_2} d\lambda \\ &\Rightarrow \lambda_{\text{ray}} = \left( \frac{\lambda_1^{-3} - \lambda_2^{-3}}{3(\lambda_2 - \lambda_1)} \right)^{-\frac{1}{4}}, \end{aligned} \quad (11)$$

to determine the representative wavelength  $\lambda_{\text{ray}}$  for the Rayleigh cross-section calculations in each band ( $\lambda$  in Equations (6) and (8)–(10)). Then, the choice of the radiative transfer method (see Section 2.1.7) defines in which bands the Rayleigh scattering opacities are used.

#### 2.1.6. Source Functions

We consider essentially two radiative sources: incident stellar flux and thermal radiation from the planetary surface and the atmosphere. Stellar spectra can be taken either directly from

the MUSCLES database<sup>12</sup> or from the VPL webpage.<sup>13</sup> The solar spectrum is taken from Gueymard (2004). Spectra that do not cover the entire wavelength range were extended with the NextGen 4 spectrum of the corresponding effective temperature of the star up to 971  $\mu\text{m}$  (Hauschildt et al. 1999). We first perform a logarithmic interpolation of the spectra to a constant resolution of 1  $\text{\AA}$  over the entire wavelength range and then bin the data into our 128 bands using an arithmetic mean.

Thermal blackbody emissions from the planetary surface and every atmospheric layer are calculated for 101 points (100 intervals) per band distributed equally in  $\nu$  following Planck’s law in wavenumbers:

$$B_\nu(\nu, T) = 2hc^2\nu^3 \frac{1}{e^{\left(\frac{h\nu}{k_B T}\right)} - 1}. \quad (12)$$

Then, a simple arithmetic mean is taken as the average blackbody source term in the given band and atmospheric layer. We tested this simple method against the computationally slightly more expensive trapezoidal rule in the Earth and Venus atmosphere runs but found no significant ( $<10^{-4}$ ) differences in cooling rates or atmospheric temperature structure. This suggests that our band model features sufficiently small bandwidths. For this reason we chose the faster band mean calculations explained above.

#### 2.1.7. Opacities and Transmission Functions

Once all individual  $k$ -coefficients  $\sigma_i$  are calculated, they are mixed for the atmosphere of interest. In random overlap,  $\sigma_{ij,mm,b}$  in units of  $\text{cm}^2 \text{ molecule}^{-1}$  of two molecules  $m$  and  $n$  and their respective quadratures  $i$  and  $j$  in band  $b$  are cross-correlated when performing radiative transfer calculations by

$$\sigma_{ij,mm,b} = \frac{\sigma_{i,m}\chi_m + \sigma_{j,n}\chi_n}{\chi_m + \chi_n}, \quad (13)$$

where  $\chi$  is the respective volume mixing ratio, and individual  $k$ -coefficients  $\sigma$  are linearly interpolated in  $T$  and  $\log(p)$  from the precalculated  $k$ -distributions. The corresponding  $16 \times 16$  quadrature weights as a result of mixing the  $k$ -coefficients from two molecules are

$$w_{ij} = w_i w_j, \quad (14)$$

with  $i$  and  $j$  each taking integer values from 1 to 16, as shown in Table 2. In REDFOX, we use *quicksort* (Press et al. 1992) to sort the mixed  $\sigma_{ij}$  and corresponding  $w_{ij}$  again as a monotonically increasing function, or  $k$ -distribution. Before adding new molecules to the mix, we bin the mixed  $k$ -distribution back into the original 16 quadratures ( $g = 1-16$ ). For the respective mean  $k$ -coefficients  $\sigma_g$ , individual  $\sigma_{ij}$  are added where the cumulative weights  $w_{c,ij}$  of the mix lie in the range  $w_{c,i-1} < w_{c,ij} < w_{c,i}$  of the original quadrature with weight  $w_i$ . The new  $k$ -coefficients are then calculated as

$$\sigma_{g,mn} = \frac{1}{w_i} \sum_{w_{c,ij}=w_{c,i-1}}^{w_{c,ij}=w_{c,i}} \left( \frac{w_{ij}}{w_i} \right) \sigma_{ij,mm}, \quad (15)$$

with

$$w_{c,i} = \sum_{i=1}^g w_i \quad \text{and} \quad w_{c,ij} = \sum_{ij=1}^{g^2} w_{ij}. \quad (16)$$

Contributions of mixed quadratures that overlap with the boundaries of the original 16 quadratures are factored into the corresponding  $\sigma_g$  accordingly. This process is repeated for every molecule added to the gas mixture. Depending on the composition of the atmosphere of interest, one cannot expect that all constituents are accounted for by our absorbers, especially when we choose to exclude specific constituents from radiative transfer calculations e.g., for performance reasons, studies of individual gas contributions, or when noble gases are excluded in calculations because they would not contribute significantly to the radiative energy budget. Since Equation (13) assumes the absorbing contribution of all constituents, we calculate the total mixing ratio of the absorbing species  $\chi_{\text{mix}}$  along with the  $k$ -coefficients and correct the cross sections of the mixture using  $\sigma_g = \sigma_g \cdot \chi_{\text{mix}}$ . This approach is especially appropriate for Earth’s atmosphere, where  $\text{N}_2$  accounts for approximately 78% of molecules while not contributing significantly to absorption. In this case, calculations can be sped up significantly when we exclude nonsignificantly absorbing species from the radiative transfer calculations.

Once opacities  $\tau = \sigma_g u$ , with  $u$  being the respective column density, are calculated, other previously described band-integrated opacities can be added flexibly. Radiative transfer is solved together with Rayleigh scattering, for which we use the quadrature  $\delta$ -two-stream approximation (Meador & Weaver 1980; Toon et al. 1989) for SW radiative transfer. For the thermal outgoing LW radiative transfer, we have the option to use either the Toon et al. (1989) hemispheric mean two-stream approximation, including Rayleigh scattering and with Planck emissions instead of the stellar component, or the faster diffusivity approximation (Mlawer et al. 1997) without scattering. In this case, the radiative transfer equation is solved for the single angular point  $\mu = \frac{1}{1.66}$ , corresponding to a polar angle  $\theta = 52.95^\circ$  (Elsässer 1942), and the linear-in-tau approach for the Planck functions (Clough et al. 1992). While implementations of the abovementioned radiative transfer solvers date back to Pavlov et al. (2000) and Segura et al. (2003), they are still useful in our cloud-free studies. Upcoming model updates including scattering by larger aerosols and cloud particles will include two-stream updates similar to Heng et al. (2018) and an option to use a discrete ordinates method, such as DISORT (e.g., Stamnes et al. 1988; Hamre et al. 2013), which will then allow for treatment of incident stellar beam, scattering, and internal source function, namely the Planck function of each layer, at the same time, ridding us of the SW–LW distinction necessary with the currently used two-stream approximations.

The globally averaged zenith angle ( $\theta$ ) for the effective path lengths of the direct stellar beam through an atmospheric layer can be chosen by the user. Cronin (2014) pointed out that zenith angle and global mean averaged irradiation ( $S$ ) have to be changed together according to the product  $S \cdot \cos \theta = S_0/4$ , where  $S_0$  is the total stellar irradiation (TSI), and the factor  $1/4$  comes from the purely geometric derivation of the planetary cross section over the planetary surface area. Note that a simple

<sup>12</sup> <http://archive.stsci.edu/prepds/muscles/>

<sup>13</sup> <http://vpl.astro.washington.edu/spectra/stellar/>

daytime-weighted global mean assumption, a zenith angle  $\theta = 60^\circ$  with  $S = S_0/2$  is commonly used in the literature. Additionally, this approximation assumes a rapidly rotating planet, such that the incident stellar flux is effectively distributed over the entire planetary surface despite only illuminating half of the planet. This would obviously be different for tidally locked planets, where a more general parameter can be introduced that simulates the efficiency of heat redistribution from the permanent day to the nightside (see, e.g., Spiegel & Burrows 2010; Malik et al. 2017).

While aerosols and clouds can be treated to some degree in the two-stream approximation via extinction coefficients that depend on particle sizes, forms, and refractive indices (see, e.g., Kitzmann et al. 2010), we do not explicitly include such particles in the current work. We parameterize cloud behavior in a simple way by increasing the surface albedo and adjusting the effective path length in radiative transfer with a zenith angle deviating from the geometric mean value of  $60^\circ$ . The appropriate choice of albedo and zenith angle, however, is generally a degenerate problem.

With all of the model updates mentioned above, calculation times are nevertheless sufficient for our purposes. While calculating opacities plus radiative fluxes in MRAC for four absorbers in 25 LW bands and 38 SW bands plus Rayleigh scattering took  $\sim 180$  ms, REDFOX with the same configuration takes  $\sim 235$  ms. With our long list of LW and SW absorbers in our 128 bands, including MT\_CKD and CIAs now takes  $\sim 1600$  ms, all on a single CPU. This is still fast compared to full LBL calculations, which can take several minutes on a server node of 20 CPUs.

### 2.1.8. Key Features of REDFOX

The following is a summary of the key features of REDFOX in the configuration validated and applied in the current work.

1. Continuous  $k$ -distribution model with 128 spectral bands (16 g Gauss–Legendre).
2. Spectral range  $\nu = 10^5 \text{ cm}^{-1}$  (100 nm) –  $0 \text{ cm}^{-1}$  ( $\infty$ ).
3. Pressure range  $0.01 \text{ Pa} - 10^3 \text{ bars}$ .
4. Temperature range  $100 - 1000 \text{ K}$ .
5. 20 absorbers (HITRAN 2016); see Table 1.
6. 81 VIS/UV/FUV absorbers (MPI Mainz Spectral Atlas); see Table 1.
7. CIAs (HITRAN CIA list); see Table 3.
8. MTCKD\_3.2; see Table 3.
9. Flexible choice of absorbers (SW/LW, CIA/CKD).
10. Flexible choice of SW/LW ranges for specific study.

### 2.2. Climate Module

The central tasks of the climate module are to calculate atmospheric and surface temperatures in radiative–convective equilibrium and temperature-dependent molecular abundances of condensible species, e.g.,  $\text{H}_2\text{O}$  or  $\text{CO}_2$ , in convective regions where temperatures change. The governing energy-conserving differential equation determining the temperature  $T$  profiles is (see, e.g., Pavlov et al. 2000)

$$\frac{d}{dt}T(z) = -\frac{g(z)}{c_p(T, z)} \frac{dF(z)}{dp(z)}, \quad (17)$$

where  $d/dt$  is the time derivative,  $g(z)$  is gravitational acceleration,  $c_p$  is the heat capacity of the atmospheric layer,

$F$  is the radiative flux, and  $p$  is the cell-centered pressure of the atmospheric layer at a mid-layer height  $z$ . Equation (17) is discretized in the model using finite differences, resulting in  $dt$  being used as the finite time step. After the radiative temperature profile is calculated for a model time step, radiative lapse rates are compared in every layer with adiabatic lapse rates to determine where convective adjustment has to be performed (i.e., Schwarzschild criterion). The decision as to the appropriate adiabatic lapse rate (moist or dry) and whether  $\text{H}_2\text{O}$  or  $\text{CO}_2$  is the condensing molecule in the moist case is based on the fraction of respective partial pressures over the corresponding saturation vapor pressure. Note that combined moist adiabatic lapse rates are not implemented. If  $\text{CO}_2$  condensation occurs, the resulting lapse rate is a  $\text{CO}_2$  moist adiabat, disregarding any possible  $\text{H}_2\text{O}$  contribution. The  $\text{H}_2\text{O}$  moist adiabatic lapse rates are calculated if  $\text{H}_2\text{O}$  condenses in the absence of  $\text{CO}_2$  condensation. The  $\text{H}_2\text{O}$  profiles are calculated using prescribed relative humidity (RH) profiles, e.g., by Manabe & Wetherald (1967), for planetary scenarios with a water reservoir, i.e., an ocean, via

$$\chi_{\text{H}_2\text{O}}(p) = \text{RH}(p) \frac{p_{\text{sat}, \text{H}_2\text{O}}(T(p))}{p}, \quad (18)$$

with  $p_{\text{sat}}$  being the saturation vapor pressure. The total surface pressure  $p_0$  of the atmosphere is calculated via  $p_0 = p_{0, \text{dry}} + p_{0, \text{H}_2\text{O}}$ ; therefore, atmospheric pressures, and with them the mixing ratios of all atmospheric constituents, are adapted for those convective layers. For a detailed description of convective adjustment and  $\text{CO}_2$  lapse rates in our model, we refer to, e.g., Kasting (1991) and Kasting et al. (1993), as well as von Paris et al. (2008) for the water vapor treatment.

Heat capacities ( $c_p$ ) for temperature and lapse rate calculations have historically been included in our model for different species using different approaches (for details, see, e.g., von Paris et al. 2008, 2010, 2015). The next 1D-TERRA update will come with updated  $c_p$  treatment. Therefore, we only give a brief summary of our currently used  $c_p$  calculations in the Appendix.

### 2.3. Photochemistry Module

The atmospheric composition profile of each species is calculated in the photochemistry module using the continuity–transport equation,

$$\frac{\partial n}{\partial t} = \frac{\partial}{\partial z} \left( K \cdot \frac{\partial n}{\partial z} \right) + P - nL, \quad (19)$$

where  $n$  denotes the number density of a certain species ( $\text{cm}^{-3}$ ),  $P$  is the production term ( $\text{cm}^{-3} \text{ s}^{-1}$ ),  $L$  is the loss rate ( $\text{s}^{-1}$ ), and  $K$  is the eddy diffusion coefficient ( $\text{cm}^2 \text{ s}^{-1}$ ). The loss and production rates are determined by the kinetic coefficients and boundary conditions. The companion paper (Wunderlich et al. 2020) describes the new photochemistry module BLACKWOLF with a flexible chemical network. The full network consists of 1127 reactions for 115 species, including photolysis for 81 absorbers.

The scheme can consider wet and dry deposition, as well as an upward flux at the surface for each species. Outgassing from volcanoes is treated as a upward flux equally distributed over



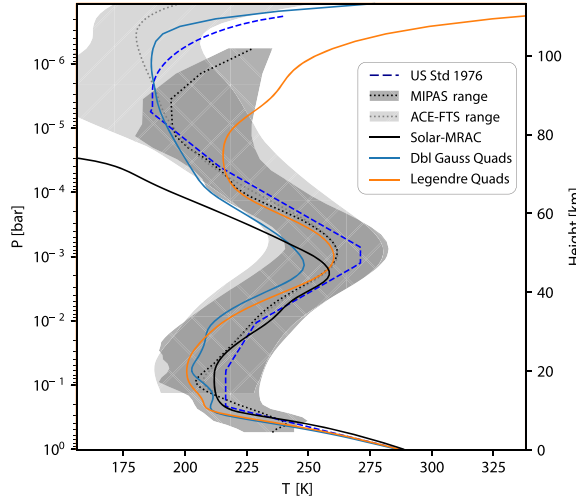


**Figure 3.** Temperature profiles for Earth’s modern atmosphere. We compare two versions of REDFOX with  $k$ -distributions calculated with Legendre (orange) and double Gaussian (blue solid) quadratures against the US standard atmosphere (blue dashed) and our original model MRAC (black). Overplotted are  $2\sigma$  ranges of Earth observation data from MIPAS and ACE-FTS.

the lower 10 km of the atmosphere. At the top of the atmosphere (TOA), the module can calculate escape fluxes and parameterized effusion flux or use predefined values. Usually, we only consider O, H, and H<sub>2</sub> to have an upper boundary flux. The profile of  $K$  can be either a fixed predefined profile or calculated in the model depending on the planetary atmosphere. See Wunderlich et al. (2020) for the calculation of  $K$  and more details on the photochemical module.

### 3. Model Validation

In this section, we restrict ourselves to the validation of the radiative transfer module, REDFOX, and its integration into the climate part of 1D-TERRA; thus, in some cases, we prescribe the atmospheric composition. The chemistry is validated separately in the companion paper (Wunderlich et al. 2020). We first validate for Earth standard conditions, then go on to Earth climate-change studies with increased amounts of CO<sub>2</sub>, before validating for other solar system planets, i.e., modern Venus and Mars, and then exoplanetary scenarios (i.e., Earth-like and steam atmospheres). In all cases, we discretize the atmosphere into 100 layers from the surface up to the TOA.

#### 3.1. Modern Earth

Figure 3 shows our 1D-TERRA results in coupled climate-chemistry mode for US standard 1976 Earth atmospheric composition. We tune surface albedo and zenith angle for radiative transfer calculations together to achieve Earth global average surface temperatures of 288.15 K in our cloud-free model and an Earth-like global mean O<sub>3</sub> column in the range 300–320 Dobson units (DU; see, e.g., Segura et al. 2010), which is achieved with a surface albedo of 0.255 and an angle  $\theta = 54^\circ 50'$ ; thus,  $S = 0.4305 S_0$ , so that  $S \cdot \cos(\theta) = S_0/4$ , for all radiative transfer calculations in climate and chemistry. This agrees well with the fact that modern Earth is partially cloudy; this angle lies well in the range for a clear sky and fully cloud-

covered planet (see, e.g., Cronin 2014). Note that zenith angles used in climate and chemistry calculations do not necessarily have to be the same; see, e.g., Hu et al. (2012) for a discussion. Unless stated otherwise, we will use this parameter set for all other tests and applications.

Temperature profiles with the original radiative transfer model MRAC (von Paris et al. 2015) were calculated using absorption by H<sub>2</sub>O, CO<sub>2</sub>, CH<sub>4</sub>, and O<sub>3</sub>, with the addition of O<sub>2</sub> in one band (752–784 nm) for stellar absorption. Those with REDFOX are calculated with all 20 HITRAN absorbers from Table 1 with the addition of UV/VIS cross sections for CH<sub>3</sub>Cl, CH<sub>4</sub>, CO, CO<sub>2</sub>, H<sub>2</sub>O, HNO<sub>3</sub>, N<sub>2</sub>, N<sub>2</sub>O, NO, O<sub>2</sub>, and O<sub>3</sub> for wavenumbers above available HITRAN data, as described in Section 2.1.4. We calculate temperature profiles with two different  $k$ -distribution quadrature settings in REDFOX, as shown in Table 2, to determine which one compares better to observations. For this, we compare to the US standard atmosphere 1976, as well as Earth observation data from MIPAS<sup>14</sup> (von Clarmann et al. 2009) and ACE-FTS<sup>15</sup> (Boone et al. 2005). From both observation data sets, we show (gray shaded regions) the 95% ( $2\sigma$ ) range and the global annual mean temperature profiles (dotted lines). While we see generally good agreement between our calculated low and mid-atmospheric temperature profiles with the US standard atmosphere and the MIPAS and ACE-FTS data (see Figure 3), in all model runs using the double Gaussian quadratures, both updated (blue solid) and original model (black solid), the stratopause peak lies slightly below US standard atmospheric values in both height and temperature, similar to other cloud-free 1D studies (see, e.g., Segura et al. 2003). Mesospheric temperatures in these cases lie slightly below the MIPAS and ACE-FTS  $2\sigma$  ranges. Figure 3 suggests that Gauss–Legendre quadratures (orange) result in a temperature profile closer to US standard atmospheric values and global mean averages from observations up to  $\sim 70$  km. The inclusion of the Gauss–Legendre quadratures therefore represents a major improvement in REDFOX.

Additionally, with the addition of O<sub>2</sub> absorption cross sections in the UV Schumann–Runge bands, the model now clearly shows mesopause and thermospheric temperature inversions that were previously lacking (in MRAC). In this range, calculations with REDFOX using the double Gaussian quadratures compare better with the observations. However, we are not taking into account any UV absorption in the atmosphere above our TOA; hence, our O<sub>2</sub> absorption might be slightly overestimated, leading to generally warmer mesopause values, especially visible in the calculations with the Gauss–Legendre quadratures. In previous studies with our 1D climate-chemistry model, the TOA was set to  $\sim 6$  Pa due to the lack of O<sub>2</sub> absorption in the UV, similar to, e.g., Segura et al. (2010), Kopparapu et al. (2013), and Ramirez et al. (2014), while other studies (e.g., Meadows et al. 2018) have set isothermal profiles above an arbitrary model pressure where model temperatures would otherwise strongly underestimate temperatures due to the missing physics.

Figure 4 shows the model TOA OLR for the two previously discussed different quadrature weightings (orange and blue) compared to LBL calculations with GARLIC (black). We use GARLIC with HITRAN 2016 and MT\_CKD for H<sub>2</sub>O

<sup>14</sup> [www.imk-asf.kit.edu/english/308.php](http://www.imk-asf.kit.edu/english/308.php)

<sup>15</sup> <http://ace.scisat.ca/publications/>

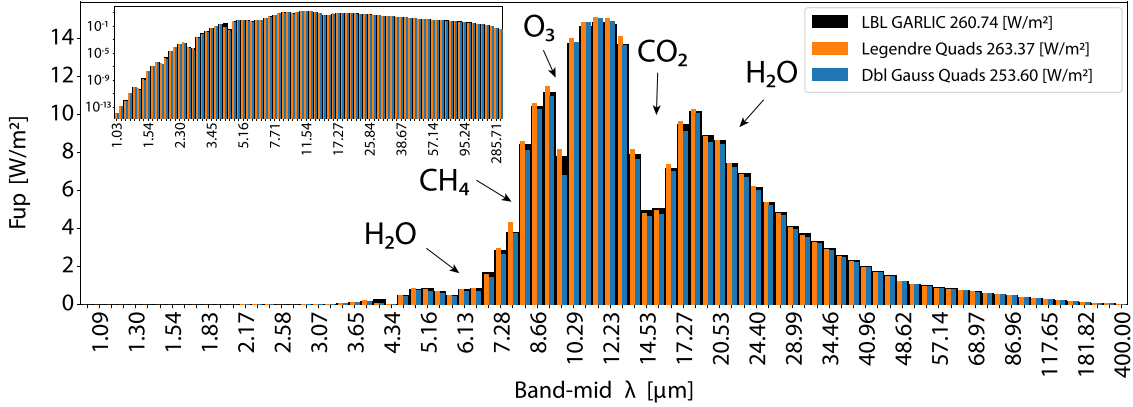


**Figure 4.** Earth validation of OLR fluxes against the LBL code GARLIC (black). The small insert shows fluxes in logarithmic scaling. We compare both quadrature settings in REDFOX (orange and blue) and indicate regions with major absorbers with arrows.

continuum, as in REDFOX. The spectral grid in GARLIC is discretized with  $\delta\nu = \gamma/4$ , and the Voigt profiles are cut at  $25 \text{ cm}^{-1}$ . The TOA OLR calculated by GARLIC is  $260.74 \text{ W m}^{-2}$ . Results for REDFOX using Gauss–Legendre quadratures ( $263.37 \text{ W m}^{-2}$ ) show very good agreement within 1.0%, while the double Gaussian quadratures ( $253.60 \text{ W m}^{-2}$ ) differ by 2.7%. Figure 4 suggests that fluxes estimated with the Gauss–Legendre method (orange columns) compare generally better with the LBL fluxes (black columns). Kopparapu et al. (2013) validated their  $k$ -distribution model, using the same double Gaussian quadratures, against a different LBL code, SMART (Meadows & Crisp 1996), for different terrestrial atmospheres, with deviations of the  $k$ -distribution model in the range between 2.7% and 4.0%, similar to our double Gaussian validation. Note that the RRTM (Mlawer et al. 1997), using the double Gaussian quadratures, was validated for Earth conditions to deviate by only  $<1 \text{ W m}^{-2}$  when compared to the same LBL model, namely LBLRTM, that was used to derive the  $k$ -distributions in the first place. Only in this way can one be certain to not mix in the differences between LBL models; see, e.g., Schreier et al. (2018a, 2018b) for an LBL model comparison. Based on this comparison, we now proceed using the Gauss–Legendre quadratures for the remaining validations and case studies.

### 3.2. Earth’s Climate Response to CO<sub>2</sub> Increase

Here we test our modeled climate response to increased levels of CO<sub>2</sub> and compare to results from studies of climate change on Earth. Rogelj et al. (2012) summarized results from an extensive list of 3D model studies and the International Panel on Climate Change (IPCC) report estimates for a doubling of CO<sub>2</sub> levels from the 1976 values of 326–652 ppm. Their findings suggest a resulting change in global mean surface temperatures in the range from  $+2.6^\circ\text{C}$  to  $+3.6^\circ\text{C}$ . Upon doubling CO<sub>2</sub>, our resulting change in global mean surface temperatures of  $+2.8^\circ\text{C}$  agrees very well with these works. Figure 5 presents our results for the 1976 CO<sub>2</sub> value (black) and gradually increased levels of CO<sub>2</sub> by factors of 2, 5, 10, and 100. We further see the typical behavior of CO<sub>2</sub> as a greenhouse gas, confining thermal radiation in the lower atmosphere, thus heating the troposphere while cooling the middle and upper atmosphere.

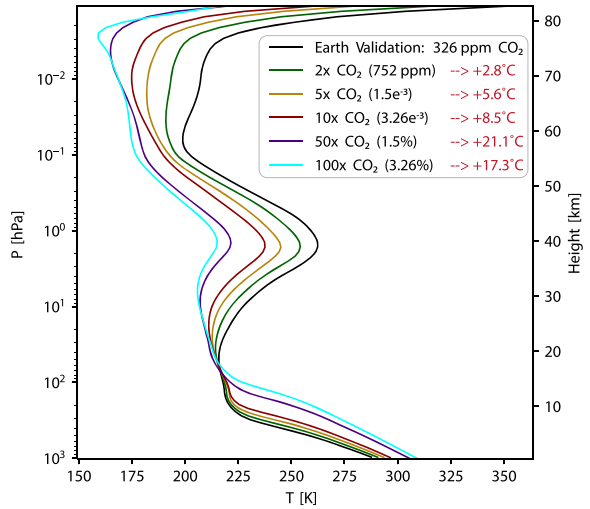


**Figure 5.** Earth climate response study for increased amounts of CO<sub>2</sub>. The red values in the legend represent the resulting increase in surface temperatures.

### 3.3. Steam Atmospheres

To further test H<sub>2</sub>O absorption in REDFOX, we compute radiative fluxes output from REDFOX for the scenarios of the model intercomparison study by Yang et al. (2016) with fixed temperatures and atmospheric compositions. We took their values for Earth-like planets having a 1 bar N<sub>2</sub> atmosphere with 376 ppm CO<sub>2</sub> and H<sub>2</sub>O steam that varies as a response to global mean surface temperatures between 250 and 360 K at saturation. With these added amounts of steam, the surface pressure changes accordingly (up to +0.5 bar), representing evaporation from oceans. Temperature profiles are set to 200 K isotherms above the tropopause. The study uses Earth-like global mean stellar irradiation of  $340 \text{ W m}^{-2}$  for all tests on specifying the abovementioned surface temperatures; thus, OLR does not balance incoming radiation. We specify the boundary parameters with REDFOX and plot output from both studies for different LBL and  $k$ -distribution models as shown in Figure 6. REDFOX compares well with the models shown and suggests the symptomatic OLR flattening for higher

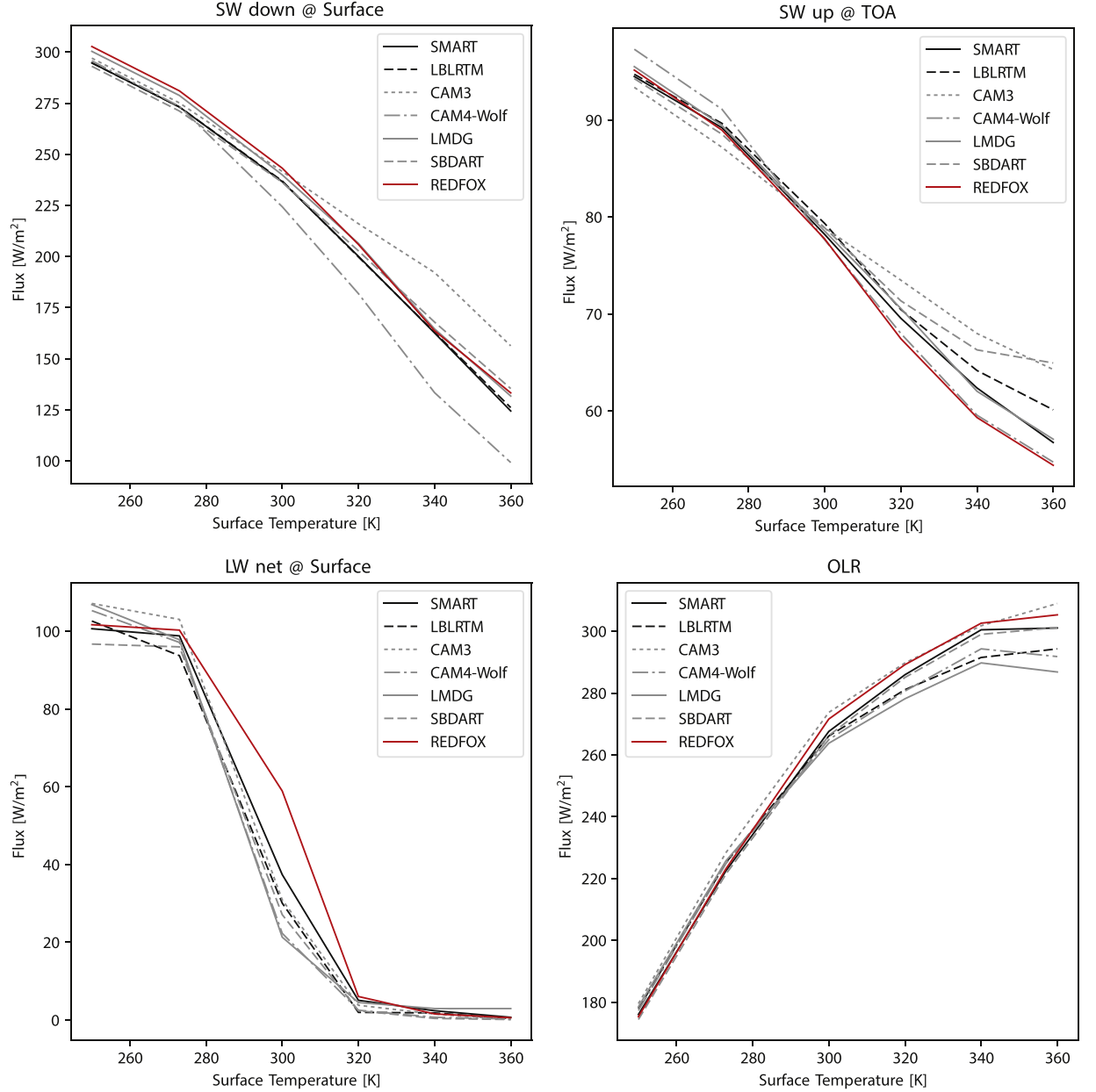


**Figure 6.** Comparison of radiative fluxes under steam atmosphere conditions against the tested models in Yang et al. (2016).

temperatures toward the Kobayashi–Ingersoll limit (see, e.g., Nakajima et al. 1992; lower right), as well as the transition from optically thin to optically thick for thermal radiation in the first atmospheric layer above the surface due to the increased steam (lower left). Note that the compared models show quite large differences in those LW net fluxes for the surface layer (lower left) for the 300 K runs. This analysis for the transition from optically thin to optically thick is generally very sensitive to modeling parameters such as individual layer heights, used line lists and continua, or exact  $\text{H}_2\text{O}$ , temperature, and pressure profiles. We read these profiles off the plots in Yang et al.

(2016), which may have introduced extra differences in addition to the already large differences of the models originally compared in their study of up to  $\sim 100\%$ . To further clarify this, we plan on doing a thorough  $k$ -distribution model intercomparison in the future. For absorption of stellar radiation in the SW, both the radiation reaching the surface (upper left) and the backscattered radiation escaping again at the TOA (upper right) compare well with the other models.

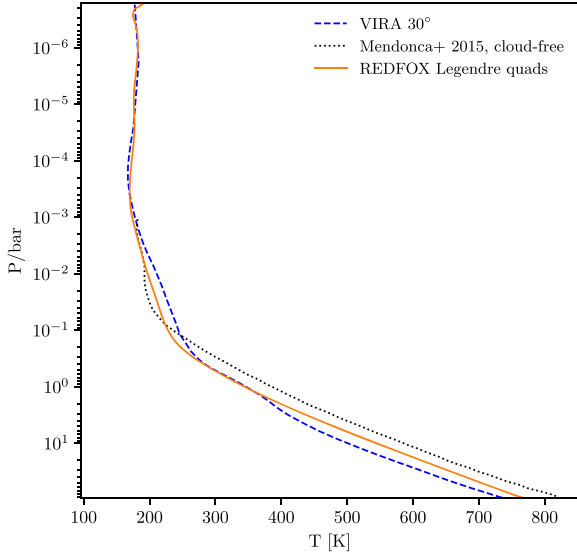


**Figure 7.** Validation for cloud-free Venus. We compare our climate model (orange) to the Venus reference atmosphere (blue) and the cloud-free model calculations from Mendonça et al. (2015; black).

### 3.4. Cloud-free Venus

While the above tests were performed for Earth-like planets, Figure 7 shows our temperature profiles for a cloud-free Venus calculated with 1D-TERRA in climate-only mode with prescribed atmospheric composition compared to the Venus International Reference Atmosphere (VIRA-1; Seiff et al. 1985) and a cloud-free Venus model result from Mendonça et al. (2015). For this test, we set the planetary parameters to represent Venus, e.g., with surface gravity  $g = 8.87 \text{ m s}^{-2}$ , surface pressure  $p_0 = 93 \text{ bars}$ , and solar constant  $1.913 S_{\text{Earth}}$ , and, due to the lack of cloud treatment in our model, we set the surface albedo to 0.755. Note, however, that due to the thick atmosphere, the influence of the surface albedo on the planetary albedo is expected to be negligible (see, e.g., von Paris et al. 2013; Godolt et al. 2016), which we also found in tests with a basaltic surface albedo of 0.13 (not shown). The atmospheric composition is prescribed with 96.5%  $\text{CO}_2$ , 3.5%  $\text{N}_2$ , 20 ppm  $\text{H}_2$ , 20 ppm  $\text{O}_2$ , and 100 ppb  $\text{O}_3$ , plus surface concentrations of 150 ppm  $\text{SO}_2$ , 32.5 ppm  $\text{H}_2\text{O}$ , 20 ppm  $\text{CO}$ , and 150 ppb  $\text{HCl}$  with profiles following Haus et al. (2015) and Tsang et al. (2008). The  $\text{H}_2\text{O}$  profiles are not calculated from saturation vapor pressures but fixed to the initial concentration, as Venus does not have a surface ocean. Our model TOA is set to 0.01 Pa, which corresponds to  $\sim 124 \text{ km}$ , and our initial temperature profile starts at 735.3 K at the surface, linearly decreasing in height up to 169 K at the model TOA. The choice of initial temperature profile does not influence the outcome but heavily influences the model runtime until full radiative-convective equilibrium is achieved. For Venus, instead of the requirement for full radiative-convective equilibrium, equilibrium was determined when OLR and temperature changes in each layer were sufficiently small over 10 Venus days ( $d\text{OLR}/dt < 0.5 \text{ W m}^{-2}$  and  $dT/dt < 0.1 \text{ K}$ ), similar to the approach by Mendonça et al. (2015). We see in Figure 7 that our cloud-free Venus temperature profile compares well with

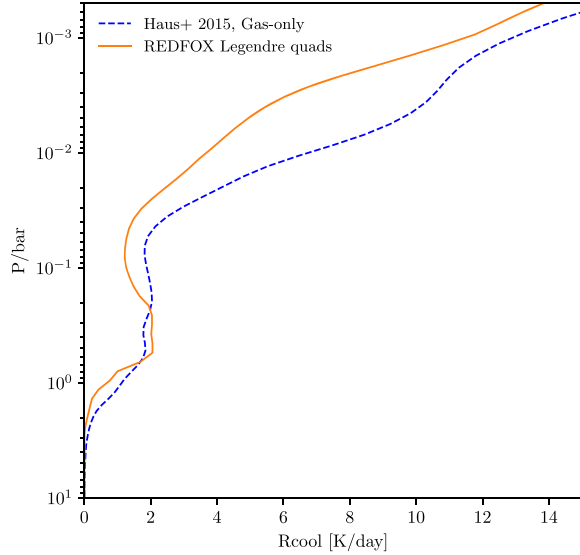


**Figure 8.** Cooling rates in our cloud-free Venus model atmosphere with REDFOX (orange) compared to gas contributions to the cooling rate in the cloudy VIRA atmosphere taken from Haus et al. (2015; blue).

the cloud-free model studies conducted by Mendonça et al. (2015) while still being remarkably close to VIRA measurements. The two features associated with the missing clouds are the missing mid-atmospheric heating from cloud absorption and convection within and the higher tropospheric temperatures due to the absorption of stellar radiation deeper down in the atmosphere.

Figure 8 compares our cloud-free cooling rates to the gas contributions to atmospheric cooling in the VIRA atmosphere modeled by Haus et al. (2015). Note that Haus et al. (2015) included the effect of clouds indirectly via the use of the cloudy VIRA atmosphere, and they used absorption data from various high-temperature line lists. Several model studies (see, e.g., Kopparapu et al. 2013) have shown that cooling rates and OLRs obtained with HITRAN versus HITEMP line lists start to diverge above  $\sim 800\text{--}1000 \text{ K}$ . As Venus surface temperatures approach those temperatures, ideally HITEMP or Exomol should be used. While both model rates follow similar trends, our cloud-free model outputs somewhat lower cooling rates, dominated by the two regions, around 1 bar and slightly above 0.1 bar, where temperature differences increase, mainly related to the missing cloud layers in our model. Lastly, we conduct a detailed TOA OLR analysis for our model temperature and composition profile, band by band against the LBL code GARLIC, shown in Figure 9. The results suggest excellent agreement for  $F_{\text{up}}$  fluxes in all  $\text{CO}_2$  and  $\text{CO}$  bands, slightly less absorption in REDFOX for  $\text{SO}_2$ , and somewhat more absorption in the LW  $\text{H}_2\text{O}$  continuum above  $20 \mu\text{m}$ . There are two apparent window regions with generally low absorption in Venus's atmosphere, where REDFOX  $F_{\text{up}}$  fluxes show significantly more (10%–20%) absorption. These are the  $6 \mu\text{m}$   $\text{H}_2\text{O}$  band and the  $3.4 \mu\text{m}$  band, a window region with negligible contributions from absorbers. The total OLR for calculations using the Gauss-Legendre quadratures ( $549.64 \text{ W m}^{-2}$ ) agrees within  $\sim 1\%$  with the LBL calculations ( $556.01 \text{ W m}^{-2}$ ). Figure 9 also shows fluxes for REDFOX with

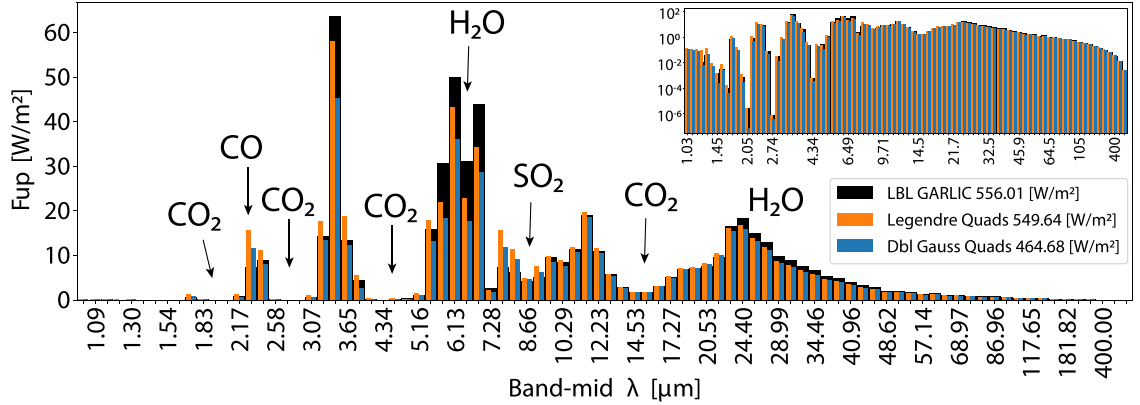


Figure 9. Same as Figure 4, but for cloud-free modern Venus conditions.

the double Gaussian quadratures (blue) for comparison to confirm that our choice of using the Gauss–Legendre quadratures is also justified for Venus and Venus-like planets.

In conclusion, for our Venus tests, results with REDFOX show slightly lower cooling rates (hence LW absorption) than the LBL model used by Haus et al. (2015) yet slightly higher overall LW absorption than the LBL model GARLIC, and temperatures compare well to measurements and other cloud-free model studies. In summary, we have shown that Venus temperatures, calculated with our new general-purpose climate model, compare very well with observations and other model studies designed to reproduce Venus.

### 3.5. Aerosol-free Mars

Our final validation, shown in Figure 10, is for an aerosol-free modern Mars scenario (orange). We compare temperatures modeled with 1D-TERRA in coupled climate-chemistry mode against the reference atmosphere of Haberle et al. (2017; black) for a low-dust scenario based on diurnal averages of observations from the MCS instrument (Kleinböhl et al. 2009). Also overplotted (green) are zonally averaged temperature ranges based on Mariner 9 IRIS data (Justus et al. 1996). As initial condition we set a 250 K isoprofile, Martian atmospheric composition of major species is taken from Owen et al. (1977), the water vapor profile and the profiles of minor species are taken from Nair et al. (1994). Mars’s planetary albedo of 0.29 (Clawson & J.P.L., 1991) is for most of the time throughout a Martian year (i.e., without global dust storms) dominated by the surface. Our cloud-free assumption in radiative transfer using a surface albedo of 0.290 is therefore reasonable. As Mars does not have a surface water ocean reservoir, we do not calculate tropospheric H<sub>2</sub>O profiles from RH profiles.

Our model results shown in Figure 10 compare reasonably well with Martian lower and upper atmospheric temperatures, while middle atmospheric temperatures are 10–30 K lower compared to Mars reference data. We are not parameterizing Mie scattering from aerosols in this work, which would lead to extra heating in the Martian lower to middle atmosphere, as discussed by, e.g., Gierasch & Goody (1972).

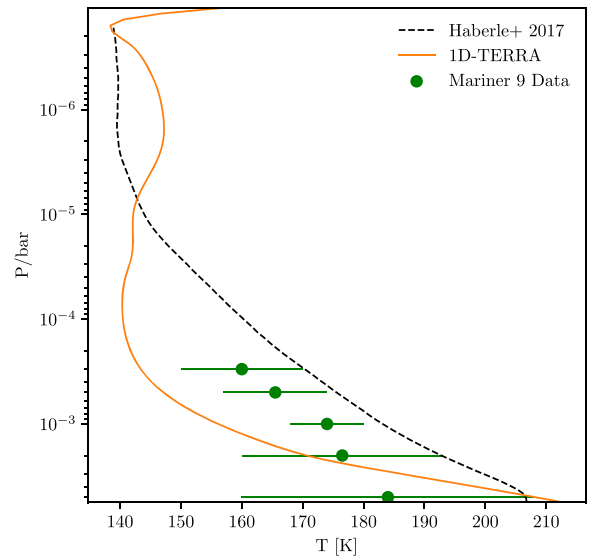


Figure 10. Validation for a hypothetically aerosol-free Mars. We compare temperatures calculated with 1D-TERRA (orange) to the Haberle et al. (2017) Mars reference atmosphere (black) and Mariner 9 IRIS data (green).

### 4. Application to K2-18B

We apply 1D-TERRA to the super-Earth/sub-Neptune planet K2-18b with recently analyzed atmospheric infrared features from combined Kepler K2, Hubble WFC3, and Spitzer observations (Benneke et al. 2019b; Tsiaras et al. 2019). This marks the first detection of H<sub>2</sub>O in the atmosphere of an exoplanet smaller than Neptune and Uranus. Planet K2-18b has a mass of  $8.63 \pm 1.35 M_{\oplus}$  and orbits an M2.5 host star ( $0.0234 L_{\odot}$ ) at 0.1429 au with a resulting  $TSI = 1.1459 TSI_{\oplus}$ . For the host star, K2-18, we use the stellar spectrum from GJ 176, an M2.5 star similar to K2-18 in stellar properties, available in the MUSCLES database, and prepare it as described in Section 2.1.6. The planetary radius of K2-18b was recently updated from  $2.27$  to  $2.711 \pm 0.065 R_{\oplus}$  due to reanalysis of K2-18’s stellar radius by Cloutier et al. (2019). Planetary radius calculations are based on the  $4.5 \mu\text{m}$  Spitzer band transit depths. We apply a simple mass–radius



**Table 6**  
Planetary and Atmospheric Scenarios for Modeled K2-18b

Scenario	$p_0$ Start (bars)	H <sub>2</sub> O Reservoir	$p_0$ End (bars)	Atm. Composition	$T$ Start	$T(p_0)$ End (K)
(1) Earth-like	1.56	Yes	132.2	US Std. 1976	US Std. 1976	604
(2) Venus-like	143.6	No	143.6	VIRA-1	ISO 500 K	550
(3) Venus + 186 bars H <sub>2</sub>	93 + 186	No	279	VIRA-1 + H <sub>2</sub>	ISO 500 K	699
(4) Venus + 800 bars H <sub>2</sub>	93 + 800	No	893	VIRA-1 + H <sub>2</sub>	ISO 500 K	893
(5) Solar metallicity	10	No	10	CEA (1× solar)	Linear 320–250 K	691
(6) Solar met. + H <sub>2</sub> O ocean	10	Yes	230.2	CEA (1× solar) + H <sub>2</sub> O	Linear 320–250 K	925
(7) 50× solar metallicity	10	No	10	CEA (50× solar)	Linear 520–250 K	719

parameterization from Noack et al. (2016) to estimate gravity at the surface–atmosphere boundary layer and find that the original radius estimate of  $2.27 R_{\oplus}$  could still be interpreted as a rocky planet with an ice-mass fraction of 35%–62% and a core-mass fraction <35%. These estimates lead to a surface gravity of  $g \sim 15 \text{ m s}^{-2}$ . The updated radius of  $2.71 R_{\oplus}$ , however, cannot be achieved using this parameterization without a significant atmospheric contribution.

We compare a variety of planetary scenarios and atmospheres calculated with the extensive capabilities of 1D-TERRA against the published observations. Our main goals here are to show the large application range of our new model and provide possible explanations and constraints when interpreting the observed spectral features of K2-18b.

#### 4.1. Scenarios

(1) For our first scenario shown in Table 6, we start with an Earth-like atmosphere based on the US standard atmosphere 1976. As a starting condition, we assume Earth’s atmospheric mass, which, with the elevated gravity, leads to a surface pressure of 1.55 bars. Recent modeling studies have shown that surface temperatures of Earth-like planets around M stars would increase relative to Earth for Earth’s TSI because of the redshifted spectrum of cooler stars, different UV environments, and atmospheric and ocean responses (see, e.g., Scheucher et al. 2018). Consequently, we expect a theoretically Earth-like K2-18b, receiving somewhat higher TSI than Earth, to significantly warm up, evaporating parts of the ocean H<sub>2</sub>O reservoir, resulting in a thick steam atmosphere. For this reason, we use the constant RH profile of 0.95 used in Equation (18) for the H<sub>2</sub>O calculation over all convective layers. For this scenario, we use 1D-TERRA in fully coupled climate-chemistry mode to capture details of the impact of increased H<sub>2</sub>O in the atmosphere.

(2) Due to the higher TSI and the size of the planet, the accumulation of a significant atmosphere and a past runaway greenhouse state are plausible; therefore, our second atmosphere of interest is an exo-Venus. As with Venus, we do not assume an H<sub>2</sub>O reservoir, and, to retain Venus’s atmospheric mass, we increase the surface pressure accordingly to 143.6 bars. All Venusian scenarios (2)–(4) are run in climate-only mode, as we focus here on the resulting H<sub>2</sub>O features in the modeled transmission spectra influenced by temperatures, pressures, and H<sub>2</sub>O amounts, rather than the full photochemistry of other trace gases. Our initial temperatures for the Venus-like runs are 500 K isoprofiles.

(3)–(4) To increase the amplitude of absorption features, we increase the atmospheric scale heights by adding H<sub>2</sub> to our exo-Venus atmospheres. First, we triple (=279 bars  $p_0$ ) our original (=93 bars  $p_0$ ) Venus atmosphere by adding 186 bars of H<sub>2</sub> (3),

and in another scenario, we add 800 bars of H<sub>2</sub> on top of the 93 bars of Venus for comparison (4). This was chosen to stay within our limit of calculated  $k$ -distributions of 1000 bars.

(5) Next, we move on to hydrogen-dominated primary atmospheres, which we model with 1D-TERRA in climate-only mode with a prescribed atmospheric composition. We have calculated the equilibrium chemical composition for an isothermal atmosphere with an equilibrium temperature of  $T_{\text{eq}} = 320 \text{ K}$  using the NASA CEA model (McBride & Gordon 1992) with initial solar elemental abundances by Asplund et al. (2009). The chemical composition is subsequently kept fixed. Radiative–convective equilibrium is calculated down to 10 bars, although the atmosphere might extend further down to higher pressures. We choose this limit because we expect H<sub>2</sub>O absorption features in the Hubble WFC3 spectral range to result from pressures up to a few hundred mbar, and we cannot make any assumption on the actual extent down to a possible surface. For all H<sub>2</sub>-dominated atmospheres, we start with a linear temperature gradient from the surface up to the TOA, in order to speed up climate calculations.

(6) We repeat the same with a potential H<sub>2</sub>O reservoir (ocean) at the lower atmospheric boundary at 10 bars, which can evaporate and mix into the atmosphere dependent on temperature, H<sub>2</sub>O saturation pressure, and assumed constant RH of 95% for convective layers as in scenario (1), due to the expected warm temperatures in the lower atmosphere. To stay well within our valid model temperature range ( $T < 1000 \text{ K}$ ), we limit the H<sub>2</sub>O saturation vapor pressure, i.e., the amount of water the atmosphere can hold in gas phase, to its value at the critical point at 647 K for temperatures above, leading to a maximum of 220 bars of H<sub>2</sub>O in the atmosphere. As in scenario (5), the chemical composition is kept fixed, except for the changes in H<sub>2</sub>O, which changes all mixing ratios accordingly.

(7) Lastly, we calculate a 50 times solar metallicity atmosphere with the NASA CEA model and perform climate calculations similar to scenario (5) without any H<sub>2</sub>O reservoir to study the effect of metallicity on atmospheric scale heights, impacting the amplitude of the resulting absorption features.

#### 4.2. Results

Table 6 shows the different planetary scenarios modeled in this work, plus the resulting bottom-of-atmosphere (BOA) pressures after the climate, or climate-chemistry calculations, respectively, as well as the respective BOA temperatures. The BOA pressures can only change in our model when mass conservation is broken by additional in- or outfluxes. This is invoked, e.g., for scenarios with an H<sub>2</sub>O reservoir, evaporating extra molecules into the atmosphere when the atmosphere is heating up or condensing them out.

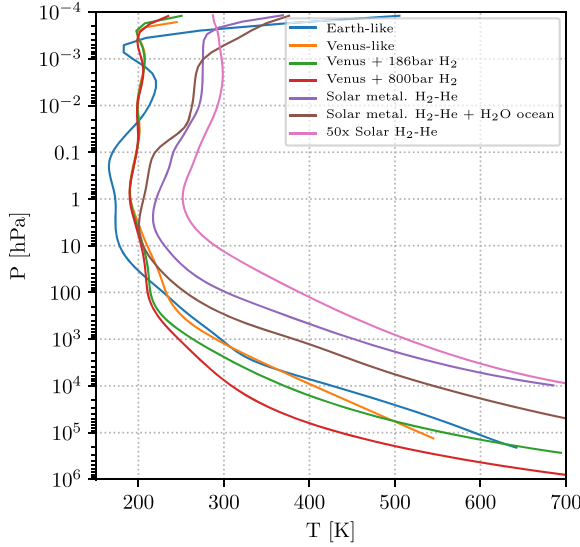


**Figure 11.** Temperature profiles for our K2-18b model atmospheres (see Table 6).

Figure 11 shows the resulting atmospheric temperature profiles for all scenarios described above. Almost all scenarios lead to global mean temperatures in the thick lower atmosphere that are too hot to be habitable. That said, at the 1 bar level, all runs, except the hydrogen-dominated cases, yield moderate temperatures with the possibility of liquid water, as also discussed by Benneke et al. (2019b). At higher pressures, temperature profiles become adiabatic. At low atmospheric pressures, UV heating leads to the temperature inversions in the upper layers.

Our main results are shown in Figure 12. We supply the modeled atmospheric compositions and temperatures from Figure 11 to calculate forward-modeled transmission spectra in GARLIC and compare them with the Kepler, Hubble, and Spitzer data of K2-18b from Benneke et al. (2019b). We plot the planetary transit depth,  $\delta(\lambda) = [(r_p + h(\lambda))/r_s]^2$ , with  $r_p$  being the planetary radius,  $r_s$  the stellar radius, and  $h(\lambda) = \sum_i (1 - T_i(\lambda)) \Delta h_i$  the effective height of the atmosphere for a given wavelength. Note that all spectra shown can, in principle, be shifted vertically within the error in the  $4.5 \mu\text{m}$  Spitzer observation, from which radius estimates for K2-18b were derived, but it was rather our aim to focus on the amplitudes of spectral features, rather than the closest observational fit. Such a shift could arise due to the lack of knowledge regarding, e.g., the interior structure and location of the planet-atmosphere boundary. Spectral absorption features in the modeled solar composition atmosphere (purple) and the 50 times solar metallicity results (pink) match the observations well within  $\pm 1\sigma$ , with the exception of the  $3.6 \mu\text{m}$  Spitzer band. A distinction between 1 and 50 times solar metallicities from the observations is difficult. Other considered scenarios cannot produce features strong enough to explain the apparent  $1\text{--}2 \mu\text{m}$   $\text{H}_2\text{O}$  absorption observations with a strength of  $\sim 100$  ppm and a  $1\sigma$  of  $\sim 23$  ppm. For example, our  $\text{H}_2$ -dominated Venus-like case (4), shown in red, produces feature strengths of only  $\sim 35$  ppm.

Furthermore, the addition of extra  $\text{H}_2\text{O}$  due to a hypothetical water-world ocean reservoir (brown) would increase

atmospheric mean molecular weights, thus drastically decreasing scale heights. For the solar metallicity case with ocean reservoir (6), the features would reduce to  $< 15$  ppm. Even if one were to shift these spectra vertically in Figure 12, it is clear that the amplitudes of features seen in any model scenarios (other than the  $\text{H}_2$ -He atmospheres without an ocean reservoir) would still not be compatible with the observations. A further test run with an Earth-like RH profile with 80% humidity at the surface and a very dry upper atmosphere to calculate the  $\text{H}_2\text{O}$  profile after Manabe & Wetherald (1967) suggested no significant changes in planetary climate and atmospheric spectral appearance. Madhusudhan et al. (2020) recently argued that the amount of  $\text{H}_2\text{O}$  mixed into an  $\text{H}_2$ /He atmosphere consistent with the Hubble Space Telescope measurements would not significantly change the planetary radius, and further, that a habitable ocean world with liquid water underneath an  $\text{H}_2$ /He atmosphere is possible for K2-18b. While it may be true that the observed radius can be achieved in such a scenario, our study considers the effect such a large  $\text{H}_2\text{O}$  reservoir would have upon the atmosphere due to strong evaporation and thereby on the observed spectral features. Our results suggest that an ocean world scenario would not fit the observed spectral features. This includes all of our terrestrial atmospheres, as well as the hypothetical Venus runs with added  $\text{H}_2$ , although the Venus run with 800 bars of added  $\text{H}_2$  (red) already shows distinguishable features. While it is clear that larger scale heights are needed to explain the observations, it is interesting that our results suggest that large amounts of the heavy molecule  $\text{CO}_2$  can also be excluded by observations, as well as the existence of a hypothetical surface ocean at our BOA temperatures. The contrast gradient between the two Spitzer observations at  $3.6$  and  $4.5 \mu\text{m}$  could come from extensive amounts of  $\text{CO}_2$  or other absorbers in the  $4.5 \mu\text{m}$  band, e.g.,  $\text{O}_3$ ,  $\text{N}_2\text{O}$ , or  $\text{CO}$  (all not shown), but all of which would further bring down scale heights. Another possibility is reduced  $\text{CH}_4$  in the middle and upper atmosphere, e.g., by freezing it out (at  $\sim 91$  K), and in doing so reducing the  $3.6 \mu\text{m}$   $\text{CH}_4$  absorption feature. The CEA solar composition atmosphere contains  $\sim 460$  ppm  $\text{CH}_4$  ( $50\times$  solar  $\sim 2.48\%$   $\text{CH}_4$ ). In Figure 13, we show how a transmission spectrum without  $\text{CH}_4$  contribution would look by comparison. Our results suggest that the depletion of  $\text{CH}_4$  could indeed explain the discrepancy between model results and observations. Benneke et al. (2019b) could only limit  $\text{CH}_4$  to  $< 0.25\%$ , while our results with 1D-TERRA limit  $\text{CH}_4$  to  $< 460$  ppm.

## 5. Summary

We describe in this work our new radiative transfer module, REDFOX, implemented in our 1D climate-chemistry model, 1D-TERRA. The model also uses the updated photochemistry reaction scheme, BLACKWOLF, which is described in depth in the companion paper (Wunderlich et al. 2020). The radiative transfer update included the user's choice of absorbing species, extended wavelength ranges of stellar and thermal calculations, flexible inclusion of CIAs, additional continua and UV absorbers, and broader pressure-temperature ranges, among others. We show an extensive verification and validation of REDFOX and 1D-TERRA against terrestrial-type solar system atmospheres and previously published modeling results for other theoretical atmospheres.

With our new model, we study the exoplanet K2-18b, with its first-ever observed atmospheric absorption features of  $\text{H}_2\text{O}$

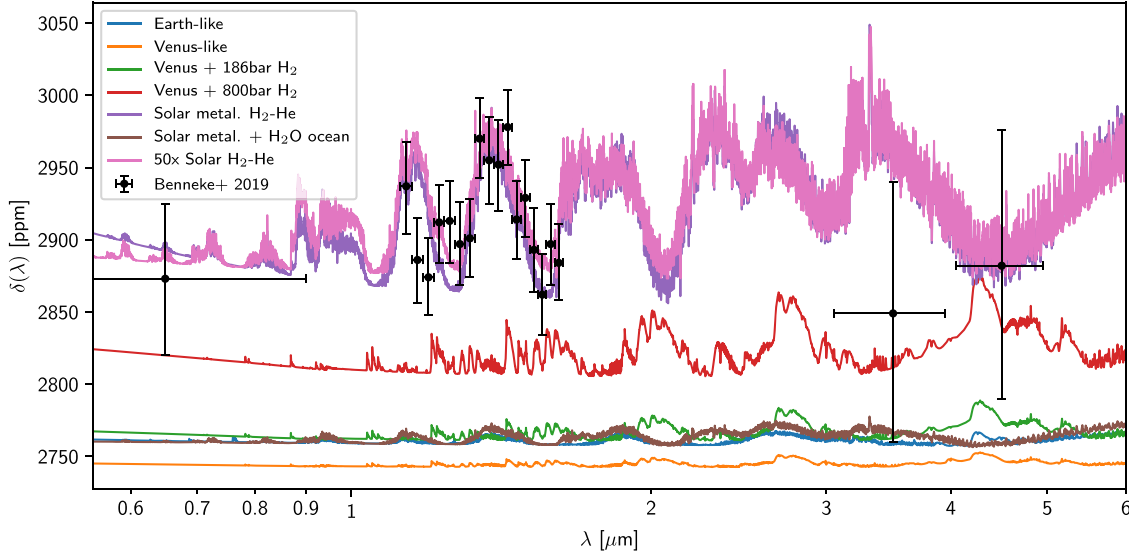


**Figure 12.** Comparison of planetary transmission spectra for K2-18b calculated with GARLIC for our 1D-TERRA model atmospheres (Table 6 and Figure 11) with Kepler, Hubble, and Spitzer data taken from Benneke et al. (2019b). Here  $\delta(\lambda)$  is the wavelength-dependent transit depth of the planet.

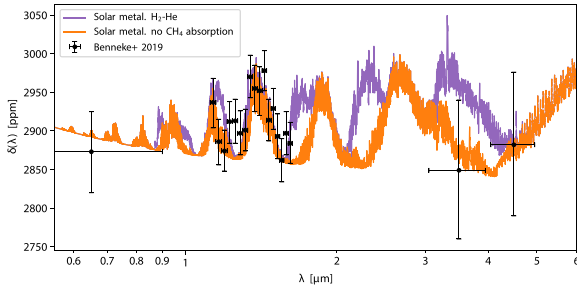


**Figure 13.** Transmission spectra for the solar metallicity atmosphere (purple) as in Figure 12 compared to the same atmosphere but without  $\text{CH}_4$  contribution (orange).

in an exoplanet with mass  $< 10 M_{\oplus}$ , and calculate climate and transmission spectra for different atmospheric and planetary scenarios.

We confirm the findings of Benneke et al. (2019b) that K2-18b likely has an  $\text{H}_2$ -He atmosphere and additionally exclude the existence of a large  $\text{H}_2\text{O}$  ocean reservoir exposed to the atmosphere. This rules out a water layer at the top of the mantle for possible interior structures, as it would decrease the atmospheric scale height, despite the newly described effect of increased radii for  $\text{H}_2\text{O}$  steam atmospheres by Turbet et al. (2020). We further confirm that the Hubble WFC3 observations between 1 and  $2 \mu\text{m}$  can be explained by  $\text{H}_2\text{O}$  absorption in a hydrogen-dominated primary atmosphere. Both solar and 50 times solar metallicity results alike can explain the observations. With the recent radius update for K2-18b and the need for a significant atmospheric contribution to the planetary radius, a hypothetical  $\text{H}_2\text{O}$  reservoir would likely be a supercritical fluid at such high temperatures, implying an envelope rather than a solid or liquid surface. This suggests that K2-18b is unlikely to be a water world or even an icy world. We also argue that significant amounts of  $\text{CH}_4$  are excluded by the Spitzer observations. The depletion of  $\text{CH}_4$  has also been

discussed in depth for the significantly larger Neptune-sized exoplanet GJ 436b (see, e.g., Madhusudhan & Seager 2011; Hu et al. 2015) and recently by Benneke et al. (2019a) for the  $12 M_{\oplus}$  sub-Neptune GJ 3470b, while Neptune itself shows significant amounts of  $\text{CH}_4$  with around 1.5% in the atmosphere.

Additionally, our results clearly show in comparison how small atmospheric contributions would be if K2-18b were to possess a terrestrial atmosphere, such as Earth- or Venus-like. Even with large added amounts of  $\text{H}_2$  to increase scale heights, spectral features are nevertheless suppressed within the error bars of state-of-the-art transit observations, which suggests that it will be challenging for next-generation telescopes to characterize Earth- or Venus-like atmospheres from primary transits. That said, we are excited at the prospect of the James Webb Space Telescope characterizing many more super-Earth atmospheres in the near future.

We thank Nadine Nettelmann for her constructive inputs and fruitful discussions and the anonymous referee for constructive comments that helped improve and clarify the manuscript.

M.S. acknowledges support from DFG project RA 714/9-1.

F.W. acknowledges support from DFG project RA 714/7-1.

M.G. gratefully acknowledges support from the DFG through project GO 2610/1-1 and priority program SPP 1992 “Exploring the Diversity of Extrasolar Planets” (GO 2610/2-1).

K.H. and J.L.G. acknowledge the International Space Science Institute and the supported International Team 464: The Role of Solar and Stellar Energetic Particles on (Exo) Planetary Habitability (ETERNAL; <http://www.issibern.ch/teams/exoeternal/>).

F.S. acknowledges support from DFG project SCHR 1125/3-1.

**Software:** GARLIC (Schreier et al. 2014, 2018a, 2018b), HITRAN 2016 (Gordon et al. 2017), MPI Mainz Spectral Atlas (Keller-Rudek et al. 2013), KSPECTRUM1.2.0 (Eymet et al. 2016), 1D climate-chemistry model legacy (Kasting &



**Table A1.**  
Parameters  $s_i$  and  $T_s$  for Heat Capacity Calculations with the Shomate Equation (Equation (A2)), Together with the Respective Validity Range

Coef.	CH <sub>4</sub> <sup>a</sup>	CO <sub>2</sub> <sup>b</sup>	H <sub>2</sub> O <sup>a</sup>	N <sub>2</sub>	O <sub>2</sub>
$s_1$	−0.703	7.7	30.092	6.76	8.27
$s_2$	108.477	$5.3 \times 10^{-3}$	6.832	$6.06 \times 10^{-4}$	$2.58 \times 10^{-4}$
$s_3$	−42.522	$-8.3 \times 10^{-7}$	6.793	$1.3 \times 10^{-7}$	...
$s_4$	5.863	...	−2.534	...	...
$s_5$	0.679	...	0.082	...	$1.877 \times 10^5$
$T_s$ (K)	1000	1	1000	1	1
Valid (K)	298–1300		500–1700		

**Notes.**

<sup>a</sup> Chase (1998); <https://webbook.nist.gov/chemistry/>.

<sup>b</sup> Kasting (1991).

Ackerman 1986; Pavlov et al. 2000; Segura et al. 2003; von Paris et al. 2015, and others), NASA CEA (McBride & Gordon 1992).

## Appendix Heat Capacities

There are in total nine heat capacities,  $c_p$  (J mol<sup>−1</sup> K<sup>−1</sup>), considered in our model: Ar, CH<sub>4</sub>, CO, CO<sub>2</sub>, H<sub>2</sub>, H<sub>2</sub>O, He, N<sub>2</sub>, and O<sub>2</sub>. These had been implemented by various researchers over several decades, most recently by Dr. Philipp von Paris in 2011 and used in, e.g., Godolt et al. (2016, 2019), Gebauer et al. (2017, 2018), Keles et al. (2018), Scheucher et al. (2018, 2020), and Wunderlich et al. (2019). Two of the  $c_p$  values are implemented as temperature-independent:  $c_{p,\text{Ar}} = 20.78600$  and  $c_{p,\text{He}} = 20.78603$  (Chase 1998).<sup>16</sup> Heat capacities for CO and H<sub>2</sub> are calculated based on the empirical formula (Deming & Shupe 1931),

$$c_p(T) = \frac{7R}{2} + R \frac{T_{\text{ref}}^2}{T} \frac{e^{\frac{T_{\text{ref}}}{T}}}{(e^{\frac{T_{\text{ref}}}{T}} - 1)^2}, \quad (\text{A1})$$

with the gas constant  $R$  and the reference temperatures  $T_{\text{ref,CO}} = 3090$  K and  $T_{\text{ref,H}_2} = 6100$  K, respectively. Other heat capacities are calculated using the Shomate equation (Parks & Shomate 1940),

$$c_p\left(\frac{T}{T_s}\right) = s_1 + s_2 \cdot \left(\frac{T}{T_s}\right) + s_3 \cdot \left(\frac{T}{T_s}\right)^2 + s_4 \cdot \left(\frac{T}{T_s}\right)^3 + s_5 \cdot \left(\frac{T}{T_s}\right)^{-2}, \quad (\text{A2})$$

with parameters  $s_i$  and temperatures  $T_s$  for different molecules shown in Table A1. For CH<sub>4</sub>, Equation (A2) is only used above 300 K within the respective validity range of parameters in Table A1. Below, we use the linear interpolation

$$c_{p,\text{CH}_4}(T) = \frac{c_{p,2} - c_{p,1}}{T_2 - T_1}(T - T_1) + c_{p,1} \quad (\text{A3})$$

of calculations from Gurvich et al. (1989) of heat capacities  $c_{p,1}$  and  $c_{p,2}$  at temperatures  $T_1$  and  $T_2$ , respectively, shown in Table A2.

## ORCID iDs

Markus Scheucher  <https://orcid.org/0000-0003-4331-2277>

<sup>16</sup> <https://webbook.nist.gov/chemistry/>

**Table A2**  
CH<sub>4</sub> Heat Capacities  $c_{p,i}$  (J mol<sup>−1</sup> K<sup>−1</sup>) from Gurvich et al. (1989), Used in Equation (A3)

Regime	$T_1$ (K)	$T_2$ (K)	$c_{p,1}$	$c_{p,2}$
100–200 K	100	200	33.28	33.51
200–300 K	200	300	33.51	35.76

F. Wunderlich  <https://orcid.org/0000-0002-2238-5269>  
J. L. Grenfell  <https://orcid.org/0000-0003-3646-5339>  
M. Godolt  <https://orcid.org/0000-0003-4770-8551>  
F. Schreier  <https://orcid.org/0000-0001-7196-6599>  
D. Kappel  <https://orcid.org/0000-0002-0518-5548>  
K. Herbst  <https://orcid.org/0000-0001-5622-4829>

## References

- Abel, M., Frommhold, L., Li, X., & Hunt, K. L. C. 2011, *JPCA*, **115**, 6805  
Abel, M., Frommhold, L., Li, X., & Hunt, K. L. C. 2012, *JChPh*, **136**, 044319  
Abramowitz, M., & Stegun, I. A. 1972, *Handbook of Mathematical Functions* (New York: Dover)  
Allen, C. W. 1973, *Astrophysical Quantities* (London: Univ. London, Athlone Press)  
Amundsen, D. S., Tremblin, P., Manners, J., Baraffe, I., & Mayne, N. J. 2017, *A&A*, **598**, A97  
Anglada-Escudé, G., Amado, P. J., Barnes, J., et al. 2016, *Natur*, **536**, 437  
Asplund, M., Grevesse, N., Sauval, A. J., & Scott, P. 2009, *ARA&A*, **47**, 481  
Baranov, Y. I., Fraser, G. T., Lafferty, W. J., & Vigasin, A. A. 2003, in *Weakly Interacting Molecular Pairs: Unconventional Absorbers of Radiation in the Atmosphere*, ed. C. Camy-Peyret & A. A. Vigasin (Dordrecht: Springer), 149  
Baranov, Y. I., Lafferty, W., & Fraser, G. 2004, *JMoSp*, **228**, 432  
Benneke, B., Knutson, H. A., Lothringer, J., et al. 2019a, *NatAs*, **3**, 813  
Benneke, B., Wong, I., Piaulet, C., et al. 2019b, *ApJL*, **887**, L14  
Boone, C. D., Nassar, R., Walker, K. A., et al. 2005, *ApOpt*, **44**, 7218  
Bucholtz, A. 1995, *ApOpt*, **34**, 2765  
Burkholder, J., Sander, S., Abbatt, J., et al. 2015, *Chemical Kinetics and Photochemical Data for use in Atmospheric Studies: Evaluation Number 18* (Pasadena, CA: JPL, NASA) <https://trs.jpl.nasa.gov/handle/2014/45510>  
Charbonneau, D., Berta, Z. K., Irwin, J., et al. 2009, *Natur*, **462**, 891  
Chase, M. W. 1998, *JPCRD*, **9**, 1  
Clawson, J. F. & (U.S.), J.P.L. 1991, *Thermal Environments No. JPL D-8160* (Pasadena, CA: JPL, Caltech)  
Clough, S. A., Iacono, M. J., & Moncet, J.-L. 1992, *JGR*, **97**, 15761  
Clough, S. A., Shephard, M. W., Mlawer, E. J., et al. 2005, *JQSRT*, **91**, 233  
Cloutier, R., Astudillo-Defru, N., Doyon, R., et al. 2019, *A&A*, **621**, A49  
Cronin, T. W. 2014, *JAIS*, **71**, 2994  
Crossfield, I. J., & Kreidberg, L. 2017, *AJ*, **154**, 261  
Deming, W. E., & Shupe, L. E. 1931, *PhRv*, **38**, 2245  
Edlén, B. 1966, *Metro*, **2**, 71  
Elsässer, W. 1942, *Heat Transfer by Infrared Radiation in the Atmosphere*, Vol. 6 (Milton, VA: Harvard Univ., Blue Hill Meteorological Observatory)  
Eymet, V., Coustet, C., & Piaud, B. 2016, *JPhCS*, **676**, 012005  
Forget, F., & Leconte, J. 2014, *RSPTA*, **372**, 20130084  
Gamache, R. R., Roller, C., Lopes, E., et al. 2017, *JQSRT*, **203**, 70

- Gebauer, S., Grenfell, J., Lehmann, R., & Rauer, H. 2018, *AsBio*, **18**, 856
- Gebauer, S., Grenfell, J., Stock, J., et al. 2017, *AsBio*, **17**, 27
- Gierasch, P. J., & Goody, R. M. 1972, *JAtS*, **29**, 400
- Gillon, M., Triaud, A. H., Demory, B.-O., et al. 2017, *Natur*, **542**, 456
- Godolt, M., Grenfell, J. L., Kitzmann, D., et al. 2016, *A&A*, **592**, A36
- Godolt, M., Tosi, N., Stracke, B., et al. 2019, *A&A*, **625**, A12
- Gordon, I., Rothman, L., Hill, C., et al. 2017, *JQSRT*, **203**, 3
- Grenfell, J. L., Griebmeier, J.-M., Patzer, B., et al. 2007, *AsBio*, **7**, 208
- Grenfell, J. L., Griebmeier, J.-M., von Paris, P., et al. 2012, *AsBio*, **12**, 1109
- Grimm, S. L., & Heng, K. 2015, *ApJ*, **808**, 182
- Gruska, M., & Borysow, A. 1997, *Icar*, **129**, 172
- Gueymard, C. A. 2004, *SoEn*, **76**, 423
- Gurvich, L. V., Veits, I. V., & Alcock, C. B. 1989, *Thermodynamics Properties of Individual Substances. Volume 1—Elements O, H/D, T/, F, Cl, Br, I, He, Ne, Ar, Kr, Xe, Rn, S, N, P, and Their Compounds. Part 1—Methods and computation. Part 2—Tables (4th revised and enlarged ed.)* (New York: Hemisphere Publishing Corp.)
- Haberle, R. M., Clancy, R. T., Forget, F., Smith, M. D., & Zurek, R. W. 2017, *The Atmosphere and Climate of Mars* (Cambridge: Cambridge Univ. Press)
- Hamre, B., Starnes, S., Starnes, K., & Starnes, J. J. 2013, in *AIP Conf. Proc.* 1531 (Melville, NY: AIP), 923
- Haus, R., Kappel, D., & Arnold, G. 2015, *P&SS*, **117**, 262
- Hauschildt, P. H., Allard, F., & Baron, E. 1999, *ApJ*, **512**, 377
- Hedges, C., & Madhusudhan, N. 2016, *MNRAS*, **458**, 1427
- Heng, K., Malik, M., & Kitzmann, D. 2018, *ApJS*, **237**, 29
- Herbst, K., Grenfell, J. L., Sinnhuber, M., et al. 2019, *A&A*, **631**, A101
- Hu, R., Seager, S., & Bains, W. 2012, *ApJ*, **761**, 166
- Hu, R., Seager, S., & Yung, Y. L. 2015, *ApJ*, **807**, 8
- Justus, C. G., James, B. F., & Johnson, D. L. 1996, *Mars Global Reference Atmospheric Model (Mars-GRAM 3.34): Programmer's Guide*, Tech. Rep. NASA-TM-108509, NASA Marshall Space Flight Center <https://ntrs.nasa.gov/search.jsp?R=19960036976>
- Karman, T., Gordon, I. E., van der Avoird, A., et al. 2019, *Icar*, **328**, 160
- Kasting, J. F. 1991, *Icar*, **94**, 1
- Kasting, J. F., & Ackerman, T. P. 1986, *Sci*, **234**, 1383
- Kasting, J. F., Whitmire, D. P., & Reynolds, R. T. 1993, *Icar*, **101**, 108
- Katyal, N., Nikolaou, A., Godolt, M., et al. 2019, *ApJ*, **875**, 31
- Keles, E., Grenfell, J. L., Godolt, M., Stracke, B., & Rauer, H. 2018, *AsBio*, **18**, 116
- Keller-Rudek, H., Moortgat, G. K., Sander, R., & Sørensen, R. 2013, *ESSD*, **5**, 365
- Kitzmann, D. 2017, *A&A*, **600**, A111
- Kitzmann, D., Patzer, A., von Paris, P., et al. 2010, *A&A*, **511**, A66
- Kleinböhl, A., Schofield, J. T., Kass, D. M., et al. 2009, *JGRE*, **114**, E10006
- Kopparapu, R. K., Ramirez, R., Kasting, J. F., et al. 2013, *ApJ*, **765**, 131
- Lacis, A. A., & Oinas, V. 1991, *JGR*, **96**, 9027
- Lincowski, A. P., Meadows, V. S., Crisp, D., et al. 2018, *ApJ*, **867**, 76
- Madhusudhan, N., Agúndez, M., Moses, J. I., & Hu, Y. 2016, *SSRv*, **205**, 285
- Madhusudhan, N., Nixon, M. C., Welbanks, L., Piette, A. A. A., & Booth, R. A. 2020, *ApJL*, **891**, L7
- Madhusudhan, N., & Seager, S. 2011, *ApJ*, **729**, 41
- Malik, M., Grosheintz, L., Mendonça, J. M., et al. 2017, *AJ*, **153**, 56
- Manabe, S., & Wetherald, R. T. 1967, *JAtS*, **24**, 241
- McBride, B., & Gordon, S. 1992, *Computer Program for Calculating and Fitting Thermodynamic Functions*, Tech. Rep. NASA RP-1271, NASA Lewis Research Center <https://ntrs.nasa.gov/search.jsp?R=19930003779>
- Meador, W. E., & Weaver, W. R. 1980, *JAtS*, **37**, 630
- Meadows, V. S., Arney, G. N., Schwietzman, E. W., et al. 2018, *AsBio*, **18**, 133
- Meadows, V. S., & Crisp, D. 1996, *JGR*, **101**, 4595
- Mendonça, J., Read, P., Wilson, C., & Lee, C. 2015, *P&SS*, **105**, 80
- Ment, K., Dittmann, J. A., Astudillo-Defru, N., et al. 2019, *AJ*, **157**, 32
- Mlawer, E. J., Payne, V. H., Moncet, J.-L., et al. 2012, *RSPTA*, **370**, 2520
- Mlawer, E. J., Taubman, S. J., Brown, P. D., Iacono, M. J., & Clough, S. A. 1997, *JGRD*, **102**, 16663
- Montet, B. T., Morton, T. D., Foreman-Mackey, D., et al. 2015, *ApJ*, **809**, 25
- Murphy, W. F. 1977, *JChPh*, **67**, 5877
- Nair, H., Allen, M., Anbar, A. D., Yung, Y. L., & Clancy, R. T. 1994, *Icar*, **111**, 124
- Nakajima, S., Hayashi, Y.-Y., & Abe, Y. 1992, *JAtS*, **49**, 2256
- Noack, L., Höning, D., Rivoldini, A., et al. 2016, *Icar*, **277**, 215
- Owen, T., Biemann, K., Rushneck, D., et al. 1977, *JGR*, **82**, 4635
- Parks, G. S., & Shomate, C. H. 1940, *JChPh*, **8**, 429
- Pavlov, A. A., Kasting, J. F., Brown, L. L., Rages, K. A., & Freedman, R. 2000, *JGR*, **105**, 11981
- Perrin, M., & Hartmann, J. 1989, *JQSRT*, **42**, 311
- Pierrehumbert, R. T. 2010, *Principles of Planetary Climate* (Cambridge: Cambridge Univ. Press)
- Pollack, J. B., Dalton, J. B., Grinspoon, D., et al. 1993, *Icar*, **103**, 1
- Press, W. H., Teukolsky, S. A., Vetterling, W. T., & Flannery, B. P. 1992, *Numerical Recipes in Fortran* (2nd ed.; Cambridge: Cambridge Univ. Press)
- Ramirez, R. M., Kopparapu, R., Zuger, M. E., et al. 2014, *NatCC*, **7**, 59
- Rauer, H., Gebauer, S., Paris, P. V., et al. 2011, *A&A*, **529**, A8
- Robinson, T. D., & Crisp, D. 2018, *JQSRT*, **211**, 78
- Rogelj, J., Meinshausen, M., & Knutti, R. 2012, *NatCC*, **2**, 248
- Rothman, L., Gordon, I., Barber, R., et al. 2010, *JQSRT*, **111**, 2139
- Scheucher, M., Grenfell, J. L., Wunderlich, F., et al. 2018, *ApJ*, **863**, 6
- Scheucher, M., Herbst, K., Schmidt, V., et al. 2020, *ApJ*, **893**, 12
- Schreier, F. 2006, *CoPhC*, **174**, 783
- Schreier, F., Gimeno García, S., Hedelt, P., et al. 2014, *JQSRT*, **137**, 29
- Schreier, F., Milz, M., Buehler, S. A., & von Clarmann, T. 2018a, *JQSRT*, **211**, 64
- Schreier, F., Städt, S., Hedelt, P., & Godolt, M. 2018b, *MolAs*, **11**, 1
- Segura, A., Krellove, K., Kasting, J. F., et al. 2003, *AsBio*, **3**, 689
- Segura, A., Walkowicz, L. M., Meadows, V., Kasting, J., & Hawley, S. 2010, *AsBio*, **10**, 751
- Seiff, A., Schofield, J., Kliore, A., et al. 1985, *AdSpR*, **5**, 3
- Shardanand, A., & Rao, A. D. P. 1977, *Absolute Rayleigh Scattering Cross Sections of Gases and Freons of Stratospheric Interest in the Visible and Ultraviolet Regions*, NASA TN D-8442 (Washington, DC: NASA) <https://ntrs.nasa.gov/archive/nasa/casi.ntrs.nasa.gov/19770012747.pdf>
- Sharp, C. M., & Burrows, A. 2007, *ApJS*, **168**, 140
- Sing, D. K., Fortney, J. J., Nikolov, N., et al. 2016, *Natur*, **529**, 59
- Sneep, M., & Ubachs, W. 2005, *JQSRT*, **92**, 293
- Spiegel, D. S., & Burrows, A. 2010, *ApJ*, **722**, 871
- Starnes, K., Tsay, S.-C., Wiscombe, W., & Jayaweera, K. 1988, *ApOpt*, **27**, 2502
- Tabataba-Vakili, F., Grenfell, J. L., Griebmeier, J.-M., & Rauer, H. 2016, *A&A*, **585**, A96
- Takagi, M., Suzuki, K., Sagawa, H., et al. 2010, *JGRE*, **115**, E06014
- Tennyson, J., Yurchenko, S. N., Al-Refaie, A. F., et al. 2016, *JMoSp*, **327**, 73
- Tonkov, M., Filippov, N., Bertsev, V., et al. 1996, *ApOpt*, **35**, 4863
- Toon, O. B., McKay, C. P., Ackerman, T. P., & Santhanam, K. 1989, *JGRD*, **94**, 16287
- Tsang, C. C. C., Irwin, P. G. J., Wilson, C. F., et al. 2008, *JGRE*, **113**, E00B08
- Tsaras, A., Waldmann, I. P., Tinetti, G., Tennyson, J., & Yurchenko, S. N. 2019, *NatAs*, **3**, 1086
- Turbet, M., Bolmont, E., Ehrenreich, D., et al. 2020, *A&A*, **638**, A41
- Vardavas, I., & Carver, J. 1984, *P&SS*, **32**, 1307
- von Clarmann, T., Höpfner, M., Kellmann, S., et al. 2009, *AMT*, **2**, 159
- von Paris, P., Gebauer, S., Godolt, M., et al. 2010, *A&A*, **522**, A23
- von Paris, P., Rauer, H., Grenfell, J. L., et al. 2008, *P&SS*, **56**, 1244
- von Paris, P., Selsis, F., Godolt, M., et al. 2015, *Icar*, **257**, 406
- von Paris, P., Selsis, F., Kitzmann, D., & Rauer, H. 2013, *AsBio*, **13**, 899
- Wordsworth, R., Forget, F., & Eymet, V. 2010a, *Icar*, **210**, 992
- Wordsworth, R., Forget, F., Selsis, F., et al. 2010b, *A&A*, **522**, A22
- Wordsworth, R., Kalugina, Y., Lokshantov, S., et al. 2017, *GeoRL*, **44**, 665
- Wordsworth, R. D., & Pierrehumbert, R. T. 2013, *ApJ*, **778**, 154
- Wunderlich, F., Godolt, M., Grenfell, J. L., et al. 2019, *A&A*, **624**, A49
- Wunderlich, F., Scheucher, M., Godolt, M., et al. 2020, *ApJ*, in press, (arXiv:2006.11349)
- Yang, J., Leconte, J., Wolf, E. T., et al. 2016, *ApJ*, **826**, 222

# 3

## **Publication II: New Insights into Cosmic-Ray-induced Biosignature Chemistry in Earth-like Atmospheres**

**Personal and co-authors contributions:** I updated the [cosmic rays](#) scheme used in our photo chemistry model from Earth-based to be more inclusive of other atmospheric conditions and conducted the parameter study, produced the synthetic spectra, and analysed the results. I also wrote the manuscript.

J. L. Grenfell provided his chemical expertise as input for the interpretation of the results; All co-authors provided comments on the manuscript and in the journal's peer-review phase.



## New Insights into Cosmic-Ray-induced Biosignature Chemistry in Earth-like Atmospheres

Markus Scheucher<sup>1</sup> , J. L. Grenfell<sup>2</sup>, F. Wunderlich<sup>1</sup>, M. Godolt<sup>1</sup>, F. Schreier<sup>3</sup> , and H. Rauer<sup>1,2</sup>

<sup>1</sup> Zentrum für Astronomie und Astrophysik, Technische Universität Berlin, D-10623 Berlin, Germany; [scheucher@tu-berlin.de](mailto:scheucher@tu-berlin.de), [markus.scheucher@dlr.de](mailto:markus.scheucher@dlr.de)

<sup>2</sup> Institut für Planetenforschung, Deutsches Zentrum für Luft- und Raumfahrt, D-12489 Berlin, Germany

<sup>3</sup> Institut für Methodik der Fernerkundung, Deutsches Zentrum für Luft- und Raumfahrt, D-82234 Oberpfaffenhofen, Germany

Received 2018 February 27; revised 2018 June 22; accepted 2018 June 22; published 2018 August 6

### Abstract

With the recent discoveries of terrestrial planets around active M-dwarfs, destruction processes masking the possible presence of life are receiving increased attention in the exoplanet community. We investigate potential biosignatures of planets having Earth-like ( $N_2$ - $O_2$ ) atmospheres orbiting in the habitable zone of the M-dwarf star AD LEO. These are bombarded by high energetic particles that can create showers of secondary particles at the surface. We apply our cloud-free 1D climate-chemistry model to study the influence of key particle shower parameters and chemical efficiencies of NO<sub>x</sub> and HO<sub>x</sub> production from cosmic rays. We determine the effect of stellar radiation and cosmic rays upon atmospheric composition, temperature, and spectral appearance. Despite strong stratospheric O<sub>3</sub> destruction by cosmic rays, smog O<sub>3</sub> can significantly build up in the lower atmosphere of our modeled planet around AD LEO related to low stellar UVB. The abundance of N<sub>2</sub>O decreases with increasing flaring energies but a sink reaction for N<sub>2</sub>O with excited oxygen becomes weaker, stabilizing its abundance. CH<sub>4</sub> is removed mainly by Cl in the upper atmosphere for the strong flaring cases and not via hydroxyl as is otherwise usually the case. Cosmic rays weaken the role of CH<sub>4</sub> in heating the middle atmosphere so that H<sub>2</sub>O absorption becomes more important. We additionally underline the importance of HNO<sub>3</sub> as a possible marker for strong stellar particle showers. In a nutshell, uncertainty in NO<sub>x</sub> and HO<sub>x</sub> production from cosmic rays significantly influences the abundance of biosignatures and spectral appearance.

**Key words:** astrobiology – astrochemistry – methods: numerical – planets and satellites: atmospheres – planets and satellites: terrestrial planets – planet–star interactions

### 1. Introduction

Cool M-dwarf stars are favored targets in exoplanetary sciences due to their high abundance in the solar neighborhood, a close-in habitable zone (HZ), hence short orbital periods, and a high planet/star contrast. For an overview see, e.g., Kasting et al. (1993); Scalo et al. (2007); and Shields et al. (2016). There are however drawbacks. Planets lying in the close-in HZ could be tidally locked (e.g., Kasting et al. 1993; Selsis 2000) and could be bombarded by high levels of energetic particles (Grießmeier et al. 2005). An additional drawback for M-star planet habitability is the long, bright, pre-main-sequence phase of the parent star, which may devolatilize planets that would later reside in their HZs (e.g., Ramirez & Kaltenegger 2014; Luger & Barnes 2015; Tian & Ida 2015). Nevertheless, planets in the HZ of M-dwarf stars could represent the first opportunity to detect atmospheric properties and even biosignatures of rocky extrasolar planets. There are numerous relevant model studies, e.g., in 1D (Segura et al. 2003, 2005, 2010; Grenfell et al. 2012; Kopparapu et al. 2013; Rugheimer et al. 2015b; Tabataba-Vakili et al. 2016) and in 3D (Leconte et al. 2013; Shields et al. 2013, 2016; Yang et al. 2014; Godolt et al. 2015; Kopparapu et al. 2016). Interpretation of such potential future observation heavily relies on our detailed understanding of atmospheric physical, chemical, and biological processes and their interaction with different electromagnetic radiation and high energetic particles (HEPs), such as galactic cosmic rays (GCRs) and stellar energetic particles (SEPs). The latter has received only limited attention in the exoplanet community so far. Our general understanding of the redistribution of incoming HEPs into secondary particles in so-called air

showers through the atmosphere and their influence upon atmospheric chemistry dates back to theoretical work done in the early 1980s (Rusch et al. 1981; Solomon et al. 1981). A more recent study by Airapetian et al. (2016) investigated the production of N<sub>2</sub>O via SEPs for the early Earth. While our own star is comparably quiescent, many M-dwarfs show high activity, in which flares with energies comparable to the devastating Carrington event on Earth in the nineteenth century regularly occur up to a few times a day and orders of magnitude higher energetic events have been observed, e.g., for the herein studied M-dwarf AD LEO (Hawley & Pettersen 1991; Atri 2017).

Recently, potentially Earth-like planets have been found in the HZ around M-dwarfs (Proxima Cen b, LHS1140 b, and TRAPPIST-1 d-f), which may be studied in further detail with upcoming instrumentation on, e.g., the *James Webb Space Telescope* (JWST; Gardner et al. 2006) and E-ELT (Kasper et al. 2010). The impact of HEPs upon atmospheric chemistry needs further investigation. HEP-induced ion pairs react with molecular oxygen, molecular nitrogen, and water to cascade into nitrogen oxides (NO<sub>x</sub> = N+NO+NO<sub>2</sub>+NO<sub>3</sub>) and hydrogen oxides (HO<sub>x</sub> = H+HO+HO<sub>2</sub>) (Porter et al. 1976; Rusch et al. 1981; Solomon et al. 1981). NO<sub>x</sub> and HO<sub>x</sub> catalytically destroy ozone (O<sub>3</sub>) in the lower and upper stratosphere respectively (Crutzen 1970) but can form O<sub>3</sub> in the troposphere due to the so-called smog mechanism (Haagen-Smit 1952). They are stored and released from reservoir molecules such as HNO<sub>3</sub>, depending on, e.g., UV radiation and temperature. Recent model studies have shown that HEP-induced NO<sub>x</sub> and HO<sub>x</sub> from particle showers can indeed significantly reduce O<sub>3</sub> in an Earth-like atmosphere (Grenfell et al. 2012; Grießmeier

et al. 2016; Tabataba-Vakili et al. 2016). Production rates of around 1.27 NO<sub>x</sub> (Porter et al. 1976; Rusch et al. 1981) and 2.0 HO<sub>x</sub> (Solomon et al. 1981) per ion pair have been assumed in numerous atmospheric studies, but recent ion-chemistry studies by, e.g., Sinnhuber et al. (2012) and Verronen & Lehmann (2013) have pointed out that the uncertainties in these complex chemical coupling coefficients might be underestimated, especially when additionally taking into account negative ion chemistry. When conducting numerical studies of rocky planets around active M-dwarfs, such uncertainties can have a major impact on atmospheric abundances, including species influenced by biogenic processes. O<sub>3</sub>, for example, is removed catalytically by HO<sub>x</sub> and NO<sub>x</sub>. Also, CH<sub>4</sub> is usually removed by OH, a member of the HO<sub>x</sub> family.

Based on the above, the main motivation of this work is to compare the influence of different M-dwarf stellar flaring energies to that of the uncertainties in atmospheric NO<sub>x</sub>–HO<sub>x</sub> production efficiencies from incoming SEPs and show their impact on overall climate and spectral features in transit observations. In Section 2 we describe the models used for this work and motivate the modeled scenarios. In Section 3 we briefly describe our results, before discussing and comparing them to other relevant works in Section 4. Finally, in Section 5 we draw our conclusions.

## 2. Modeling Framework

### 2.1. Model Description

We investigate the influence of GCRs and SEPs from quiescent and flaring stars on atmospheric chemistry and potential biosignatures like O<sub>3</sub>, nitrous oxide (N<sub>2</sub>O), CH<sub>4</sub>, and chloromethane (CH<sub>3</sub>Cl). We build upon our stationary, global mean, cloud-free coupled climate-chemistry 1D model (Tabataba-Vakili et al. 2016), and update the cosmic rays’ propagation. First we compute the fluxes of primary HEPs, either GCRs or SEPs, that arrive at the top of our model atmosphere (TOA) at 6.6 Pa, using the magnetospheric model from Grießmeier et al. (2005, 2009). For Earth reference cases we take GCR and SEP measurements outside the Earth’s magnetic field for solar minimum conditions and use cutoff energies from Grießmeier et al. (2016) for the Earth’s magnetic shielding. For exoplanet runs we assume the same planetary magnetic field, but scale the HEP fluxes in all energy ranges as follows. For SEPs we use a simplified (conservative) inverse squared scaling with distance from the star (see Grenfell et al. 2012), hence neglect possible magnetic diffusion processes in the heliosphere, which would further increase the power-law exponent beyond 2.0 in the scaling of HEP fluxes for short-period orbits. We partly compensate for this effect with higher intrinsic HEP flux scenarios from the star (see model scenarios). For GCRs at exoplanets we adopt enhanced shielding modulation closer to the star, as described by Grießmeier et al. (2009). Once we have the TOA HEP fluxes, we use the Gaisser–Hillas approach (see, e.g., Tabataba-Vakili et al. 2016) to calculate the atmospheric ion-pair production profiles ( $Q$ ). In the case of the Earth, we can compare our approach to more sophisticated models like, e.g., the PLANETOCOSMICS Monte Carlo simulations of the cosmic-ray-induced secondary-particle showers performed by the Christian-Albrechts University (CAU) in Kiel, Germany (Fichtner et al. 2013), and find them to be in qualitatively good agreement, as shown in Figure 1. Consequently, these ion pairs

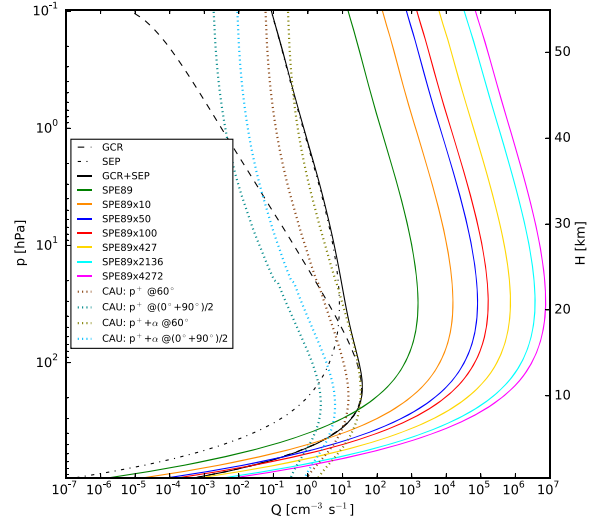


**Figure 1.** Ion-pair production rate ( $Q$ ) profiles for different HEP fluxes through the Earth’s atmosphere calculated in our model (solid). Coplotted are comparison profiles with PLANETOCOSMICS (CAU) (dotted line) for protons ( $p^+$ ) and alpha particles ( $\alpha$ ) and different locations on Earth (60° latitude, or the average of polar (90°) and equatorial (0°)). The black lines represent solar minimum conditions on Earth from our model, with air showers from GCRs (dashed line), SEPs (dotted line), and both combined (solid line). The other solid lines represent  $Q$ -profiles for a theoretical flaring Sun, shown in multiples of the SPE89 (green line), where fluxes in all energy ranges were multiplied by 10 (orange line), 50 (blue line), and 100 (red line).  $Q$ -profiles SPE89x427 (yellow line), SPE89x2136 (cyan line), and SPE89x4272 (magenta line), represent separate cases where Earth at 1 au would receive the same SEP flux density as a virtual Earth around AD LEO at a distance of 0.153 au with stellar flaring strengths of SPE89x10 (orange line), SPE89x50 (blue line), and SPE89x100 (red line), respectively.

cascade into NO<sub>x</sub> and HO<sub>x</sub> species. The NO<sub>x</sub>–HO<sub>x</sub> production efficiencies describing how many NO<sub>x</sub> and HO<sub>x</sub> are subsequently produced per cosmic-ray-induced ion pair are widely used in ion-chemistry models with values that were calculated by Rusch et al. (1981) and Solomon et al. (1981). These values are based on an Earth atmospheric composition assuming ionization to be directly proportional to ionization cross sections, which themselves are taken to be independent of pressure and temperature. Note that negative ion chemistry was taken into account much later by Verronen & Lehmann (2013), which further influences the NO<sub>x</sub>–HO<sub>x</sub> production efficiencies. In our study we made the cosmic-ray air-shower parameters in our climate-chemistry model flexible so that we could analyze the influence of the uncertainties of these chemical production efficiencies  $f_{\text{NO}_x}$  and  $f_{\text{HO}_x}$  on potential biosignatures compared with the impact of potential stellar flaring scenarios.

Lastly, transit spectra, i.e., transmission spectra ( $\mathcal{T}(\lambda)$ ) are calculated using the “Generic Atmospheric Radiation Line-by-line Infrared Code” GARLIC (Schreier et al. 2014) that has been extensively verified (e.g., Schreier et al. 2018a) and validated (Schreier et al. 2018b), a FORTRAN90 version of MIRART/SQUIRRL (see, e.g., von Clarmann et al. 2003; Melsheimer et al. 2005) used by (e.g., Rauer et al. 2011; Grießmeier et al. 2016; Tabataba-Vakili et al. 2016). In this study we use GARLIC with HITRAN2012 (Rothman et al. 2013) along with the “CKD” continua (Clough et al. 1989) for calculations of line absorption and Rayleigh scattering parameterization from Snee & Ubachs (2005),



Marcq et al. (2011), Murphy (1977). We use temperature, pressure, water vapor, and concentration profiles of those species (23 in total)<sup>4</sup>, which are present in both HITRAN2012 as well as in our climate-chemistry model. The corresponding transit depths  $\delta(\lambda)$  are calculated using:

$$\delta(\lambda) = \left( \frac{r_p + h(\lambda)}{r_s} \right)^2, \quad (1)$$

where  $r_p$  is the planetary radius,  $r_s$  the stellar radius, and  $h(\lambda) = \sum_i (1 - T_i(\lambda)) \Delta h_i$  is the effective height of the atmosphere for a given wavelength.

## 2.2. Model Scenarios

In this study we focus on virtual Earth-like planets around the active red M4.5 dwarf star AD Leonis, hereafter AD LEO. In doing so, we place a virtual Earth (1 g planet, 1 atm surface pressure, albedo of 0.21—tuned to obtain global mean surface temperatures of 288.15 K on Earth) in the HZ around AD LEO in two different positions, starting with the Earth US standard 1976 reference atmosphere (COESA) and allow the climate and chemistry to relax into a new steady-state solution. First we start with an Earth around the Sun reference case, using the incoming stellar electromagnetic flux based on Gueymard (2004). To be comparable to earlier studies we next place the planet at a distance of 0.153 au around AD LEO, where the total stellar irradiance (TSI) equals the amount the Earth receives from the Sun before moving it further outward to 0.161 au (0.9 TSI<sub>⊕</sub>) around AD LEO where it receives only 90% of the Earth's TSI. In all AD LEO cases we use the electromagnetic spectrum based on Segura et al. (2005). The former approach of 1.0 TSI<sub>⊕</sub> together with an Earth-like relative humidity profile (Manabe & Wetherald 1967) leads to surface temperatures larger than 288 K (see also the scaling arguments in Segura et al. 2003 and references therein). Various modeling studies, including early 1D studies (e.g., Cess 1976; Kasting & Ackerman 1986), as well as more recent 3D studies (e.g., Leconte et al. 2013; Popp et al. 2015; Godolt et al. 2016; Fujii et al. 2017) have argued that for increased surface temperatures the relative humidity profile may differ from that of the Earth (e.g., Manabe & Wetherald 1967), which we use here and has also been assumed in previous studies (Segura et al. 2010; Rauer et al. 2011; Grenfell et al. 2012; Rugheimer et al. 2015a). Other studies, e.g., Kasting et al. (1993) and Kopparapu et al. (2013), assumed a fully saturated atmosphere and found that an Earth-like planet around AD LEO would be close to or even inside the inner edge of the HZ. This assumption of a fully saturated atmosphere may however overestimate the water concentrations, as shown by 3D studies, see, e.g., Leconte et al. (2013), Yang et al. (2014), and Kopparapu et al. (2016). The 3D modeling results by Shields et al. (2013) show that an Earth-like planet around AD LEO receiving 90% insolation may have similar surface temperatures as the Earth around the Sun. Hence, for this case, the assumption of an Earth-like relative humidity profile to determine the water profile in the 1D model seems to be better justified and in line with 3D model results (see, e.g., Godolt et al. 2016). Whereas the approach of placing the planet at 0.161 au (0.9 TSI<sub>⊕</sub>) around AD LEO is

model dependent, it has the advantage of lying closer to Earth conditions, where our model is validated.

For each of the above cases we investigate various stellar activity scenarios for the HEP shower through the atmosphere, all based on measurements on Earth, and scaled for AD LEO according to the abovementioned functions. We start with the GCR and SEP stellar-minimum background cases, as described above. Then we compare various stellar flaring scenarios, all based on GOES 6 and 7 measurements of the medium-hard spectrum flare that hit the Earth in 1989 (Smart & Shea 2002), hereafter SPE89. We assume quasi-constant flaring conditions, i.e., a flaring frequency faster than the relevant chemical response timescales to investigate long-term climate and composition effects of such violent environments rather than short-term variations. We justify our assumption because, e.g., the Earth's mean O<sub>3</sub> column does not change significantly with the day–night cycle, whereas flaring on AD LEO has been extensively measured to be in the order of a few per day, with event energies exceeding those of the largest recorded events on Earth ( $\sim 10^{32}$  erg; Atri 2017). Additionally, from the *Kepler* survey we have multiple M-star observations with flaring energies of up to  $10^{36}$  erg and frequencies of up to 100 times those of G-stars (Maehara et al. 2012; Shibayama et al. 2013; Candelaresi et al. 2014). With this in mind, we model higher flaring scenarios by multiplying the SPE89 particle fluxes in all energy ranges by 10, 50, and 100. For AD LEO runs this adds to the ( $\sim 40\times$ ) enhanced flux density due to proximity to the host star. This means that our virtual Earth at a distance of 0.153 au around an AD LEO flaring with 100 times enhanced SPE89 strength, hereafter SPE89x100, actually receives 4,272 times the SEP flux than Earth received during SPE89. For comparison we also investigated an Earth in its current position receiving the same SEP flux densities and added these three scenarios as separate cases only for the Earth around the Sun cases, flaring with SPE89x427, SPE89x2136, and SPE89x4272 to compare with the AD LEO SPE89x10, SPE89x50, and SPE89x100 cases, respectively.

Lastly, for all of the above scenarios, we perform our parameter study and vary the NO<sub>x</sub>–HO<sub>x</sub> production efficiencies per cosmic-ray-induced ion pair ( $Q$ ) within their plausible parameter ranges (Rusch et al. 1981; Solomon et al. 1981; Sinnhuber et al. 2012; Verronen & Lehmann 2013) for every combination of  $f_{\text{NO}_x} = [1.0, 1.27, 1.44, 1.6, 2.0]$  and  $f_{\text{HO}_x} = [0.0, 1.0, 2.0]$ . The full set of model scenarios can be seen in Table 1.

We would like to remark that in the thought experiment of an Earth-like planet around AD LEO we assume that life would still be present in the form of biogenic surface emissions as on Earth even in the highest flaring cases, despite the hostility from its host star. Also we assume Earth's evolutionary history, and a mean global daytime average, which might not strictly hold in the case of tidal locking. We do this for the sake of simplicity to study the impact of HEPs alone.

## 3. Results

Figure 2 shows the atmospheric temperature profiles for our three planetary positions, the Earth around the Sun (black line), the virtual Earth around AD LEO at a distance of 0.153 au with a TSI = 1.0 TSI<sub>⊕</sub> (red line), and the virtual Earth around AD LEO at 0.161 au with a TSI = 0.9 TSI<sub>⊕</sub> (blue line), all with a scaled GCR background. The reference is always the GCR background, but a solar minimum SEP background leads to

<sup>4</sup> Atmospheric species used for transmission spectra in GARLIC are OH, HO<sub>2</sub>, H<sub>2</sub>O<sub>2</sub>, H<sub>2</sub>CO, H<sub>2</sub>O, H<sub>2</sub>, O<sub>3</sub>, CH<sub>4</sub>, CO, N<sub>2</sub>O, NO, NO<sub>2</sub>, HNO<sub>3</sub>, ClO, CH<sub>3</sub>Cl, HOCl, HCl, ClONO<sub>2</sub>, H<sub>2</sub>S, SO<sub>2</sub>, O<sub>2</sub>, CO<sub>2</sub>, and N<sub>2</sub>.

**Table 1**  
Model Scenarios in This Work

Star	Distance [au]	HEPs	$f_{\text{NOx}}$	$f_{\text{HOx}}$
Sun	1.0	GCR		
		SEP		
		SPE89	1.0	
		SPE89x10	1.27	0.0
		SPE89x50	1.44	1.0
		SPE89x100	1.6	2.0
		SPE89x427	2.0	
		SPE89x2136		
		SPE89x4272		
AD LEO	0.153 0.161	GCR	1.0	
		SEP	1.27	0.0
		SPE89	1.44	1.0
		SPE89x10	1.6	2.0
		SPE89x50	2.0	
		SPE89x100		

**Note.** “Star” indicates here the host star of our planet, “distance” shows the orbital distance of our planet to its host star, and “HEP” is the energetic particle bombardment on our planet.  $f_{\text{NOx}}$  and  $f_{\text{HOx}}$  are the chemical air-shower production efficiencies for NOx and HOx production per ion pair, respectively, studied for each configuration.

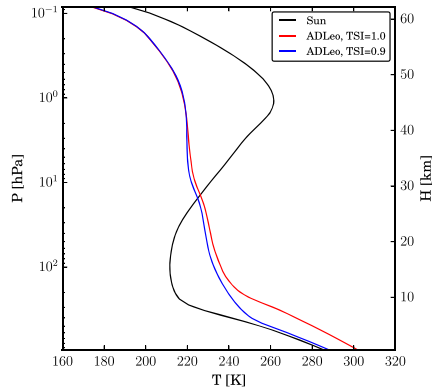


**Figure 2.** Temperature profiles for the Earth around the Sun case (black line), the Earth around AD LEO at a distance of 0.153 au where  $\text{TSI} = 1.0 \text{ TSI}_{\oplus}$  (red line), and the Earth around AD LEO at 0.161 au or  $0.9 \text{ TSI}_{\oplus}$  (blue line), all with a GCR background.

indistinguishable results for our analysis and is therefore not shown in this work. Until stated otherwise, we show results for the chemical air-shower production efficiencies  $f_{\text{NOx}} = 1.27$  and  $f_{\text{HOx}} = 2.0$ , in order to be comparable to other works. For the M-dwarf case at  $1.0 \text{ TSI}_{\oplus}$  (red line), we calculate an increase in surface temperature to over 300 K mainly due to an enhanced methane greenhouse as found in previous works (e.g., Segura et al. 2005). In addition the stratospheric temperature inversion is essentially nonexistent mainly because of the lower near-UV flux compared with the Sun, which reduces  $\text{O}_3$  abundance and heating, as already discussed in previous studies (Segura et al. 2010; Rauer et al. 2011). On moving the planet further away from AD LEO to 0.161 au ( $0.9 \text{ TSI}_{\oplus}$ ), the surface temperature in our model reaches an Earth-like 289 K, similar to the results of Shields et al. (2013), also lacking the stratospheric temperature inversion. The

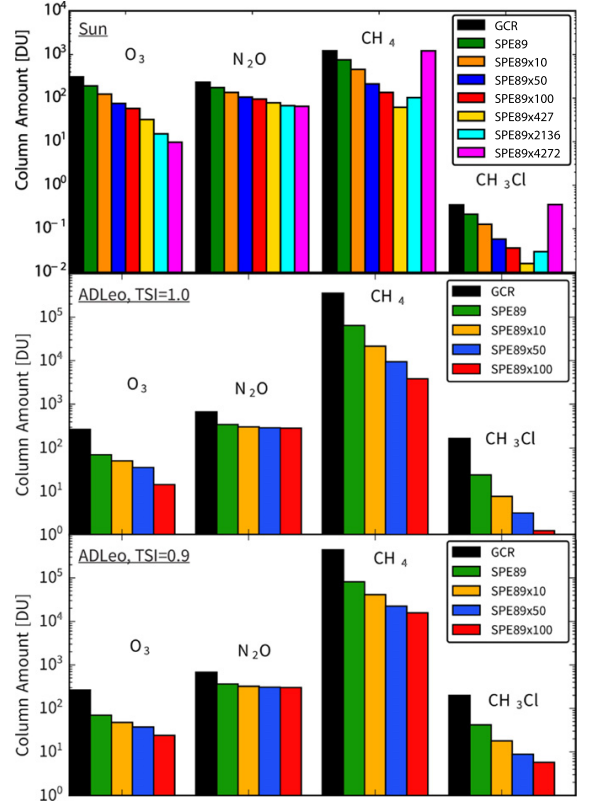


**Figure 3.** Atmospheric column amounts for  $\text{O}_3$ ,  $\text{N}_2\text{O}$ ,  $\text{CH}_4$ , and  $\text{CH}_3\text{Cl}$ , presented in Dobson units ( $1 \text{ DU} = 2.687 \times 10^{16} \text{ molec. cm}^{-2}$ ) for the Earth around the Sun (top), the Earth around AD LEO at  $\text{TSI} = 1.0 \text{ TSI}_{\oplus}$  (middle), and the Earth around AD LEO at  $0.9 \text{ TSI}_{\oplus}$  (bottom) cases. In each panel we show model runs for the GCR background (black), stellar flaring scaled from the SPE89 on Earth (green), and the enhanced flaring runs SPE89 multiplied by 10 (orange), 50 (blue), and 100 (red). All particle fluxes received by the planet are scaled from the observed value (at 1 au) to the appropriate planetary orbital distance. The results for the solar minimum SEP background are indistinguishable from the GCR background, and therefore are not shown. The upper panel additionally shows the three cases (SPE89x427 (yellow), SPE89x2136 (cyan), and SPE89x4272 (magenta)) where the Earth around the Sun case would receive the same SEP flux density from the Sun as the virtual Earth around AD LEO at  $\text{TSI} = 1.0 \text{ TSI}_{\oplus}$  (middle panel) receives from an AD LEO flaring with SPE89x10 (orange), SPE89x50 (blue), and SPE89x100 (red) strength, respectively (see Section 2 for further explanation).

position of the tropopause (i.e., the end of the convective regime) in these two AD LEO runs changes significantly from 11 km for the  $1.0 \text{ TSI}_{\oplus}$  case to 5.5 km for the  $0.9 \text{ TSI}_{\oplus}$  case, compared with  $\sim 8.5 \text{ km}$  for our Earth around the Sun case.

Figure 3 shows atmospheric column amounts of  $\text{O}_3$ ,  $\text{N}_2\text{O}$ ,  $\text{CH}_4$ , and  $\text{CH}_3\text{Cl}$ , in Dobson units ( $1 \text{ DU} = 2.687 \times 10^{16} \text{ molec. cm}^{-2}$ ) for the same planet–star configurations, as shown in Figure 2. For each configuration we compare runs with different HEP conditions and show the GCR background run (black line) as a reference. We compare different stellar flaring strengths by multiplying the measured fluxes from SPE89 and scaling the incoming particle flux to the planet’s position for the AD LEO runs. The different flaring strength cases vary from SPE89x1 to SPE89x100 for the AD LEO runs and from SPE89x1 to SPE89x4272 for the Earth around the Sun runs (see Figure 3). As expected, with increasing flaring

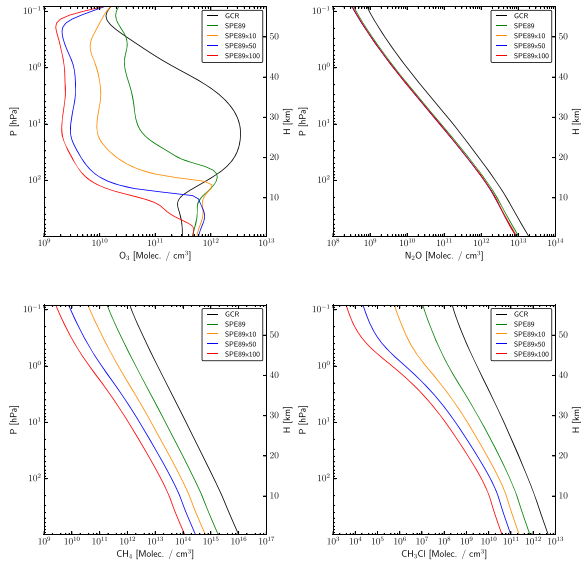


**Figure 4.** Molecular profiles for our virtual Earth around AD LEO at 1.0  $\text{TSI}_{\oplus}$  as shown in Figure 3 (middle panel) and by the red line in Figure 2. The ozone profile (upper left),  $\text{N}_2\text{O}$  (upper right), methane (lower left), and  $\text{CH}_3\text{Cl}$  profile (lower right) are each compared for the different flaring scenarios from Figure 3 (middle).

strength the  $\text{O}_3$  column is depleted, similar to results of, e.g., Grenfell et al. (2012) and Tabataba-Vakili et al. (2016). The same holds qualitatively for  $\text{N}_2\text{O}$  although note that we calculate here a “saturation” behavior, i.e., where increasing flaring energy has no further effect upon the  $\text{N}_2\text{O}$  column. Both the  $\text{CH}_4$  and  $\text{CH}_3\text{Cl}$  columns also follow the same trend of depletion, e.g., from  $\sim 1.6$  ppmv Earth tropospheric  $\text{CH}_4$  concentrations down to  $\sim 0.2$  ppmv of tropospheric  $\text{CH}_4$  in the SPE89x100 case. An exception presents the interesting increase in  $\text{CH}_4$  and  $\text{CH}_3\text{Cl}$  for our most active Sun cases (upper panel), SPE89x2136 (cyan) and SPE89x4272 (magenta), which were added for comparison purposes with the AD LEO cases and which we will discuss in Section 4. When we compare the GCR background runs for the Earth around the Sun case with the AD LEO case, we see an increase of two orders of magnitude in the  $\text{CH}_4$  and  $\text{CH}_3\text{Cl}$  column amounts around AD LEO due to slower  $\text{O}_3$  photolysis resulting in lower OH densities, as discussed in Segura et al. (2005).

In order to investigate the column behavior in Figure 3, Figure 4 shows the atmospheric profiles in molecules  $\text{cm}^{-3}$  in the case of our virtual Earth around AD LEO at 1.0  $\text{TSI}_{\oplus}$  as shown in Figure 3 (middle panel). The color coding for different flaring strengths is the same as shown in Figure 3. We calculate the stratospheric ozone loss (upper left) with the increasing influx of SEPs, compared with a quiescent AD LEO (black line), as well as increased ozone in the troposphere, which is discussed in Section 4. The  $\text{N}_2\text{O}$  (upper right) on the other hand, responds only weakly to increasing flare strength, decreasing from  $\sim 800$  ppbv ( $2 \times 10^{13}$  molec.  $\text{cm}^{-3}$ ) (GCR case) to  $\sim 250$  ppbv ( $9 \times 10^{12}$  molec.  $\text{cm}^{-3}$ ) (SPE89x100) in the lower atmosphere. Methane and  $\text{CH}_3\text{Cl}$  (lower row) both feature lower concentrations throughout the whole atmosphere with increasing flare strength. The greatly enhanced surface concentration of  $\sim 400$  ppmv ( $10^{16}$  molec.  $\text{cm}^{-3}$ )  $\text{CH}_4$  and  $\sim 200$  ppbv

( $5 \times 10^{12}$  molec.  $\text{cm}^{-3}$ )  $\text{CH}_3\text{Cl}$  in the AD LEO GCR case (compared with  $\sim 1.6$  ppmv ( $3.9 \times 10^{13}$  molec.  $\text{cm}^{-3}$ )  $\text{CH}_4$  and  $\sim 0.5$  ppbv ( $1.2 \times 10^{10}$  molec.  $\text{cm}^{-3}$ )  $\text{CH}_3\text{Cl}$  Earth tropospheric concentrations) decreases in our simulations down to  $\sim 5$  ppmv ( $10^{14}$  molec.  $\text{cm}^{-3}$ ) of  $\text{CH}_4$  and  $\sim 2$  ppbv ( $4 \times 10^{10}$  molec.  $\text{cm}^{-3}$ )  $\text{CH}_3\text{Cl}$  for the AD LEO SPE89x100 case.

In order to investigate the methane response, whose main sinks are OH (lower to mid atmosphere) and Cl (upper atmosphere), we analyze chlorine containing species in our model atmospheres, as shown in Figure 5. For all our three planetary configurations we compare background GCR runs (black line) with the 50 times enhanced SPE89 flaring cases (blue line). The solid lines represent total chlorine ( $\text{Cl}_y$ ), i.e., the sum of all chlorine-bearing species, which increases by two orders of magnitude in molecules  $\text{cm}^{-3}$  when we go from the Earth to an Earth-like planet around AD LEO. For all cases the majority of stratospheric chlorine is in the form of HCl (dashed line), while in the upper stratosphere, atomic chlorine, Cl, also reaches significant levels above 40 km. This is the region where  $\text{CH}_4$  production becomes controlled by Cl (dashed-dotted line), instead of OH, which is the major methane destroying reaction below around 40 km, as discussed in Section 4.  $\text{ClONO}_2$  (dotted line) is only the dominant chlorine-bearing species for a small fraction of the Earth’s mid-stratosphere for quiescent solar cases.

Figure 6 compares the influence of varying the chemical air-shower production efficiencies  $f_{\text{NO}_x}$  and  $f_{\text{HO}_x}$  for the different flaring cases for the Earth (top), the 1.0  $\text{TSI}_{\oplus}$  AD LEO case (middle), and the 0.9  $\text{TSI}_{\oplus}$  AD LEO case (bottom). We show the resulting ozone profiles (left), temperature (middle), and the UVB environment profile in  $\text{W/m}^2$  (right). Shades of green represent the SPE89 flaring cases for different SEP-induced  $\text{NO}_x$ – $\text{HO}_x$  production efficiencies; shades of orange represent the same runs for 10 times enhanced flaring; and shades of blue represent the 100 times enhanced flaring cases, respectively. Within the green, orange, and blue scenarios, the darkest colors represent the lowest parameter values  $f_{\text{NO}_x} = 1.0$  and  $f_{\text{HO}_x} = 0.0$ , while the lightest colors represent the highest values of  $f_{\text{NO}_x} = 2.0$  and  $f_{\text{HO}_x} = 2.0$ , with all other combinations in between. For all quiescent star (GCR) cases (black line) all modeled combinations of  $f_{\text{NO}_x}$  and  $f_{\text{HO}_x}$  result in virtually indistinguishable profiles, hence only the cases of  $f_{\text{NO}_x} = 1.27$   $\text{NO}_x/Q$  and  $f_{\text{HO}_x} = 2.0$   $\text{HO}_x/Q$ , as used by other works, are shown. For the Earth around the Sun case, the results suggest that the influence of changing the  $\text{NO}_x$ – $\text{HO}_x$  production efficiencies is less important than varying the Sun’s flaring strength, i.e., the amount of incoming SEPs. In the AD LEO cases, on the other hand,  $f_{\text{NO}_x}$  and  $f_{\text{HO}_x}$  influence at least the atmospheric temperature and ozone profiles significantly, up to a point where for the 0.9  $\text{TSI}_{\oplus}$  case, a high flaring AD LEO (50 times enhanced SPE89) can lead to an atmospheric temperature profile similar to a quiescent AD LEO case, if the chemical air-shower parameters through the planet’s atmosphere are  $f_{\text{NO}_x} = 2.0$  and  $f_{\text{HO}_x} = 0.0$ . In contrast with  $f_{\text{NO}_x} = 2.0$  and  $f_{\text{HO}_x} = 2.0$ , the temperature may be reduced by up to 40 K throughout most of the stratosphere.

To investigate whether the abovementioned differences in stratospheric temperature and composition due to different  $\text{NO}_x$ – $\text{HO}_x$  production efficiencies in the SPE89x50 strong flaring AD LEO cases with a planet at 0.9  $\text{TSI}_{\oplus}$  (bottom row of Figure 6) have any distinguishable effect on atmospheric spectra, Figure 7 shows the corresponding transit depths  $\delta(\lambda)$ .



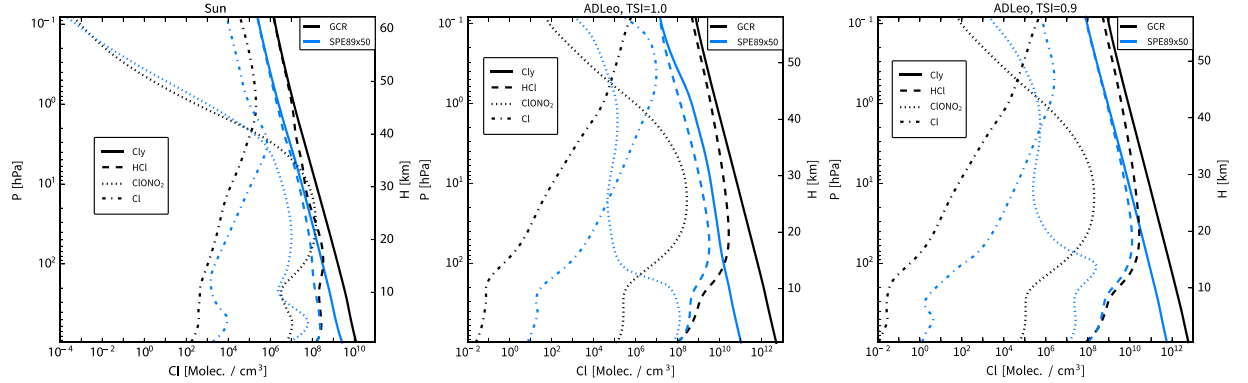


**Figure 5.** Atmospheric profiles of several species containing chlorine for the Earth around the Sun case (left), AD LEO at 1.0  $TSI_{\oplus}$  (middle), and AD LEO at 0.9  $TSI_{\oplus}$  (right). For each case we compare runs with the GCR background (black line) with runs for the 50 times enhanced SPE89 flaring cases (blue line). We show the sum of all chlorine containing species (Cly) in our model (solid line), HCl (dashed line),  $ClONO_2$  (dotted line), and atomic Cl (dashed-dotted line).

The spectra are shown with constant spectral resolution  $R = \lambda / \Delta\lambda = 100$  over the wavelength range of 0.3–30  $\mu\text{m}$ . This corresponds to, e.g., one mode of the near-infrared spectrograph NIRSpec on board the upcoming *JWST* mission. We show the contribution of the planetary body, i.e., without the atmospheric contribution (dashed-black line), which we calculate to be 551.3 ppm. Similar to before, our reference case is the GCR background (black line) with  $f_{NOx} = 1.27$  and  $f_{HOx} = 2.0$ , because runs for all the above described combinations of  $f_{NOx}$  and  $f_{HOx}$  for the GCR or SEP background cosmic rays result in qualitatively identical atmospheric concentration profiles for all our modeled molecules. First, we compare this to the SPE89x50 run for  $f_{NOx} = 2.0$  and  $f_{HOx} = 0.0$  (dashed-blue line), which results in an almost indistinguishable stratospheric temperature profile. We see the destruction of ozone due to flaring in the weakened 9.6  $\mu\text{m}$  absorption band as well as reduced absorption by water and methane in the near-infrared (1–2  $\mu\text{m}$ ). We also see  $HNO_3$  absorption above 10  $\mu\text{m}$  becoming visible. The second comparison in Figure 7 is with the SPE89x50 run for  $f_{NOx} = 2.0$  and  $f_{HOx} = 2.0$  (light blue line). Here we see even stronger suppression of the near-infrared water and methane features, and even stronger  $HNO_3$  absorption in the far-infrared. There are also new  $HNO_3$  features visible around 17 and 21  $\mu\text{m}$ . The 9.6  $\mu\text{m}$   $O_3$  absorption band is a little less reduced than in the  $f_{HOx} = 0.0$  case, due to  $NOx$ – $HOx$  reactions, which limit the  $NOx$  sink for  $O_3$ , similar to Tabataba-Vakili et al. (2016). All three runs clearly show the slope due to Rayleigh scattering toward the visible and into the ultraviolet.

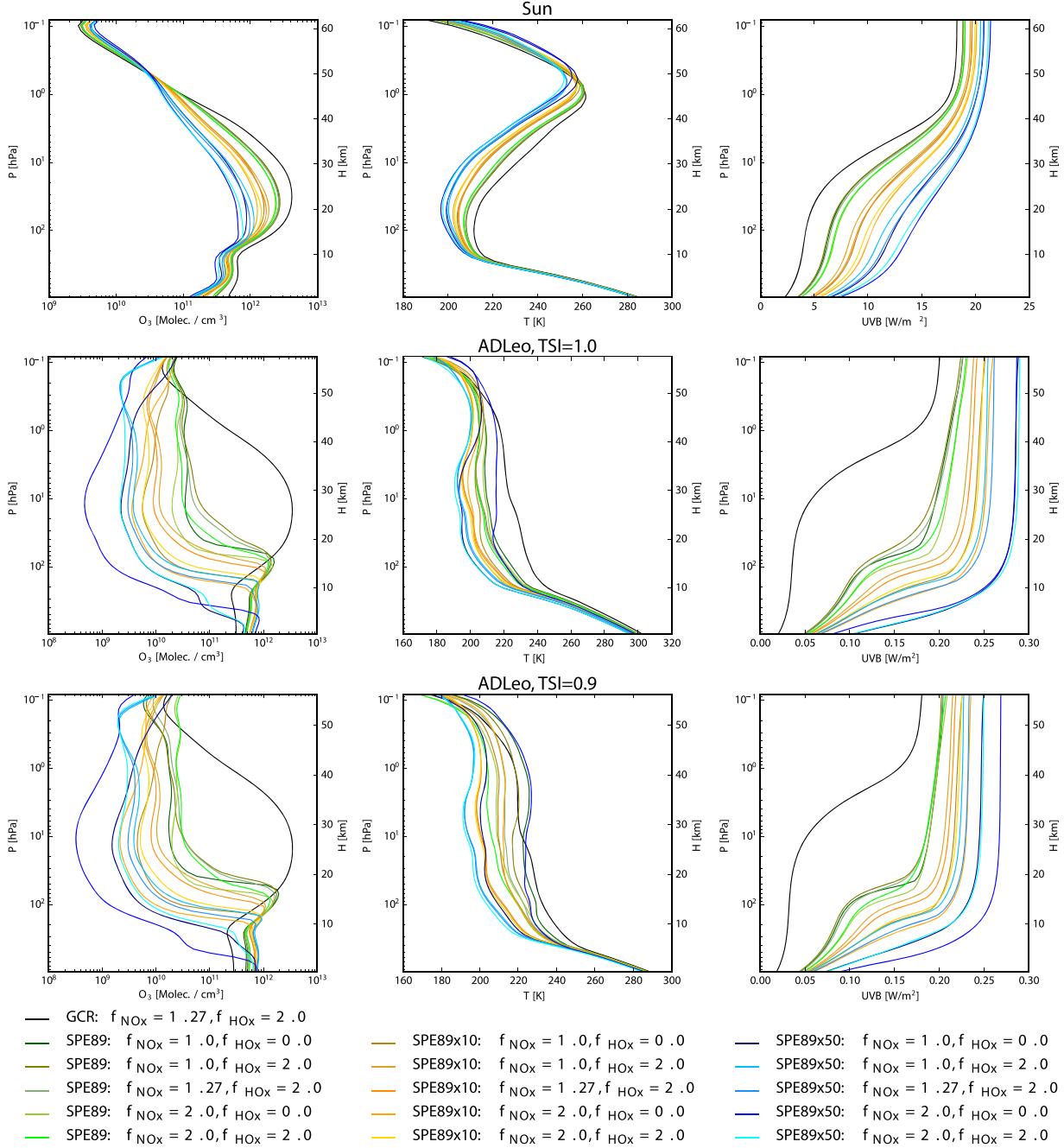
To further explain the differences in the transit spectra of Figure 7, Figure 8 shows the corresponding atmospheric profiles of temperature,  $O_3$ ,  $CH_4$ ,  $H_2O$ ,  $N_2O$ , and  $HNO_3$  for the three AD LEO runs at 0.9  $TSI_{\oplus}$  using the same color scheme ( $O_3$  and temperature are also shown and explained in Figure 6). Compared with the GCR case (black line) with a fairly constant  $CH_4$  concentration of  $\sim 500$  ppmv ( $1.3 \times 10^{16}$  molec.  $\text{cm}^{-3}$ ) throughout our model atmosphere  $CH_4$  is reduced throughout the whole atmosphere in both SPE89x50 cases,  $f_{NOx} = 2.0$  and  $f_{HOx} = 0.0$  (dashed-blue line), resulting in  $\sim 60$  ppmv ( $1.4 \times 10^{15}$  molec.  $\text{cm}^{-3}$ )  $CH_4$ , and  $f_{NOx} = 2.0$  and  $f_{HOx} = 2.0$  (light blue) leaving  $\sim 20$  ppmv ( $5 \times 10^{14}$  molec.  $\text{cm}^{-3}$ )  $CH_4$ . The  $H_2O$  profiles show a similar behavior, although the  $H_2O$  abundance is clearly less affected by the HEPs in the SPE89x50

$f_{HOx} = 0.0$  case, with still  $\sim 60$ –100 ppmv ( $\sim 10^{14}$  molec.  $\text{cm}^{-3}$ ) in the mid and upper atmosphere than in the SPE89x50  $f_{HOx} = 2.0$  case leaving only  $\sim 2$ –20 ppmv ( $\sim 2 \times 10^{12}$  molec.  $\text{cm}^{-3}$ ) in the mid and upper atmosphere, similar to the respective temperature profiles. Again,  $N_2O$  shows only weak responses to both flaring and  $f_{HOx}$  variation. The  $HNO_3$  profiles in both SPE89x50 cases are greatly enhanced, as seen in the spectra in Figure 7. In the lower- and mid-stratosphere  $HNO_3$  is further increased in the  $f_{HOx} = 2.0$  case peaking at  $\sim 8$  ppmv ( $2 \times 10^{13}$  molec.  $\text{cm}^{-3}$ ), which is about 10,000 times the modern Earth’s atmospheric concentration compared with the  $f_{HOx} = 0.0$  case resulting in only  $\sim 90$  ppbv ( $\sim 3$ – $5 \times 10^{11}$  molec.  $\text{cm}^{-3}$ )  $HNO_3$ , which explains the additional spectral  $HNO_3$  features in Figure 7.

#### 4. Discussion

In this study we analyze how increased HEP fluxes associated with active M-stars like AD LEO, influence the atmospheric chemistry and climate of Earth-like planets in comparison to the impact of chemical production efficiencies. Our special focus lies on biosignatures, i.e., species which on Earth are associated with life. Our results in Figure 2 (red line) show that the surface temperature would increase by over 12 K on placing a virtual Earth-like planet at 1.0  $TSI_{\oplus}$  around AD LEO when assuming an Earth-like relative humidity profile. However, such a temperature increase would likely change the hydrological cycle leading to a strong water feedback, as shown for a planet around K-stars by Godolt et al. (2015). This could place such planets outside the HZ as suggested by, e.g., Kopparapu et al. (2013). Assuming a planet around AD LEO that receives only 90%  $TSI_{\oplus}$  (blue line), we obtain a moderate surface temperature of 289 K, which is in good agreement with the 3D model results of Shields et al. (2013).

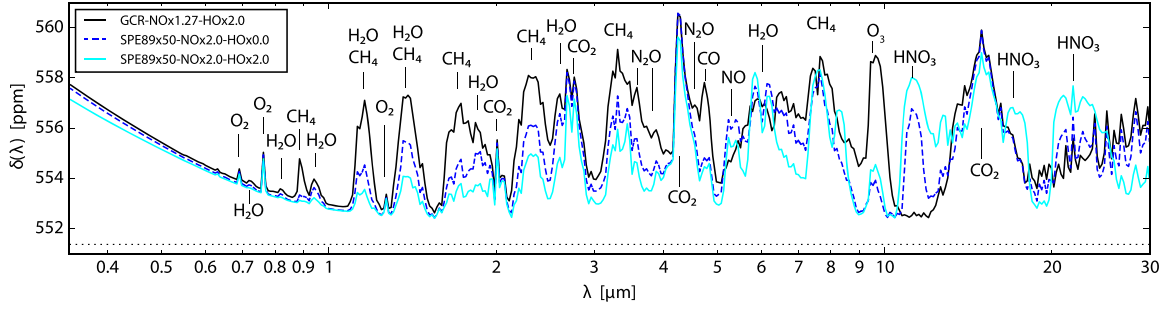
The results for different flaring strengths of the same star (Figure 3) suggest stratospheric  $O_3$  destruction with increasing HEP fluxes due to increased catalytic destruction from mainly  $NOx$ . All our runs for the Sun and AD LEO cases show this trend. As indicated in Figure 6, the effect of increasing flaring energy upon  $O_3$  is different for the Earth, compared with an Earth-like planet around AD LEO. While the Earth would moderately lose  $O_3$  in the troposphere and stratosphere, around AD LEO the impact on stratospheric  $O_3$  is much fiercer, while in the troposphere the enhanced smog  $O_3$  from  $NOx$  (see



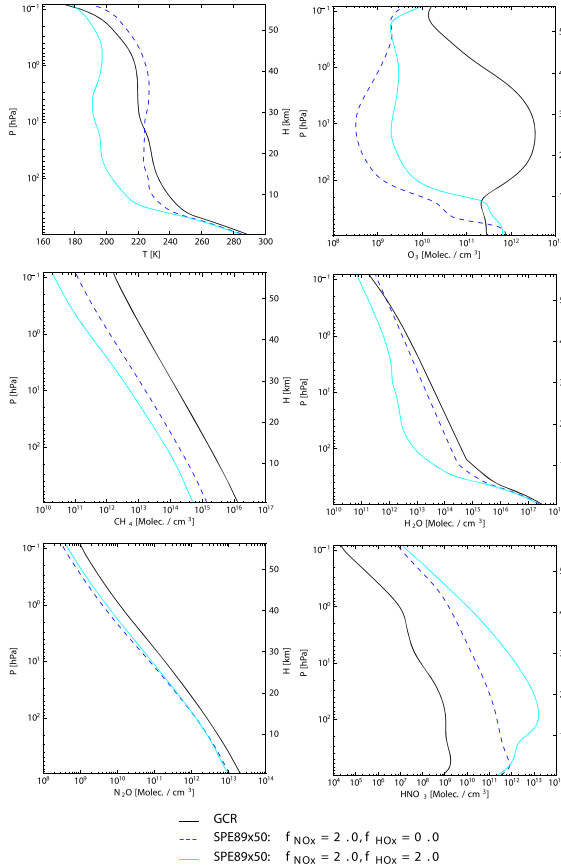
**Figure 6.** The influence of chemical NO<sub>x</sub>–HO<sub>x</sub> fractionation of HEP-induced ion pairs for the flaring scenarios from Figure 3, except the highest flaring cases SPE89x100. The rows show the cases for the Earth around the Sun (top three panels), the Earth around AD LEO at 1.0 TSI<sub>⊕</sub> (middle three panels), and the Earth around AD LEO at 0.9 TSI<sub>⊕</sub> (bottom three panels). The columns show O<sub>3</sub> (left), temperature (middle), and UVB (right). The color ranges represent the GCR reference case (black), SPE89 (green colors), SPE89 × 10 (orange colors), and SPE89 × 50 (blue colors). The different shades of green, orange, and blue, represent model runs with different NO<sub>x</sub>–HO<sub>x</sub> fractionation for the same respective HEP case.

Figure 9 for smog O<sub>3</sub>) together with much lower stellar UVB input, i.e., less tropospheric O<sub>3</sub> destruction by photolysis, leads to enhanced tropospheric O<sub>3</sub> abundance. This behavior was confirmed by a detailed analysis of reaction rates of sources and sinks and related pathways. For a theoretically flaring Sun

lower stratospheric O<sub>3</sub> abundance yields higher UVB radiation in the troposphere, i.e., higher tropospheric O<sub>3</sub> photolysis rates, limiting the smog O<sub>3</sub> build-up. For AD LEO the much lower UVB radiation cannot impact tropospheric smog O<sub>3</sub> build-up efficiently. In the high flaring cases of each host star, however,



**Figure 7.** Modeled transit depths  $\delta(\lambda)$  in parts per million over the wavelength  $\lambda$  ( $R = 100$ ) for a virtual Earth around AD LEO at  $0.9 \text{ TSI}_{\oplus}$ . Shown are three runs from the bottom row of Figure 6: GCR (black line), and the last two runs of the high flaring case SPE89x50: one with  $f_{\text{NOx}} = 2.0$  and  $f_{\text{HOx}} = 0.0$  (dashed-blue line) that shows a similar temperature profile to the GCR case and one with  $f_{\text{NOx}} = 2.0$  and  $f_{\text{HOx}} = 2.0$  (light-blue line) that shows significantly reduced stratospheric temperatures. The dotted-black line at the bottom represents the transit depth for the virtual planet without atmosphere (551.3 ppm).



**Figure 8.** Atmospheric profiles of temperature,  $\text{O}_3$ ,  $\text{CH}_4$ ,  $\text{H}_2\text{O}$ ,  $\text{N}_2\text{O}$ , and  $\text{HNO}_3$  for a virtual Earth around AD LEO at  $0.9 \text{ TSI}_{\oplus}$ . Shown are the three runs analyzed in Figure 7: GCR (black line), and the last two runs of the high flaring case SPE89x50:  $f_{\text{NOx}} = 2.0$  and  $f_{\text{HOx}} = 0.0$  (dashed-blue line) and  $f_{\text{NOx}} = 2.0$  and  $f_{\text{HOx}} = 2.0$  (light-blue line).

our analysis shows that tropospheric  $\text{O}_3$  undergoes a transition from a smog-dominated build-up to a so-called titration limited regime, where the single reaction  $\text{NO} + \text{O}_3 \rightarrow \text{NO}_2 + \text{O}_2$  dominates atmospheric  $\text{O}_3$  destruction, i.e., efficiently limits  $\text{O}_3$  build-up.

The main sink for nitrous oxide ( $\text{N}_2\text{O}$ ) is photolysis, which is generally much slower than  $\text{O}_3$  photolysis. Despite decreased  $\text{O}_3$  for increasing flare energies (Figures 3 and 4), increased UVB,  $\text{N}_2\text{O}$  values nevertheless appear to “saturate.” We can further see this in the UVB profiles in Figure 6: where stratospheric  $\text{O}_3$  is significantly reduced, UVB absorption in the stratosphere is negligible. The dependence on  $\text{O}_3$  is clearly visible in the AD LEO cases between 18 and 20 km, where  $\text{O}_3$  shows a strong decrease with height. Only the increase in atmospheric density in the troposphere leads to a significant UVB absorption, where the abundance of  $\text{O}_3$  is low.  $\text{N}_2\text{O}$  is never significantly destroyed by UVB in our study, even where  $\text{O}_3$  is least abundant across all our model runs.  $\text{N}_2\text{O}$  photolysis is already slower in the stratosphere than  $\text{O}_3$  photolysis. Additionally eddy diffusion might redistribute  $\text{N}_2\text{O}$  faster than it is photolytically destroyed by UVB and the  $\text{N}_2\text{O}$  reaction with  $\text{O}(^1\text{D})$  becomes  $\text{O}(^1\text{D})$  starved and hence is significantly reduced where  $\text{O}_3$  abundance is lower. Such effects together may explain the  $\text{N}_2\text{O}$  behavior over a wide variety of flaring conditions. See Figure 9 for an overview.

Due to the direct increase of OH (an important  $\text{CH}_4$  sink), one would also expect a steady reduction of  $\text{CH}_4$  with increasing flare intensity (see Figure 3). For the AD LEO cases this holds, but for the high flaring Sun cases we see a turning point, above which  $\text{CH}_4$  becomes more abundant again. This is a result of decreased OH production. In the troposphere and up to the mid-stratosphere, OH is the main sink of  $\text{CH}_4$ . Above that, direct reaction with chlorine becomes the dominant contribution, at least for the stellar flaring cases. This effect contributes only weakly to the total column amount, however, because of the low number density. In the troposphere, where most of the methane lies, OH is produced by three main sources, the reaction of  $\text{O}(^1\text{D})$  with  $\text{H}_2\text{O}$ , NO reacting with  $\text{HO}_2$ , and the lesser studied photolysis of  $\text{HNO}_2$  (see Grenfell et al. 1995), which becomes dominant in the lower stratosphere (this requires future work).  $\text{O}(^1\text{D})$  itself is formed almost entirely from  $\text{O}_3$  photolysis. With higher flaring and hence reduced ozone levels, there is a tipping point, where less  $\text{O}(^1\text{D})$  produced from  $\text{O}_3$  leads to a reduction in OH. The same also happened in the AD LEO runs, but at higher flaring strengths of around 200 times enhanced SPE89 SEP fluxes, due to increased levels of smog  $\text{O}_3$  and lower UVB radiation coming from AD LEO resulting in lower OH production, i.e.,  $\text{CH}_4$  destruction. Chloromethane, in all cases, follows the methane trends, only with smaller molecular abundance.

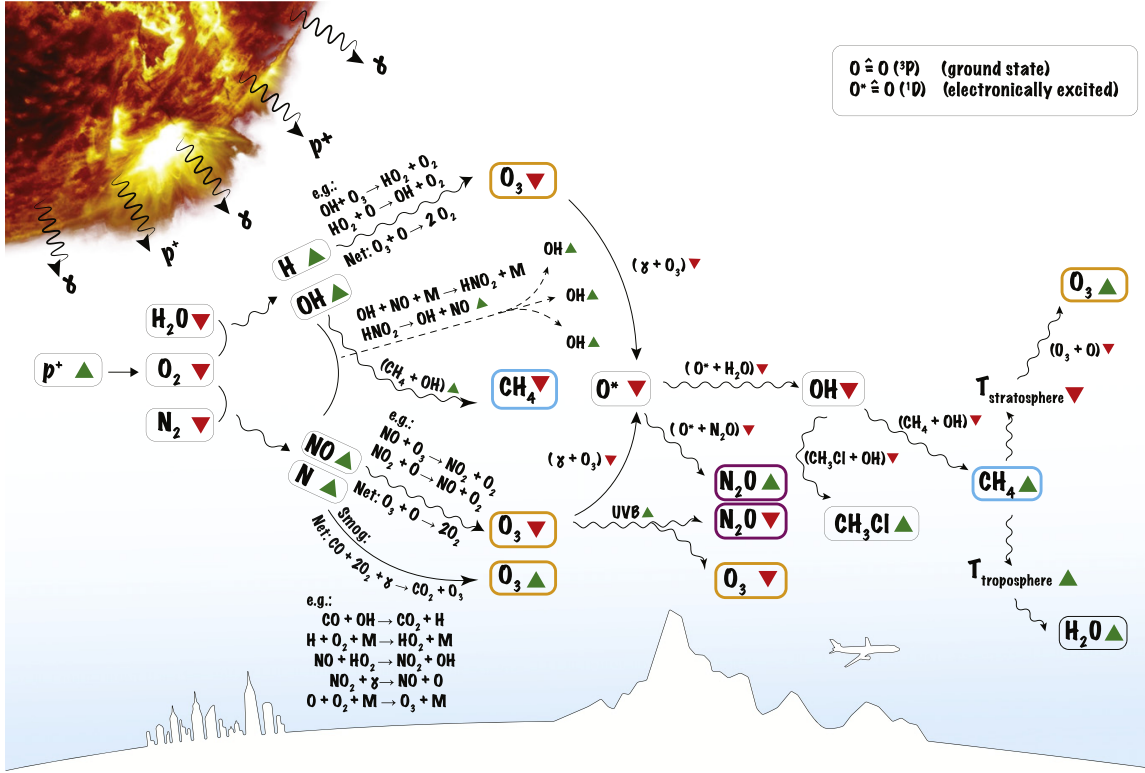


**Figure 9.** Schematic diagram showing the biosignature response (simplified) to cosmic rays ( $p^+$ ) and photons ( $\gamma$ ) from the star (upper left corner): influx of  $p^+$  directly decreases (red downward arrows) the abundance of  $H_2O$ ,  $O_2$ , and  $N_2$  by producing (green upward arrows)  $H$ ,  $OH$ ,  $NO$ , and  $N$ . Subsequently the abundance of other molecules also decreases (red arrows) and some increase (green arrows) via several paths and reactions (black). There are several different possible reasons for an  $O_3$  or  $CH_4$  increase or decrease, and depending on the host star radiation and  $p^+$  activity, some paths are more prominent than others, leading to different levels of abundance. The vertical positions in the diagram provide an indication where these processes dominate in the atmosphere. Reactions including “+ M” are three-body reactions, while “+  $\gamma$ ” denotes photolysis. O is the ground state atomic oxygen  $O(^3P)$ , and  $O^*$  its excited state  $O(^1D)$ .

While the effect of varying  $f_{NOx}$  and  $f_{HOx}$  is rather weak for the Earth around the Sun case, even for an artificially high flaring Sun, the effect of varying these parameters for the AD LEO cases becomes very important. The lower row of Figure 6 for a virtual Earth around AD LEO at a distance of 0.161 au, i.e., 0.9  $TSI_{\odot}$ , shows in the high flaring SPE89x50 case that especially varying  $f_{HOx}$  can result in temperature differences throughout most of the stratosphere of around 40 K. Interestingly, the parameter combination of  $f_{NOx} = 2.0$  and  $f_{HOx} = 0.0$  around a high flaring AD LEO leads to a temperature profile similar to a quiescent AD LEO, while stratospheric ozone abundance in this case is significantly lower (up to four orders of magnitude) than in the quiescent AD LEO cases.  $O_3$  is known to drive the stratospheric temperature inversion in the Earth’s atmosphere, but we would like to note here that for low stratospheric  $O_3$  abundance caused by stellar flaring, i.e., reduced or complete lack of temperature inversion, other molecules such as  $CH_4$  and  $H_2O$  determine stratospheric temperatures, as already discussed by, e.g., Segura et al. (2005), Rauer et al. (2011), Tabataba-Vakili et al. (2016). We see the main contribution to stratospheric heating in our model from the absorption of incoming stellar photons in the near-infrared range between 1 and 2  $\mu m$ . As indicated in the transmission spectra in Figure 7 the  $H_2O$  and

$CH_4$  bands have overlapping contributions and are therefore hard to distinguish. However, in contrast to the studies mentioned above, in our study of  $f_{NOx}$  and  $f_{HOx}$  (see Figure 8) we see a stronger correlation between temperatures and stratospheric  $H_2O$  profiles and a weakened role of  $CH_4$ .

In the modeled transit spectra in Figure 7 we clearly show the effect of reduced ozone, methane, and water for the high flaring scenarios when compared with the GCR reference case. All water and methane absorption features are reduced for the flaring case with  $f_{HOx} = 0.0$ , and even more suppressed for the  $f_{HOx} = 2.0$  case (light-blue line). Because  $NOx$  and  $HOx$  from HEPs can form  $HNO_3$  via the reaction  $NO_2 + OH + M \rightarrow HNO_3 + M$ , this leads to the absorption features seen in Figure 7. We confirm the  $HNO_3$  absorption around 11  $\mu m$  to be an indicator of an  $N_2$ - $O_2$  atmosphere exposed to a high flaring stellar environment, as proposed by Tabataba-Vakili et al. (2016). The second absorption feature of nitric acid around 17  $\mu m$  is only visible for the case of high  $HOx$  production from cosmic-ray-induced ion pairs. Hence, the measurement of this absorption band may be a hint of these values of  $HOx$  production per ion pair. Rauer et al. (2011) and Hedelt et al. (2013) have already analyzed the telescope time needed with a configuration based on *JWST* to identify various spectral features. With the S/N derived after Hedelt et al. (2013) we estimate that  $\sim 35$  transits of a theoretical planet around AD



LEO (distance to observer 4.9 pc) would be needed to identify the  $11\ \mu\text{m}$   $\text{HNO}_3$  band with a spectral resolution  $R = 100$ . The second  $\text{HNO}_3$  feature around  $17\ \mu\text{m}$  might require already a few hundred transits compared with an estimated three to four transits with NIRSpec (in the  $R = 100$  mode) on board *JWST* for the  $4.2\ \mu\text{m}$   $\text{CO}_2$  band. The third  $\text{HNO}_3$  absorption feature around  $21\ \mu\text{m}$  might be hard to detect at all, as it already lies in the far-infrared where the  $\text{H}_2\text{O}$  continuum dominates.

### 5. Conclusions

We have performed atmospheric simulations of virtual Earth-like planets around the flaring M-star AD LEO with our cloud-free 1D climate-chemistry model and have compared the influence of flaring strength with the uncertainty ranges of chemical  $\text{NO}_x$ – $\text{HO}_x$  production efficiencies.

New chemical insights found in this work are:

1.  $\text{NO}_x$ – $\text{HO}_x$ : The chemical production efficiencies  $f_{\text{NO}_x}$  and  $f_{\text{HO}_x}$  can significantly influence biosignature chemistry and abundance in our model, as well as stratospheric temperatures, and are therefore potentially important for Earth-like planets around M-dwarf stars like AD LEO. In the Earth's atmosphere, on the other hand, the influx of SEPs has a much stronger effect than  $f_{\text{NO}_x}$  and  $f_{\text{HO}_x}$ , which makes the empirical determination of the latter challenging.
2.  $\text{HNO}_3$ : Spectroscopic transit measurements of exoplanets may be able to help constrain their stellar environments by looking at, e.g.,  $\text{HNO}_3$  features above  $10\ \mu\text{m}$  together with infrared  $\text{O}_3$ ,  $\text{H}_2\text{O}$ , and  $\text{CH}_4$  absorption bands. Especially the measurement of the  $\text{HNO}_3$  features at  $17$  and  $21\ \mu\text{m}$  would hint toward high  $f_{\text{HO}_x}$  production.
3. Cl: We introduce and discuss a change of the major  $\text{CH}_4$  sink in the stratosphere from OH (lower stratosphere) to Cl (upper stratosphere). This may also become important for worlds with, e.g., high volcanic chlorine emissions.
4.  $\text{O}_3$ : We show that on Earth the UVB radiation from the Sun (G-star) is sufficient to limit global tropospheric smog  $\text{O}_3$  abundance even in hypothetical high flaring Sun scenarios, while we confirm lower atmospheric build-up of  $\text{O}_3$  for Earth-like planets around active M-stars like AD LEO, as has been modeled in multiple studies, e.g., Segura et al. (2005), Grenfell et al. (2012), Tabataba-Vakili et al. (2016).
5.  $\text{N}_2\text{O}$ : Atmospheric  $\text{N}_2\text{O}$  abundance runs into “saturation” for flaring cases regardless of stellar spectrum, flaring strengths, or stratospheric  $\text{O}_3$  levels.  $\text{N}_2\text{O}$  reactions, e.g., with  $\text{O}(^1\text{D})$ , in addition to diffusion processes within the atmosphere counteract the  $\text{O}_3$ –UV– $\text{N}_2\text{O}$  coupling (see Figure 9). Hence, destruction of  $\text{N}_2\text{O}$  by cosmic rays is ineffective in our model.

Additionally, in our model OH is the major sink for  $\text{CH}_4$  in the lower- to mid-atmosphere and is directly produced by SEPs, but we find that around high flaring solar-like stars atmospheric  $\text{O}_3$  abundance can significantly drop, which itself is a major source of tropospheric OH production (see Figure 9). This lack of OH from  $\text{O}_3$  can outweigh OH production from SEPs, subsequently causing unexpectedly high  $\text{CH}_4$  abundance (see Figures 3 and 9). Furthermore, in the absence of other sources  $\text{HNO}_2$  can become the main OH source throughout our entire model atmosphere for high flaring host star cases. Further



work on this is needed to see for which range of planetary atmospheres  $\text{HNO}_2$  may become important.

We would like to emphasize once more that  $\text{NO}_x$  and  $\text{HO}_x$  produced by cosmic rays can become important when studying Earth-like atmospheres around active M-stars.

The authors express their thanks to Christina Ciardullo for her assistance with the graphics. M.S. acknowledges support from DFG project RA 714/9-1. M.G. acknowledges support from DFG project GO 2610/1-1. F.S. acknowledges support from DFG project SCHR 1125/3-1.

*Software:* GARLIC (Schreier et al. 2014, 2018a, 2018b), HITRAN2012 (Rothman et al. 2013).

### ORCID iDs

Markus Scheucher  <https://orcid.org/0000-0003-4331-2277>  
F. Schreier  <https://orcid.org/0000-0001-7196-6599>

### References

- Airapetian, V., Glocer, A., Gronoff, G., Hébrard, E., & Danchi, W. 2016, *NatGe*, **9**, 452
- Atri, D. 2017, *MNRAS*, **465**, L34
- Candelaesi, S., Hillier, A., Machara, H., Brandenburg, A., & Shibata, K. 2014, *ApJ*, **792**, 67
- Cess, R. D. 1976, *JatS*, **33**, 1831
- Clough, S., Kneizys, F., & Davies, R. 1989, *AtmRe*, **23**, 229
- Crutzen, P. J. 1970, *QJRM*, **96**, 320
- Fichtner, H., Heber, B., Herbst, K., Kopp, A., & Scherer, K. 2013, in *Climate and Weather of the Sun-Earth System (CAWSES)*, ed. F.-J. Lübken (Berlin: Springer), 55
- Fujii, Y., Del Genio, A. D., & Amundsen, D. S. 2017, *ApJ*, **848**, 100
- Gardner, J. P., Mather, J. C., Clampin, M., et al. 2006, *SSRv*, **123**, 485
- Godolt, M., Grenfell, J. L., Hamann-Reinus, A., et al. 2015, *P&SS*, **111**, 62
- Godolt, M., Grenfell, J. L., Kitzmann, D., et al. 2016, *A&A*, **592**, A36
- Grenfell, B. T., Bolker, B. M., & Kleczkowski, A. 1995, *RSPSB*, **259**, 97
- Grenfell, J. L., Griebmeier, J.-M., von Paris, P., et al. 2012, *AsBio*, **12**, 1109
- Griebmeier, J.-M., Stadelmann, A., Grenfell, J. L., Lammer, H., & Motschmann, U. 2009, *Icar*, **199**, 526
- Griebmeier, J.-M., Stadelmann, A., Motschmann, U., et al. 2005, *AsBio*, **5**, 587
- Griebmeier, J.-M., Tabataba-Vakili, F., Stadelmann, A., Grenfell, J. L., & Atri, D. 2016, *A&A*, **587**, A159
- Gueymard, C. A. 2004, *SoEn*, **76**, 423
- Haagen-Smit, A. J. 1952, *Ind. Eng. Chem.*, **44**, 1342
- Hawley, S. L., & Pettersen, B. R. 1991, *ApJ*, **378**, 725
- Hedelt, P., von Paris, P., Godolt, M., et al. 2013, *A&A*, **553**, A9
- Kasper, M., Beuzit, J.-L., Verinaud, C., et al. 2010, *Proc. SPIE*, **7735**, 77352E
- Kasting, J. F., & Ackerman, T. P. 1986, *Sci*, **234**, 1383
- Kasting, J. F., Whitmire, D. P., & Reynolds, R. T. 1993, *Icar*, **101**, 108
- Kopparapu, R. K., Ramirez, R., Kasting, J. F., et al. 2013, *ApJ*, **765**, 131
- Kopparapu, R. K., Wolf, E. T., Haqq-Misra, J., et al. 2016, *ApJ*, **819**, 84
- Leconte, J., Forget, F., Charnay, B., Wordsworth, R., & Pottier, A. 2013, *Natur*, **504**, 268
- Luger, R., & Barnes, R. 2015, *AsBio*, **15**, 119
- Maehara, H., Shibayama, T., Notsu, S., et al. 2012, *Natur*, **485**, 478
- Manabe, S., & Wetherald, R. T. 1967, *JatS*, **24**, 241
- Marcq, E., Belyaev, D., Montmessin, F., et al. 2011, *Icar*, **211**, 58
- Melsheimer, C., Verdes, C., Buehler, S., et al. 2005, *RaSc*, **40**, RS1007
- Murphy, W. F. 1977, *JChPh*, **67**, 5877
- Popp, M., Schmidt, H., & Marotzke, J. 2015, *JatS*, **72**, 452
- Porter, H. S., Jackman, C. H., & Green, A. E. S. 1976, *JChPh*, **65**, 154
- Ramirez, R. M., & Kaltenegger, L. 2014, *ApJL*, **797**, L25
- Rauer, H., Gebauer, S., Paris, P. V., et al. 2011, *A&A*, **529**, A8
- Rothman, L. S., Gordon, I. E., Babikov, Y., et al. 2013, *JQSRT*, **130**, 4
- Rugheimer, S., Kaltenegger, L., Segura, A., Linsky, J., & Mohanty, S. 2015a, *ApJ*, **809**, 57
- Rugheimer, S., Segura, A., Kaltenegger, L., & Sasselov, D. 2015b, *ApJ*, **806**, 137
- Rusch, D., Gérard, J.-C., Solomon, S., Crutzen, P., & Reid, G. 1981, *P&SS*, **29**, 767
- Scalo, J., Kaltenegger, L., Segura, A. G., et al. 2007, *AsBio*, **7**, 85
- Schreier, F., Gimeno García, S., Hedelt, P., et al. 2014, *JQSRT*, **137**, 29

- Schreier, F., Milz, M., Buehler, S., & von Clarmann, T. 2018a, [JQSRT](#), **211**, 64
- Schreier, F., Städt, S., Hedelt, P., & Godolt, M. 2018b, [MolAs](#), **11**, 1
- Segura, A., Kasting, J. F., Meadows, V., et al. 2005, [AsBio](#), **5**, 706
- Segura, A., Krelove, K., Kasting, J. F., et al. 2003, [AsBio](#), **3**, 689
- Segura, A., Walkowicz, L. M., Meadows, V., Kasting, J., & Hawley, S. 2010, [AsBio](#), **10**, 751
- Selsis, F. 2000, in ESA Special Publication 451, Darwin and Astronomy: the Infrared Space Interferometer, ed. B. Schürmann (Noordwijk: ESA), 133
- Shibayama, T., Maehara, H., Notsu, S., et al. 2013, [ApJS](#), **209**, 5
- Shields, A. L., Ballard, S., & Johnson, J. A. 2016, [PhR](#), **663**, 1
- Shields, A. L., Meadows, V. S., Bitz, C. M., et al. 2013, [AsBio](#), **13**, 715
- Sinnhuber, M., Nieder, H., & Wieters, N. 2012, [SGeo](#), **33**, 1281
- Smart, D. F., & Shea, M. A. 2002, [AdSpR](#), **30**, 1033
- Sneep, M., & Ubachs, W. 2005, [JQSRT](#), **92**, 293
- Solomon, S., Rusch, D., Gérard, J., Reid, G., & Crutzen, P. 1981, [P&SS](#), **29**, 885
- Tabataba-Vakili, F., Grenfell, J. L., Griebmeier, J.-M., & Rauer, H. 2016, [A&A](#), **585**, A96
- Tian, F., & Ida, S. 2015, [NatGe](#), **8**, 177
- Verronen, P. T., & Lehmann, R. 2013, [AnGeo](#), **31**, 909
- von Clarmann, T., Hopfner, M., Funke, B., et al. 2003, [JQSRT](#), **78**, 381
- Yang, J., Boué, G., Fabrycky, D. C., & Abbot, D. S. 2014, [ApJL](#), **787**, L2

# 4

## **Publication III: Proxima Centauri b: A Strong Case for Including Cosmic-Ray-induced Chemistry in Atmospheric Biosignature Studies**

**Personal and co-authors contributions:** I integrated our atmospheric model into a comprehensive model suite, provided initial planetary parameters and neutral atmospheres, processed ionization rates and [chemical production efficiencies](#) from the other models, provided diagnostics for the convergence of the model suite towards steady state, calculated the synthetic spectra, and processed our results. I wrote most of the manuscript.

S. Banjac provided ionization rates; K. Herbst edited parts of the manuscript related to the particle precipitation model; V. Schmidt provided [CPEs](#); M. Sinnhuber edited parts of the manuscript related to ion chemistry; All co-authors provided comments on the manuscript and in the journal's peer-review phase.



# Proxima Centauri b: A Strong Case for Including Cosmic-Ray-induced Chemistry in Atmospheric Biosignature Studies

M. Scheucher<sup>1,2</sup> , K. Herbst<sup>3</sup> , V. Schmidt<sup>4</sup>, J. L. Grenfell<sup>2</sup> , F. Schreier<sup>5</sup> , S. Banjac<sup>3</sup>, B. Heber<sup>3</sup> , H. Rauer<sup>1,2,6</sup>, and M. Sinnhuber<sup>4</sup>

<sup>1</sup> Zentrum für Astronomie und Astrophysik, Technische Universität Berlin, D-10623 Berlin, Germany; [scheucher@tu-berlin.de](mailto:scheucher@tu-berlin.de), [markus.scheucher@dlr.de](mailto:markus.scheucher@dlr.de)

<sup>2</sup> Institut für Planetenforschung, Deutsches Zentrum für Luft- und Raumfahrt, D-12489 Berlin, Germany

<sup>3</sup> Institut für Experimentelle und Angewandte Physik, Christian-Albrechts-Universität zu Kiel, D-24118 Kiel, Germany

<sup>4</sup> Institut für Meteorologie und Klimaforschung, Karlsruher Institut für Technologie, D-76344 Eggenstein-Leopoldshafen, Germany

<sup>5</sup> Institut für Methodik der Fernerkundung, Deutsches Zentrum für Luft- und Raumfahrt, D-82234 Oberpfaffenhofen, Germany

<sup>6</sup> Institut für Geologische Wissenschaften, Freie Universität Berlin, D-12249 Berlin, Germany

Received 2019 December 10; revised 2020 February 19; accepted 2020 February 28; published 2020 April 8

## Abstract

Due to its Earth-like minimum mass of  $1.27 M_{\oplus}$  and its close proximity to our solar system, Proxima Centauri b is one of the most interesting exoplanets for habitability studies. Its host star, Proxima Centauri, is however a strongly flaring star, which is expected to provide a very hostile environment for potentially habitable planets. We perform a habitability study of Proxima Centauri b assuming an Earth-like atmosphere under high stellar particle bombardment, with a focus on spectral transmission features. We employ our extensive model suite calculating energy spectra of stellar particles, their journey through the planetary magnetosphere, ionosphere, and atmosphere, ultimately providing planetary climate and spectral characteristics, as outlined in Herbst et al. Our results suggest that together with the incident stellar energy flux, high particle influxes can lead to efficient heating of the planet well into temperate climates, by limiting  $\text{CH}_4$  amounts, which would otherwise run into antigreenhouse for such planets around M stars. We identify some key spectral features relevant for future spectral observations: First,  $\text{NO}_2$  becomes the major absorber in the visible, which greatly impacts the Rayleigh slope. Second,  $\text{H}_2\text{O}$  features can be masked by  $\text{CH}_4$  (near-infrared) and  $\text{CO}_2$  (mid- to far-infrared), making them nondetectable in transmission. Third,  $\text{O}_3$  is destroyed and instead  $\text{HNO}_3$  features become clearly visible in the mid- to far-infrared. Lastly, assuming a few percent of  $\text{CO}_2$  in the atmosphere,  $\text{CO}_2$  absorption at  $5.3 \mu\text{m}$  becomes significant (for flare and nonflare cases), strongly overlapping with a flare related  $\text{NO}$  feature in Earth's atmosphere.

*Unified Astronomy Thesaurus concepts:* Exoplanets (498); Atmospheric science (116); Cosmic rays (329); Exoplanet atmospheric composition (2021); Exoplanet atmospheres (487); Photoionization (2060); Biosignatures (2018)

## 1. Introduction

Given the recent, exciting discoveries of terrestrial-sized planets orbiting M stars, together with the higher activity of many M stars compared to our Sun (e.g., Reid & Hawley 2005; Scalo et al. 2007), a better understanding of the influence and impact of such active host stars upon planetary habitability is crucial for the search for extraterrestrial life and improving our understanding of Earth-like planets. Proxima Centauri b (hereafter Prox Cen b) is one of the most interesting exoplanets to date in terms of studying potential habitability (see, e.g., Turbet et al. 2016; Dong et al. 2017; Meadows et al. 2018; Berdyugina & Kuhn 2019). With a minimum of  $1.27 M_{\oplus}$  (Anglada-Escudé et al. 2016), it may be similar in bulk properties to Earth. Although it receives only 65% of the mean total stellar irradiation (TSI) compared to Earth, Meadows et al. (2018) showed that an Earth-like atmosphere with, e.g., a surface carbon dioxide concentration of a few percent could lead to habitable conditions.

Proxima Centauri (hereafter Prox Cen), is an M5.5Ve flaring star. While direct observations of coronal mass ejections (CMEs) and corotating interaction regions (CIRs) are still challenging, model extrapolations from the Sun's flare–CME correlation can be used to estimate the bombardment by stellar energetic particles (SEP). While the planetary magnetosphere could shield the planet from the majority of low-energy SEPs, the multitude of flares—and possible CMEs—of active M stars

may cause long-lasting changes to the planet's atmospheric mass, composition, and surface conditions (e.g., Vidotto et al. 2013). There is an ongoing debate as to whether such close-in planets orbiting active M stars would be stripped of their atmospheres, e.g., if they lie within the star's Alfvén sphere, leaving them without magnetospheric protection (e.g., Lammer et al. 2010; Airapetian et al. 2017a).

Including the impact of stellar high energetic particles in habitability studies in a self-consistent way requires a broad understanding of stellar, astrospheric, magnetospheric, and ion and neutral chemical processes within the planet's atmosphere. Modeling efforts by, e.g., Segura et al. (2010), Grenfell et al. (2012), Tabataba-Vakili et al. (2016), Tilley et al. (2019), and Scheucher et al. (2018) have parameterized the top-of-atmosphere (TOA) incoming particle energy distributions, secondary particle generation in air showers, ionization of the atmosphere, and its impact on neutral atmospheric composition, using different methods. Herbst et al. (2019a) took this one step further by coupling cosmic-ray-induced magnetospheric, ionospheric, and lower atmospheric processes in an interactive model suite.

Such studies are crucial in order to understand the expected range of atmospheres of such planets lying in—or close to—the habitable zone, as well as to better understand and interpret atmospheric spectra of next generation space missions such as the *James Webb Space Telescope* (JWST), *HabEX*, and



*LUVUOIR*, plus ground-based telescopes like the Extremely Large Telescope (ELT).

## 2. Methodology

We apply the comprehensive model suite described in Herbst et al. (2019a) to study the habitability of Prox Cen b as influenced by the strong stellar activity of its host star.

### 2.1. Initial Atmosphere

We use our 1D climate-chemistry model (1D CCM; see, e.g., Rauer et al. 2011; von Paris et al. 2015; Scheucher et al. 2018) to calculate initial climate and neutral atmospheric composition for Prox Cen b without SEP or galactic cosmic-ray (GCR) impacts. The stellar energy spectrum is taken from the Virtual Planetary Laboratory Spectral Database,<sup>7</sup> described in Meadows et al. (2018), and the incoming stellar irradiation is scaled to Prox Cen b's distance of 0.0485 au. To build our planet, we start with the observed minimum mass of  $1.27 M_E$  and use the mass–radius relationship from Valencia et al. (2007) with an Earth-like ice-mass fraction of 0.1%, which results in a radius  $R$  of  $1.065 R_E$  and a surface gravity  $g_{\text{surf}}$  of  $10.98 \text{ m s}^{-2}$  via  $m R^{-2}$ .

We start with the Earth US standard 1976 atmosphere (Committee on Extension to the Standard Atmosphere—COESA) and increase the surface pressure to  $p_{\text{surf}} = 1.119 \text{ bar}$ , in order to maintain Earth's atmospheric mass. We use Earth reference surface fluxes in our model similar to Segura et al. (2005) and Meadows et al. (2018) which result in the modern-Earth 1976 surface mixing ratios of 1.5 ppm  $\text{CH}_4$ , 190 ppm  $\text{CO}$ , and 270 ppm  $\text{N}_2\text{O}$ . This is achieved in our chemical scheme with  $8.2 \times 10^{10} \text{ CH}_4$ ,  $1.8 \times 10^{11} \text{ CO}$ , and  $1.1 \times 10^9 \text{ molecules cm}^{-2} \text{ s}^{-1} \text{ N}_2\text{O}$ . These fluxes together with initial surface mixing ratios of 500 ppm  $\text{H}_2$ , 21.1%  $\text{O}_2$ , and 0.934%  $\text{Ar}$  are used as boundary conditions for all our Prox Cen b runs. With cloud-free conditions and a basaltic surface albedo of  $A_{\text{surf}} = 0.13$ , we increase the  $\text{CO}_2$  amount in the atmosphere by replacing  $\text{N}_2$  with  $\text{CO}_2$  step-by-step. Our aim is to investigate potential surface habitability. We start with 5%  $\text{CO}_2$  (72.4%  $\text{N}_2$ ) and increase in steps of 5% up to 20%  $\text{CO}_2$  (57.4%  $\text{N}_2$  respectively). The tropospheric temperatures and water amounts are calculated via adiabatic lapse rates after Manabe & Wetherald (1967) with a surface relative humidity,  $\text{RH} = 80\%$ . For kinetic transport in the chemistry calculations we use eddy diffusion parameterized for Earth after Massie & Hunten (1981).

### 2.2. Galactic and Stellar Cosmic-Ray Spectra

To model the impact of energetic particles on planetary atmospheres both GCRs and SEPs have to be considered. Since Prox Cen is our nearest neighbor it is reasonable to assume the same local interstellar medium (LISM) conditions as for our Sun. However, analytical studies by Struminsky et al. (2017) and Sadovskii et al. (2018) showed that GCRs with energies below 1 TeV are not able to reach Prox Cen b. Besides, the flux of such high energetic GCR particles in the LISM is vanishingly small and can be neglected to a first-order approximation. However, due to the high stellar activity of Prox Cen, SEPs most likely have a strong impact on Prox Cen

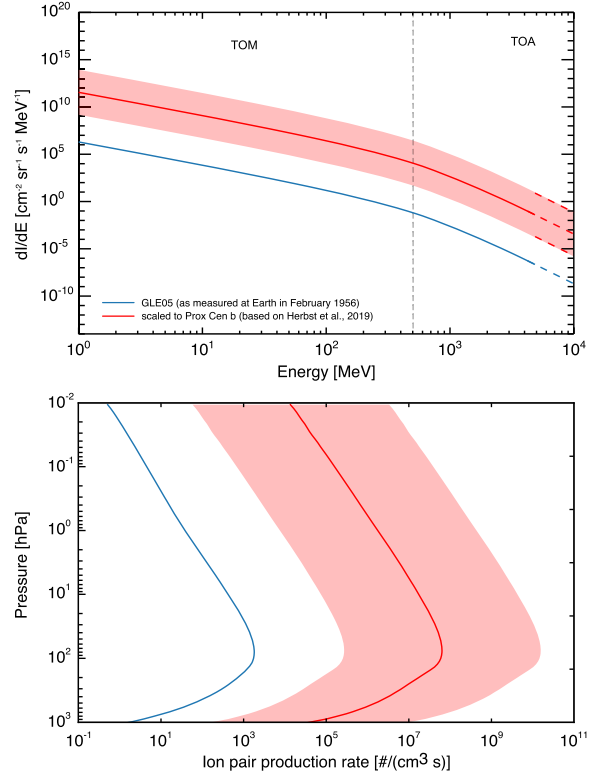


**Figure 1.** Upper panel: observed GLE event spectrum of GLE05 (blue) compared to the scaled event spectrum at Prox Cen b (red) including the corresponding error band (red shaded region) and cutoff energy on TOA (gray dashed). Lower panel: corresponding event-induced atmospheric ion-pair production rates at Earth (blue) and at Prox Cen b (red).

b. For example, Howard et al. (2018) most recently found strong optical flares with intensities at 0.0485 au of up to  $92 \text{ W m}^{-2}$  on Prox Cen. Herbst et al. (2019b) suggested that such high flare intensities correspond to stellar proton fluences of  $10^8$ – $10^{14} \text{ protons/(cm}^2 \text{ sr s)}$  around Prox Cen at 0.048 au. To derive our actual particle spectrum, we scale from a well-known measured event spectrum. Our study is based on one of the strongest events measured on Earth, the ground level enhancement (GLE) of 1956 February (GLE05, see the upper panel of Figure 1).

### 2.3. Planetary Magnetic Field and Atmospheric Ionization

From Earth we know that low-energetic particles are deflected by the geomagnetic field which acts as an additional particle filter. Thus, the CR flux at the top of the magnetosphere (TOM) is not the same as that at the TOA, which further depends on the magnitude and geometry of the planetary magnetic field (see, e.g., Herbst et al. 2013).

Assuming an Earth-like magnetic field, the so-called cutoff rigidity  $R_c$ , an equivalent to the energy that particles require to enter the atmosphere at a given location, is computed with PLANETOCOSMICS (see, e.g., Desorgher et al. 2006). As a first-order approximation, in this study we utilize the implemented International Geomagnetic Reference Field (see, e.g., Thébault et al. 2015) model to describing the modern-Earth internal terrestrial magnetic field. The globally distributed

<sup>7</sup> <http://depts.washington.edu/naivpl/content/spectral-databases-and-tools>

cutoff rigidity values have been modeled based on the highest planetary disturbance value ( $k_p > 7$ ). However, since no information on the spatial resolution of the exoplanetary atmospheric transmission is available, in this study, we assume planetary midlatitudes around  $60^\circ$ , corresponding to a mean cutoff rigidity of 1.11 GV (around 510 MeV), as indicated by the dashed line in the upper panel of Figure 1. As can be seen, this cutoff separates the TOM from the TOA spectrum.

However, we note that the magnetospheric structure of Prox Cen b could be different from that of the Earth, for example, due to strong Joule heating caused by fast stellar winds impinging on the upper planetary atmosphere (see, e.g., Cohen et al. 2014).

Nevertheless, energetic charged particles that reach the planetary atmosphere will lose energy due to collisions with the surrounding atmospheric constituents, resulting in an ionization of the upper planetary atmosphere. Further, interactions with, for example, nitrogen, oxygen, or argon atoms might trigger the development of a secondary particle shower and associated photochemical effects. The deeper a particle is able to enter into the atmosphere, the more likely a collision with these species becomes. The generated secondary particles may further interact, resulting in the formation of atmospheric particle cascades (see, e.g., Dorman et al. 2004) and an altitude-dependent atmospheric ionization. This, however, strongly depends on the type and energy of the primary particle, the atmospheric altitude, and the location.

Neglecting GCRs and their astrophysical modulation, the SEP-induced ionization rates  $Q$  can numerically be described by

$$Q(E_c, x) = \sum_i \int_{E_c}^{E_u} J_i(E) \cdot Y_i(E, x) dE, \quad (1)$$

with  $i$  representing the primary particle type,  $E_u$  the upper energy of the stellar particle event,  $J_i$  the stellar differential particle event spectrum, and  $Y_i$  the so-called atmospheric ionization yield function given as  $\alpha \cdot \frac{1}{W_{\text{ion}}} \frac{\Delta E_i}{\Delta x}$ , where  $\frac{\Delta E_i}{\Delta x}$  reflects the mean specific energy loss, while  $W_{\text{ion}}$  represents the atmospheric ionization energy (see, e.g., Porter et al. 1976; Simon Wedlund et al. 2011).

The event-dependent atmospheric ionization rates are modeled with the newly developed Atmospheric Radiation Simulator (AtRIS, see Banjac et al. 2019), utilizing the provided planetary and atmospheric conditions, as well as the particle event spectrum.

#### 2.4. Impact on Atmospheric Ionization, Neutral Chemistry, and Climate

The impact of ionization on neutral composition is modeled with the 1D Exoplanetary Terrestrial Ion Chemistry model (ExoTIC; Herbst et al. 2019a, based on the UBIC model described, e.g., in Winkler et al. 2009; Sinnhuber et al. 2012; Nieder et al. 2014), taking global averages of the particle-induced ionization calculated by AtRIS (Banjac et al. 2019). ExoTIC considers 60 neutral and 120 ion species for neutral, neutral-ion, and photochemical reactions. Primary ions as well as excited species are provided from the ionization, dissociation and dissociative ionization of  $\text{O}_2$ ,  $\text{N}_2$ , and  $\text{O}$ ; an increase in  $\text{CO}_2$  mixing ratios may therefore lower the amount of primary ions from  $\text{N}_2$ ,  $\text{O}_2$ , and  $\text{O}$ , but  $\text{CO}_2$  dissociative ionization is not considered.

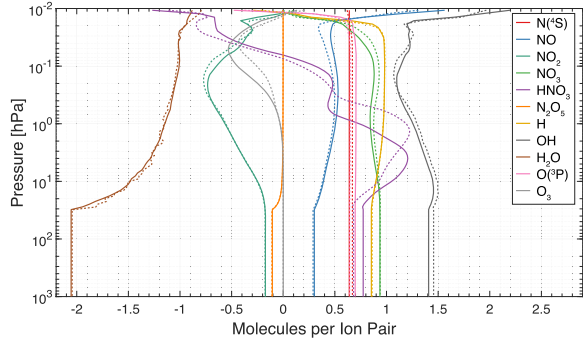


**Figure 2.** Production and loss rates of neutral species due to ion-chemistry processes calculated with ExoTIC for the 5%  $\text{CO}_2$  (solid) and 20%  $\text{CO}_2$  (dotted) atmospheres for the GLE05 event scaled to Prox Cen b. Below 30 hPa, rates are set to isoprofiles.

Both particle-induced ionization and the production and loss rates of NOx ( $\text{N}(^2\text{D})$ ,  $\text{N}(^4\text{S})$ , NO,  $\text{NO}_2$ ,  $\text{NO}_3$ ,  $\text{N}_2\text{O}_5$ ), HOx (H, OH),  $\text{HNO}_3$ ,  $\text{H}_2\text{O}$ ,  $\text{O}_3$ ,  $\text{O}(^3\text{P})$ , and  $\text{O}(^1\text{D})$  per initial ion, are then transferred from ExoTIC to the 1D CCM, which produces atmospheric climate and composition under SEP and GCR bombardment as input for the next iteration with AtRIS and ExoTIC. Planetary conditions are considered to be in equilibrium when neither ionization, redistribution rates, nor atmospheric conditions change.

#### 2.5. Spectral Characteristics

For spectral analysis we supply output ( $p$ ,  $T$ , composition) from the coupled model suite as input into the “Generic Atmospheric Radiation Line-by-line Infra-red Code” (GARLIC; e.g., Schreier et al. 2014, 2018a, 2018b) using HITRAN2016 (Gordon et al. 2017), CKD continua derived from Clough et al. (1989), visible and near-infrared (IR) cross sections from the Mainz Spectral Atlas (Keller-Rudek et al. 2013), and Rayleigh scattering parameterization from Snee & Ubachs (2005), Marcq et al. (2011), and Murphy (1977).

### 3. Results

The upper panel of Figure 1 shows the energy spectrum of GLE05 at Earth (blue) and its scaling to the energy spectrum at Prox Cen b (red, see Herbst et al. 2019b); the lower panel displays the corresponding cosmic-ray-induced ion-pair production rate calculated for the GLE05 from Earth scaled to Prox Cen b for the initial atmospheres described in Section 2.1. We see the typical ion-pair production peak in the lower stratosphere due to increasing atmospheric density.

Figure 2 shows the ion-chemistry response for the species submitted from the ion-chemistry model to the 1D CCM. Tropospheric values are set to constants based on the lowermost stratospheric values. Rates for H and  $\text{N}(^4\text{S})$  are similar to Earth-like values of 1 and 0.6 respectively (compare, e.g., Sinnhuber et al. 2012; Herbst et al. 2019a), while values, e.g., for NO and OH are different. The NO formation rate is smaller than on Earth ( $<0.5$  compared to  $\sim 0.58$ ), with values for the 20%  $\text{CO}_2$  atmosphere being smaller than for the 5%  $\text{CO}_2$  case, indicating that this difference is due to the change in bulk atmosphere. The OH formation rate is distinctly larger than for Earth ( $\sim 1.5$  compared to  $\leq 1$ ), with values for the 20%  $\text{CO}_2$  case larger than for the 5%  $\text{CO}_2$  case, again indicating that

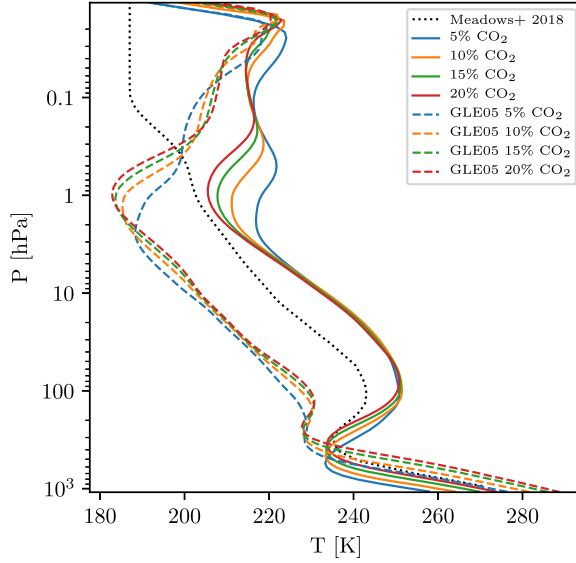


**Figure 3.** Atmospheric temperature profiles for an Earth-like Prox Cen b with varying amounts (vmr) of atmospheric  $\text{CO}_2$  (colors). We compare results for a virtually quiescent Prox Cen (solid) with a high flaring host star (dashed). Overplotted (black dotted) are results from Meadows et al. (2018).

this difference is due to the change in bulk atmospheric composition. Further analysis shows that the formation rates of NO and OH from positive ion-chemistry reactions are similar to Earth values, while those from negative ion chemistry are very different (not shown). Note the strong changes of the formation rates of  $\text{HNO}_3$  and  $\text{O}_3$  between the 5% and 20%  $\text{CO}_2$  cases. This might indicate that the different formation rates of OH and NO on Earth may be due to a different composition of negative  $\text{NO}_3^-$  containing cluster ions which also play a role in  $\text{HNO}_3$  formation via recombination (e.g., Sinnhuber et al. 2012). This demonstrates the importance of considering the full ion chemistry even for Earth-like ( $\text{O}_2$ – $\text{N}_2$ ) atmospheres.

Figure 3 shows temperature profiles for scenarios having Earth-like atmospheres but with varying amounts of  $\text{CO}_2$  for quiescent stellar conditions (solid lines) and with GCRs and SEPs based on GLE05 (dashed lines). Figure 3 suggests  $\text{CO}_2$  greenhouse warming in the lower atmosphere together with associated mesospheric cooling. Associated with the weak stellar irradiation, results suggest 20% mixing ratio by volume (vmr) of  $\text{CO}_2$  is needed in the nonflare cases to achieve global average temperatures that support liquid surface water. In the middle atmosphere, results suggest that the temperature is not sensitive to changes in  $\text{CO}_2$ . A comparison of our 5%  $\text{CO}_2$  run (solid blue) with Meadows et al. (2018) who assumed an Earth-like Prox Cen b with 5%  $\text{CO}_2$  and who did not consider cosmic rays (black dotted), generally shows reasonable agreement, although some differences arise due to the different assumptions used for  $\text{CH}_4$  surface fluxes. Our model with post-industrial surface fluxes (solid blue line, 5%  $\text{CO}_2$  in Figure 4) yields  $\text{CH}_4$  concentrations of  $\sim 5300$  ppm, while Meadows et al. (2018) reported  $\sim 1000$  ppm with lower preindustrial  $\text{CH}_4$  fluxes. In our model this leads to a stronger  $\text{CH}_4$  antigreenhouse, hence lower surface temperatures with a warmer stratosphere.

Figure 3 additionally shows (dashed lines) atmospheric temperatures for flaring scenarios of Prox Cen with the

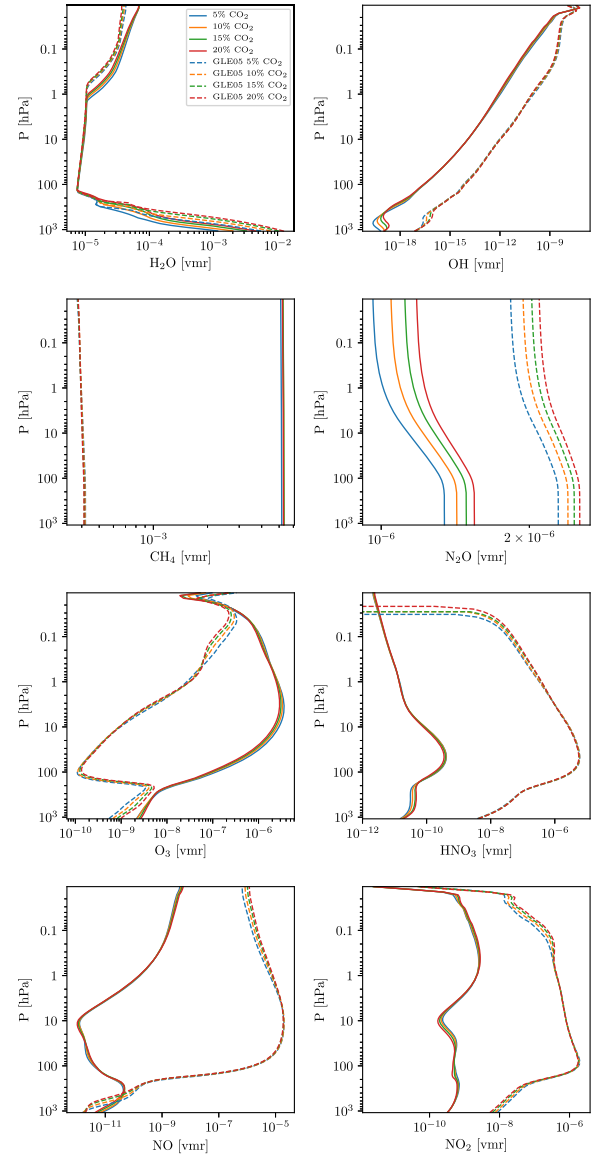


**Figure 4.** Volume mixing ratios of  $\text{H}_2\text{O}$ , OH,  $\text{CH}_4$ ,  $\text{N}_2\text{O}$ ,  $\text{O}_3$ ,  $\text{HNO}_3$ , NO, and  $\text{NO}_2$  for the scenarios of Figure 3.

calculated GLE05 induced ionization from Figure 1 and chemical production/loss rates from Figure 2. Surface  $\text{CH}_4$  here is decreased from 5300 down to 400 ppm (although  $\text{CH}_4$  vmr are still essentially isoprofiles as shown in Figure 4), yielding a weaker antigreenhouse effect, resulting in higher surface temperatures for the flaring cases. Interestingly, all four tested  $\text{CO}_2$  concentrations are sufficient for the flaring cases to warm the surface and lead to habitable conditions. The 15%  $\text{CO}_2$  scenario outputs Earth-like 288 K global average surface temperatures.

Figure 4 shows atmospheric vmr profiles of  $\text{H}_2\text{O}$ , OH,  $\text{CH}_4$ ,  $\text{N}_2\text{O}$ ,  $\text{O}_3$ ,  $\text{HNO}_3$ , NO, and  $\text{NO}_2$  for the quiescent and flaring cases from Figure 3. Our  $\text{CH}_4$  abundances are strongly

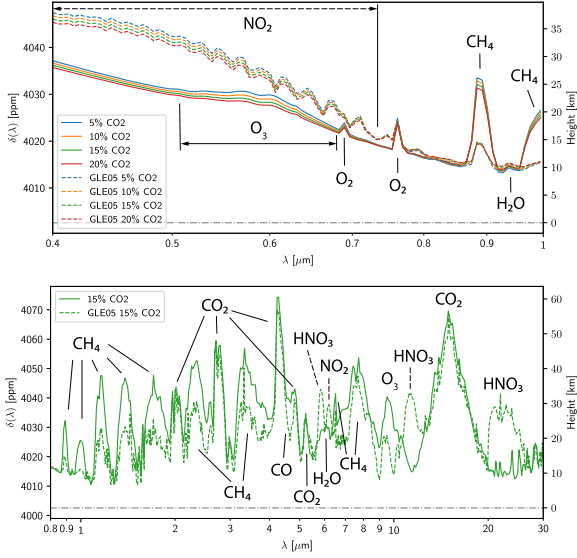


**Figure 5.** Upper: transmission spectra ( $R = 100$ ) from 400 to 1000 nm for the scenarios shown in Figures 3 and 4. Lower: IR transmission spectral comparison for the two 15% CO<sub>2</sub> scenarios, the quiescent host star (solid), and GLE05 conditions (dashed).

increased compared to Earth. This arises (see Segura et al. 2005) due to lower UVB radiation which lowers O<sub>3</sub> photolysis; this then lowers O(<sup>1</sup>D) (a product of O<sub>3</sub> photolysis), which lowers the rate of H<sub>2</sub>O + O(<sup>1</sup>D), and hence lowers OH and increases CH<sub>4</sub>. For the flaring cases, however, CH<sub>4</sub> is effectively reduced by high amounts of cosmic-ray-induced OH, via  $\text{CH}_4 + \text{OH} \rightarrow \text{CH}_3 + \text{H}_2\text{O}$ . Stratospheric ozone strongly decreases similarly to Scheucher et al. (2018). Increases in OH and NO (which can remove stratospheric ozone and stimulate smog ozone) for the flaring cases are a result of the cosmic-ray-induced production rates from ion redistribution into neutral species. HNO<sub>3</sub> increases by up to four orders of magnitude compared to the nonflaring case, mostly due to photochemistry (its main in situ source is via the reaction:  $\text{NO}_2 + \text{OH} + \text{M} \rightarrow \text{HNO}_3 + \text{M}$  (“M” refers to any third body). The gas-phase precursors of HNO<sub>3</sub>, i.e., NO<sub>2</sub> and OH, are stimulated by cosmic-ray-induced chemistry. H<sub>2</sub>O does not show significant changes in molecular abundance. NO<sub>2</sub> shows up to four orders of magnitude increased concentrations for the flaring compared to the quiescent case. Figure 2 shows cosmic-ray-induced ion-chemical destruction of NO<sub>2</sub>. NO<sub>2</sub> is incorporated into cluster ions which release other N-containing species under recombination, either NO, NO<sub>3</sub>, or HNO<sub>3</sub>, which then form NO<sub>2</sub> in a multitude of secondary neutral gas-phase reactions, overwhelming the apparent loss. One important source is the higher UVB radiation environment in the lower-middle atmosphere because of the lowered O<sub>3</sub> concentration, hence reduced UVB absorption. This increases photolysis of, most importantly, HNO<sub>3</sub>, HO<sub>2</sub>NO<sub>2</sub>, and N<sub>2</sub>O<sub>5</sub>, producing large amounts of NO<sub>2</sub>. Further, NO<sub>2</sub> is a direct product of the O<sub>3</sub> destruction mechanism starting with  $\text{NO} + \text{O}_3 \rightarrow \text{NO}_2 + \text{O}_2$ , and cosmic-ray-induced NO<sub>x</sub> and HO<sub>x</sub> also contribute significantly via the two reactions  $\text{NO} + \text{HO}_2 \rightarrow \text{NO}_2 + \text{OH}$  and  $\text{NO} + \text{NO}_3 \rightarrow 2\text{NO}_2$ . N<sub>2</sub>O, on the contrary, does not show changes due to cosmic rays significant enough to show up in

our simulated spectra (Figure 5). The ~65% increase in overall abundance in Figure 4 for our flaring cases compared to the quiescent runs is a little counterintuitive at first, because with the large decrease in O<sub>3</sub> amounts the overall UVB and UVC radiation environment, i.e., photolysis of other species, increases. Our analysis showed that UVC fluxes <198 nm are decreased significantly, reducing N<sub>2</sub>O photolysis—the major N<sub>2</sub>O sink in our model. From a detailed investigation of changes in molecular abundances of other major absorbers overlapping in wavelength range with N<sub>2</sub>O photolysis (significant ~175–240 nm), together with their photolysis cross sections, showed a steep increase of HNO<sub>3</sub> and NO<sub>2</sub> (and some increase for HO<sub>2</sub>NO<sub>2</sub> below ~20 hPa) photolysis rates, hence shielding of N<sub>2</sub>O. Small changes in N<sub>2</sub>O with the variation of CO<sub>2</sub> contents are most importantly related to temperature changes, i.e., H<sub>2</sub>O steam amounts and photolysis rates in the atmosphere.

Figure 5 shows synthetic transmission spectra calculated by GARLIC. The visible to near-IR (Figure 5, upper panel) is a key region, e.g., for biosignature studies of, for example, O<sub>2</sub> with the ELT (e.g., Rodler & López-Morales 2014; Snellen 2014). Bétrémieux & Kaltenegger (2013) noted the importance of including, for example, O<sub>2</sub> and O<sub>3</sub> absorption in this region, which is overlooked by many biosignature studies, but which is included in our work. Our results (Figure 5, upper panel) suggest a significant difference between the flaring and quiescent runs—but smaller differences due to changing composition for the individual flaring or quiescent runs. All quiescent runs show the O<sub>3</sub> Chappuis bands around 600 nm known from Earth, with minor differences in strength, due to the slightly different strato-/mesospheric O<sub>3</sub> amounts. This absorption feature is rather small compared with Earth’s atmosphere because of the generally lower O<sub>3</sub> amounts of ~70 Dobson units for the quiescent case. In the flaring runs, there is a striking broad absorption feature from ~400 to 700 nm attributed to NO<sub>2</sub>. Due to high amounts of cosmic-ray-induced NO<sub>2</sub>, these features act almost as a continuum in the visible (making the sky brownish-red), stronger than the 600 nm O<sub>3</sub> feature previously mentioned, and could potentially be misinterpreted as a steeper Rayleigh slope. We propose the NO<sub>2</sub> feature as a spectral “marker” of N<sub>2</sub>–O<sub>2</sub> atmospheres which are subject to cosmic rays (see also Airapetian et al. 2017b).

The IR spectrum (Figure 5, lower panel) shows a direct comparison of the 15% CO<sub>2</sub> runs, where the flaring case leads to Earth-like temperatures of 288 K in Figure 3. Again, the effect of varying composition was minor (not shown). As expected, the CH<sub>4</sub> features in the mid IR, coinciding with H<sub>2</sub>O features, are significantly reduced because of reduced CH<sub>4</sub> in the flaring runs. Similar to Tabataba-Vakili et al. (2016) and Scheucher et al. (2018), strong flare features from HNO<sub>3</sub> occur around 11 and 21 μm, but the O<sub>3</sub> absorption feature around 9.6 μm is greatly reduced.

Around 5.3 μm, we see a narrow but distinct absorption feature around 10 ppm (in  $\delta(\lambda)$ ) above the lower-atmosphere H<sub>2</sub>O absorption background. On the modern Earth, there is a band at 5.3 μm from NO via stratospheric N<sub>2</sub>O oxidation which varies considerably with geomagnetic activity, due to fast solar wind, CIRs and CMEs, as well as from extra NO production in the upper mesosphere/lower thermosphere from far-UV and EUV photoionization, and particle impact ionization. Therefore the strength of this NO feature can be treated



as an SEP indicator in Earth's atmosphere (see, e.g., Airapetian et al. 2017b). However, in our modeled spectra, this feature (peaking at  $5.35\ \mu\text{m}$ ) has the same strength for both the flaring and the quiescent cases. We identified this as a weak absorption band of  $\text{CO}_2$ , which generally receives little attention in the literature, e.g., because of the much stronger  $\text{CO}_2$  bands in the spectral vicinity at  $4.3$  and  $4.8\ \mu\text{m}$ . This  $5.3\ \mu\text{m}$  spectral feature could therefore lead to misinterpretation of future observations because of the above discussed clear correlation with flares in Earth's atmosphere.

It is striking that there is no single significant  $\text{H}_2\text{O}$  feature in the spectrum. We tested this up to *JWST*-like spectral resolutions of  $R = 3000$  in the near-IR (not shown) by removing  $\text{H}_2\text{O}$  absorption from the spectrum. The resulting spectra showed differences of no more than 2 ppm (in  $\delta(\lambda)$ ) in selected  $\text{CH}_4$  window regions.  $\text{H}_2\text{O}$  concentrations in an Earth-like troposphere decrease rapidly with height with the existence of a cold trap, hence major  $\text{H}_2\text{O}$  absorption features arise lower down in the atmosphere. For example, in the  $15\ \mu\text{m}$   $\text{CO}_2$  band  $\text{H}_2\text{O}$  would become optically thick at 28 km in our runs shown in Figure 5, whereas  $\text{CO}_2$  makes the atmosphere opaque at heights of 61 km in transmission; thus, the absorption due to  $\text{H}_2\text{O}$  could not be measured. Similarly, between 1 and  $4\ \mu\text{m}$  all  $\text{H}_2\text{O}$  absorption bands are overlapped by strong  $\text{CH}_4$  absorption, which makes the atmosphere opaque at around 40 km. It is noteworthy, that in the absence of SEPs there is a weak feature from the  $\text{H}_2\text{O}$  absorption band around  $6\ \mu\text{m}$  as pointed out by Meadows et al. (2018) and indicated in Figure 5, which would be difficult to distinguish from background noise in our simulations.

#### 4. Summary

We performed a habitability study of Prox Cen b assuming an Earth-like atmosphere, focusing on the influence of SEPs from stellar flares upon spectral transmission features. We applied our extensive model suite discussed in Herbst et al. (2019a), which includes the calculation of SEP fluxes and spectral energy distributions, their precipitation through a planetary magnetosphere and atmosphere, cosmic-ray-induced atmospheric ionization, ion redistribution within the atmosphere, and atmospheric climate and neutral composition. Our results suggest a few words of caution for the analysis of spectra from future observations of such planets around M-dwarf stars.

Given the general lack of in situ particle measurements from flaring events of Prox Cen, we scale the known SEP flux of GLE05 measured at Earth to the intensity of the measured flare (Herbst et al. 2019b) and the orbit of Prox Cen b, then calculate the ion-pair production in a theoretical Earth-like atmosphere with elevated  $\text{CO}_2$  amounts in order to warm the planet at its position of 0.65 TSI. Together with the production and loss rates of neutral species from the redistribution of cosmic-ray-induced ions, we find steady-state climate and atmospheric compositions that enable liquid surface water. Our results suggest that SEPs might play a crucial role in efficiently warming such planets, which would otherwise be too cold to be habitable (by reducing the antigreenhouse gas  $\text{CH}_4$ ). Numerous studies (e.g., Segura et al. 2005; Rauer et al. 2011) have suggested that planets with Earth-like biomasses could develop methane abundances orders of magnitude higher than on Earth because of the different stellar spectrum (especially the reduced

UVB), which can then lead to antigreenhouse methane cooling (see Figure 3).

By including SEPs from stellar flares, strong production of cosmic-ray-induced OH efficiently reduces  $\text{CH}_4$ , hence results in temperate global average surface temperatures for all our test atmospheres. This result is exciting because strong SEPs and flares are generally considered to be unfavorable for planetary habitability, because of potentially increased atmospheric escape and increases in surface dosage. We suggest that the habitability of Earth-like planets near the outer habitable zone (HZ) of cooler stars could depend strongly on both,  $\text{CH}_4$  and  $\text{CO}_2$ . Methane, in turn, can be sensitive to cosmic-ray-induced chemistry.

We identify some key features in our synthetic planetary transmission spectra (Figure 5), some related to SEPs, and note some cautions related to the possible misinterpretation of future spectral observations.

1.  $\text{N}_2\text{--O}_2$ -dominated atmospheres could produce large cosmic-ray-induced amounts of  $\text{NO}_2$ , strongly absorbing between 400 and 700 nm. This could lead to erroneous Rayleigh slope extraction from observations, which could potentially influence estimates of, e.g., bulk atmospheric composition or/and atmospheric dust and aerosols/hazes.
2. No significant  $\text{H}_2\text{O}$  absorption feature can be seen in our modeled transmission spectra. This is because  $\text{H}_2\text{O}$  absorption bands are strongly overlapped by  $\text{CH}_4$  and  $\text{CO}_2$  absorption, which occurs higher up in the atmosphere, thus making these spectral regions opaque for radiation. One would need high-resolution spectroscopy to infer  $\text{H}_2\text{O}$  from near-mid IR transmission spectroscopy of such planets.
3. Results suggest  $\text{HNO}_3$  spectral features become apparent in the mid- and far-IR, similar to results discussed in Tabataba-Vakili et al. (2016) and Scheucher et al. (2018). These features might not only be an indicator for SPES bombarding a planet with an  $\text{N}_2\text{--O}_2$  atmosphere, but could potentially be used as an indirect hint for the presence of  $\text{H}_2\text{O}$  where one cannot see its absorption features in the spectrum.
4.  $\text{O}_3$  features are rather weak for scenarios around quiescent mid-late type M-dwarfs. This arises mainly due to photochemical responses due to the different stellar spectrum (see, e.g., Segura et al. 2005; Grenfell et al. 2012). The weakened ozone features are then even further reduced by SEPs.
5. We calculate a  $5.3\ \mu\text{m}$  feature with similar strength in both our nonflaring as well as flaring star runs. This comes from a weak  $5.35\ \mu\text{m}$  absorption band of  $\text{CO}_2$  and overlaps strongly with the  $5.3\ \mu\text{m}$  NO absorption feature that is evident after SEP events on Earth. Therefore one might misinterpret the presence of such a feature as an Earth-like  $\text{N}_2\text{--O}_2$  atmosphere under strong SEP bombardment.

In a nutshell, we applied our extensive model suite to study the influence of cosmic rays on Prox Cen b as a potentially Earth-like planet and identified some interesting spectral features with strong potential for general characterization and misinterpretation of atmospheric compositions of Earth-like planets in the HZ around M stars.

M.Sch. acknowledges support from DFG project RA 714/9-1. K.H. and J.L.G. acknowledge the International Space Science Institute and the supported International Team 464: *The Role Of Solar And Stellar Energetic Particles On (Exo) Planetary Habitability (ETERNAL, <http://www.issibern.ch/teams/exoeternal/>)*. V.S. and M.Si. acknowledge support from DFG project SI 1088/4-1. F.S. acknowledges support from DFG project SCHR 1125/3-1.

*Software:* GARLIC (Schreier et al. 2014, 2018a, 2018b), HITRAN2016 (Gordon et al. 2017), MPI Mainz Spectral Atlas (Keller-Rudek et al. 2013).

### ORCID iDs

M. Scheucher  <https://orcid.org/0000-0003-4331-2277>  
 K. Herbst  <https://orcid.org/0000-0001-5622-4829>  
 J. L. Grenfell  <https://orcid.org/0000-0003-3646-5339>  
 F. Schreier  <https://orcid.org/0000-0001-7196-6599>  
 B. Heber  <https://orcid.org/0000-0003-0960-5658>  
 M. Sinnhuber  <https://orcid.org/0000-0002-3527-9051>

### References

- Airapetian, V. S., Gloer, A., Khazanov, G. V., et al. 2017a, *ApJL*, **836**, L3  
 Airapetian, V. S., Jackman, C. H., Mlynchak, M., Danchi, W., & Hunt, L. 2017b, *NatSR*, **7**, 14141  
 Anglada-Escudé, G., Amado, P. J., Barnes, J., et al. 2016, *Natur*, **536**, 437  
 Banjac, S., Herbst, K., & Heber, B. 2019, *JGRA*, **124**, 50  
 Berdyugina, S. V., & Kuhn, J. R. 2019, *AJ*, **158**, 246  
 Bétrémieux, Y., & Kaltenegger, L. 2013, *ApJL*, **772**, L31  
 Clough, S., Kneizys, F., & Davies, R. 1989, *AtmRe*, **23**, 229  
 Cohen, O., Drake, J. J., Gloer, A., et al. 2014, *ApJ*, **790**, 57  
 Desorgher, L., Flückiger, E. O., & Gurtner, M. 2006, in 36th COSPAR Scientific Assembly, **2361**  
 Dong, C., Lingam, M., Ma, Y., & Cohen, O. 2017, *ApJL*, **837**, L26  
 Dorman, L. I., Pustil’Nik, L. A., Sternlieb, A., et al. 2004, *ITPS*, **32**, 1478  
 Gordon, I., Rothman, L., Hill, C., et al. 2017, *JQSRT*, **203**, 3  
 Grenfell, J. L., Griebmeier, J.-M., von Paris, P., et al. 2012, *AsBio*, **12**, 1109  
 Herbst, K., Grenfell, J., Sinnhuber, M., et al. 2019a, *A&A*, **631**, A101  
 Herbst, K., Kopp, A., & Heber, B. 2013, *AnGeo*, **31**, 1637  
 Herbst, K., Papaioannou, A., Banjac, S., & Heber, B. 2019b, *A&A*, **621**, A67  
 Howard, W. S., Tilley, M. A., Corbett, H., et al. 2018, *ApJL*, **860**, L30  
 Keller-Rudek, H., Moortgat, G. K., Sander, R., & Sörensen, R. 2013, *ESSD*, **5**, 365  
 Lammer, H., Selsis, F., Chassefière, E., et al. 2010, *AsBio*, **10**, 45, pMID: <https://www.ncbi.nlm.nih.gov/pubmed/20307182>  
 Manabe, S., & Wetherald, R. T. 1967, *JAtS*, **24**, 241  
 Marcq, E., Belyaev, D., Montmessin, F., et al. 2011, *Icar*, **211**, 58  
 Massie, S., & Hunten, D. 1981, *JGRC*, **86**, 9859  
 Meadows, V. S., Arney, G. N., Schwieterman, E. W., et al. 2018, *AsBio*, **18**, 133, pMID: <https://www.ncbi.nlm.nih.gov/pubmed/29431479>  
 Murphy, W. F. 1977, *JChPh*, **67**, 5877  
 Nieder, H., Winkler, H., Marsh, D. R., & Sinnhuber, M. 2014, *JGRA*, **119**, 2137  
 Porter, H. S., Jackman, C. H., & Green, A. E. S. 1976, *JChPh*, **65**, 154  
 Rauer, H., Gebauer, S., Paris, P. V., et al. 2011, *A&A*, **529**, A8  
 Reid, I. N., & Hawley, S. L. 2005, *New Light on Dark Stars: Red Dwarfs, Low-Mass Stars, Brown Dwarfs* (Berlin: Springer)  
 Rodler, F., & López-Morales, M. 2014, *ApJ*, **781**, 54  
 Sadoski, A. M., Struminsky, A. B., & Belov, A. 2018, *AstL*, **44**, 324  
 Scalzo, J., Kaltenegger, L., Segura, A., et al. 2007, *AsBio*, **7**, 85, pMID: <https://www.ncbi.nlm.nih.gov/pubmed/17407405>  
 Scheucher, M., Grenfell, J., Wunderlich, F., et al. 2018, *ApJ*, **863**, 6  
 Schreier, F., Gimeno García, S., Hedelt, P., et al. 2014, *JQRST*, **137**, 29  
 Schreier, F., Milz, M., Buehler, S. A., & von Clarmann, T. 2018a, *JQSRT*, **211**, 64  
 Schreier, F., Städt, S., Hedelt, P., & Godolt, M. 2018b, *MolAs*, **11**, 1  
 Segura, A., Kasting, J. F., Meadows, V., et al. 2005, *AsBio*, **5**, 706  
 Segura, A., Walkowicz, L. M., Meadows, V., Kasting, J., & Hawley, S. 2010, *AsBio*, **10**, 751  
 Simon Wedlund, C., Gronoff, G., Liliensten, J., Ménager, H., & Barthélemy, M. 2011, *AnGeo*, **29**, 187  
 Sinnhuber, M., Nieder, H., & Wieters, N. 2012, *SGeo*, **33**, 1281  
 Sneep, M., & Ubachs, W. 2005, *JQSRT*, **92**, 293  
 Snellen, I. 2014, *RSPTA*, **372**, 20130075  
 Struminsky, A., Sadoski, A., & Belov, A. 2017, *Cosmic Rays near Proxima Centauri b*, v2, *Zenodo*, <https://zenodo.org/record/1314441>  
 Tabataba-Vakili, F., Grenfell, J. L., Griebmeier, J.-M., & Rauer, H. 2016, *A&A*, **585**, A96  
 Thébault, E., Finlay, C. C., Beggan, C. D., et al. 2015, *EP&S*, **67**, 79  
 Tilley, M. A., Segura, A., Meadows, V. S., Hawley, S., & Davenport, J. 2019, *AsBio*, **19**, 64  
 Turbet, M., Leconte, J., Selsis, F., et al. 2016, *A&A*, **596**, A112  
 Valencia, D., Sasselov, D. D., & O’Connell, R. J. 2007, *ApJ*, **665**, 1413  
 Vidotto, A. A., Jardine, M., Morin, J., et al. 2013, *A&A*, **557**, A67  
 von Paris, P., Selsis, F., Godolt, M., et al. 2015, *Icar*, **257**, 406  
 Winkler, H., Kazeminejad, S., Sinnhuber, M., Kallenrode, M. B., & Notholt, J. 2009, *JGRD*, **114**, D00103

# 5

## Summary & Outlook

### 5.1 Summary

Exoplanet diversity is as fascinating as it is wide-ranging. Studying such planets and their atmospheres requires advanced models capable of handling a wide variety of boundary and initial conditions over wide parameter ranges. A key emerging aspect is the interplay between the incoming energy (in the form of radiation and energetic particles) and the atmospheric composition.

**Publication I** (Scheucher et al., [2020b](#)) therefore presents a substantial upgrade to the group’s climate model, with unprecedented flexibility in handling incoming radiation of diverse stellar types, as well as a wide range of atmospheric conditions and compositions. Especially the diversity of absorbing species, spectral ranges, and continua, as well as a modular approach for easy integration of new line-list, continua, or cross section data where available, makes the new radiative transfer module [REDFOX](#) truly world class amongst climate models. The fact that [REDFOX](#) is able to reproduce qualitatively atmospheric temperatures of Earth, Mars, and Venus conditions, illustrates this point. Benneke et al. ([2019b](#)) and Tsiaras et al. ([2019](#)) reported the first ever observation of [H<sub>2</sub>O](#) features in a potentially temperate sub-Neptune / super-Earth atmosphere. This marks an exciting step towards establishing the occurrence of habitable planets. Publication I

## 5. Summary & Outlook

---

applied the updated model **1D-TERRA** (i.e. **REDFOX** plus coupled updated chemistry) and calculated synthetic spectra based on theoretical Earth-like, Venus-like, and primary (**H<sub>2</sub>-He**) atmospheres. These spectra were then compared with near-**IR** transit observations of **HST** and **SST** for K2-18b. The observed strong **H<sub>2</sub>O** absorption features can be reproduced with primary atmospheres of different metallicities but results do not support heavier atmospheres and do not support a large **H<sub>2</sub>O** reservoir directly exposed to the atmosphere. Publication I suggests methane depletion in K2-18b's **H<sub>2</sub>** atmosphere, as already discussed in the literature for warmer Neptune and sub-Neptune sized exoplanets such as GJ436b or GJ 3470b (e.g. Madhusudhan and Seager, 2011; Hu et al., 2015; Benneke et al., 2019a).

**Publication II** (Scheucher et al., 2018) investigated atmospheric chemical responses to incoming **SEPs** starting with the thought experiment of placing an Earth-like planet (assuming Earth's biomass, instellation etc.) in the **HZ** around the active M-dwarf AD Leonis. Since direct observations of **SEPs** from stars other than the Sun have yet to be observed, particle bombardment fluxes of active stars upon planetary atmospheres are quite uncertain. Therefore publication II took a well observed particle event spectrum on Earth, the **Stellar Proton Event (SPE)** from 1989, scaled it to this theoretical planet around AD Leonis, and varied the **SPE** strength over a reasonable range. A central goal was to study the sensitivity of climate and **biosignature** abundances to **CRs**. The same particle fluxes were then applied to simulate the actual Earth around a hypothetically high flaring Sun, to separate out potential effects of the different stellar types. Also uncertain are the **CPEs** of neutral species due to **CRs**. Therefore, publication II also varied the **CPEs**-induced sum of nitrogen- and hydrogen-oxides (referred to as **NO<sub>x</sub>** and **HO<sub>x</sub>**) within their uncertainty ranges in Earth's atmosphere for all studied incoming **SPE** strengths. One major result of this study was that small variations in **CPEs** of **NO<sub>x</sub>** and **HO<sub>x</sub>** can lead to significantly different stratospheric temperatures, **O<sub>3</sub>** and **CH<sub>4</sub>** abundances, as well as **UV** surface dosage in the M-dwarf case. Results suggest that such effects could strongly influence spectral signatures of **biosignatures**. For Earth itself, publication II suggests that **CPE** uncertainties may play a relatively minor role, even for very strong **SEP** events. In the synthetic planetary transit spectra for the **SEP** cases, two molecules show spectral features that can be attributed to



CR-enhanced abundances, namely in NO (at  $\sim 5.3 \mu\text{m}$ ) and HNO<sub>3</sub> (beyond  $10 \mu\text{m}$ ). While NO is already known on Earth to spike during SEP events, both may be considered CR markers.

**Publication III** (Scheucher et al., 2020a) conducted a case study of the influence of CRs upon the potentially terrestrial-sized exoplanet Proxima Centauri b. An extensive model suite, also discussed in Chap. 1.3, was used to consistently calculate various phenomenon including the intrinsic SEP SED, the propagation of particles through interplanetary space around Proxima Centauri, modulation by a potential planetary magnetosphere, ionization rates for various atmospheric compositions, full ion chemical responses and CPEs, photochemical responses in the atmosphere, and the main planetary climate responses. This analysis was performed based on the Ground Level Enhancement (GLE) event measured on Earth in February 1956 (GLE05), and assumed as constant particle influxes, since Proxima Centauri is known to be a strongly flaring star. The basis atmosphere was assumed to be Earth-like, but adapted for planetary size and mass, and with increased amounts of the greenhouse gas CO<sub>2</sub> (up to 20%) in order to warm the planet well into temperate surface conditions. Surprisingly, in the absence of CRs, CH<sub>4</sub> abundances reached up to  $\sim 5300$  ppm, which absorbed incoming radiation and acted as an anti-greenhouse gas, the former effect leading to a stratospheric temperature inversion in some ways similar to the O<sub>3</sub> temperature inversion on Earth. CR-induced production of OH and subsequent destruction of CH<sub>4</sub> weakened the CH<sub>4</sub> anti-greenhouse effect, leading to heating in the presence of SEP bombardment. Large amounts of CR-induced NO<sub>2</sub> were produced with significant absorption features in the VIS spectral range, which would make Rayleigh slope extractions from observations challenging, which are commonly used to constrain atmospheric bulk composition as well as dust and aerosol abundances. With increased amounts of CO<sub>2</sub>, its spectral feature around  $5.3 \mu\text{m}$  became apparent but which overlaps with the NO feature discussed in Scheucher et al. (2018) hence questioning the broader suitability of NO as a CR marker.

### 5.2 Outlook

The recent discovery by Benneke et al. (2019b) and Tsiaras et al. (2019) of  $\text{H}_2\text{O}$  in a potentially temperate exoplanet atmosphere has shown how far we have come in our search for habitable exoplanets. What we see now in terms of potentially terrestrial exoplanetary atmospheres and exoplanetary space weather, is however likely to be just the tip of the iceberg. The field of exoplanetary space weather is young but nevertheless is growing and diversifying substantially. Observations of CMEs and SEPs from other stars are sparse but are important input to e.g. confirm whether terrestrial planets in or near the HZ around active stars (which many M-dwarf stars seem to be) can even hold on to their atmospheres. The highly anticipated launch of the next generation large space telescope, the JWST will help clarify such issues. With a number of highly capable spectrographs onboard, JWST observations are expected to help us characterize exoplanets and their atmospheres with unprecedented detail from space. These may then be followed up with high resolution spectrographs mounted on ground-based 20+ m class telescopes, such as the upcoming TMT, GMT, or ELT. In space, multiple prospects may provide invaluable new discoveries, such as the RST, or the *Decadal Survey Mission Concepts* HabEx and LUVOIR especially in combination with a *star shade*, if selected for launch. With our new model 1D-TERRA, as demonstrated for K2-18b and Proxima Centauri b, we are one of the major players investigating the impact of stellar type and exoplanetary space weather upon habitability and spectral appearance for a wide range of possible atmospheres. Furthermore we are in a position to react quickly to new discoveries. Such models however need to evolve rapidly to keep in line with the rapidly developing field. In such spirit, a dedicated working group at the *International Space Science Institute* (ISSI) in Bern was formed, and a follow up project was proposed to the *Deutsche Forschungsgemeinschaft* (DFG) as part of their priority programme *Exploring the Diversity of Extrasolar Planets* (SPP1992) in order to take 1D-TERRA and with it the whole CR model suite (Herbst et al., 2019; Scheucher et al., 2020a) to the next stage of development, by studying to what extent terrestrial worlds around cooler stars are able to retain their atmospheres, and how different atmospheres evolve for cool star systems. To address properly these questions, such a model would need to include for example:

- a physical description of atmospheric escape processes, such as hydrodynamic, *Jeans*, and non-thermal processes such as *sputtering*. To appropriately treat such processes, the model would be extended up to pressures around the exobase
- *Joule heating* from the increased CR-induced energetic electron flux may become significant for thermospheric temperatures and possibly escape processes, both with potentially significant effects on the deeper atmosphere
- A more sophisticated treatment of convection in 1D, such as *mixing-length-theory* is needed to capture dynamical changes of shorter time scales, such as variable stellar activities and transient SEP events
- In such an extended atmospheric model, additional processes of potential importance are, e.g. *ion heating*, *atomic scattering*, and *molecular diffusion*

There are further CR-induced climate relevant processes whose inclusion would further significantly enhance 1D-TERRA. These include e.g. the formation of aerosols as well as cloud nucleation, although the influence of these is debated. Inclusion of aerosols in 1D-TERRA would also enable more detailed Mars and Titan related studies, since the climates of both are known to be significantly influenced by aerosols. Proper treatment of cloud formation and scattering by cloud particles in an atmosphere, with significant impacts on the global atmospheric energy budget, would additionally open up possibilities of more detailed Venus and exo-Venus studies, as well as the interpretation of observations of other cloudy atmospheres, such as those anticipated on warm water-worlds. The coming decades will surely be fascinating to behold.



## References

- Aartsen, M. G. et al. (Aug. 2013). “Measurement of the cosmic ray energy spectrum with IceTop-73”. In: *Phys. Rev. D* 88 (4), p. 042004. DOI: [10.1103/PhysRevD.88.042004](https://doi.org/10.1103/PhysRevD.88.042004).
- Adriani, O., G. C. Barbarino, G. A. Bazilevskaya, R. Bellotti, M. Boezio, E. A. Bogomolov, L. Bonechi, M. Bongi, V. Bonvicini, S. Borisov, et al. (2011). “PAMELA measurements of cosmic-ray proton and helium spectra”. In: *Science* 332.6025, pp. 69–72. DOI: [10.1126/science.1199172](https://doi.org/10.1126/science.1199172).
- Airapetian, V. S. et al. (2020). “Impact of space weather on climate and habitability of terrestrial-type exoplanets”. In: *International Journal of Astrobiology* 19.2, pp. 136–194. DOI: [10.1017/S1473550419000132](https://doi.org/10.1017/S1473550419000132).
- Anderson, H. R. (1973). “Cosmic ray total ionization, 1970–1972”. In: *Journal of Geophysical Research (1896-1977)* 78.19, pp. 3958–3960. DOI: [10.1029/JA078i019p03958](https://doi.org/10.1029/JA078i019p03958).
- Apel, W. D. et al. (Apr. 2013). “Ankle-like feature in the energy spectrum of light elements of cosmic rays observed with KASCADE-Grande”. In: *Phys. Rev. D* 87 (8), p. 081101. DOI: [10.1103/PhysRevD.87.081101](https://doi.org/10.1103/PhysRevD.87.081101).
- Banjac, S., B. Heber, K. Herbst, L. Berger, and S. Burmeister (2019a). “On-the-Fly Calculation of Absorbed and Equivalent Atmospheric Radiation Dose in A Water Phantom with the Atmospheric Radiation Interaction Simulator (AtRIS)”. In: *Journal of Geophysical Research: Space Physics* 124.12, pp. 9774–9790. DOI: [10.1029/2019JA026622](https://doi.org/10.1029/2019JA026622).
- Banjac, S., L. Berger, S. Burmeister, J. Guo, B. Heber, K. Herbst, and R. Wimmer-Schweingruber (2019b). “Galactic Cosmic Ray induced absorbed dose rate in deep space - Accounting for detector size, shape, material, as well as for the solar modulation”. In: *J. Space Weather Space Clim.* 9, A14. DOI: [10.1051/swsc/2019014](https://doi.org/10.1051/swsc/2019014).

## REFERENCES

---

- Banjac, S., K. Herbst, and B. Heber (2019c). “The Atmospheric Radiation Interaction Simulator (AtRIS): Description and Validation”. In: *Journal of Geophysical Research: Space Physics* 124.1, pp. 50–67. DOI: [10.1029/2018JA026042](https://doi.org/10.1029/2018JA026042).
- Bazilevskaya, G. A. et al. (2008). “Cosmic Ray Induced Ion Production in the Atmosphere”. In: *Planetary Atmospheric Electricity*. Ed. by F. Leblanc, K. L. Aplin, Y. Yair, R. G. Harrison, J. P. Lebreton, and M. Blanc. New York, NY: Springer New York, pp. 149–173. ISBN: 978-0-387-87664-1. DOI: [10.1007/978-0-387-87664-1\\_10](https://doi.org/10.1007/978-0-387-87664-1_10).
- Benneke, B., H. A. Knutson, J. Lothringer, I. J. Crossfield, J. I. Moses, C. Morley, L. Kreidberg, B. J. Fulton, D. Dragomir, A. W. Howard, et al. (2019a). “A sub-Neptune exoplanet with a low-metallicity methane-depleted atmosphere and Mie-scattering clouds”. In: *Nature Astronomy* 3.9, pp. 813–821. DOI: [10.1038/s41550-019-0800-5](https://doi.org/10.1038/s41550-019-0800-5).
- Benneke, B. et al. (Dec. 2019b). “Water Vapor and Clouds on the Habitable-zone Sub-Neptune Exoplanet K2-18b”. In: *The Astrophysical Journal Letters* 887.1, p. L14. DOI: [10.3847/2041-8213/ab59dc](https://doi.org/10.3847/2041-8213/ab59dc).
- Bétrémieux, Y. and L. Kaltenegger (July 2013). “Transmission Spectrum of Earth as a Transiting Exoplanet from the Ultraviolet to the Near-Infrared”. In: *The Astrophysical Journal* 772.2, p. L31. DOI: [10.1088/2041-8205/772/2/L31](https://doi.org/10.1088/2041-8205/772/2/L31).
- Blasi, P. (2013). “Origin of Galactic Cosmic Rays”. In: *Nuclear Physics B - Proceedings Supplements* 239-240. Proceedings of the 9th workshop on Science with the New Generation of High Energy Gamma-ray Experiments: From high energy gamma sources to cosmic rays, one century after their discovery, pp. 140–147. ISSN: 0920-5632. DOI: [10.1016/j.nuclphysbps.2013.05.023](https://doi.org/10.1016/j.nuclphysbps.2013.05.023).
- Caballero-Lopez, R. A. and H. Moraal (2004). “Limitations of the force field equation to describe cosmic ray modulation”. In: *Journal of Geophysical Research: Space Physics* 109.A1. DOI: [10.1029/2003JA010098](https://doi.org/10.1029/2003JA010098).
- Candelaresi, S., A. Hillier, H. Maehara, A. Brandenburg, and K. Shibata (Aug. 2014). “Superflare Occurrence and Energies on G-, K-, and M-Type Dwarfs”. In: *The Astrophysical Journal* 792.1, p. 67. DOI: [10.1088/0004-637x/792/1/67](https://doi.org/10.1088/0004-637x/792/1/67).
- Carrington, R. C. (Nov. 1859). “Description of a Singular Appearance seen in the Sun on September 1, 1859”. In: *Monthly Notices of the Royal*

## REFERENCES

---

- Astronomical Society* 20.1, pp. 13–15. ISSN: 0035-8711. DOI: [10.1093/mnras/20.1.13](https://doi.org/10.1093/mnras/20.1.13).
- Catling, D. C. and J. F. Kasting (2017). *Atmospheric evolution on inhabited and lifeless worlds*. Cambridge University Press. ISBN: 9781139020558. DOI: [10.1017/9781139020558](https://doi.org/10.1017/9781139020558).
- Chandrasekhar, S. (1960). *Radiative transfer*. Dover Books on Physics, Engineering. Dover Publications, Inc.
- Clough, S. A., M. J. Iacono, and J.-L. Moncet (1992). “Line-by-line calculations of atmospheric fluxes and cooling rates: Application to water vapor”. In: *Journal of Geophysical Research: Atmospheres* 97.D14, pp. 15761–15785. DOI: [10.1029/92JD01419](https://doi.org/10.1029/92JD01419).
- Cockell, C. et al. (2016). “Habitability: A Review”. In: *Astrobiology* 16.1. PMID: 26741054, pp. 89–117. DOI: [10.1089/ast.2015.1295](https://doi.org/10.1089/ast.2015.1295).
- Cronin, J. W., T. K. Gaisser, and S. P. Swordy (1997). “Cosmic Rays at the Energy Frontier”. In: *Scientific American* 276.1, pp. 44–49. ISSN: 00368733, 19467087. URL: <http://www.jstor.org/stable/24993563>.
- Crutzen, P. J., I. S. A. Isaksen, and G. C. Reid (1975). “Solar Proton Events: Stratospheric Sources of Nitric Oxide”. In: *Science* 189.4201, pp. 457–459. ISSN: 0036-8075. DOI: [10.1126/science.189.4201.457](https://doi.org/10.1126/science.189.4201.457).
- Cummings, A. C., E. C. Stone, and C. D. Steenberg (Oct. 2002). “Composition of Anomalous Cosmic Rays and Other Heliospheric Ions”. In: *The Astrophysical Journal* 578.1, pp. 194–210. DOI: [10.1086/342427](https://doi.org/10.1086/342427).
- Davenport, J. R. A. (Sept. 2016). “The Kepler Catalog of Stellar Flares”. In: *The Astrophysical Journal* 829.1, p. 23. DOI: [10.3847/0004-637x/829/1/23](https://doi.org/10.3847/0004-637x/829/1/23).
- Desai, M. and J. Giacalone (2016). “Large gradual solar energetic particle events”. In: *Living Reviews in Solar Physics* 13.1, p. 3. DOI: [10.1007/s41116-016-0002-5](https://doi.org/10.1007/s41116-016-0002-5).
- Desorgher, L., E. O. Flückiger, M. Gurtner, M. R. Moser, and R. Bütikofer (2005). “ATMOCOSMICS: A GEANT 4 Code for Computing the Interaction of Cosmic Rays with the Earth’s Atmosphere”. In: *International Journal of Modern Physics A* 20.29, pp. 6802–6804. DOI: [10.1142/S0217751X05030132](https://doi.org/10.1142/S0217751X05030132).
- Dong, C., M. Jin, M. Lingam, V. S. Airapetian, Y. Ma, and B. van der Holst (2018). “Atmospheric escape from the TRAPPIST-1 planets and implications for habitability”. In: *Proceedings of the National Academy*

## REFERENCES

---

- of Sciences* 115.2, pp. 260–265. ISSN: 0027-8424. DOI: [10.1073/pnas.1708010115](https://doi.org/10.1073/pnas.1708010115).
- Drake, J. F., M. Opher, M. Swisdak, and J. N. Chamoun (Jan. 2010). “A Magnetic Reconnection Mechanism for the Generation of Anomalous Cosmic Rays”. In: *The Astrophysical Journal* 709.2, pp. 963–974. DOI: [10.1088/0004-637x/709/2/963](https://doi.org/10.1088/0004-637x/709/2/963).
- Edwards, D. (1988). “Atmospheric transmittance and radiance calculations using line-by-line computer models”. In: *Modelling of the Atmosphere*. Vol. 928, pp. 94–116. DOI: [10.1117/12.975622](https://doi.org/10.1117/12.975622).
- Favata, F. and J. Schmitt (1999). “Spectroscopic analysis of a super-hot giant flare observed on Algol by BeppoSAX on 30 August 1997”. In: *Astronomy and Astrophysics* 350, pp. 900–916. URL: <http://aa.springer.de/bibs/9350003/2300900/small.htm>.
- Ferrari, F. and E. Szuszkiewicz (2009). “Cosmic Rays: A Review for Astrobiologists”. In: *Astrobiology* 9.4, pp. 413–436. DOI: [10.1089/ast.2007.0205](https://doi.org/10.1089/ast.2007.0205).
- Franciosini, E., R. Pallavicini, and G. Tagliaferri (2001). “BeppoSAX observation of a large long-duration X-ray flare from UX Arietis”. In: *A&A* 375.1, pp. 196–204. DOI: [10.1051/0004-6361:20010830](https://doi.org/10.1051/0004-6361:20010830).
- Funke, B. et al. (2011). “Composition changes after the "Halloween" solar proton event: the High Energy Particle Precipitation in the Atmosphere (HEPPA) model versus MIPAS data intercomparison study”. In: *Atmospheric Chemistry and Physics* 11.17, pp. 9089–9139. DOI: [10.5194/acp-11-9089-2011](https://doi.org/10.5194/acp-11-9089-2011).
- Gaisser, T. K., R. Engel, and E. Resconi (2016). *Cosmic rays and particle physics*. second. Cambridge University Press. ISBN: 9780521016469. URL: <https://www.cambridge.org/de/academic/subjects/physics/cosmology-relativity-and-gravitation/cosmic-rays-and-particle-physics-2nd-edition?format=HB>.
- Gaisser, T. K. and A. M. Hillas (1977). “Reliability of the method of constant intensity cuts for reconstructing the average development of vertical showers”. In: *International Cosmic Ray Conference*. Vol. 8, pp. 353–357. URL: <http://articles.adsabs.harvard.edu/full/1977ICRC....8.353G>.
- Gebauer, S., J. L. Grenfell, R. Lehmann, and H. Rauer (2018). “Evolution of Earth-like Planetary Atmospheres around M Dwarf Stars: Assessing the



## REFERENCES

---

- Atmospheres and Biospheres with a Coupled Atmosphere Biogeochemical Model”. In: *Astrobiology* 18.7. PMID: 30035637, pp. 856–872. DOI: [10.1089/ast.2017.1723](https://doi.org/10.1089/ast.2017.1723).
- Gebauer, S., J. L. Grenfell, J. W. Stock, R. Lehmann, M. Godolt, P. von Paris, and H. Rauer (2017). “Evolution of Earth-like Extrasolar Planetary Atmospheres: Assessing the Atmospheres and Biospheres of Early Earth Analog Planets with a Coupled Atmosphere Biogeochemical Model”. In: *Astrobiology* 17.1. PMID: 28103105, pp. 27–54. DOI: [10.1089/ast.2015.1384](https://doi.org/10.1089/ast.2015.1384).
- Gieseler, J., B. Heber, and K. Herbst (2017). “An Empirical Modification of the Force Field Approach to Describe the Modulation of Galactic Cosmic Rays Close to Earth in a Broad Range of Rigidities”. In: *Journal of Geophysical Research: Space Physics* 122.11, pp. 10, 964–10, 979. DOI: [10.1002/2017JA024763](https://doi.org/10.1002/2017JA024763).
- Godolt, M., J. L. Grenfell, D. Kitzmann, M. Kunze, U. Langematz, A. B. C. Patzer, H. Rauer, and B. Stracke (July 2016). “Assessing the habitability of planets with Earth-like atmospheres with 1D and 3D climate modeling”. In: *A&A* 592, A36, A36. DOI: [10.1051/0004-6361/201628413](https://doi.org/10.1051/0004-6361/201628413).
- Godolt, M., N. Tosi, B. Stracke, J. L. Grenfell, T. Ruedas, T. Spohn, and H. Rauer (2019). “The habitability of stagnant-lid Earths around dwarf stars”. In: *A&A* 625, A12. DOI: [10.1051/0004-6361/201834658](https://doi.org/10.1051/0004-6361/201834658).
- Goody, R. M. and Y. L. Yung (Mar. 1996). *Atmospheric radiation: theoretical basis*. second. Oxford university press. ISBN: 9780195102918. URL: <https://global.oup.com/academic/product/atmospheric-radiation-theoretical-basis-9780195102918>.
- Gopalswamy, N., S. Akiyama, and S. Yashiro (2008). “Major solar flares without coronal mass ejections”. In: *Proceedings of the International Astronomical Union* 4.S257, pp. 283–286. DOI: [10.1017/S174392130902941X](https://doi.org/10.1017/S174392130902941X).
- Gopalswamy, N., P. Mäkelä, S. Akiyama, S. Yashiro, H. Xie, N. Thakur, and S. W. Kahler (June 2015). “Large solar energetic particle events associated with filament eruptions outside active regions”. In: *The Astrophysical Journal* 806.1, p. 8. DOI: [10.1088/0004-637x/806/1/8](https://doi.org/10.1088/0004-637x/806/1/8).
- Gordon, I. et al. (2017). “The HITRAN2016 molecular spectroscopic database”. In: *Journal of Quantitative Spectroscopy and Radiative Transfer* 203. HITRAN2016 Special Issue, pp. 3–69. ISSN: 0022-4073. DOI: [10.1016/j.jqsrt.2017.06.038](https://doi.org/10.1016/j.jqsrt.2017.06.038).

## REFERENCES

---

- Grenfell, J. L., S. Gebauer, M. Godolt, K. Palczynski, H. Rauer, J. Stock, P. von Paris, R. Lehmann, and F. Selsis (2013). “Potential Biosignatures in Super-Earth Atmospheres II. Photochemical Responses”. In: *Astrobiology* 13.5. PMID: 23683046, pp. 415–438. DOI: [10.1089/ast.2012.0926](https://doi.org/10.1089/ast.2012.0926).
- Grenfell, J. L., J.-M. Grießmeier, P. von Paris, A. B. C. Patzer, H. Lammer, B. Stracke, S. Gebauer, F. Schreier, and H. Rauer (Dec. 2012). “Response of Atmospheric Biomarkers to NO<sub>x</sub>-Induced Photochemistry Generated by Stellar Cosmic Rays for Earth-like Planets in the Habitable Zone of M Dwarf Stars”. In: *Astrobiology* 12, pp. 1109–1122. DOI: [10.1089/ast.2011.0682](https://doi.org/10.1089/ast.2011.0682).
- Grenfell, J. L. (2017). “A review of exoplanetary biosignatures”. In: *Physics Reports* 713. A Review of Exoplanetary Biosignatures, pp. 1–17. ISSN: 0370-1573. DOI: [10.1016/j.physrep.2017.08.003](https://doi.org/10.1016/j.physrep.2017.08.003).
- Grenfell, J. L., J.-M. Grießmeier, B. Patzer, H. Rauer, A. Segura, A. Stadelmann, B. Stracke, R. Titz, and P. Von Paris (2007). “Biomarker Response to Galactic Cosmic Ray-Induced NO<sub>x</sub> And The Methane Greenhouse Effect in The Atmosphere of An Earth-Like Planet Orbiting An M Dwarf Star”. In: *Astrobiology* 7.1. PMID: 17407408, pp. 208–221. DOI: [10.1089/ast.2006.0129](https://doi.org/10.1089/ast.2006.0129).
- Hairer, E. and G. Wanner (1996). *Solving ordinary differential equations II. Stiff and Differential-Algebraic Problems*. 2nd ed. Springer Berlin Heidelberg. DOI: [10.1007/978-3-642-05221-7](https://doi.org/10.1007/978-3-642-05221-7).
- Helled, R., N. Nettelmann, and T. Guillot (Mar. 2020). “Uranus and Neptune: Origin, Evolution and Internal Structure”. In: *Space Science Reviews* 216.3, p. 38. ISSN: 1572-9672. DOI: [10.1007/s11214-020-00660-3](https://doi.org/10.1007/s11214-020-00660-3).
- Heng, K. (2017). *Exoplanetary atmospheres: theoretical concepts and foundations*. Vol. 30. Princeton Series in Astrophysics. Princeton University Press. ISBN: 9780691166988. URL: <https://press.princeton.edu/books/paperback/9780691166988/exoplanetary-atmospheres>.
- Heng, K., M. Malik, and D. Kitzmann (Aug. 2018). “Analytical Models of Exoplanetary Atmospheres. VI. Full Solutions for Improved Two-stream Radiative Transfer, Including Direct Stellar Beam”. In: *The Astrophysical Journal Supplement Series* 237.2, p. 29. DOI: [10.3847/1538-4365/aad199](https://doi.org/10.3847/1538-4365/aad199).

## REFERENCES

- Herbst, K., A. Kopp, and B. Heber (2013). “Influence of the terrestrial magnetic field geometry on the cutoff rigidity of cosmic ray particles”. In: vol. 31. 10, pp. 1637–1643. DOI: [10.5194/angeo-31-1637-2013](https://doi.org/10.5194/angeo-31-1637-2013).
- Herbst, K., K. Scherer, S. E. S. Ferreira, L. R. Baalman, N. E. Engelbrecht, H. Fichtner, J. Kleimann, R. D. T. Strauss, D. M. Moeketsi, and S. Mohamed (July 2020). “On the Diversity of M-star Astrospheres and the Role of Galactic Cosmic Rays Within”. In: *The Astrophysical Journal* 897.2, p. L27. DOI: [10.3847/2041-8213/ab9df3](https://doi.org/10.3847/2041-8213/ab9df3).
- Herbst, K. et al. (2019). “A new model suite to determine the influence of cosmic rays on (exo)planetary atmospheric biosignatures - Validation based on modern Earth”. In: *A&A* 631, A101. DOI: [10.1051/0004-6361/201935888](https://doi.org/10.1051/0004-6361/201935888).
- Hess, V. F. (1912). “Observations of the penetrating radiation on seven balloon flights”. In: *Physik. Zeitschr* XIII, pp. 1084–1091. URL: <https://www.mpi-hd.mpg.de/hfm/HESS/public/HessArticle.pdf>.
- Hillas, A. M. (Apr. 2005). “Can diffusive shock acceleration in supernova remnants account for high-energy galactic cosmic rays?” In: *Journal of Physics G: Nuclear and Particle Physics* 31.5, R95–R131. DOI: [10.1088/0954-3899/31/5/r02](https://doi.org/10.1088/0954-3899/31/5/r02).
- Houdebine, E. R., B. H. Foing, and M. Rodono (Nov. 1990). “Dynamics of flares on late-type dMe stars. I. Flare mass ejections and stellar evolution.” In: *A&A* 238, p. 249. URL: <https://ui.adsabs.harvard.edu/abs/1990A&A...238..249H>.
- Hu, R., S. Seager, and Y. L. Yung (June 2015). “Helium Atmospheres on Warm Neptune- and Sub-Neptune-Sized Exoplanets and Applications to GJ 436b”. In: *The Astrophysical Journal* 807.1, p. 8. DOI: [10.1088/0004-637x/807/1/8](https://doi.org/10.1088/0004-637x/807/1/8).
- Huang, X. and Y. L. Yung (July 2004). “A Common Misunderstanding about the Voigt Line Profile”. In: *Journal of the Atmospheric Sciences* 61.13, pp. 1630–1632. ISSN: 0022-4928. DOI: [10.1175/1520-0469\(2004\)061<1630:ACMATV>2.0.CO;2](https://doi.org/10.1175/1520-0469(2004)061<1630:ACMATV>2.0.CO;2).
- Irwin, P., N. Teanby, R. de Kok, L. Fletcher, C. Howett, C. Tsang, C. Wilson, S. Calcutt, C. Nixon, and P. Parrish (2008). “The NEMESIS planetary atmosphere radiative transfer and retrieval tool”. In: *Journal of Quantitative Spectroscopy and Radiative Transfer* 109.6. Spectroscopy

## REFERENCES

---

- and Radiative Transfer in Planetary Atmospheres, pp. 1136–1150. ISSN: 0022-4073. DOI: [10.1016/j.jqsrt.2007.11.006](https://doi.org/10.1016/j.jqsrt.2007.11.006).
- Jackman, C. H., J. E. Frederick, and R. S. Stolarski (1980). “Production of odd nitrogen in the stratosphere and mesosphere: An intercomparison of source strengths”. In: *Journal of Geophysical Research: Oceans* 85.C12, pp. 7495–7505. DOI: [10.1029/JC085iC12p07495](https://doi.org/10.1029/JC085iC12p07495).
- Jackman, C. H., M. T. DeLand, G. J. Labow, E. L. Fleming, D. K. Weisenstein, M. K. W. Ko, M. Sinnhuber, and J. M. Russell (2005). “Neutral atmospheric influences of the solar proton events in October–November 2003”. In: *Journal of Geophysical Research: Space Physics* 110.A9. DOI: [10.1029/2004JA010888](https://doi.org/10.1029/2004JA010888).
- Jackman, C. H., R. D. McPeters, G. J. Labow, E. L. Fleming, C. J. Praderas, and J. M. Russell (2001). “Northern hemisphere atmospheric effects due to the July 2000 Solar Proton Event”. In: *Geophysical Research Letters* 28.15, pp. 2883–2886. DOI: [10.1029/2001GL013221](https://doi.org/10.1029/2001GL013221).
- Joseph, J. H., W. J. Wiscombe, and J. A. Weinman (Dec. 1976). “The Delta-Eddington Approximation for Radiative Flux Transfer”. In: *Journal of the Atmospheric Sciences* 33.12, pp. 2452–2459. ISSN: 0022-4928. DOI: [10.1175/1520-0469\(1976\)033<2452:TDEAFR>2.0.CO;2](https://doi.org/10.1175/1520-0469(1976)033<2452:TDEAFR>2.0.CO;2).
- Kallenrode, M. (Apr. 2003). “Current views on impulsive and gradual solar energetic particle events”. In: *Journal of Physics G: Nuclear and Particle Physics* 29.5, pp. 965–981. DOI: [10.1088/0954-3899/29/5/316](https://doi.org/10.1088/0954-3899/29/5/316).
- Kaltenegger, L., W. A. Traub, and K. W. Jucks (Mar. 2007). “Spectral Evolution of an Earth-like Planet”. In: *The Astrophysical Journal* 658.1, pp. 598–616. DOI: [10.1086/510996](https://doi.org/10.1086/510996).
- Kasting, J. F. and T. P. Ackerman (Dec. 1986). “Climatic Consequences of Very High Carbon Dioxide Levels in the Earth’s Early Atmosphere”. In: *Science* 234, pp. 1383–1385. DOI: [10.1126/science.234.4782.1383](https://doi.org/10.1126/science.234.4782.1383).
- Kasting, J. F., D. P. Whitmire, and R. T. Reynolds (1993). “Habitable Zones around Main Sequence Stars”. In: *Icarus* 101.1, pp. 108–128. ISSN: 0019-1035. DOI: [10.1006/icar.1993.1010](https://doi.org/10.1006/icar.1993.1010).
- Keles, E., J. L. Grenfell, M. Godolt, B. Stracke, and H. Rauer (2018). “The Effect of Varying Atmospheric Pressure upon Habitability and Biosignatures of Earth-like Planets”. In: *Astrobiology* 18.2. PMID: 29364704, pp. 116–132. DOI: [10.1089/ast.2016.1632](https://doi.org/10.1089/ast.2016.1632).

## REFERENCES

- Koch, D. G. et al. (Mar. 2010). “Kepler Mission Design, Realized Photometric Performance, and Early Science”. In: *The Astrophysical Journal* 713.2, pp. L79–L86. DOI: [10.1088/2041-8205/713/2/179](https://doi.org/10.1088/2041-8205/713/2/179).
- Kopparapu, R. K., R. Ramirez, J. F. Kasting, V. Eymet, T. D. Robinson, S. Mahadevan, R. C. Terrien, S. Domagal-Goldman, V. Meadows, and R. Deshpande (Feb. 2013). “Habitable zones around main-sequence stars: new estimates”. In: *The Astrophysical Journal* 765.2, p. 131. DOI: [10.1088/0004-637x/765/2/131](https://doi.org/10.1088/0004-637x/765/2/131).
- Kopparapu, R. K., E. T. Wolf, G. Arney, N. E. Batalha, J. Haqq-Misra, S. L. Grimm, and K. Heng (Aug. 2017). “Habitable Moist Atmospheres on Terrestrial Planets near the Inner Edge of the Habitable Zone around M Dwarfs”. In: *The Astrophysical Journal* 845.1, p. 5. DOI: [10.3847/1538-4357/aa7cf9](https://doi.org/10.3847/1538-4357/aa7cf9).
- Kraft, R. P. (1967). “Studies of stellar rotation. V. The dependence of rotation on age among solar-type stars”. In: *The Astrophysical Journal* 150, p. 551. DOI: [10.1086/149359](https://doi.org/10.1086/149359).
- Li, G., A. Shalchi, X. Ao, G. Zank, and O. Verkhoglyadova (2012). “Particle acceleration and transport at an oblique CME-driven shock”. In: *Advances in Space Research* 49.6, pp. 1067–1075. ISSN: 0273-1177. DOI: <https://doi.org/10.1016/j.asr.2011.12.027>.
- Liou, K.-n. (July 1974). “Analytic Two-Stream and Four-Stream Solutions for Radiative Transfer”. In: *Journal of the Atmospheric Sciences* 31.5, pp. 1473–1475. ISSN: 0022-4928. DOI: [10.1175/1520-0469\(1974\)031<1473:ATSAFS>2.0.CO;2](https://doi.org/10.1175/1520-0469(1974)031<1473:ATSAFS>2.0.CO;2).
- Lynch, B. J., S. Masson, Y. Li, C. R. DeVore, J. G. Luhmann, S. K. Antiochos, and G. H. Fisher (2016). “A model for stealth coronal mass ejections”. In: *Journal of Geophysical Research: Space Physics* 121.11, pp. 10, 677–10, 697. DOI: [10.1002/2016JA023432](https://doi.org/10.1002/2016JA023432).
- Lynden-Bell, R. M., S. C. Morris, J. D. Barrow, J. L. Finney, and C. Harper (2010). *Water and life: the unique properties of H2O*. CRC Press. ISBN: 9781439803561. URL: <https://www.routledge.com/Water-and-Life-The-Unique-Properties-of-H2O/Lynden-Bell-Morris-Barrow-Finney-Harper/p/book/9781439803561>.
- Madhusudhan, N. and S. Seager (Feb. 2011). “High Metallicity and Non-Equilibrium Chemistry in the Dayside Atmosphere of Hot-Neptune GJ

## REFERENCES

---

- 436b”. In: *The Astrophysical Journal* 729.1, p. 41. DOI: [10.1088/0004-637x/729/1/41](https://doi.org/10.1088/0004-637x/729/1/41).
- Maehara, H., T. Shibayama, S. Notsu, Y. Notsu, T. Nagao, S. Kusaba, S. Honda, D. Nogami, and K. Shibata (May 2012). “Superflares on solar-type stars”. In: *Nature* 485.7399, pp. 478–481. ISSN: 1476-4687. DOI: [10.1038/nature11063](https://doi.org/10.1038/nature11063).
- Maehara, H., T. Shibayama, Y. Notsu, S. Notsu, S. Honda, D. Nogami, and K. Shibata (Apr. 2015). “Statistical properties of superflares on solar-type stars based on 1-min cadence data”. In: *Earth, Planets and Space* 67.1, p. 59. ISSN: 1880-5981. DOI: [10.1186/s40623-015-0217-z](https://doi.org/10.1186/s40623-015-0217-z).
- Mayor, M. and D. Queloz (Nov. 1995). “A Jupiter-mass companion to a solar-type star”. In: *Nature* 378.6555, pp. 355–359. ISSN: 1476-4687. DOI: [10.1038/378355a0](https://doi.org/10.1038/378355a0).
- McComas, D. J. et al. (2007). “Understanding coronal heating and solar wind acceleration: Case for in situ near-Sun measurements”. In: *Reviews of Geophysics* 45.1. DOI: [10.1029/2006RG000195](https://doi.org/10.1029/2006RG000195).
- Meador, W. E. and W. R. Weaver (Mar. 1980). “Two-Stream Approximations to Radiative Transfer in Planetary Atmospheres: A Unified Description of Existing Methods and a New Improvement”. In: *Journal of the Atmospheric Sciences* 37.3, pp. 630–643. ISSN: 0022-4928. DOI: [10.1175/1520-0469\(1980\)037<0630:TSATRT>2.0.CO;2](https://doi.org/10.1175/1520-0469(1980)037<0630:TSATRT>2.0.CO;2).
- Meadows, V. S. and D. Crisp (1996). “Ground-based near-infrared observations of the Venus nightside: The thermal structure and water abundance near the surface”. In: *Journal of Geophysical Research: Planets* 101.E2, pp. 4595–4622. DOI: [10.1029/95JE03567](https://doi.org/10.1029/95JE03567).
- Mewaldt, R. A., C. M. S. Cohen, A. W. Labrador, R. A. Leske, G. M. Mason, M. I. Desai, M. D. Looper, J. E. Mazur, R. S. Selesnick, and D. K. Haggerty (2005). “Proton, helium, and electron spectra during the large solar particle events of October–November 2003”. In: *Journal of Geophysical Research: Space Physics* 110.A9. DOI: [10.1029/2005JA011038](https://doi.org/10.1029/2005JA011038).
- Mewaldt, R. A. et al. (2001). “Long-term fluences of energetic particles in the heliosphere”. In: vol. 598. 1, pp. 165–170. DOI: [10.1063/1.1433995](https://doi.org/10.1063/1.1433995).
- Mironova, I. A., K. L. Aplin, F. Arnold, G. A. Bazilevskaya, R. G. Harrison, A. A. Krivolutsky, K. A. Nicoll, E. V. Rozanov, E. Turunen, and I. G. Usoskin (Nov. 2015). “Energetic Particle Influence on the Earth’s

## REFERENCES

- Atmosphere”. In: *Space Science Reviews* 194.1, pp. 1–96. ISSN: 1572-9672. DOI: [10.1007/s11214-015-0185-4](https://doi.org/10.1007/s11214-015-0185-4).
- Moraal, H. (June 2013). “Cosmic-Ray Modulation Equations”. In: *Space Science Reviews* 176.1, pp. 299–319. ISSN: 1572-9672. DOI: [10.1007/s11214-011-9819-3](https://doi.org/10.1007/s11214-011-9819-3).
- Morbidelli, A., J. Chambers, J. I. Lunine, J. M. Petit, F. Robert, G. B. Valsecchi, and K. E. Cyr (2000). “Source regions and timescales for the delivery of water to the Earth”. In: *Meteoritics & Planetary Science* 35.6, pp. 1309–1320. DOI: [10.1111/j.1945-5100.2000.tb01518.x](https://doi.org/10.1111/j.1945-5100.2000.tb01518.x).
- Muheki, P., E. W. Guenther, T. Mutabazi, and E. Jurua (2020). “High-resolution spectroscopy of flares and CMEs on AD Leonis”. In: *A&A* 637, A13. DOI: [10.1051/0004-6361/201936904](https://doi.org/10.1051/0004-6361/201936904).
- Muller, H.-R., P. C. Frisch, V. Florinski, and G. P. Zank (Aug. 2006). “Heliospheric Response to Different Possible Interstellar Environments”. In: *The Astrophysical Journal* 647.2, pp. 1491–1505. DOI: [10.1086/505588](https://doi.org/10.1086/505588).
- Neher, H. V. (1971). “Cosmic rays at high latitudes and altitudes covering four solar maxima”. In: *Journal of Geophysical Research (1896-1977)* 76.7, pp. 1637–1651. DOI: [10.1029/JA076i007p01637](https://doi.org/10.1029/JA076i007p01637).
- Neher, H. V. (1967). “Cosmic-ray particles that changed from 1954 to 1958 to 1965”. In: *Journal of Geophysical Research (1896-1977)* 72.5, pp. 1527–1539. DOI: [10.1029/JZ072i005p01527](https://doi.org/10.1029/JZ072i005p01527).
- Notsu, Y., H. Maehara, S. Honda, S. L. Hawley, J. R. A. Davenport, K. Namekata, S. Notsu, K. Ikuta, D. Nogami, and K. Shibata (May 2019). “Do Kepler Superflare Stars Really Include Slowly Rotating Sun-like Stars?—Results Using APO 3.5 m Telescope Spectroscopic Observations and Gaia-DR2 Data”. In: *The Astrophysical Journal* 876.1, p. 58. DOI: [10.3847/1538-4357/ab14e6](https://doi.org/10.3847/1538-4357/ab14e6).
- Notsu, Y., T. Shibayama, H. Maehara, S. Notsu, T. Nagao, S. Honda, T. T. Ishii, D. Nogami, and K. Shibata (June 2013). “Superflares on solar-type stars observed with Kepler II. Photometric variability of superflare-generating stars: a signature of stellar rotation and starspots”. In: *The Astrophysical Journal* 771.2, p. 127. DOI: [10.1088/0004-637x/771/2/127](https://doi.org/10.1088/0004-637x/771/2/127).
- Odert, P., M. Leitzinger, A. Hanslmeier, and H. Lammer (Aug. 2017). “Stellar coronal mass ejections – I. Estimating occurrence frequencies and mass-



## REFERENCES

---

- loss rates”. In: *Monthly Notices of the Royal Astronomical Society* 472.1, pp. 876–890. ISSN: 0035-8711. DOI: [10.1093/mnras/stx1969](https://doi.org/10.1093/mnras/stx1969).
- Owen, T. (1980). “The Search for Early Forms of Life in Other Planetary Systems: Future Possibilities Afforded by Spectroscopic Techniques”. In: *Strategies for the Search for Life in the Universe: A Joint Session of Commissions 16, 40, and 44, Held in Montreal, Canada, During the IAU General Assembly, 15 and 16 August, 1979*. Ed. by M. D. Papagiannis. Dordrecht: Springer Netherlands, pp. 177–185. ISBN: 978-94-009-9115-6. DOI: [10.1007/978-94-009-9115-6\\_17](https://doi.org/10.1007/978-94-009-9115-6_17).
- Pallavicini, R., L. Golub, R. Rosner, G. S. Vaiana, T. Ayres, and J. L. Linsky (Aug. 1981). “Relations among stellar X-ray emission observed from Einstein, stellar rotation and bolometric luminosity.” In: *The Astrophysical Journal* 248, pp. 279–290. DOI: [10.1086/159152](https://doi.org/10.1086/159152).
- Paris, P. von, S. Gebauer, M. Godolt, J. L. Grenfell, P. Hedelt, D. Kitzmann, A. B. C. Patzer, H. Rauer, and B. Stracke (2010). “The extrasolar planet Gliese 581d: a potentially habitable planet?” In: *A&A* 522, A23. DOI: [10.1051/0004-6361/201015329](https://doi.org/10.1051/0004-6361/201015329).
- Paris, P. von, F. Selsis, M. Godolt, J. L. Grenfell, H. Rauer, and B. Stracke (2015). “Effect of O<sub>3</sub> on the atmospheric temperature structure of early Mars”. In: *Icarus* 257, pp. 406–416. ISSN: 0019-1035. DOI: [10.1016/j.icarus.2015.05.028](https://doi.org/10.1016/j.icarus.2015.05.028).
- Paris, P. von, F. Selsis, D. Kitzmann, and H. Rauer (2013). “The Dependence of the Ice-Albedo Feedback on Atmospheric Properties”. In: *Astrobiology* 13.10. PMID: 24111995, pp. 899–909. DOI: [10.1089/ast.2013.0993](https://doi.org/10.1089/ast.2013.0993).
- Paris, P. von, H. Rauer, J. L. Grenfell, B. Patzer, P. Hedelt, B. Stracke, T. Trautmann, and F. Schreier (2008). “Warming the early earth—CO<sub>2</sub> reconsidered”. In: *Planetary and Space Science* 56.9, pp. 1244–1259. ISSN: 0032-0633. DOI: [10.1016/j.pss.2008.04.008](https://doi.org/10.1016/j.pss.2008.04.008).
- Parker, E. (1965). “The passage of energetic charged particles through interplanetary space”. In: *Planetary and Space Science* 13.1, pp. 9–49. ISSN: 0032-0633. DOI: [10.1016/0032-0633\(65\)90131-5](https://doi.org/10.1016/0032-0633(65)90131-5).
- Pavlov, A. A., J. F. Kasting, L. L. Brown, K. A. Rages, and R. Freedman (2000). “Greenhouse warming by CH<sub>4</sub> in the atmosphere of early Earth”. In: *Journal of Geophysical Research: Planets* 105.E5, pp. 11981–11990. DOI: [10.1029/1999JE001134](https://doi.org/10.1029/1999JE001134).



## REFERENCES

- Perryman, M. (2018). *The Exoplanet Handbook*. 2nd ed. Cambridge University Press. DOI: [10.1017/9781108304160](https://doi.org/10.1017/9781108304160).
- Pfotzer, G. (Jan. 1936). “Dreifachkoinzidenzen der Ultrastrahlung aus vertikaler Richtung in der Stratosphäre”. In: *Zeitschrift für Physik* 102.1, pp. 23–40. ISSN: 0044-3328. DOI: [10.1007/BF01336829](https://doi.org/10.1007/BF01336829).
- Pierrehumbert, R. T. (2010). *Principles of Planetary Climate*. Cambridge University Press. DOI: [10.1017/CB09780511780783](https://doi.org/10.1017/CB09780511780783).
- Porter, H. S., C. H. Jackman, and A. E. S. Green (1976). “Efficiencies for production of atomic nitrogen and oxygen by relativistic proton impact in air”. In: *The Journal of Chemical Physics* 65.1, pp. 154–167. DOI: [10.1063/1.432812](https://doi.org/10.1063/1.432812).
- Prandtl, L. (1925). “7. Bericht über Untersuchungen zur ausgebildeten Turbulenz”. In: *ZAMM - Journal of Applied Mathematics and Mechanics / Zeitschrift für Angewandte Mathematik und Mechanik* 5.2, pp. 136–139. DOI: [10.1002/zamm.19250050212](https://doi.org/10.1002/zamm.19250050212).
- Press, W. H., S. A. Teukolsky, W. T. Vetterling, and B. P. Flannery (2007). *Numerical recipes 3rd edition: The art of scientific computing*. Cambridge university press. ISBN: 9780521880688. URL: <https://www.cambridge.org/de/academic/subjects/mathematics/numerical-recipes/numerical-recipes-art-scientific-computing-3rd-edition>.
- Ramirez, R. M. (2018). “A More Comprehensive Habitable Zone for Finding Life on Other Planets”. In: *Geosciences* 8.8. ISSN: 2076-3263. DOI: [10.3390/geosciences8080280](https://doi.org/10.3390/geosciences8080280).
- Rapp, D. and P. Englander-Golden (1965). “Total Cross Sections for Ionization and Attachment in Gases by Electron Impact. I. Positive Ionization”. In: *The Journal of Chemical Physics* 43.5, pp. 1464–1479. DOI: [10.1063/1.1696957](https://doi.org/10.1063/1.1696957).
- Rauer, H., S. Gebauer, P. V. Paris, J. Cabrera, M. Godolt, J. L. Grenfell, A. Belu, F. Selsis, P. Hedelt, and F. Schreier (May 2011). “Potential biosignatures in super-Earth atmospheres. I. Spectral appearance of super-Earths around M dwarfs”. In: *A&A* 529, A8, A8. DOI: [10.1051/0004-6361/201014368](https://doi.org/10.1051/0004-6361/201014368).
- Robertson, P., S. Mahadevan, M. Endl, and A. Roy (2014). “Stellar activity masquerading as planets in the habitable zone of the M dwarf Gliese 581”. In: *Science* 345.6195, pp. 440–444. ISSN: 0036-8075. DOI: [10.1126/science.1253253](https://doi.org/10.1126/science.1253253).

## REFERENCES

---

- Rothman, L., I. Gordon, R. Barber, H. Dothe, R. Gamache, A. Goldman, V. Perevalov, S. Tashkun, and J. Tennyson (2010). “HITEMP, the high-temperature molecular spectroscopic database”. In: *Journal of Quantitative Spectroscopy and Radiative Transfer* 111.15. XVIth Symposium on High Resolution Molecular Spectroscopy (HighRus-2009), pp. 2139–2150. ISSN: 0022-4073. DOI: [10.1016/j.jqsrt.2010.05.001](https://doi.org/10.1016/j.jqsrt.2010.05.001).
- Rugheimer, S., L. Kaltenegger, A. Segura, J. Linsky, and S. Mohanty (Aug. 2015). “Effect of UV radiation on the spectral fingerprints of Earth-like planets orbiting M stars”. In: *The Astrophysical Journal* 809.1, p. 57. DOI: [10.1088/0004-637x/809/1/57](https://doi.org/10.1088/0004-637x/809/1/57).
- Rugheimer, S., L. Kaltenegger, A. Zsom, A. Segura, and D. Sasselov (2013). “Spectral Fingerprints of Earth-like Planets Around FGK Stars”. In: *Astrobiology* 13.3, pp. 251–269. DOI: [10.1089/ast.2012.0888](https://doi.org/10.1089/ast.2012.0888).
- Rusch, D., J.-C. Gérard, S. Solomon, P. Crutzen, and G. Reid (1981). “The effect of particle precipitation events on the neutral and ion chemistry of the middle atmosphere—I. Odd nitrogen”. In: *Planetary and Space Science* 29.7, pp. 767–774. ISSN: 0032-0633. DOI: [10.1016/0032-0633\(81\)90048-9](https://doi.org/10.1016/0032-0633(81)90048-9).
- Rusov, V. D., A. V. Glushkov, V. N. Vaschenko, O. T. Myhalus, Y. A. Bondartchuk, V. P. Smolyar, E. P. Linnik, S. C. Mavrodiev, and B. I. Vachev (2010). “Galactic cosmic rays-clouds effect and bifurcation model of the Earth global climate. Part 1. Theory”. In: *Journal of Atmospheric and Solar-Terrestrial Physics* 72.5, pp. 398–408. ISSN: 1364-6826. DOI: [10.1016/j.jastp.2009.12.007](https://doi.org/10.1016/j.jastp.2009.12.007).
- Sagan, C., W. R. Thompson, R. Carlson, D. Gurnett, and C. Hord (Oct. 1993). “A search for life on Earth from the Galileo spacecraft”. In: *Nature* 365.6448, pp. 715–721. ISSN: 1476-4687. DOI: [10.1038/365715a0](https://doi.org/10.1038/365715a0).
- Scalo, J. et al. (2007). “M Stars as Targets for Terrestrial Exoplanet Searches And Biosignature Detection”. In: *Astrobiology* 7.1, pp. 85–166. DOI: [10.1089/ast.2006.0125](https://doi.org/10.1089/ast.2006.0125).
- Scherer, K., A. van der Schyff, D. J. Bomans, S. E. S. Ferreira, H. Fichtner, J. Kleimann, R. D. Strauss, K. Weis, T. Wiengarten, and T. Wodzinski (2015). “Cosmic rays in astrospheres”. In: *A&A* 576, A97. DOI: [10.1051/0004-6361/201425091](https://doi.org/10.1051/0004-6361/201425091).
- Scheucher, M., J. L. Grenfell, F. Wunderlich, M. Godolt, F. Schreier, and H. Rauer (Aug. 2018). “New Insights into Cosmic-Ray-induced Biosignature

## REFERENCES

---

- Chemistry in Earth-like Atmospheres”. In: *The Astrophysical Journal* 863.1, p. 6. DOI: [10.3847/1538-4357/aacf03](https://doi.org/10.3847/1538-4357/aacf03).
- Scheucher, M., K. Herbst, V. Schmidt, J. L. Grenfell, F. Schreier, S. Banjac, B. Heber, H. Rauer, and M. Sinnhuber (Apr. 2020a). “Proxima Centauri b: A Strong Case for Including Cosmic-Ray-induced Chemistry in Atmospheric Biosignature Studies”. In: *The Astrophysical Journal* 893.1, p. 12. DOI: [10.3847/1538-4357/ab7b74](https://doi.org/10.3847/1538-4357/ab7b74).
- Scheucher, M. (2015). “2.5 D MHD Simulations of the Kelvin-Helmholtz instability under coronal plasma conditions”. Master’s thesis. Graz, Austria: Karl-Franzens University. URL: <https://unipub.uni-graz.at/obvugrhs/download/pdf/762475?originalFilename=true>.
- Scheucher, M., F. Wunderlich, J. L. Grenfell, M. Godolt, F. Schreier, D. Kappel, R. Haus, K. Herbst, and H. Rauer (July 2020b). “Consistently Simulating a Wide Range of Atmospheric Scenarios for K2-18b with a Flexible Radiative Transfer Module”. In: *The Astrophysical Journal* 898.1, p. 44. DOI: [10.3847/1538-4357/ab9084](https://doi.org/10.3847/1538-4357/ab9084).
- Schlickeiser, R. (2002). *Cosmic Ray Astrophysics*. Astronomy and Astrophysics Library book series. Springer, Berlin, Heidelberg. ISBN: 978-3-642-08573-4. DOI: [10.1007/978-3-662-04814-6](https://doi.org/10.1007/978-3-662-04814-6).
- Schreier, F., S. Gimeno García, P. Hedelt, M. Hess, J. Mendrok, M. Vasquez, and J. Xu (Apr. 2014). “GARLIC - A general purpose atmospheric radiative transfer line-by-line infrared-microwave code: Implementation and evaluation”. In: *JQSRT* 137, pp. 29–50. DOI: [10.1016/j.jqsrt.2013.11.018](https://doi.org/10.1016/j.jqsrt.2013.11.018).
- Schreier, F. (June 2009). “Comments on “A Common Misunderstanding about the Voigt Line Profile””. In: *Journal of the Atmospheric Sciences* 66.6, pp. 1860–1864. ISSN: 0022-4928. DOI: [10.1175/2009JAS2906.1](https://doi.org/10.1175/2009JAS2906.1).
- Schreier, F., M. Milz, S. A. Buehler, and T. [ Clarmann] (2018a). “Intercomparison of three microwave/infrared high resolution line-by-line radiative transfer codes”. In: *Journal of Quantitative Spectroscopy and Radiative Transfer* 211, pp. 64–77. ISSN: 0022-4073. DOI: [10.1016/j.jqsrt.2018.02.032](https://doi.org/10.1016/j.jqsrt.2018.02.032).
- Schreier, F., S. Städt, P. Hedelt, and M. Godolt (2018b). “Transmission spectroscopy with the ACE-FTS infrared spectral atlas of Earth: A model validation and feasibility study”. In: *Molecular Astrophysics* 11, pp. 1–22. ISSN: 2405-6758. DOI: [10.1016/j.molap.2018.02.001](https://doi.org/10.1016/j.molap.2018.02.001).

## REFERENCES

---

- Schwieterman, E. W. et al. (2018). “Exoplanet Biosignatures: A Review of Remotely Detectable Signs of Life”. In: *Astrobiology* 18.6, pp. 663–708. DOI: [10.1089/ast.2017.1729](https://doi.org/10.1089/ast.2017.1729).
- Seager, S., W. Bains, and R. Hu (Oct. 2013). “Biosignature gases in H<sub>2</sub>-dominated atmospheres on rocky exoplanets”. In: *The Astrophysical Journal* 777.2, p. 95. DOI: [10.1088/0004-637x/777/2/95](https://doi.org/10.1088/0004-637x/777/2/95).
- Segura, A., K. Krelowe, J. Kasting, D. Sommerlatt, V. Meadows, D. Crisp, M. Cohen, and E. Mlawer (Dec. 2003). “Ozone Concentrations and Ultraviolet Fluxes on Earth-Like Planets Around Other Stars”. In: *Astrobiology* 3, pp. 689–708. DOI: [10.1089/153110703322736024](https://doi.org/10.1089/153110703322736024).
- Segura, A., J. F. Kasting, V. Meadows, M. Cohen, J. Scalo, D. Crisp, R. A. Butler, and G. Tinetti (2005). “Biosignatures from Earth-Like Planets Around M Dwarfs”. In: *Astrobiology* 5.6, pp. 706–725. DOI: [10.1089/ast.2005.5.706](https://doi.org/10.1089/ast.2005.5.706).
- Segura, A., L. M. Walkowicz, V. Meadows, J. Kasting, and S. Hawley (2010). “The Effect of a Strong Stellar Flare on the Atmospheric Chemistry of an Earth-like Planet Orbiting an M Dwarf”. In: *Astrobiology* 10.7, pp. 751–771. DOI: [10.1089/ast.2009.0376](https://doi.org/10.1089/ast.2009.0376).
- Shettle, E. P. and J. A. Weinman (Oct. 1970). “The Transfer of Solar Irradiance Through Inhomogeneous Turbid Atmospheres Evaluated by Eddington’s Approximation”. In: *Journal of the Atmospheric Sciences* 27.7, pp. 1048–1055. ISSN: 0022-4928. DOI: [10.1175/1520-0469\(1970\)027<1048:TTOSIT>2.0.CO;2](https://doi.org/10.1175/1520-0469(1970)027<1048:TTOSIT>2.0.CO;2).
- Shibata, K. et al. (June 2013). “Can Superflares Occur on Our Sun?” In: *Publications of the Astronomical Society of Japan* 65.3. ISSN: 0004-6264. DOI: [10.1093/pasj/65.3.49](https://doi.org/10.1093/pasj/65.3.49).
- Shibayama, T., H. Maehara, S. Notsu, Y. Notsu, T. Nagao, S. Honda, T. T. Ishii, D. Nogami, and K. Shibata (Oct. 2013). “Superflares on solar-type stars observed with Kepler. I. Statistical properties of superflares”. In: *The Astrophysical Journal Supplement Series* 209.1, p. 5. DOI: [10.1088/0067-0049/209/1/5](https://doi.org/10.1088/0067-0049/209/1/5).
- Shields, A. L., S. Ballard, and J. A. Johnson (2016). “The habitability of planets orbiting M-dwarf stars”. In: *Physics Reports* 663. The habitability of planets orbiting M-dwarf stars, pp. 1–38. ISSN: 0370-1573. DOI: [10.1016/j.physrep.2016.10.003](https://doi.org/10.1016/j.physrep.2016.10.003).

## REFERENCES

- Shine, K., A. Campargue, D. Mondelain, R. McPheat, I. Ptashnik, and D. Weidmann (2016). “The water vapour continuum in near-infrared windows — Current understanding and prospects for its inclusion in spectroscopic databases”. In: 327. *New Visions of Spectroscopic Databases, Volume II*, pp. 193–208. DOI: [10.1016/j.jms.2016.04.011](https://doi.org/10.1016/j.jms.2016.04.011).
- Shine, K., I. Ptashnik, and G. Rädcl (2012). “The Water Vapour Continuum: Brief History and Recent Developments”. In: *Surv. Geophys.* 33.3-4, pp. 535–555. DOI: [10.1007/s10712-011-9170-y](https://doi.org/10.1007/s10712-011-9170-y).
- Simpson, J. A. (1983). “Elemental and Isotopic Composition of the Galactic Cosmic Rays”. In: *Annual Review of Nuclear and Particle Science* 33.1, pp. 323–382. DOI: [10.1146/annurev.ns.33.120183.001543](https://doi.org/10.1146/annurev.ns.33.120183.001543).
- Sing, D. K. et al. (Jan. 2016). “A continuum from clear to cloudy hot-Jupiter exoplanets without primordial water depletion”. In: *Nature* 529.7584, pp. 59–62. ISSN: 1476-4687. DOI: [10.1038/nature16068](https://doi.org/10.1038/nature16068).
- Sinnhuber, M., H. Nieder, and N. Wieters (Nov. 2012). “Energetic Particle Precipitation and the Chemistry of the Mesosphere/Lower Thermosphere”. In: *Surveys in Geophysics* 33.6, pp. 1281–1334. ISSN: 1573-0956. DOI: [10.1007/s10712-012-9201-3](https://doi.org/10.1007/s10712-012-9201-3).
- Sinnhuber, M. and B. Funke (2020). “Chapter 9 - Energetic electron precipitation into the atmosphere”. In: *The Dynamic Loss of Earth’s Radiation Belts*. Ed. by A. N. Jaynes and M. E. Usanova. Elsevier, pp. 279–321. ISBN: 978-0-12-813371-2. DOI: [10.1016/B978-0-12-813371-2.00009-3](https://doi.org/10.1016/B978-0-12-813371-2.00009-3).
- Smart, D. F., M. A. Shea, and E. O. Flückiger (2000). “Magnetospheric Models and Trajectory Computations”. In: *Cosmic Rays and Earth*. Ed. by J. W. Bieber, E. Eroshenko, P. Evenson, E. O. Flückiger, and R. Kallenbach. Dordrecht: Springer Netherlands, pp. 305–333. ISBN: 978-94-017-1187-6. DOI: [10.1007/978-94-017-1187-6\\_15](https://doi.org/10.1007/978-94-017-1187-6_15).
- Smart, D. F., M. A. Shea, A. J. Tylka, and P. R. Boberg (2006). “A geomagnetic cutoff rigidity interpolation tool: Accuracy verification and application to space weather”. In: *Advances in Space Research* 37.6. Space weather prediction: Applications and validation, pp. 1206–1217. ISSN: 0273-1177. DOI: [10.1016/j.asr.2006.02.011](https://doi.org/10.1016/j.asr.2006.02.011).
- Solomon, S., D. Rusch, J. Gérard, G. Reid, and P. Crutzen (1981). “The effect of particle precipitation events on the neutral and ion chemistry of the middle atmosphere: II. Odd hydrogen”. In: *Planetary and Space Science*

## REFERENCES

---

- 29.8, pp. 885–893. ISSN: 0032-0633. DOI: [10.1016/0032-0633\(81\)90078-7](https://doi.org/10.1016/0032-0633(81)90078-7).
- Stamnes, K., S.-C. Tsay, W. Wiscombe, and K. Jayaweera (June 1988). “Numerically stable algorithm for discrete-ordinate-method radiative transfer in multiple scattering and emitting layered media”. In: *Appl. Opt.* 27.12, pp. 2502–2509. DOI: [10.1364/AO.27.002502](https://doi.org/10.1364/AO.27.002502).
- Tabataba-Vakili, F., J. L. Grenfell, J.-M. Grießmeier, and H. Rauer (Jan. 2016). “Atmospheric effects of stellar cosmic rays on Earth-like exoplanets orbiting M-dwarfs”. In: *A&A* 585, A96, A96. DOI: [10.1051/0004-6361/201425602](https://doi.org/10.1051/0004-6361/201425602).
- Takagi, M., K. Suzuki, H. Sagawa, P. Baron, J. Mendrok, Y. Kasai, and Y. Matsuda (2010). “Influence of CO<sub>2</sub> line profiles on radiative and radiative-convective equilibrium states of the Venus lower atmosphere”. In: *Journal of Geophysical Research: Planets* 115.E6. DOI: [10.1029/2009JE003488](https://doi.org/10.1029/2009JE003488).
- Tennyson, J. et al. (2016). “The ExoMol database: Molecular line lists for exoplanet and other hot atmospheres”. In: *Journal of Molecular Spectroscopy* 327. New Visions of Spectroscopic Databases, Volume II, pp. 73–94. ISSN: 0022-2852. DOI: [10.1016/j.jms.2016.05.002](https://doi.org/10.1016/j.jms.2016.05.002).
- Thoudam, S., J. P. Rachen, A. van Vliet, A. Achterberg, S. Buitink, H. Falcke, and J. R. Hörandel (2016). “Cosmic-ray energy spectrum and composition up to the ankle: the case for a second Galactic component”. In: *A&A* 595, A33. DOI: [10.1051/0004-6361/201628894](https://doi.org/10.1051/0004-6361/201628894).
- Toon, O. B., C. P. McKay, T. P. Ackerman, and K. Santhanam (1989). “Rapid calculation of radiative heating rates and photodissociation rates in inhomogeneous multiple scattering atmospheres”. In: *Journal of Geophysical Research: Atmospheres* 94.D13, pp. 16287–16301. DOI: [10.1029/JD094iD13p16287](https://doi.org/10.1029/JD094iD13p16287).
- Tsiaras, A., I. P. Waldmann, G. Tinetti, J. Tennyson, and S. N. Yurchenko (2019). “Water vapour in the atmosphere of the habitable-zone eight-Earth-mass planet K2-18 b”. In: *Nature Astronomy*. ISSN: 2397-3366. DOI: [10.1038/s41550-019-0878-9](https://doi.org/10.1038/s41550-019-0878-9).
- Usoskin, I. G. and G. A. Kovaltsov (2006). “Cosmic ray induced ionization in the atmosphere: Full modeling and practical applications”. In: *Journal of Geophysical Research: Atmospheres* 111.D21. DOI: [10.1029/2006JD007150](https://doi.org/10.1029/2006JD007150).

## REFERENCES

---

- Velinov, P. I. and L. N. Mateev (Feb. 1990). “The response of the middle atmosphere to the effects of galactic cosmic rays.” In: *Geomagnetism and Aeronomy* 30.4, pp. 500–504.
- Verronen, P. T., M. E. Andersson, D. R. Marsh, T. Kovács, and J. M. C. Plane (2016). “WACCM-D—Whole Atmosphere Community Climate Model with D-region ion chemistry”. In: *Journal of Advances in Modeling Earth Systems* 8.2, pp. 954–975. DOI: [10.1002/2015MS000592](https://doi.org/10.1002/2015MS000592).
- Vitt, F. M. and C. H. Jackman (1996). “A comparison of sources of odd nitrogen production from 1974 through 1993 in the Earth’s middle atmosphere as calculated using a two-dimensional model”. In: *Journal of Geophysical Research: Atmospheres* 101.D3, pp. 6729–6739. DOI: [10.1029/95JD03386](https://doi.org/10.1029/95JD03386).
- Walker, J. C. G., P. B. Hays, and J. F. Kasting (1981). “A negative feedback mechanism for the long-term stabilization of Earth’s surface temperature”. In: *Journal of Geophysical Research: Oceans* 86.C10, pp. 9776–9782. DOI: [10.1029/JC086iC10p09776](https://doi.org/10.1029/JC086iC10p09776).
- Walter, F. M. (Apr. 1981). “On the coronae of rapidly rotating stars. II. A period-activity relation in G stars.” In: *The Astrophysical Journal* 245, pp. 677–681. DOI: [10.1086/158843](https://doi.org/10.1086/158843).
- Walter, F. M. (Feb. 1982). “On the Coronae of rapidly rotating stars. III. an improved coronal rotation-activity relation in late type dwarfs.” In: *The Astrophysical Journal* 253, pp. 745–751. DOI: [10.1086/159675](https://doi.org/10.1086/159675).
- Walter, F. M. and S. Bowyer (Apr. 1981). “On the coronae of rapidly rotating stars. I. The relation between rotation and coronal activity in RS CVn systems.” In: *The Astrophysical Journal* 245, pp. 671–676. DOI: [10.1086/158842](https://doi.org/10.1086/158842).
- Weber, E. J. and J. Davis Leverett (Apr. 1967). “The Angular Momentum of the Solar Wind”. In: *The Astrophysical Journal* 148, pp. 217–227. DOI: [10.1086/149138](https://doi.org/10.1086/149138).
- Winkler, H., S. Kazeminejad, M. Sinnhuber, M.-B. Kallenrode, and J. Notholt (2009). “Conversion of mesospheric HCl into active chlorine during the solar proton event in July 2000 in the northern polar region”. In: *Journal of Geophysical Research: Atmospheres* 114.D1. DOI: [10.1029/2008JD011587](https://doi.org/10.1029/2008JD011587).
- Wolszczan, A. and D. A. Frail (Jan. 1992). “A planetary system around the millisecond pulsar PSR1257 + 12”. In: *Nature* 355.6356, pp. 145–147. ISSN: 1476-4687. DOI: [10.1038/355145a0](https://doi.org/10.1038/355145a0).

## REFERENCES

---

- Wunderlich, F., M. Godolt, J. L. Grenfell, S. Städt, A. M. S. Smith, S. Gebauer, F. Schreier, P. Hedelt, and H. Rauer (2019). “Detectability of atmospheric features of Earth-like planets in the habitable zone around M dwarfs”. In: *A&A* 624, A49. DOI: [10.1051/0004-6361/201834504](https://doi.org/10.1051/0004-6361/201834504).
- Wunderlich, F., M. Scheucher, M. Godolt, J. L. Grenfell, F. Schreier, P. C. Schneider, D. J. Wilson, A. Sánchez López, M. López Puertas, and H. Rauer (2020). “Distinguishing between wet and dry atmospheres of TRAPPIST-1 e and f”. In: *The Astrophysical Journal* in print. arXiv: [2006.11349 \[astro-ph.EP\]](https://arxiv.org/abs/2006.11349).
- Zahnle, K. J. and J. C. G. Walker (1982). “The evolution of solar ultraviolet luminosity”. In: *Reviews of Geophysics* 20.2, pp. 280–292. DOI: [10.1029/RG020i002p00280](https://doi.org/10.1029/RG020i002p00280).
- Zank, G. P., W. K. M. Rice, and C. C. Wu (2000). “Particle acceleration and coronal mass ejection driven shocks: A theoretical model”. In: *Journal of Geophysical Research: Space Physics* 105.A11, pp. 25079–25095. DOI: [10.1029/1999JA000455](https://doi.org/10.1029/1999JA000455).
- Zdunkowski, W., T. Trautmann, and A. Bott (2007). *Radiation in the atmosphere: a course in theoretical meteorology*. Cambridge University Press. ISBN: 9780511535796. DOI: [10.1017/CB09780511535796](https://doi.org/10.1017/CB09780511535796).





## **Appendix**



T=300 [K] p=1.0 [bar] (R=50)

$\lambda$  [ $\mu\text{m}$ ]

0.2 0.4 0.6 0.8 1 2 4 6 8 10 20 40 60 80 100 200 400 600 800 1000

